HAL
open science

Nanostructured electrodeposited polymers : design and properties of films derived from thienothiophene and pyrene monomers

Gabriela Ramos Chagas

To cite this version:

Gabriela Ramos Chagas. Nanostructured electrodeposited polymers : design and properties of films derived from thienothiophene and pyrene monomers. Other. COMUE Université Côte d'Azur (2015 - 2019), 2017. English. NNT : 2017AZUR4108 . tel-01719225

HAL Id: tel-01719225

https://theses.hal.science/tel-01719225v1

Submitted on 28 Feb 2018

HAL is a multi-disciplinary open access archive for the deposit and dissemination of scientific research documents, whether they are published or not. The documents may come from teaching and research institutions in France or abroad, or from public or private research centers.

L'archive ouverte pluridisciplinaire **HAL**, est destinée au dépôt et à la diffusion de documents scientifiques de niveau recherche, publiés ou non, émanant des établissements d'enseignement et de recherche français ou étrangers, des laboratoires publics ou privés.

Université Côte d'Azur
École doctorale *« Sciences Fondamentales et Appliquées»*

Thèse de doctorat

Présentée en vue de l'obtention du
grade de docteur en Chimie
de
l'Université Côte d'Azur

par

Gabriela RAMOS CHAGAS

NANOSTRUCTURED ELECTRODEPOSITED POLYMERS: DESIGN AND PROPERTIES OF FILMS DERIVED FROM THIENOTHIOPHENE AND PYRENE MONOMERS

Dirigée par Prof. Frédéric GUITTARD et codirigée par Dr. Thierry DARMANIN

Soutenue le 27/11/2017 devant le jury composé de :

A. GAUCHER	Maitre de Conférences, HDR Université de Versailles-St Quentin, France	Rapporteur
C. GOURGON	Directeur de Recherche CNRS CEA Grenoble, France	Rapporteur
F. GUITTARD	Professeur Université Nice Sophia Antipolis, France	Directeur de thèse
T. DARMANIN	Maitre de Conférences, HDR Université Nice Sophia Antipolis, France	Co-directeur de thèse
C. DERAIL	Professeur Université de Pau et des Pays de l'Adour, France	Examinateur
D. E. WEIBEL	Associate Professor Universidade Federal do Rio Grande do Sul, Brésil	Examinateur
C. BRESSY	Maitre de Conférences, HDR Université de Toulon, France	Invité
M. L. FOCARETE	Associate Professor Universitá di Bologna, Italie	Invité

This work is dedicated to my parents,
Cristina and Francisco, who have not measured
their efforts in educating me and loving me,
always offering their best and being the best.

Acknowledgments

Firstly I want to thank to CNPq, Conselho Nacional de Desenvolvimento Científico e Tecnológico - Brazil, for the fellowship (Process Nº 202280/2014-4) that allow me to take my PhD and for the Program Science without Borders from Brazil.

To Dr. Christine Bressy, Prof. Christophe Derail, Dr. Maria Letizia Focarete, Dr. Anne Gaucher, Dr. Cecile Gourgon and Dr. Daniel Weibel who provide me the honor to join the thesis jury and evaluate my work.

To Prof. Frédéric Guittard for allowing me to integrate his group twice and welcomed me so well, offering me this amazing opportunity to guide my PhD studies. Thanks you all the opportunities you offer me, for your advices and to be always present when was necessary. For all your efforts in helping me and sincere words, thank you so much!

To Dr. Thierry Darmanin for being by my side guiding me and teaching me so patiently during this long period. Your motivation and inspiration lead us to build a beautiful work. I will be always grateful for your continuous support, availability and motivation words when I lost faith. I could not imagine having a better mentor than you for my studies. My deepest thank to you!

To Dr. Guilhem Godeau for all your help in the synthesis and experiments, for all the discussions about the results, for all the conferences presentations that you were always there listening my training, for all the manuscripts and french corrections and mainly for your advices and comments encouraging us to continue. My sincere thank you!

To Dr. Sonia Amigoni and Dr. Arnaud Zenerino for your encouragement, optimism, help and company during these 3 years of thesis.

To Prof. Rachel Méallet-Renault for our collaborative work and for receiving me in your lab as your student. It was a pleasure to meet you and to be able to work with you. I also want to thank Dr. Xiao Xie and MS Gabriela Morán for your help in the manipulation for the fluorescence and bio experiments and for always being available for a good work discussion.

To Prof. Franck Celestini and Dr. Christophe Raufaste for the beautiful work we did with the ejection tests and the bouncy droplets. I am happy to have the opportunity to work and to learn with you. Thanks Franck for the encouragement and the help in the experiments.

To all the colleagues from Surfaces and Interfaces team that received me so warmly both times I came to the lab and for the moments we shared: André, Elena, Jeanne, Marie, Ophelie, Olivier and Raziyeh. I thank to my dears Jessica and Yosra, my beloved room neighbors whom I shared many good moments; Cynthia for your friendship and for being in our side every time was necessary; Hernando, our *selfieboy!*, thank you for be such a good friend and for recording each moment together; Emna and Rawia, for being my friends since the first day even if we could only communicate by mimic. A special thank for my dear friends Cécile, Janwa and Sabri, who received all of us so lovingly! Thanks for introducing the lab, the *gateau* routine for beginners, the lab security system and shops. I will never find enough words to say how much special for me was to meet you and to be your friend. I miss you guys!

To my american sister Caroline, the one who was my friend, my sister, my teacher, my advisor, my listener. Thank you for understanding me and for sharing such good moments in the lab, on the beach, in the city and to be always open to listen and support me in anything. I hope to meet you again one day. I am already missing you!

To my dear friend Claudio for sharing with me the joys and suffering of these 3 years of PhD. I cannot imagine having a better lab mate than you who turns everything into a simple fun joke. For all

the lunches, dinners, beers, reactions and conferences: thank you, chief Claudito, for all these good (and bad) moments during these 3 years!

To all the good friends I could meet in the chemistry building: Anh, Alex, Alexandra, Cecile, Celine, Charlotte, Estelle, Hamza, Hélène, Janah, Lou, Nelli, Ngoan, Pascal, Rime, Seb, Serena, Tom and Vincent. Thank you guys for each single moment, for the picnics on the beach, for the daily lunches downstairs, for the *repas de non-permanents*, dinners, barbecues, beers, *randonnées*, day trips, conferences and events we shared. I am glad to meet each one of you and have shared special moments that I will carry with me forever.

To the good friends Nice gave me: Ana, Angelo, Maria, Mathieu, Maysa, Rogério, Rui, Sabine, Sabrina, Siguara and Wil. Thank you for being my family here, for giving me a little bit of home feeling and for all our moments together. I will never forget "The Terrace" crazy parties, the picnics on the beach, the Brazilian lunches & dinners and the salsa courses. Hope to meet all of you again in Brazil, France, Portugal, Belgium, Colombia or anywhere else in the world!

A todos os meus mestres e professores, em especial aos meus orientadores Claudia Rhoden, Nadya Silveira, Rosane Soares e Daniel Weibel pelo incentivo, apoio e inserção na vida científica. Vocês me guiaram e me levaram ao caminho que cheguei. Eu não podia ter feito escolhas melhores em cada época da minha vida. A vocês e todos os outros professores, o meu muito obrigado!

Às amigas Andresa e Daia que foram minha casa na Europa, meu chão, minha família, meu alicerce. Foi com vocês que segurei a barra do primeiro (e mais difícil) ano aqui, onde dividimos todas as alegrias e os perrengues que a vida europeia pode nos dar. Por todas as mensagens diárias, as viagens & visitas, os conselhos, as correções. O meu muito obrigado do fundo do coração, pois a minha vida aqui não teria sido a mesma sem vocês! Eu amo vocês!

À melhor geração da Química, pela amizade mais linda e sincera que se formou: Clau, Jô, Maria, Mila e Nathi, com quem parece que a distância mais uniu que afastou e o tempo mais reforçou que destruiu. Obrigada por entenderem minha ausência em alguns momentos difíceis, em muitos momentos bons e por sempre me deixaram por dentro de tudo o que acontece na vida de vocês. Obrigada pela amizade leve, sincera e leal que construímos. Eu amo vocês, minhas melhores!

Aos amigos Aline, Ana, Bruno, Camila, Cê, Cintia, Gabi, Gui, Ju, Kari, Liege, Nado, Rafa e Tintia, por estarem sempre presentes mesmo que distantes fisicamente. Obrigada meus amigos!

A toda minha família pelo amor, apoio e compreensão. Eu amo vocês!

Aos meus sogros, Suzane e Mauro, por todo apoio, incentivo e amor. Obrigada por entenderam minhas escolhas e por compartilharem cada sonho junto.

À minha vozinha Estela, minha grande companheira e confidente que sempre me dá os melhores conselhos e sabe me acalmar nas horas difíceis. Obrigada por ser minha avó, minha mãe, minha conselheira, minha parceira de viagem, minha amiga, tudo ao mesmo tempo. Obrigada por toda criação, amor e educação. Obrigada por incentivar meus estudos, meus planos e sonhar sempre muito longe comigo. Tu é o amor da minha vida, eu te amo vó!

À minha terceira avó, Ia, por me criar, me cuidar e me amar como uma filha e uma neta. Nunca vou esquecer a emoção (de ambas as partes) de ouvir tua voz pelo telefone pela primeira vez quase um mês depois que eu cheguei aqui. Obrigada por ter pra ti cada emoção de um momento vivido ou contado e por entender minha ausência. Eu te amo muito e estou louca de saudades!

À minha maninha e minha metade, Júlia, por me amar e acreditar em mim, por me incentivar quando eu tento desistir, por me abraçar quando eu preciso sem nem ao menos eu pedir. Obrigada por dividir uma vida inteira comigo e por entender minha ausência. Obrigada por ser eu: a filha, a amiga, a neta, quando eu não estou presente pra ser. Obrigada por toda ajuda, por toda compreensão, por todo apoio, por ser a outra metade de mim. Em especial, obrigada por me dar o

irmão que não tive. A ti, Nik, obrigada pela amizade e irmandade que construímos mesmo com tão pouco tempo de convivência. Eu amo vocês!

Aos meus pais, Francisco e Cristina, por tudo o que fizeram até hoje por mim. Obrigada pelo amor, carinho e por toda educação que me deram que me permitiram chegar aqui hoje. Obrigada por acreditarem em mim quando nem eu mesma era capaz. Obrigada por incentivarem e respeitarem minhas escolhas, por suportarem essa distância que tanto nos machuca, por fazerem o possível e impossível para nos ver felizes. A cada passo que dou, é pensando em vocês e em tentar agradecer e fazer valer tudo o que vocês me proporcionaram. Não existem palavras para agradecer por tudo. Eu amo vocês imensamente!

Ao meu amor, Mauro, por simplesmente ser a melhor pessoa do mundo, o amigo mais leal, o colega mais fiel, o parceiro mais dedicado, a companhia mais agradável. Obrigada por diante de tantas perguntas e pedidos, tua resposta ser sempre "SIM". Te agradeço por me dar os melhores anos da minha vida, por aceitar desbravar essa "aventura" comigo, por partir pro desconhecido sem olhar pra trás, por sair da zona de conforto e largar o certo pelo duvidoso sem nunca se arrepender, por respeitar minhas escolhas e incentivar meus passos, por vibrar pelas minhas conquistas, por aceitar todas as minhas ideias mais malucas e insanas, mas principalmente, por me amar acima de tudo. Obrigado pelo teu amor, amizade, respeito e carinho durante esses lindos 7 anos. Je t'aime!

Aos meus anjos da guarda, Vô Nando e Zizira, por onde quer que estejam, estão sempre me iluminando e me guiando. Obrigada pela proteção e benção de sempre. Levo vocês onde quer que eu vá! Saudades sempre!

Table of Contents

Introduction **1**

CHAPTER 1: State of Art **7**

1.1 WETTING THEORIES 7

1.2 BIOINSPIRED SURFACES 11

1.3 METHODS TO FABRICATE STRUCTURED SURFACES 15

1.3.1 Top-down Methods 16

1.3.2 Bottom-up methods 19

1.4 ELECTROPOLYMERIZATION OF CONDUCTING POLYMERS 22

1.4.1 Conducting polymers 22

1.4.1.1 *Pyrenes* 24

1.4.1.2 *Thiophenes* 26

1.4.2 Principles of electropolymerization 28

1.4.3 Factors that influence the electropolymerization 30

1.5 MICRO-NANOSTRUCTURED SURFACES AND THEIR POTENTIAL APPLICATIONS 34

REFERENCES OF CHAPTER 1 48

CHAPTER 2: Thienothiophenes: hydrophobicity and water adhesion **61**

2.1 STUDY THE EFFECT OF THE AROMATIC CORE 61

2.1.1 Influence of the Electrochemical Method 62

2.1.1.1 *Cyclic Voltammetry* 63

2.1.1.2 *Constant Potential* 70

2.1.1.3 *Galvanostatic deposition* 74

2.1.1.4 *Square Pulse deposition* 78

2.1.2. Influence of the Electrolyte 81

2.1.3 Discussion about the mechanism of porous structures formation 85

2.1.4 Discussion about the wettability results 89

2.2 STUDY THE EFFECT OF THE SUBTITUENTS 91

2.2.1 Monomer Synthesis 92
2.2.2 Electrochemical Polymerization and Surface Characterization 93
2.3 GENERAL DISCUSSION 103
REFERENCES OF CHAPTER 2 104
CHAPTER 3: Pyrenes: superhydrophobicity, fluorescence and anti-bioadhesion 107
3.1 INFLUENCE OF NON-FLUORINATED CHAINS 107
3.1.1 Monomer Synthesis 108
3.1.2 Electrochemical Polymerization and Surface Characterization 109
3.2 INFLUENCE OF FLUORINATED CHAINS 119
3.2.1 Monomer Synthesis 120
3.2.2 Electrochemical Polymerization and Surface Characterization 121
3.3 INFLUENCE OF THE PARAMETERS OF ELECTROPOLYMERIZATION 131
3.3.1 Influence of the Electrolyte 131
3.3.2 Influence of the Electrochemical Method 134
3.3.3 Influence of the Solvent 136
3.4 FLUORESCENCE PROPERTIES 138
3.4.1 Spectroscopic Properties of Pyrene Monomers 138
3.4.2 Spectroscopic Properties of Pyrene Polymers 138
3.5 ANTI-BACTERIAL PROPERTIES 142
3.6 COPOLYMERS Py-nF_6 *vs* Py-COOH: pH-sensitivity 148
3.6.1. Characterization of Surface Morphology and Wettability 149
3.6.2. Surface characterization after pH treatment 155
3.7 COPOLYMERS Py-OF_6 *vs* Py-Adam: water adhesion control 159
3.7.1. Characterization of Surface Morphology and Wettability 161
3.7.2. Water adhesion by ejection tests 165
3.8 GENERAL DISCUSSION 170
REFERENCES OF CHAPTER 3 172
Conclusions 177
Outlooks 185

ANNEX A1 – MONOMER SYNTHESIS 187

A1 1. SYNTHESIS OF THIENOTHIOPHENE MONOMERS 187

A1.2 SYNTHESIS OF PYRENE MONOMERS 193

ANNEX A2 – ELECTROPOLYMERIZATION PROCESS 207

A2.1 ELECTROPOLYMERIZATION OF CONDUCTING POLYMERS 207

A2.2 ELECTROPOLYMERIZATION OF ANALOGOUS SMOOTH POLYMERS 208

A2.3 OXIDATION POTENTIAL AND WORKING POTENTIAL 209

ANNEX A3 – METHODS 213

A3.1 MONOMER CHARACTERIZATION 213

A3.2 SURFACE CHARACTERIZATION 214

A3.3 BIOEXPERIMENTS 216

A3.4 EJECTION TESTS 217

List of Tables

Chapter 2

Table 2.1. Apparent contact angles of water (θ_w) and roughness data as a function of the polymer and the number of deposition scans. Polymerization at 0.1 M solution Bu_4NClO_4/dichloromethane. 68

Table 2.2. Apparent contact angles of water (θ_w) and roughness data as a function of the polymer and the deposition charge (Qs). Polymerization at 0.1 M solution Bu_4NClO_4/dichloromethane. 72

Table 2.3. Roughness data for PThienothiophene-2 electropolymerized by galvanostatic method as function of the current density (mA) and the deposition time (s). Polymerization at 0.1 M solution Bu_4NClO_4/dichloromethane..... 77

Table 2.4. Roughness data for PThienothiophene-2 electropolymerized by pulse deposition method as function of the polymerization time (t_p) and the number of repetitions/deposition time (s). Polymerization at 0.1 M solution of Bu_4NClO_4/dichloromethane. Relaxing time (t_r) = 2 s. 79

Table 2.5. Apparent contact angles for water (θ_w) and roughness data for PThienothiophene-2 electropolymerized by constant potential as a function of the electrolyte and the deposition charge. Polymerization at 0.1 M solution electrolyte/dichloromethane..... 82

Table 2.6. Apparent contact angles for water (θ_w) and roughness data for PThienothiophene-2 electropolymerized by cyclic voltammetry as a function of the electrolyte and the number of scans. Polymerization at 0.1 M solution electrolyte/dichloromethane..... 85

Table 2.7. Apparent contact angles for water (θ_w) and roughness data for PThienothiophene-2 electropolymerized by cyclic voltammetry as a function of the solvent and the number of scans. Polymerization at 0.1 M solution Bu_4NClO_4/solvent. 88

Table 2.8. Apparent contact angles for water (θ_w) and roughness data for PThienothiophene-2 electropolymerized by constant potential as a function of the solvent and the deposition charge. Polymerization at 0.1 M solution Bu_4NClO_4/solvent. 89

Table 2.9. Apparent contact angles of water (θ_w) and roughness data for the smooth corresponding polymers. Polymerization at 0.1 M solution Bu_4NClO_4/dichloromethane. 90

Table 2.10. Apparent contact angles of water (θ_w) and roughness data as a function of the polymer and the number of deposition scans of the substituent-derivatives of thienothiophenes. Polymerization at 0.1 M solution Bu_4NClO_4/dichloromethane. 101

Table 2.11. Apparent contact angles of water (θ_w) and roughness data for the smooth corresponding polymers of the substituent-derivatives of thienothiophenes. Polymerization at 0.1 M solution Bu_4NClO_4/dichloromethane..... 102

Chapter 3

Table 3.1. Data of non-fluorinated polymer chain length obtained by GPC. Polymerization in 0.1 M Bu_4NClO_4/acetonitrile. Number of scans: 3. 110

Table 3.2. Apparent and dynamic contact angles and roughness data as a function of the polymer and the number of deposition scans of the non-fluorinated polypyrenes. Polymerization at 0.1 M solution Bu_4NClO_4/acetonitrile. 117

Table 3.3. Apparent contact angles of water (θ_w) and roughness data for the smooth corresponding polymers of the non-fluorinated pyrenes. Polymerization at 0.1 M solution Bu_4NClO_4/acetonitrile. 119

Table 3.4. Data of fluorinated polymer chain length obtained by GPC. Polymerization in 0.1 M Bu_4NClO_4/acetonitrile. Number of scans: 3. 123

Table 3.5. Apparent and dynamic contact angles and roughness data as a function of the polymer and the number of deposition scans of the fluorinated polypyrenes bearing ester, thioester and amide linkers. Polymerization at 0.1 M solution Bu_4NClO_4/acetonitrile. 127

Table 3.6. Apparent and dynamic contact angles and roughness data as a function of the polymer and the number of deposition scans of the fluorinated polypyrenes bearing carbamate, thiocarbamate and urea linkers. Polymerization at 0.1 M solution Bu_4NClO_4/acetonitrile. 128

Table 3.7. Apparent contact angles and roughness data for the smooth corresponding polymers of the non-fluorinated pyrenes. Polymerization at 0.1 M solution Bu_4NClO_4/acetonitrile. 130

Table 3.8. Apparent and dynamic contact angles and roughness data of the probe liquids as function of electrolyte and the number of deposition scans for PPy-OF_6 surfaces. Polymerization in solution 0.1 M of electrolyte/acetonitrile. Deposition on ITO plates. 134

Table 3.9. Apparent and dynamic contact angles and roughness data as function of the deposition charge for PPy-OF_6 surfaces in the oxidized state (by constant potential) and in the reduced state (by constant potential followed by cyclic voltammetry). Polymerization in solution 0.1 M of Bu_4NClO_4/acetonitrile. Deposition on ITO plates..... 136

Table 3.10. Apparent contact angles and roughness data for the smooth corresponding polymers of PPy-OF_6 in the oxidized and reduced state. Polymerization at 0.1 M solution Bu_4NClO_4/acetonitrile. Deposition on ITO plates. 136

Table 3.11. Apparent and dynamic contact angles and roughness data as function of the number of deposition scans and the solvent for PPy-OF_6 surfaces. Polymerization at 0.1 M solution Bu_4NClO_4/solvent. Deposition on ITO plates. 137

Table 3.12. Spectroscopic Parameters of Pyrene Derivatives Polymers. Polymerization in solution 0.1 M Bu_4NClO_4/acetonitrile. Number of scans: 2. Deposition in ITO plates..... 140

Table 3.13. Dynamic contact angle (hysteresis H and sliding angle α) of the copolymers as function of mol% of Py-nF_6 *vs* Py-COOH. Polymerization at 0.1 M Bu_4NClO_4/acetonitrile solution after 3 deposition scans. 153

Table 3.14. Apparent contact angles and roughness data for analogous smooth polymers for mol% of Py-OF_6 *vs* Py-COOH. Polymerization at 0.1 M Bu_4NClO_4/acetonitrile solution after 3 deposition scans..... 154

Table 3.15. Apparent contact angles and roughness data for analogous smooth polymers for mol% of Py-NF_6 *vs* Py-COOH. Polymerization at 0.1 M Bu_4NClO_4/acetonitrile solution after 3 deposition scans..... 154

Table 3.16. Apparent contact angles and roughness data for analogous smooth polymers for mol% of Py-OF_6 *vs* Py-Adam. Polymerization at solution 0.1 M Bu_4NClO_4/acetonitrile. Number of scans: 2. Deposition in ITO plates. 165

Table 3.17. Water adhesion data for the surfaces studied by dynamic contact angle and by the ejection tests. V_p is related with the maximum loaded *A* achieved until the water droplet fragmentation (NF = no fragmentation, F = fragmentation). Polymerization at 0.1 M solution Bu_4NClO_4/acetonitrile in ITO plates. Number of scans: 2..... 169

Annex A2

Table A2.1. E^{ox} and E^{w} for each monomer presented in the Section 2.1 by electrochemical process. Electropolymerization in 0.1 M of Dichloromethane/Bu_4NClO_4. 209

Table A2.2. E^{ox} and E^{w} for Thienothiophene-2 presented in the Section 2.1 by electrochemical process using different conditions of polymerization. 209

Table A2.3. E^{ox} and E^{w} for each monomer presented in the Section 2.2 by electrochemical process. Electropolymerization in 0.1 M of Dichloromethane/Bu_4NClO_4. 210

Table A2.4. E^{ox} and E^{w} for each non-fluorinated pyrene monomer presented in the Section 3.1 by electrochemical process. Electropolymerization in 0.1 M of Acetonitrile/Bu_4NClO_4..... 210

Table A2.5. E^{ox} and E^{w} for each fluorinated pyrene monomer presented in the Section 3.2 by electrochemical process. Electropolymerization in 0.1 M of Acetonitrile/Bu_4NClO_4..... 211

Table A2.6. E^{ox} and E^{w} for polymerization of Py-OF_6 presented in the Section 3.3 by electrochemical process using different conditions. 211

Table A2.7. E^{ox} and E^{w} as function of mol% of Py-*n*F_6 *vs* Py-COOH presented in the Section 3.6. Electropolymerization at 0.1 M of Bu_4NClO_4/acetonitrile. 212

Table A2.8. E^{ox} and E^{w} as function of mol% of Py-OF_6 *vs* Py-Adam presented in the Section 3.7. Electropolymerization at 0.1 M of Bu_4NClO_4/acetonitrile. 212

List of Figures

Chapter 1

Figure 1.1. Illustration of the wetting behavior proposed by Young. 8

Figure 1.2. Illustration of the wetting behavior proposed by Wenzel and Cassie-Baxter..... 9

Figure 1.3. Illustration of the tilted-drop method to measure the dynamic contact angles. 10

Figure 1.4. (a-b) Images of Salvinia molesta at different magnifications and (c) a schematic representation of the leaf structure.[11] (d-e) Scanning Electron Microscopy (SEM) images of the surface of red rose petal and (f) a sticky water droplet on the red rose petal when the surface is turned upset down.[12] 12

Figure 1.5. Images of different scales and colors observed in different species of butterflies.[22] 13

Figure 1.6. Images of the nanostructures present in different species of cicada. [23] 14

Figure 1.7. Image of the filefish and the SEM image of it structure.[33] 15

Figure 1.8. Schematic representation of “top-down” and “bottom-up” methods. 16

Figure 1.9. Overview of some techniques to fabricate structured surfaces..... 16

Figure 1.10. (i) Schematic illustration of overall processes for fabrication of simple overhang structure. (ii) SEM images of different types of nanopatterns embedded overhang structures: (a) cone-, (b) pillar-, (c) hole-, and (d) lineshaped nanopatterns (scale bar = 2 µm).[35]..... 17

Figure 1.11 (a)-(c) SEM images of a Tokay Gecko (Gekko gecko) and (b)-(d) fabricated hierarchical PS nanohairs with high aspect ratio. Inset in (b): θ_w of the elongated hierarchical PS nanohairs.[37] 18

Figure 1.12. SEM images and diameter distribution of (a) PLA, (b) PLA/chitosan 4, (c) PLA/chitosan 7 and (d) PLA/chitosan 13 fiber mats. Note: 4, 7 and 13 means the percentage (%wt) of chitosan added to the PLA solution.[41]..... 19

Figure 1.13. Schematic illustration of the polymer-free transfer process by CVD method.[43] . 20

Figure 1.14. (a) SEM image of the ZnO thin film and (b) Sensor response of ZnO thin film to NH3 (50–600 ppm) at an operating temperature of 150 ºC.[47]..... 21

Figure 1.15. Schematic representation of the spray-coating process forming colored coatings on stainless steel substrates by spraying white, cinerous, purple, aurantium and blue stearates, respectively, and the representation of the anti-corrosive properties.[49] 22

Figure 1.16. I) Molecular structures of benzoylpyrene and II) photographic images of crystals in daylight (above) and under UV illumination (below).[91] 25

Figure 1.17. (a) SEM image of the polypyrene/silica hybrid film after electropolymerization and CVD of TEOS and POTS. Inset: the apparent (WCA) and dynamic (SA) contact angle of

the studied surface. (b) Fluorescence emission spectra of the polypyrene film (λex = 408 nm, red) and polypyrene/silica (FPSH) film (λ_{ex} = 408 nm, green). Inset: the excitation spectra of the polypyrene (λ_{em} = 498.5 nm, black) and polypyrene/silica (λ_{em} = 490.5 nm) films. (c) Fluorescence photograph of the polypyrene film (blue-green fluorescence under 365 nm UV light.[95] 26

Figure 1.18. (a) Static contact angle, (b) dynamic contact angle and (c) SEM images for the surfaces (i) by a direct click chemistry reaction (parahydrophobic) and (ii) by the nanoparticle-grafted click chemistry reaction (superhydrophobic).[124] 28

Figure 1.19. SEM images of PEDOT derivative obtained by electropolymerization in different solvents: (a) propylene carbonate, (b) benzonitrile, (c) nitrobenzene and (d) dichloromethane. Constant Potential method at 200 mC cm^{-2}, Bu_4NPF_6 as electrolyte.[134] 31

Figure 1.20. SEM images of electrodeposited PEDOT derivatives by applying a constant voltage of 1.4 V (vs Ag/Ag+) at (a-c) 25 ºC for 30 s and (b-d) 0 ºC for 90 s.[165] 33

Figure 1.21. (a) SEM images of polymer (PU-PMMA-$FSiO_2$) surface before and after the abrasion test (300 cycles). PU-PMMA-$FSiO_2$ coating on a variety of substrates including (b) absorbent paper towel, (c) clay-stone, (d) wood and (e) aluminum.[167] 35

Figure 1.22. SEM images of pinecone-like structures fabricated by Li and co-workers at different magnifications: (a) 5000x and (b) 30000x and in (c) the self-cleaning effect on the surface.[168] 36

Figure 1.23. SEM images of rough stainless-steel meshes and their structures fabricated by (a-b) etching process using hydrochloric acid proposed by Grynyov and co-authors [175] and (c-d) by an electrodeposition process fluorinated EDOP proposed by Darmanin and co-authors.[176] 37

Figure 1.24. (a) Schematic representation of the in situ polymerization approach to the synthesis of fluorinated polybenzoxazine incorporated silica nanoparticles modified cellulose acetate nanofibrous membranes. (b) Water contact angle, (c) SEM image and (d) optical profilometry image for the as-prepared membrane. (e) Demonstration of the facile oil–water separation for the membranes. The water and oil were dyed by methyl blue and oil red, respectively. (f) Photograph of the large-scalable membrane (60 x 60 cm^2).[178] 38

Figure 1.25. (a) Relation of the freezing delay with the surface wettability and roughness for rough and smooth surfaces. SEM images of (a) rough coating surface made with a mixture of poly(methyl methacrylate), poly(vinylidene fluoride) and Poly(tetrafluoroethylene) and (c) low roughness coating of epoxy based inorganic-organic hybrid sol-gel coating.[188] (d) and (e) are the structured surfaces during icing and deicing cycles, respectively.[185] 39

Figure 1.26. Time-lapse images of the formation of ice on the four metal surfaces. The air temperature was −10 ± 1 ºC and the surface temperature was −20 ± 1 ºC. The ice-covered area is shown as white and area without ice is shown as black.[181] 41

Figure 1.27. Effect of cicada wing surface structure on P. aeruginosa for (a-b) uncoated wing and (c-d) gold-coated wing. (a)-(c) shows the SEM images with nanopillar penetration on the bacterial cell and (b)-(d) the line profiles of surface topography.[26] 42

Figure 1.28. Vapor deposited surfaces at (a) randomly nanosized surface and (b) microstructured ordered surface. (I) 10 x 10 μm^2 AFM image and (II) cross section. (III) 10 x 10 μm^2 AFM image of P. fluorescens aggregates onto the analyzed substrate.[199] 43

Figure 1.29. (a) SEM image of the rough drape-like monolayer of graphene deposited on copper substrate after electroplating, thermal anneling and CVD process. Inset is the contact angle of the surface. (b) Illustration of water harvesting test set-up and (c) dropwise condensation on the graphene surface.[205] 44

Figure 1.30. Optical microscopic image of (a) the as-printed dopamine droplet on the superhydrophobic surface and (b) of the polydopamine patterns on the surface. (c-d) SEM images of the polydopamine patterns.[206] 45

Figure 1.31. (a) Procedure to fabricate the cactus-like structures and (b-d) the corresponding optical and SEM images. Scale bars: (b-c) 1 mm and (d) 50 µm. (e) Illustration of the magnetically induced conical array responses to the magnetic field. (f) Fog collection on the cactus-like structures when the arrays are placed upwards (left) and downwards (right).Scale bars: 500 µm.[207,208] 46

Chapter 2

Figure 2.1. Cyclic voltammograms of the thienothiophene monomers in 0.1 M Bu_4NClO_4/dichloromethane at a scan rate of 20 mV s^{-1}. Black line: scan 1, red line: scan 2, blue line: scan 3, green line: scan 4, magenta line: scan 5. 64

Figure 2.2. Cyclic voltammograms (6 scans at 20 mV s^{-1}) for the thienothiophene monomers after electrodeposition of 3 scans. Solution of 0.1 M Bu_4NClO_4/dichloromethane. 65

Figure 2.3. SEM images of the polymers electrodeposited by cyclic voltammetry (3 scans) in a 0.1 M solution of Bu_4NClO_4/dichloromethane. Magnifications: 5000x and 25000x. 66

Figure 2.4. Water droplet images for (a) PThienothiophene-2 after 1 scan and (b) PThienothiophene-5 after 3 scans showing a sticky and non-sticky behavior, respectively. Polymerization at 0.1 M solution Bu_4NClO_4/dichloromethane. 68

Figure 2.5. SEM images of PThienothiophene-1 (left) and PThienothiophene-2 (right) electrodeposited by cyclic voltammetry in Bu_4NClO_4/dichloromethane for different number of scans. 69

Figure 2.6. SEM images (flat and inclined at 60°) of PThienothiophene-2 electrodeposited at constant potential using different deposition charges. Polymerization at 0.1 M solution Bu_4NClO_4/dichloromethane. 71

Figure 2.7. SEM images of the polymers electrodeposited by constant potential as function of the deposition charge (Qs) in a 0.1 M solution of Bu_4NClO_4/dichloromethane. 73

Figure 2.8. SEM images of PThienothiophene-2 electropolymerized by galvanostatic method during i) 20 s and ii) 80 s for the current densities: A) 0.1, B) 0.5, C) 1.0, D) 5.0 and E) 10.0 mA. Polymerization at 0.1 M solution Bu_4NClO_4/dichloromethane. 75

Figure 2.9. SEM images after substrate inclination of 60º of PThienothiophene-2 polymerized by galvanostatic method during 80 s for the current densities: a) 0.1, b) 1 and c) 10 mA. Polymerization at 0.1 M solution Bu_4NClO_4/dichloromethane. 76

Figure 2.10. Apparent contact angle for water (θ_w) for PThienothiophene-2 electropolymerized by galvanostatic method as function of the current density (mA) and the deposition time (s). Polymerization at 0.1 M solution Bu_4NClO_4/dichloromethane. 77

Figure 2.11. SEM images of PThienothiophene-2 electropolymerized by pulse deposition method at t_p = 5 s for a repetition of A) 4x (20 s) and B) 16x (80 s) and at t_p = 10 s for C) 2x (20 s) and D) 8x (80 s). Polymerization at 0.1 M solution of Bu_4NClO_4/dichloromethane. Relaxing time (t_r) = 2 s. 79

Figure 2.12. Apparent contact angle for water (θ_w) for PThienothiophene-2 electropolymerized by pulse deposition method as function of the polymerization time (t_p) and the deposition time (s). Polymerization at 0.1 M solution of Bu_4NClO_4/dichloromethane. Relaxing time (t_r) = 2 s. 80

Figure 2.13. Apparent contact angle for water (θ_w) *vs* roughness data for PThienothiophene-2 electropolymerized by pulse deposition method as function of the repetition cycles at t_p = 5 s and t_r = 2 s. Polymerization at 0.1 M solution of Bu_4NClO_4/dichloromethane. 81

Figure 2.14. SEM images (flat and inclined at 60°) of PThienothiophene-2 electrodeposited at constant potential using different deposition charges in a solution 0.1 M Bu_4NBF_4/dichloromethane 83

Figure 2.15. SEM images (flat and inclined at 60°) of PThienothiophene-2 electrodeposited at constant potential using different deposition charges in a solution 0.1 M Bu_4NPF_6/dichloromethane. 83

Figure 2.16. SEM images of PThienothiophene-2 electrodeposited at cyclic voltammetry using Bu_4NBF_4 (left) and Bu_4NPF_6 (right) as an electrolyte in solution 0.1 M of electrolyte/dichloromethane. 84

Figure 2.17. SEM images of PThienothiophene-2 electrodeposited by cyclic voltammetry (3 scans) and by constant potential in Bu_4NClO_4/dichloromethane + 0.5 % water. 86

Figure 2.18. SEM images of PThienothiophene-2 electrodeposited by cyclic voltammetry (3 scans) and by constant potential in Bu_4NClO_4/dichloromethane + 1 % $HClO_4$. 87

Figure 2.19. Schematic representation of a water droplet deposited on intrinsically hydrophilic nanotubes and tree-like structures. 90

Figure 2.20. Cyclic voltammograms of the thienothiophene derived monomers in 0.1 M Bu_4NClO_4/ dichloromethane at a scan rate of 20 mV s^{-1}. Scan 1 = black line, Scan 2 = red line, Scan 3 = blue line, Scan 4 = green line and Scan 5 = magenta line. 94

Figure 2.21. SEM images of the PTh-H and the linear-substituent polythienothiophenes electrodeposited by cyclic voltammetry (3 scans) in a 0.1 M solution of Bu_4NClO_4/dichloromethane. 96

Figure 2.22. SEM images of the branched- and aromatic-substituent polythienothiophenes electrodeposited by cyclic voltammetry (3 scans) in a 0.1 M solution of Bu_4NClO_4/dichloromethane. 97

Figure 2.23. SEM images (flat and inclined at 45º) of PTh-Na electrodeposited by cyclic voltammetry in Bu_4NClO_4/dichloromethane for different number of scans. 98

Figure 2.24. Comparison between the apparent contact angles of water for smooth and structured (3 deposition scans) surfaces for the substituent-derivatives of thienothiophenes. Polymerization at 0.1 M Bu_4NClO_4/dichloromethane. Solid line: 90º. 102

Chapter 3

Figure 3.1. Cyclic voltammograms of the non-fluorinated pyrene monomers in 0.1 M Bu_4NClO_4/ acetonitrile at a scan rate of 20 mV s^{-1}. Black line: scan 1, red line: scan 2, blue line: scan 3, green line: scan 4, magenta line: scan 5. 111

Figure 3.2. IR spectra of the non-fluorinated polypyrenes in 0.1 M Bu_4NClO_4/anhydrous acetonitrile at a scan rate of 20 mV s^{-1}. Number of scans: 5. 112

Figure 3.3. SEM images of the non-substituted and hydrocarbon polymers electrodeposited by cyclic voltammetry (3 scans) in a 0.1 M solution of Bu_4NClO_4/acetonitrile. Magnifications: 5000x. 113

Figure 3.4. SEM images of the branched hydrocarbons, phenyl-, glycol- and adamantyl-subtstituent in polymers electrodeposited by cyclic voltammetry (3 scans) in a 0.1 M solution of Bu_4NClO_4/acetonitrile. Magnifications: 5000x. 114

Figure 3.5. Comparison between the apparent contact angles of water for smooth and structured (3 deposition scans) surfaces for the non-fluorinated polymers. Polymerization at 0.1 M Bu_4NClO_4/acetonitrile. Solid line: 90º. 118

Figure 3.6. Cyclic voltammograms of the fluorinated pyrene monomers in 0.1 M Bu_4NClO_4/anhydrous acetonitrile at a scan rate of 20 mV s^{-1}. Black line: scan 1, red line: scan 2, blue line: scan 3, green line: scan 4, magenta line: scan 5. 122

Figure 3.7. IR spectra of the fluorinated polypyrenes in 0.1 M Bu_4NClO_4/acetonitrile at a scan rate of 20 mV s^{-1}. Number of scans: 5. 124

Figure 3.8. SEM images of the fluorinated polymers (ester, thioester and amide) electrodeposited by cyclic voltammetry (3 scans) in a 0.1 M solution of Bu_4NClO_4/acetonitrile. Magnifications: 5000x. 125

Figure 3.9. SEM images of the fluorinated polymers (carbamate, thiocarbamate and urea) electrodeposited by cyclic voltammetry (3 scans) in a 0.1 M solution of Bu_4NClO_4/acetonitrile. Magnifications: 5000x. 126

Figure 3.10. Picture of the droplets deposited on PPy-NOF_6 surfaces with all probe liquids. Polymerization in solution of 0.1 M Bu_4NClO_4/acetonitrile. 129

Figure 3.11. Comparison between the apparent contact angles of water for smooth and structured (3 deposition scans) surfaces for the fluorinated polymers. Polymerization at 0.1 M Bu_4NClO_4/acetonitrile. Solid line: 90º. 131

Figure 3.12. SEM images of PPy-OF_6 electrodeposited using different electrolytes in solution 0.1 M electrolyte/acetonitrile. (Magnification of X5000; Number of scans: 2; ITO plates). 133

Figure 3.13. Picture of the droplets deposited on PPy-OF_6 surfaces with all probe liquids using $LiTf_2N$ as an electrolyte in solution 0.1 M electrolyte/acetonitrile. 133

Figure 3.14. SEM images of PPy-OF_6 electrodeposited using different Qs by constant potential in solution 0.1 M Bu_4NClO_4/acetonitrile. Deposition on ITO plates. 135

Figure 3.15. SEM images of PPy-OF_6 electrodeposited using dichloromethane as a solvent in solution with 0.1 M of Bu_4NClO_4. Deposition on ITO plates. Number of scans: 3. ACN = Acetonitrile, DCM = Dichloromethane. 137

Figure 3.16. Absorption and emission spectra (normalization to 1 at the maximum intensity of every spectrum) for the non-substituted pyrene (Py) and Py-Ph. Absorption spectra of the monomers in DCM (black lines), emission spectra of the monomers in DCM with λ_{ex} = 343 nm (red lines), absorption spectra of the polymers (blue lines), emission spectra of the polymers with λ_{ex} = 343 nm (magenta lines). Polymerization in solution 0.1 M Bu_4NClO_4/acetonitrile. Number of scans: 2. Deposition in ITO plates. 139

Figure 3.17. Emission spectra for the polypyrene films with number of carbons = 6. Polymerization in solution 0.1 M Bu_4NClO_4/acetonitrile. Number of scans: 2. Deposition in ITO plates. 141

Figure 3.18. Confocal fluorescence microscopy of polypyrene films: fluorescence mode (left) and transmission mode (right). Polymerization in solution 0.1 M Bu_4NClO_4/acetonitrile. Number of scans: 2. Deposition in ITO plates. 142

Figure 3.19. Average percentage of coverage (%cover) after incubation of 2 h (bacterial adhesion) and 24 h (biofilm formation) for *S. aureus* (SA) and *P. aeruginosa* (PA) for the polypyrene surfaces and glass control. 144

Figure 3.20. Fluorescence imaging of the surfaces after 2 h and 24 h incubation of *S. aureus*. The surrounding medium is an aqueous saline (150 mM) solution. Images taken at zoom 3. Polymer marked in green channel and FM®5-95 dye (bacteria) in red channel. 146

Figure 3.21. Fluorescence imaging of the surfaces after 2 h and 24 h incubation of *P. aeruginosa*. The surrounding medium is an aqueous saline (150 mM) solution. Images taken at zoom 3. Polymer marked in green channel and FM®5-95 dye (bacteria) in red channel. 147

Figure 3.22. SEM images of the copolymers as function of mol% of Py-nF_6 *vs* Py-COOH. Polymerization at 0.1 M Bu_4NClO_4/acetonitrile solution after 3 deposition scans. 150

Figure 3.23. Roughness data for the copolymers as function of mol% of Py-nF_6 *vs* Py-COOH. Polymerization at 0.1 M Bu_4NClO_4/acetonitrile solution after 3 deposition scans. 152

Figure 3.24. Static contact angle of the copolymers as function of mol% of Py-nF_6 *vs* Py-COOH. Polymerization at 0.1 M Bu_4NClO_4/acetonitrile solution after 3 deposition scans. . 153

Figure 3.25. Comparison between the apparent contact angles of water for smooth and structured (3 deposition scans) surfaces for the mol% of copolymers of Py-nF_6 *vs* Py-COOH. Polymerization at 0.1 M Bu_4NClO_4/acetonitrile. Solid line: 90º. 155

Figure 3.26. Static contact angle of copolymer mol% of 75% of Py-OF_6 *vs* Py-COOH for a treatment in solution 0.01 and 0.1 M NaOH during different times. Polymerization at 0.1 M Bu_4NClO_4/acetonitrile solution after 3 deposition scans. 156

Figure 3.27. Static contact angle of the copolymers as function of mol% of Py-nF$_6$ *vs* Py-COOH after electrodeposition, NaOH and H_2SO_4 treatment. Polymerization at 0.1 M Bu_4NClO_4/acetonitrile solution after 3 deposition scans. Basic and acid treatment at 0.1 M aqueous solution and during 3 h of immersion. 158

Figure 3.28. Water droplet pictures after electrodeposition, basic treatment and acid treatment, respectively, on copolymer of mol% 50% of Py-NF$_6$ *vs* Py-COOH. Polymerization at 0.1 M Bu_4NClO_4/acetonitrile solution after 3 deposition scans. Basic and acid treatment at 0.1 M aqueous solution and during 3 h of immersion. 159

Figure 3.29. Reversible switching of the θ_w for the copolymer surfaces after 3 cycles of basic-acid treatment. Polymerization at 0.1 M Bu_4NClO_4/acetonitrile solution after 3 deposition scans. Basic and acid treatment at 0.1 M aqueous solution and during 3 h of imm 159

Figure 3.30. SEM images of the copolymers as function of mol% of Py-OF$_6$ *vs* Py-Adam. Polymerization at solution 0.1 M Bu_4NClO_4/acetonitrile. Number of scans: 2. Deposition in ITO plates. 162

Figure 3.31. SEM images of the homopolymers Py-OF$_6$ and Py-Adam. Polymerization at solution 0.1 M Bu_4NClO_4/acetonitrile. Number of scans: 2. Deposition in ITO plates..... 162

Figure 3.32. Static contact angle of the copolymers as function of mol% of Py-OF$_6$ *vs* Py-Adam. Polymerization at solution 0.1 M Bu_4NClO_4/acetonitrile. Number of scans: 2. Deposition in ITO plates. 163

Figure 3.33. Dynamic contact angle of the homopolymers PPy-OF$_6$ and PPy-Adam. Polymerization at solution 0.1 M Bu_4NClO_4/acetonitrile. Number of scans: 2. Deposition in ITO plates. 164

Figure 3.34. Comparison between the apparent contact angles of water for smooth and structured (2 deposition scans) surfaces for the %mol of copolymers Py-OF$_6$ *vs* Py-Adam. Polymerization at 0.1 M Bu_4NClO_4/acetonitrile. Solid line: 90º. 165

Figure 3.35. Schematic representation of the catapult-like apparatus. The first image displays the experimental setup loaded and maintained with an electro-magnet in the rest position. In the second image, the plate is suddenly accelerated and the droplet is ejected with a V_g at the take-off time (t_e). 166

Figure 3.36. Image sequences of the water droplet ejection at A ≈ 0.30 cm standing on the substrates for a given concentration of the homopolymer/copolymer in mol% of Py-OF$_6$ *vs* Py-Adam. Polymerization at 0.1 M solution Bu_4NClO_4/acetonitrile in ITO plates. Number of scans: 2. 167

Figure 3.37. Image sequences of the water droplet ejection standing on the copolymer mol% 50% of Py-OF$_6$ *vs* Py-Adam substrate for a V_p > 0.68 m/s. Polymerization at 0.1 M solution Bu_4NClO_4/acetonitrile in ITO plates. Number of scans: 2..... 168

Figure 3.38. Coefficient of restitution (CR = V_g/V_p) as function of V_p for the surfaces containing a mol% 50-100% of Py-OF$_6$ *vs* Py-Adam. The bars represented the range of V_p studied with no fragmentation of the droplets. Polymerization at 0.1 M solution Bu_4NClO_4/acetonitrile in ITO plates. Number of scans: 2..... 169

Conclusions

Figure 1C. SEM images of electropolymerization of: thieno[3,2-*b*]thiophene in Bu_4NClO_4/dichloromethane by cyclic voltammetry at (a) 3 scans, (b) 5 scans; thieno[3,2-*b*]thiophene in Bu_4NClO_4/dichloromethane + 0.5% of water by (c) cyclic voltammetry at 3 scans and (d) by constant potential at 12.5 mC cm^{-2}; (e) PTh-Na in Bu_4NClO_4/dichloromethane by cyclic voltammetry at 3 scans. 178

Figure 2C. SEM images of various polypyrene surfaces electrodeposited by cyclic voltammetry at 3 deposition scans in 0.1 M solution of Bu_4NClO_4/acetonitrile. 179

Annex A2

Figure A2.1. Schematic curve for square pulse deposition method. 208

List of Schemes

Chapter 1

Scheme 1.1. Examples of conducting polymers. 23

Scheme 1.2. General mechanism of electropolymerization. 29

Chapter 2

Scheme 2.1. Monomers studied in this work. 62

Scheme 2.2. Monomers synthesized and studied in this section. 92

Scheme 2.3. Synthesis pathway to the thieno[3,4-*b*]thiophene derivatives. 92

Chapter 3

Scheme 3.1. Original non-fluorinated monomers synthesized and studied in this section. ... 108

Scheme 3.2. Synthesis pathway to the non-fluorinated pyrenes studied. 109

Scheme 3.3. Original fluorinated monomers synthesized and studied in this Section. 120

Scheme 3.4. Synthesis pathway to the fluorinated pyrenes studied bearing ester, thioester and amide linkers. 121

Scheme 3.5. Synthesis pathway to the fluorinated pyrenes studied bearing carbamate, thiocarbamate and urea linkers. 121

Scheme 3.6. Monomers used for the electro-copolymerization. 149

Scheme 3.7. Monomers used for the electro-copolymerization of water adhesion control copolymers. 161

Annex A1

Scheme A1.1. Synthetic route to the thieno[3,4-*b*]thiophene derivatives synthesized in this study. 187

Scheme A1.2. Synthetic route to the non-fluorinated pyrenes synthesized in this study. 193

Scheme A1.3. Synthetic route to synthesize the fluorinated pyrenes bearing ester, thioester and amide linkers. 196

Scheme A1.4. Synthetic route to synthesize the fluorinated pyrenes bearing carbamate, thiocarbamate and urea linkers. 200

Scheme A1.5. Synthetic route to synthesize the starting product pyren-1-ylmethanethiol (Py-SH). 201

Glossary

POTS	1*H*,1*H*,2*H*,2*H*-perfluorooctyltriethoxysilane
Py-COOH	1-pyreneacetic acid
EDOP	3,4-ethylenedioxypyrrole
EDOT	3,4-ethylenedioxythiophene
NaphDOT	3,4-naphthalenedioxthiophene
PhEDOT	3,4-phenylenedioxythiophene
ProDOT	3,4-propylenedioxythiophene
DMAP	4-(dimethylamino)pyridine
θ_{adv}	Advancing Angle
$(1 - \varphi_S)$	Air Fraction
A	Amplitude
θ^{CB}	Apparent Contact Angle by Cassie-Baxter
θ^{W}	Apparent Contact Angle by Wenzel
θ^{Y}	Apparent Contact Angle by Young
θ_{diiodo}	Apparent Contact Angle for Diiodomethane
θ_{hexa}	Apparent Contact Angle for Hexadecane
θ_{w}	Apparent Contact Angle for Water
Ra	Arithmetic Roughness
BFEE	Boron trifluoride diethyl etherate
CVD	Chemical Vapor Deposition
Co-MPs	Cobalt Magnetic Particles
CR	Coefficient of Restitution
Qs	Deposition charge
t	Deposition Time
$CDCl_3$	Deuterated Chloroform
MeOD	Deuterated Methanol
∅	Diameter
DCM	Dichloromethane
DSC	Differential Scanning Calorimetry
t_e	Ejection time
F	Fragmentation
GPC	Gel Permeation Chromatography
HSQ	Hydrogen silsesquioxane
H	Hysteresis
ITO	Indium Tin Oxide
IR	Infrared
$LiTf_2N$	Lithium bis(trifluoromethane) sulfonimide
$LiClO_4$	Lithium perchlorate

mol%	Molar Percentage
EDC	*N*-(3-Dimethylaminopropyl)-*N′*-ethylcarbodiimide hydrochloride
NMP	*N*-methylpyrrolidinone
NF	No Fragmentation
Mn	Number-Average Molar Mass
NMR	Nuclear Magnetic Ressonance
E^{ox}	Oxidation Potential
%cover	Percentage of Bacteria Coverage
PSI	Phase Shift Interference
PET	Poly(ethylene terephthalate)
PLA	Poly(lactic acid)
PTFE	Poly(tetrafluoroethylene)
PDMS	Polydimethylsiloxane
PD	Polymerization Degree
t_p	Polymerization Time
PPy	Polypyrene
PS	Polystyrene
PTh	Polythienothiophene
PVA	Polyvinyl alcohol
PA	*Pseudomonas aeruginosa*
Py	Pyrene
Rq	Quadratic Roughness
θ_{rec}	Receding Angle
t_r	Relaxing Time
r	Roughness Factor
SCE	Saturated Calomel Electrode
SEM	Scanning Electron Microscopy
α	Sliding Angle
φ_S	Solid Fraction in contact with the droplet
SA	*Staphylococcus aureus*
γ_{LV}	Surface Tension at liquid-vapor Interface
γ_{SL}	Surface Tension at solid-liquid Interface
γ_{SV}	Surface Tension at solid-vapor Interface
γ^D_{SV}	Surface Tension at solid-vapor Interface (Dispersive Component)
γ^P_{SV}	Surface Tension at solid-vapor Interface (Polar Component)
Bu_4NTf_2N	Tetrabutylammonium bis(trifluoromethane) sulfonimide
Bu_4NPF_6	Tetrabutylammonium hexafluorophosphate
Bu_4NClO_4	Tetrabutylammonium perchlorate
$Bu_4NC_4F_9SO_3$	Tetrabutylammonium perfluorobutanesulfonate
Bu_4NBF_4	Tetrabutylammonium tetrafluoroborate
$Bu_4NCF_3SO_3$	Tetrabutylammonium trifluoromethanesulfonate
TEOS	Tetraethoxysilane

THF	Tetrahydrofuran
Th	Thienothiophene
TEA	Triethylamine
UV	Ultraviolet
V_p	Velocity of the Plate/Substrate
V_g	Velocity of the Water Droplet
λ_{abs}	Wavelength of Absorption
λ_{em}	Wavelength of Emission
λ_{ex}	Wavelength of Excitation
Mw	Weight-Average Molar Mass
E^w	Working Potential

Introduction

The design of new surfaces with controlled wettability is of great interest in many practical applications.[1] According to the Wenzel and Cassie-Baxter theories, the presence of roughness induced by surface structures can be a key factor to regulate the surface hydrophobicity.[2,3] Indeed, the surface hydrophobicity is highly dependent on the geometrical parameters of the surface structures and the material surface energy. Thus, it is extremely important to develop a method to easily tune these two parameters.

Superhydrophobic surfaces are characterized by high apparent contact angles with water (greater than 150º) and low water adhesion.[4] They can be reached combining surface structures often at a micro/nanoscale with low surface energy materials. These surfaces are abundant in nature, such as the lotus leaves and some butterfly wings. In opposition, the so-called parahydrophobicity, which are characterized by high water contact angle and high water adhesion, can also be found in the nature in the rose petals, gecko foot and cicada wings, for example. They can capture water droplets even in arid and hot environments. High water adhesion can be obtained by using materials of high surface energy and/or with surface structures allowing a high solid-liquid interface.

The source of inspiration for synthetic development of surfaces with unique wetting behaviors has come from these natural examples that can repel or interact with water in a unique manner. Various strategies have been applied to produce surfaces with those properties by controlling both the surface morphology and energy.

Conducting polymers are extremely promising materials due to their unique optoelectronic properties with the possibility to introduce various dopants (smart materials) and especially for their high capacity to form various self-assembled structures in solution.[5] They can be prepared by electropolymerization which is a direct method to obtain micro and nanostructured films on any conductive substrate. Moreover, it is a versatile technique because many parameters influence the polymer morphology. These parameters include the

(1) Darmanin, T.; Guittard, F. Recent Advances in the Potential Applications of Bioinspired Superhydrophobic Materials. *J. Mater. Chem. A* **2014**, *2* (39), 16319–16359 |.
(2) Wenzel, R. N. Resistance of Solid Surfaces To Wetting By Water. *Ind. Eng. Chem.* **1936**, *28* (8), 988–994.
(3) Cassie, A. B. D.; Baxter, S. Wettability of Porous Surfaces. *Trans. Faraday Soc.* **1944**, *40* (5), 546–551.
(4) Darmanin, T.; Guittard, F. Superhydrophobic and Superoleophobic Properties in Nature. *Mater. Today* **2015**, *18* (5), 273–285.
(5) Li, C.; Bai, H.; Shi, G. Conducting Polymer Nanomaterials: Electrosynthesis and Applications. *Chem. Soc. Rev.* **2009**, *38* (8), 2397–2409.

monomer structure and concentration, the solvent, the salt, the deposition time, etc. The electropolymerization presents many advantages:

- ✓ Polymerization, structuring and deposition of the film in only one step;
- ✓ Easily implemented;
- ✓ Low-cost method;
- ✓ Fast reaction;
- ✓ Possibility to tailor the monomer by grafting functional side chains avoiding additional coating steps;
- ✓ Control of deposition conditions: nature of the electrolyte and solvent, monomer structure and concentration, deposition charge, deposition time, deposition method, etc.
- ✓ Polymerization in soft conditions: room temperature and atmospheric pressure;

The main goal of this work is to create new surfaces using pyrene and thienothiophene monomers by electrochemical polymerization. These films were evaluated by their electrochemical behavior, surface wettability and morphology. Indeed, we wished to create structures that mimic the functionalities of some natural surfaces that can be potentially applied in different domains. The monomers had been chosen due to featured functionalities:

- ➢ The thiophenes derivatives are very known to generate special wetting properties with tunable morphology by electropolymerization, such as fibers, tubes, cauliflower-like structures, etc.[6,7] Our strategy was to change key factors in order to study the stability of these films by the electrochemical parameters and how we can play with their morphology and wettability;
- ➢ The pyrenes derivatives are very used to design sensors due to their known fluorescent properties.[8,9] Here we synthesizedoriginals monomers by tethering the pyrene with perfluorocarbon and hydrocarbon chains to study the effect of the substituent on the photophysical properties of monomers and films and mainly on the surface wettability and morphology.

(6) Darmanin, T.; Guittard, F. A One-Step Electrodeposition of Homogeneous and Vertically Aligned Nanotubes with Parahydrophobic Properties (High Water Adhesion). *J. Mater. Chem. A* **2016**, *4* (9), 3197–3203.

(7) Godeau, G.; Darmanin, T.; Guittard, F. Staudinger Vilarassa Reaction: A Powerful Tool for Surface Modification and Superhydrophobic Properties. *J. Colloid Interface Sci.* **2015**, *457*, 72–77.

(8) Xu, L.; Tong, F.; Lu, X.; Lu, K.; Lu, Q. Multifunctional Polypyrene/Silica Hybrid Coatings with Stable Excimer Fluorescence and Robust Superhydrophobicity Derived from Electrodeposited Polypyrene Films. *J. Mater. Chem. C* **2015**, *3*, 2086–2092.

(9) Chhatwal, M.; Kumar, A.; Gupta, R. D.; Awasthi, S. K. A Pyrene-Based Electropolymerized Film as a Solid-State Platform for Multi-Bit Memory Storage and Fluorescence Sensing of Nitroaromatics in Aqueous Solutions. *J. Mater. Chem. C* **2016**, *4*, 4129–4133.

All these challenges are summarized in the scheme presented in next page. This work is divided into three chapters. ***Chapter 1*** will present a review about the wetting theories and the bioinspired examples in the nature. A detailed account with innovative fabrication technologies to prepare nano and microstructured surfaces will be provided. A special section will be dedicated to the presentation of conducting polymers, especially pyrenes and thiophenes molecules, and an overview about the electropolymerization method emphasizing the mechanism and the main factors that affect the reaction will be also discussed. At the end, some examples of micro and nanostructured surfaces with their potential application will be presented.

Chapter 2 will come in the next bringing the results concerning the thienothiophene monomers and its derivatives. A first narrative will present the main factors that influence the electropolymerization of five thienothiophene derivatives and the possible explanations for the formation of the structures during this process. Indeed, the introduction of alkyl and aromatic substituents on thienothiophene will be discussed as well as the way of each side chain is affecting the final properties.

Chapter 3 will finish this work presenting the use of pyrene monomer to fabricate surfaces with tunable hydrophobicity and various morphologies. Substituents varying by their size, hydrophobicity and flexibility are grafted to the pyrene ring and their wetting and morphological properties will be studied. The use of pyrene monomer in the surface science field is relatively new and there are not so many studies encompassing its surface morphology and wettability. Further studies, such as the fluorescence, anti-bacterial properties and pH-sensitivity will be also done using the hydrophobic and superhydrophobic pyrene films. In the end, it will be presented a new method that allows measuring the water adhesion of sticky and non-sticky surfaces using copolymers of pyrenes with different water adhesive behavior.

State of Art

NATURAL SURFACES → ARTIFICIAL SURFACES

Bioinspired Surfaces

Superhydrophobic

Parahydrophobic

Electropolymerization

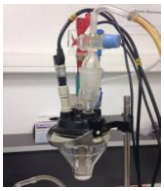

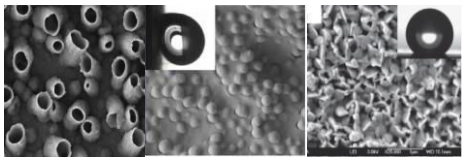

Nano and Microstructured Surfaces with varied Wettability

Thienothiophenes: hydrophobicity and water adhesion

Nanotube Formation

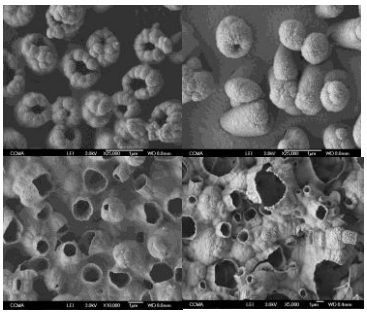

Parahydrophobic Surface

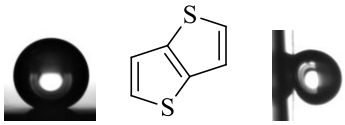

Electrochemical Parameters Effect

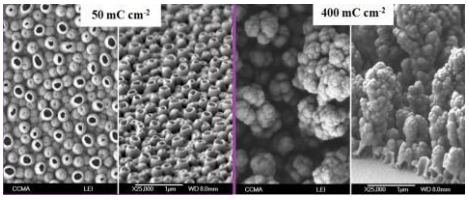

Tree-like Structures Formation

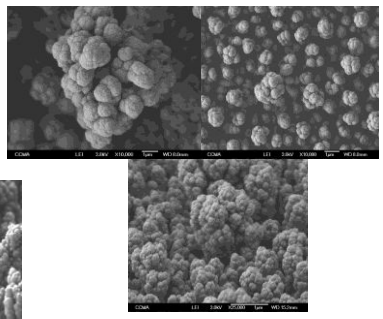

Pyrenes: superhydrophobicity, fluorescence and anti-bioadhesion

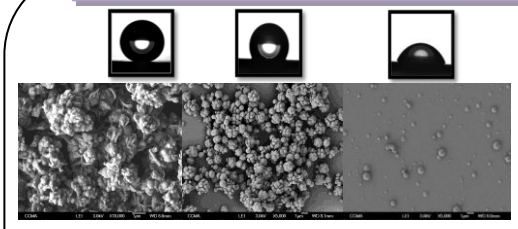

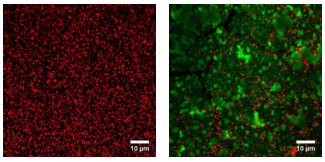

Anti-bacterial properties

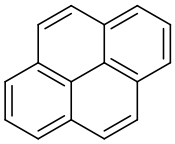

Spherical particles
Superhydrophobic
Low water adhesion
Highly oleophobic

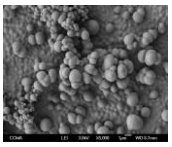

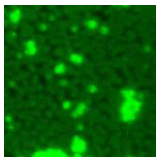

Fluorescence

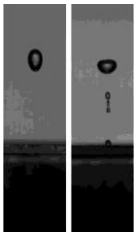

Water adhesion

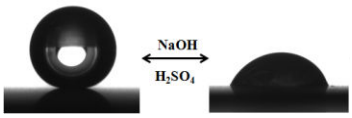

pH-sensitivity

CHAPTER 1
State of Art

The rapid advance of surface science on the design of materials with controlled morphology both in shape and dimension has pushed toward an intensive exploitation of new possibilities concerning chemical, physical, biological and electronic applications. As a result, the researchers have been fabricated new materials employing a range of new methods to obtain specific properties, including anti-bacterial materials, optical and electronic devices, anti-icing surfaces, etc.[1]

Meanwhile, the surface wettability has been calling attention in the manufacturing of new materials opening new fields of potential applications. The control of surface wettability and morphology is very important to a wide range of applications as in separation membranes, anti-biofouling, water harvesting and biosensors.[1–4] Inspired by the nature, where many plants and insects possess special wetting properties, there are recent developments of multifunctional structured surfaces with tunable wettability.

This chapter will point out the wettability theories that are the basis for this study, the bioinspired surfaces (surfaces presented in the nature, such as some leaves, flowers, insects, animals, etc) and the different ways to fabricate structured surfaces as well as examples of their potential applications.

1.1 WETTING THEORIES

When a liquid droplet is deposited on a surface, the apparent contact angle θ is taken at the triple point solid-liquid-vapor and many are the theories governing the wetting behavior. In 1805, the pioneer in wettability theory Thomas Young developed an equation where the angle between the solid, liquid and vapor interfaces is related with their surface tension when a liquid droplet was added to the surface.[5] The Young equation is expressed as follows:

$$cos\theta^{Y} = \frac{\gamma_{SV} - \gamma_{SL}}{\gamma_{LV}} \qquad \textbf{Equation 1.1}$$

where θ^Y is the Young's angle for a flat and smooth surface and γ_{SV}, γ_{SL} and γ_{LV} represent the surface tension at the solid-vapor, solid-liquid and liquid-vapor interfaces, respectively. An illustration of the model proposed by Young is represented in **Figure 1.1**.

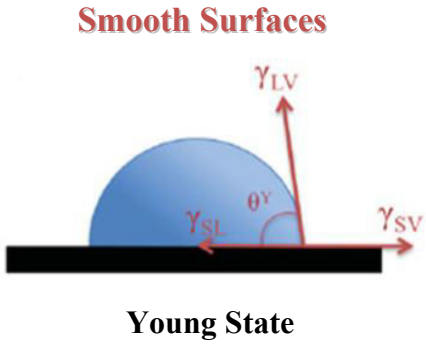

Figure 1.1. Illustration of the wetting behavior proposed by Young.

However, the Young theory was proposed for an ideal surface: flat, smooth, homogeneous and inert. In this case, when real surfaces were analyzed, in many times the wettability could not be explained by **Equation 1.1** and therefore Young's model could not be applied. Then, in 1930-1940's, two other models proposed by Wenzel and Cassie-Baxter tried to explain the wettability of real surfaces in function of the influence of surface roughness and morphology. In 1936, Wenzel created a new equation where he took into account a roughness factor (r) in the Young's equation generating θ^W as showed the **Equation 1.2**:[6]

$$cos\theta^W = r.cos\theta^Y \qquad \textbf{Equation 1.2}$$

where θ^W is the apparent contact angle proposed by Wenzel for a rough surface and r is the roughness parameter which is the ratio between the real area of the solid surface (rough) and the ideal surface area (smooth). In this case, for rough surfaces $r > 1$, enhancing the intrinsic hydrophobicity or hydrophilicity of the rough surface. In the Wenzel model, illustrated in **Figure 1.2**, the liquid droplet maintains contact with the surface and penetrates into the asperities increasing the surface contact area. As a consequence, a high liquid adhesion often exists between the surface and the liquid droplet. In this case, highly hydrophobic properties can be predicted for intrinsically hydrophobic surfaces ($\theta^Y_{water} > 90º$), but with high water adhesion.

Differently from Wenzel, in 1944-1945, Cassie and Baxter considered that the liquid droplet is on a rough and porous substrate and, in this case, the droplet is suspended over the

microstructures and air is trapped inside them, as showed **Figure 1.2**.[7] Then, in the Cassie-Baxter equation, the solid fraction (φ_S) is added to Young's equation:

$$cos\theta = \varphi_s(cos\theta^Y + 1) - 1 \qquad \textbf{Equation 1.3}$$

where θ^{CB} is the apparent contact angle proposed by Cassie and Baxter for rough and porous surface, φ_S is the solid fraction in contact with the droplet and $(1 - \varphi_S)$ is the air fraction. In the Cassie-Baxter equation, the presence of air inside the surface roughness can induce an increase of θ whatever θ^Y because the solid-liquid interface decreases while the liquid-vapor interface increases. It is also possible to obtain ultra-low adhesion (superhydrophobic properties) if the amount of air between the surface and the water droplet is sufficiently important.

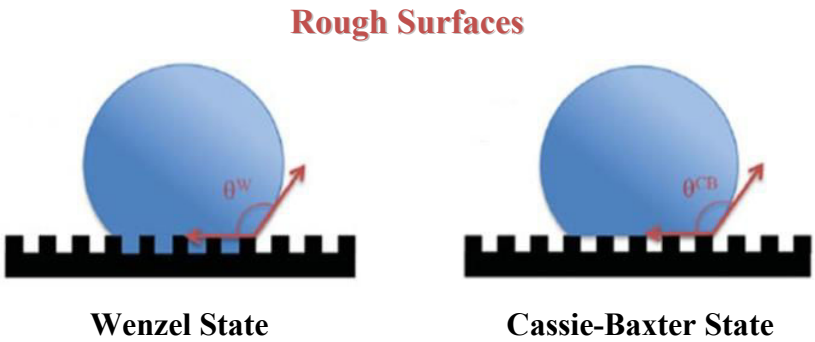

Figure 1.2. Illustration of the wetting behavior proposed by Wenzel and Cassie-Baxter.

Both Wenzel and Cassie-Baxter equations are related to Young's one, which means that they are dependent on the surface energy (γ_{SV}), but also the surface tension of the liquid (γ_{LV}) deposited on it. Hence, if the γ_{LV} decreases, the difficulty for the surface to imped its spreading increases. Due to the presence of many hydrogen bonds, water is a liquid of high surface tension (γ_{LV} = 72.8 mN/m) while oils have much lower surface tension (γ_{LV} < 35 mM/m).

Hence, to characterize the wetting properties of the materials, not only the apparent contact angle θ is necessary, but also the dynamic contact angles, which is characterized by various parameters, in order to provide the adhesive behavior of the surface. The sliding angle (α), which is the inclination angle of the surface from which the droplet can roll off it, and the contact angle of hysteresis (H) which is the difference between the advancing angle (θ_{adv}) and

the receding angle (θ_{rec}) are the most used measures to evaluate the dynamic contact angles. Usually, the most employed method to determine α and H for surfaces with low adhesion (non-sticky surfaces) is the tilted-drop method as represented in **Figure 1.3**. This method consists in the deposition of a droplet on a substrate which is inclined until a maximum angle where the droplet will roll off from the substrate. The H has to be determined just before the droplet rolls off the substrate and α is the maximum slope that the substrate achieves immediately before droplet slides down.

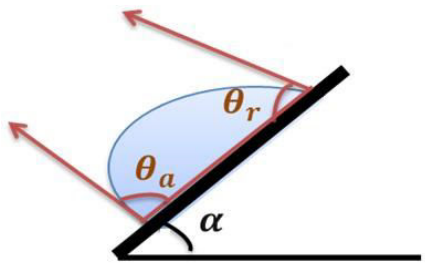

Tilted-Drop Method

Figure 1.3. Illustration of the tilted-drop method to measure the dynamic contact angles.

Having the dynamic contact angles, it is possible to know in which regime the working surface is following to. When a liquid droplet follows Wenzel model, H and α are very high because of the increase in the solid-liquid interface and the surfaces can be called as sticky. By contrast, when a liquid droplet follows Cassie-Baxter regime, H and α are very low (usually < 10º) due to the increase in the liquid-vapor interface and the surfaces can be called as non-sticky. Moreover, Wenzel and Cassie-Baxter states are two extremes wetting states for rough and structured surfaces. An intermediate wetting state between Wenzel and Cassie-Baxter states, also referred as composite states, had been proven by Bhushan and Nosomovsky.[8] One example is the *Cassie-Impregnating* regime, which can occur on surfaces with dual-scale features where some of them lend to Wenzel regime while others follow the Cassie-Baxter regime. The *Cassie-Impregnating* regime can explain the adhesive behavior found on many chemically homogeneous surfaces that have dual-scale hierarchical topography.

More recently, Marmur proposed to use the term "parahydrophobic" to distinguish surfaces with this unique wetting phenomenon of composite interface between the Wenzel and Cassie-Baxter regimes. The prefix "*para-*" ("beyond" in greek) was proposed to use in the cases where the wettability is achieved due to the roughness, beyond the effect of the surface

chemistry given by θ^{Y}.[9] Then, the term parahydrophobicity has been used to refer surfaces with contact angles greater than θ^{Y} and strong liquid adhesion, also called as sticky surfaces. From this point on, we will refer the surfaces as to:

- Superhydrophilic: when $\theta_{water} < 10º$;
- Hydrophilic: when $10º < \theta_{water} < 90º$;
- Hydrophobic: when $\theta_{water} > 90º$;
- Parahydrophobic: when $\theta_{water} > \theta^{Y}$ and high H and α;
- Superhydrophobic: when $\theta_{water} > 150º$ and low H and α;

The same terminology will be used to refer the repellence of liquids with lower surface energy: superoleophilic, oleophilic, oleophobic, paraoleophobic and superoleophobic.

1.2 BIOINSPIRED SURFACES

In 1997, two german researchers, Neinhuis and Barthlott, were doing a classification in certain families of plants when they noticed a curious phenomenon on the surface of lotus leaves: a self-cleaning behavior.[10] This peculiar characteristic is due to the synergic effect between the chemical composition of the surface, composed by hydrophobic waxes (θ^{Y} = 110º), combined with hierarchical micro and nanoscale structures. The lotus leaves showed a very high contact angle (θ_{water} = 161º) with ultra-low water adhesion (H = 2º) explaining the self-cleaning condition. Therefore, the water droplet cannot get fixed on the lotus surface and slides along the surface easily taking all the contaminants present on the leaf surface. Later, this phenomenon was called as “Lotus Effect”.

Nowadays, the lotus leaves are the most famous example of superhydrophobicity in the nature. It is also a symbol of purity in many Asian religions, because its leaf remains always clean and free of any contamination or pollution despite being born in marshy regions. Since this discovery, the importance of the technological application of the “Lotus Effect” has done many researchers investigate different species in the nature to better understand the phenomenon of *bioinspiration* and for the development of the biomimetic materials.

In the nature, there are many species of plants presenting special wetting behaviors. Barthlott and co-authors also studied other floating leaves such as *Salvinia molesta* (**Figure 1.4**).[11] These plants present in their surface multi-cellular hairs that forms an eggbeater-shaped cap.

In the "head" of the structure, hydrophilic patches allow the pinning of the air-water interface which increases the stability of this interface and maintain the leaves surface dry. The rose petal is another famous example in the nature as showed in **Figure 1.4**. Differently from the lotus leaves, the so called "Petal Effect" describes the phenomenon when a water droplet was deposited on the petal surface forming a spherical shape, but does not roll off from it even when the petal is turned upset down.[12,13] This property is due to the unique surface structure that consists in convex conic cells, also called as micropapillae, with a cuticular nanofolding. When a water droplet wets the petal surface, the liquid can enter in the large spaces between the micropapillae, but not inside the nanofolds. The authors demonstrated that the wetting behavior of the rose petal follows the *Cassie-Impregnating* regime. Feng and co-authors also studied other flower petals presenting the same adhesive properties of the rose petal, including the Chinese Kafir Lily and the sunflower.[12] Similar adhesive properties were also found for scallion and garlic leaves as reported by Chang and co-authors.[14]

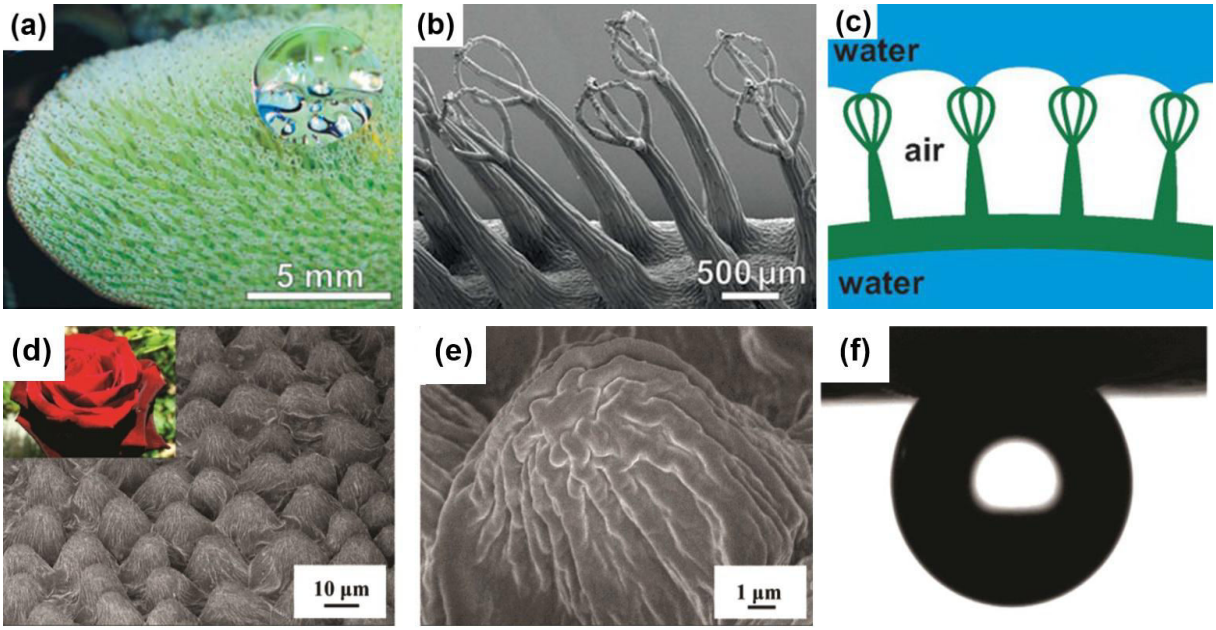

Figure 1.4. (a-b) Images of Salvinia molesta at different magnifications and (c) a schematic representation of the leaf structure.[11] (d-e) Scanning Electron Microscopy (SEM) images of the surface of red rose petal and (f) a sticky water droplet on the red rose petal when the surface is turned upset down.[12]

A famous example of bioinspiration that has calling the researchers attention is the peanut leaf and its strong water adhesion.[15] This plant lives in arid or semiarid habitats and can survive in a dry climate with a very low amount of water. The partial penetration of water into its dual-

scale structured surface creates a three phase contact line between solid-liquid-vapor. The hierarchical structure combined with the hydrophobic waxy layer present on the leaf surface makes the peanut leaves very effective to capture and collect water from fog.

Many are the leaves presented in the nature and that have been used to inspire researchers. The rice leaves had called attention due to it anisotropic superhydrophobic properties.[16,17] This means that when the water droplet is deposited on the leaf surface, the droplet remains stuck on it after inclination in the perpendicular direction to the structures, but the droplet can roll off the leaf if it is inclined in the parallel direction of the structures.

However, it is not only in leaves and flowers that superhydrophobic and parahydrophobic surfaces can be found in the nature. They are also present in the animal kingdom. Similarly to plants with strong water adhesion, the Namib Desert beetle were found to be able to collect water from fog allowing them to survive in arid climates with a minimal water exposure.[18,19] It was reported that this ability is due to the patterned waxy regions and hydrophilic spaced bumps dispersed along its back. When the droplet achieves a certain size and mass, it rolls from the hydrophilic region on its back and is guided by the hydrophobic domains towards to the beetle's mouth.

The wings of various insects and birds also present the water repellent properties. These can reduce the dust contamination and enhance their flight capacity. Some butterflies wings have scales regularly arranged which are overlapping like roof tiles, whose length and width of these scales vary from 50 – 150 µm and 35 – 70 µm, respectively, giving them superhydrophobic properties.[20,21] Indeed, the color of some butterfly wings is directly dependent of their wings structures. Prum and co-authors showed the superhydrophobicity with anisotropic adhesion for 12 species of butterflies and the relation of the nanostructures on the scales that provide the visibility of different colors for the wings, such as green, blue or violet, as showed in **Figure 1.5**.[22]

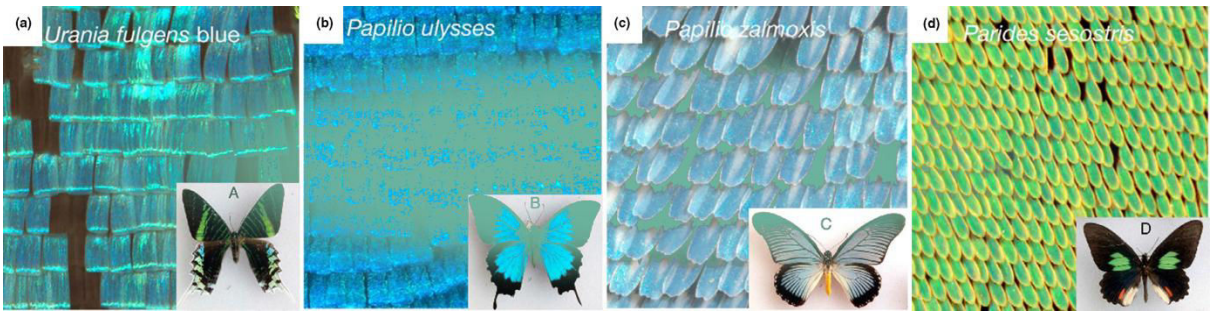

Figure 1.5. Images of different scales and colors observed in different species of butterflies.[22]

After the study of 15 species of cicada, Sun and co-authors observed high θ_{water} and high adhesive properties in different morphologies.[23,24] In opposition, other species of cicada reported by Watson and co-workers are superhydrophobic with ultra-low water adhesion.[25] The main differences between these species cited by Sun and Watson groups are the height and the spacing of nanodome structures presented on the cicada wings (**Figure 1.6**). Indeed, studies done by Ivanova and co-workers extended the investigation with cicada wings and demonstrated their ability to kill Gram-negative bacteria only by physical contact, however, no effect was visible for Gram-positive bacteria.[26,27] This was the first reported work that demonstrates an example of effective anti-bacterial properties due to the physical structure of natural surfaces.

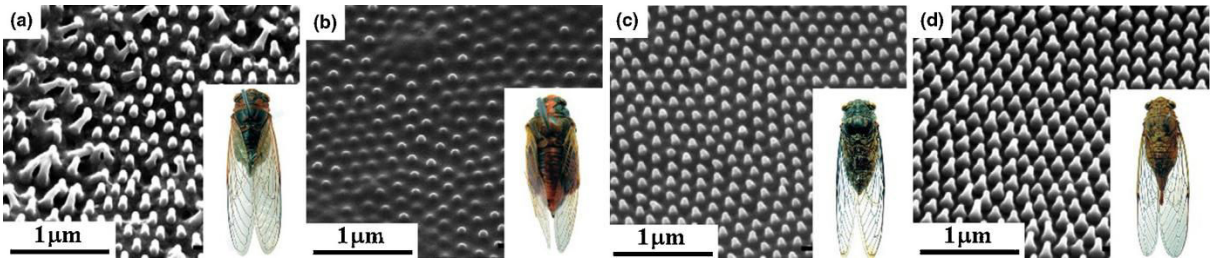

Figure 1.6. Images of the nanostructures present in different species of cicada. [23]

A similar example of the rose petal behavior is the adhesive properties of the gecko feet enabling its ability to walk up inclined or inverted surfaces. When a water droplet is deposited on a gecko foot, a high adhesive property was found with θ_{water} = 160º. This behavior is explained by the presence of well-aligned microscopic hair on their feet, also called setae. These setae adapt when they come to contact with a surface providing a high contact area. The high adhesive force, which was found to be in the range of 10-60 μN by Jiang and co-authors, can be explained by strong intermolecular Van der Waals forces between the setae and the contacting surface area.[28]

On the other hand, some marine species also present underwater superoleophobicity that corresponds to a solid-liquid(water)-liquid(oil) interface. It is known that this underwater superoleophobicity act as a protection for the marine animals when repel the pollution induced by oil spills although they are wetted by water, for example. The shark skin is a famous example of underwater superoleophobic surface which is covered by tooth-like scales also called as dermical denticles.[29,30] These structures are covered by sized and spaced riblets with longitudinal grooves oriented parallel to the local flow direction of the water, resulting in

an increase of the shark speed. This kind of structure is calling attention to the fabrication of low drag surfaces which is very important for anti-biofouling and anti-bacterial applications, for example.[31,32] Jiang and co-authors also reported the anisotropic underwater superoleophobicity of the filefish skin (**Figure 1.7**).[33] The presence of hook-like spines oriented in the head-to-tail direction avoids accumulation of oil in the head and stuck the oil droplet in the opposite direction. However, if these surfaces were found to be superoleophobic when they are immersed in water, they are oleophilic when the media is air.

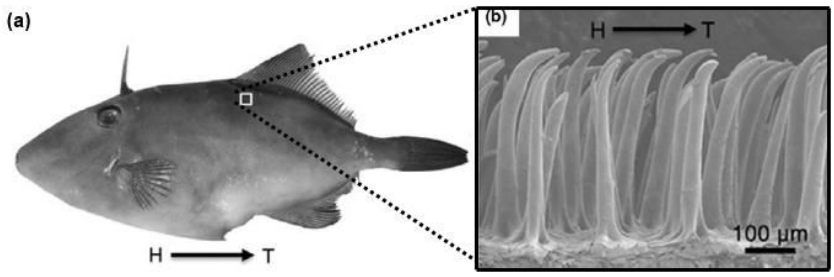

Figure 1.7. Image of the filefish and the SEM image of it structure.[33]

All these surfaces have been fascinating researchers who are currently trying to mimic them to obtain similar properties. Studies on nano and miscrostructured surfaces with super-wetting behavior based on biomimicry have been increasing exponentially since 2000s. Nowadays, more and more the researchers are trying to search for new examples on the nature. Many methods had been used in order to fabricate artificially the structures and properties found in the nature and some of them will be presented in the next section.

1.3 METHODS TO FABRICATE STRUCTURED SURFACES

The “top-down” and “bottom-up” approaches are the most famous fabrication methods for obtaining structured surfaces (**Figure 1.8**).[34] They are used in the elaboration of surfaces with high controlled or randomly structured topography. Top-down methods are based in large scale patterns through sculpture, engraving and modeling, for example, that reduces its dimensions to form nanostructured materials. Some examples are etching, lithography, templating, etc. On the other hand, bottom-up approaches involve developing more complex constructions through the integration of atoms or molecules to build up nanostructures.

Electrospinning, layer-by-layer, chemical deposition, sol-gel process can be regarded as a combination of bottom-up approaches.

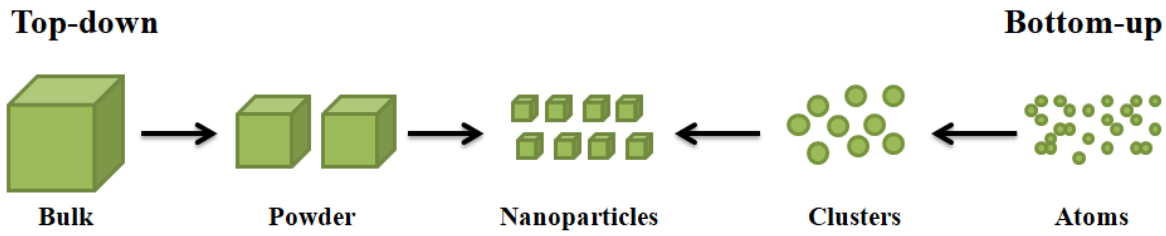

Figure 1.8. Schematic representation of "top-down" and "bottom-up" methods.

In this topic, it will be presented most of the techniques that are employed to fabricate bioinspired surfaces. **Figure 1.9** summarizes the techniques presented here.

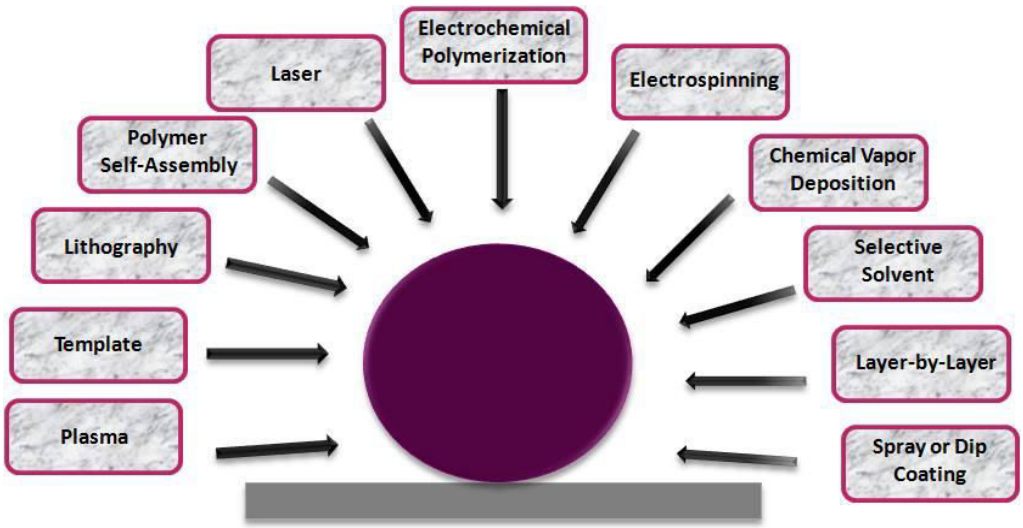

Figure 1.9. Overview of some techniques to fabricate structured surfaces.

1.3.1 Top-down Methods

Lithography is a high-cost technique that allows controlling the surface morphology yielding well defined and reproducible structures. Here, the light is irradiated through a mask with desired features to the substrates. Lithography can be subdivided in photolithography, soft lithography, nanoimprint lithography, X-ray lithography, etc. Choi and co-authors fabricated an overhang structure by reverse nanoimprinting lithography employed in conjunction with

reactive ion etching.[35] Firstly, a template mold was prepared with polydimethylsiloxane (PDMS) followed by the spin-coating of hydrogen silsesquioxane (HSQ). Then, a polyvinyl alcohol (PVA) molding is placed and a pressure was applied at room temperature under vacuum to detach the PDMS mold and the surface layer was oxidized by ultraviolet (UV) and O_3 exposure. The PVA template was removed with the residual HSQ layer. The obtained overhang structure was coated with a fluoroalkylsilane monolayer to reduce its surface energy and yield superhydrophobicity. **Figure 1.10** shows the nanopatterns resulting in overhang angles, enhancing the oil repellence properties.

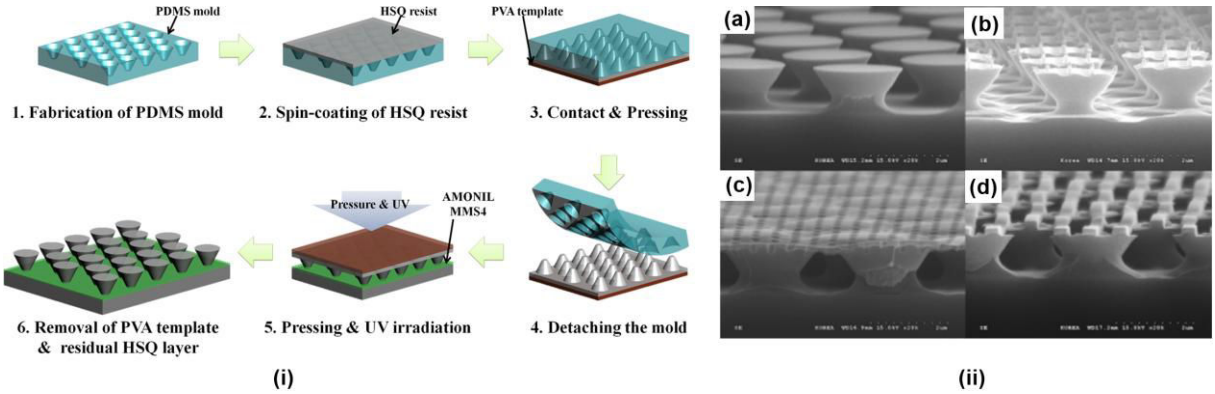

Figure 1.10. (i) Schematic illustration of overall processes for fabrication of simple overhang structure. (ii) SEM images of different types of nanopatterns embedded overhang structures: (a) cone-, (b) pillar-, (c) hole-, and (d) lineshaped nanopatterns (scale bar = 2 μm).[35]

A highly versatile tool to fabricate varied nanostructures is the colloidal lithography. Hanarp and co-authors reported the development of polystyrene (PS) particle films on flat titanium oxide substrates with potential application for biological and catalysis fields.[36] A wide range of particle coverage and size was observed, but high coverage films were difficult to obtain due to the aggregation of the particles.

Another imprint-related method, template is a process that includes the preparing a featured template master, then molding the replica and finally removes the template. The biggest advantage of this method is that the template can be reused after a processing. A very typical example of template method is to fabricate superhydrophobic surfaces by mimicking the hairy structure of the gecko foot.[37] By using multi-branched anodic aluminium oxide membranes as template method, the nanohairs presented on gecko foot can be made with versatile pore and nanopillars dimensions depending of the anodizing parameters. As shown in **Figure 1.11**, a replication had a very close morphology to the Tokay gecko foot. The method was prepared

by two-steps: the first has a diameter ∅ of 380 nm and a depth of 900 nm and inside them there are smaller pores with a ∅ = 100 nm and depth of 180 nm. After replication by thermal molding and template peeling-off, a hierarchical PS surface with nanohairs was produced with superhydrophobic behavior with low hysteresis.

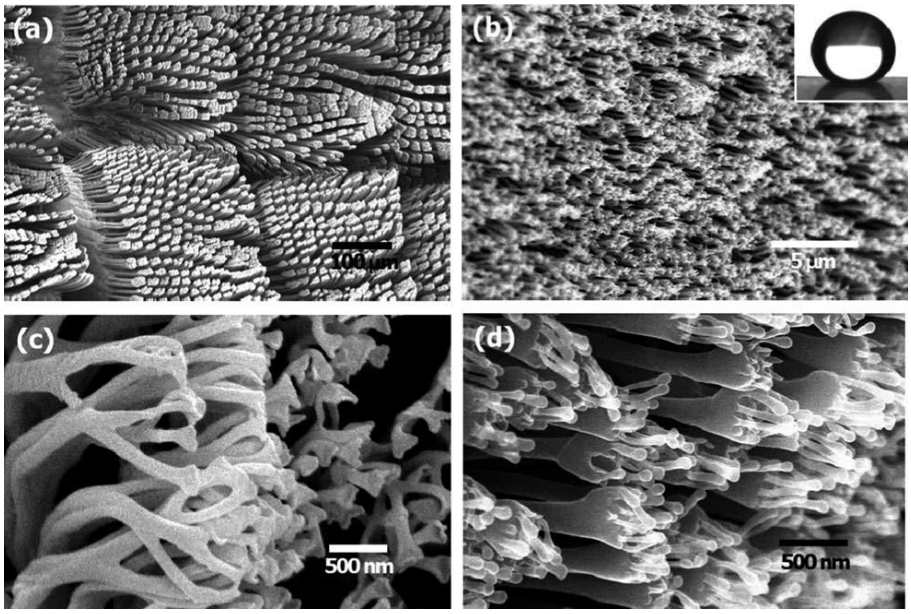

Figure 1.11 (a)-(c) SEM images of a Tokay Gecko (Gekko gecko) and (b)-(d) fabricated hierarchical PS nanohairs with high aspect ratio. Inset in (b): θ_w of the elongated hierarchical PS nanohairs.[37]

Plasma is a very versatile method which allows depositing materials on the surface or even etching a surface to make an appropriate roughness. Plasma can also be used before or after the template or lithography methods. Plasma etching is a dry technique in which reactive atoms or ions are generated in a gas discharge. The research group of Prof. Henry Ramos showed robust superhydrophobic poly(tetrafluoroethylene) (PTFE) surfaces after exposure to oxygen, hydrogen and tetrafluoromethane plasma produced by gas discharge ion source facility.[38,39] The improvement of the wetting properties is due to high plasma energies, such as discharge current, discharge voltage, irradiation time, etc. The treated PTFE exhibited a reduced *Escherichia coli* attachment when compared with the polymer with no treatment which made them good candidates for anti-bacterial coatings.

A structured hydrophobic zirconium dioxide film was fabricated on Mg–Ca and Mg–Sr alloys by dual zirconium and oxygen ion implantation.[40] The corrosion rate was reduced after the plasma treatment and the amount of adherent bacteria on the Zr–O-implanted and Zr-implanted samples diminished remarkably compared to the unimplanted control.

1.3.2 Bottom-up methods

One of the most employed method to make fibers network is electrospinning. It consists in an extrusion process where an electric field is applied to design thin fibers through a liquid. This method can be applied for natural and synthetic polymers, polymer alloys and also for polymers loaded with chromophores, nanoparticles, active agents, etc. Siqueira and co-authors produced electrospun fibers from poly(lactic acid) (PLA))/chitosan blends to evaluate the influence of these materials as support for lipase immobilization.[41] The percentage of chitosan influenced morphology, hydrophobicity and mechanical properties of PLA nanofibers (**Figure 1.12**). The results concerning the enzyme immobilization suggested that not only chemical composition of the support's surface influenced on the enzyme coupling but a mix among chemical nature, morphology and topography.

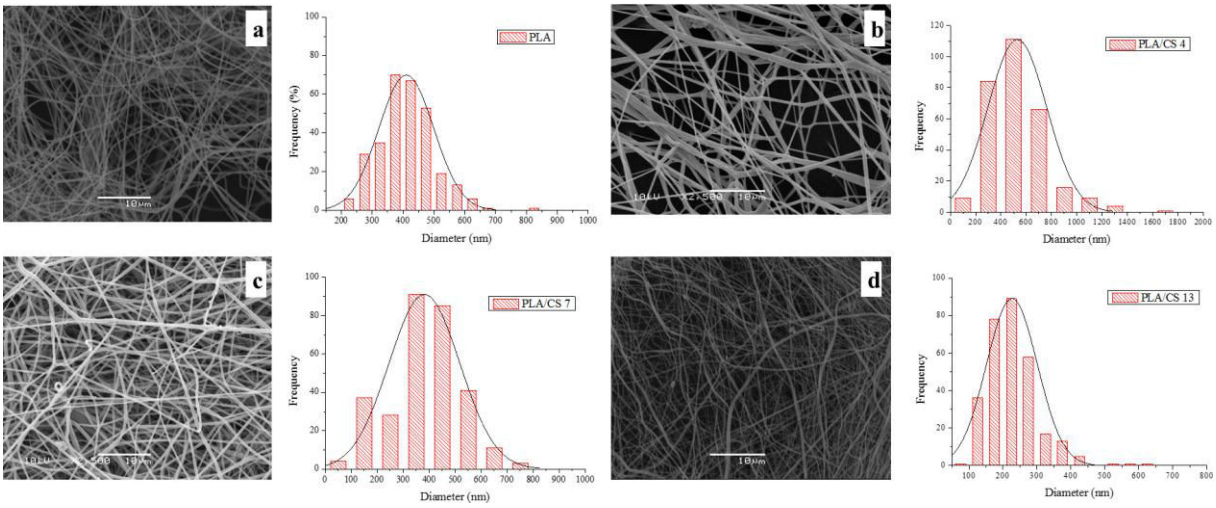

Figure 1.12. SEM images and diameter distribution of (a) PLA, (b) PLA/chitosan 4, (c) PLA/chitosan 7 and (d) PLA/chitosan 13 fiber mats. Note: 4, 7 and 13 means the percentage (%wt) of chitosan added to the PLA solution.[41]

A blend electrospinning produced a poly(ε-caprolactone) core and UV-induced graft polymerization to make up the outer polyethylene glycol shell were fabricated by Yu and co-workers to be applied as controlled drug release.[42] A hydrophilic drug, salicylic acid, was loaded in the core/sheath fibers. The existence of hydrogen bonds between salicylic acid and the poly(ε-caprolactone) matrix improved drug compatibility and the drug release rate in the sustained period could be tailored by adjusting the polyethylene glycol shell thickness.

One of the most used methods, chemical vapor deposition (CVD) process refers to exposing the selected substrate to a gaseous precursor to deposit the desired powder or film in which chemical reactions are involved during this process. Lin and co-authors reported a new polymer-free graphene transfer process that enables direct CVD-grown graphene to be transferred from copper to any substrate. The graphene film presented advanced electrical properties and superior atomic and chemical structures as compared to the graphene sheets transferred with conventional polymer-assisted methods.[43] **Figure 1.13** showed the schematic process proposed by the authors. The graphene films had grown on copper foils and can be easily replaced in the end of the film formation. This would not be possible in a standard polymer-based method, such as using poly(methylmetacrylate) as temporary support, because a rigid support would be needed for transferring the graphene film to prevent destroying the atomically thin graphene. To minimize the external force around graphene, it was also designed a graphite holder to reduce the external force from ambient or solution that would apply on graphene and to prevent it from degrading (folding or tearing) during the transfer process.

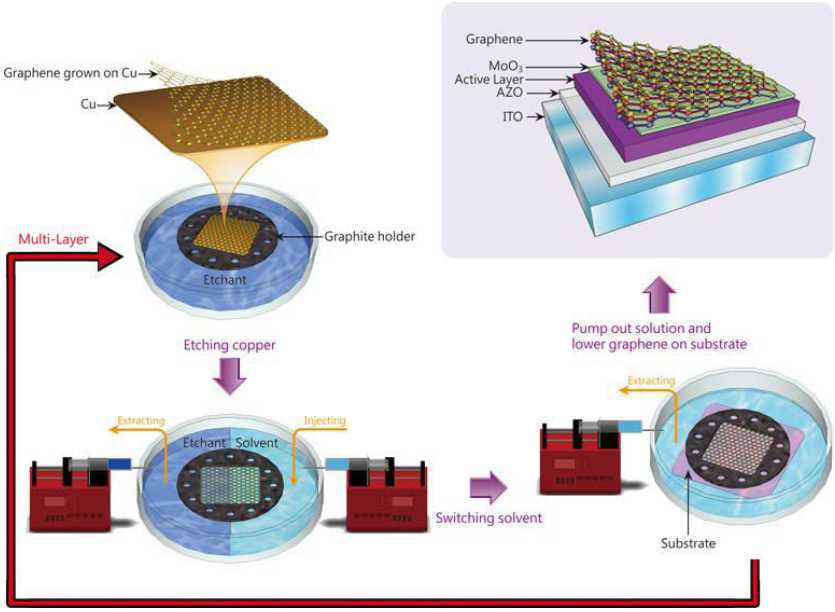

Figure 1.13. Schematic illustration of the polymer-free transfer process by CVD method.[43]

For layer-by-layer process, it is not necessary to use a master for replication like in template or lithography methods or even provide a particular environment chamber like plasma and CVD. Here, the deposition occurs spontaneously by the assembly of layers with adsorptions which can better control the thickness of the produced film. It is an economical, practical and

easy method to fabricate superhydrophobic surfaces. Wang and co-authors could better control the number of layer deposited by the layer-by-layer method through sulfurization of MoO_2 microcrystals.[44]

The sol-gel process is a type of chemical solution deposition where the solution is the precursor in the selected substrate to form a gel-like network. Usually, these coatings are temperature-resistant and they are highly dependent on how the sol was prepared and the surface functional groups of the resulted gel. This method is very used to fabricate metal oxides for photocatalytic activity.[45,46] NH_3 sensor was prepared via sol–gel method at 500 ºC using zinc acetate, 2-methoxyethanol, and monoethanolamine as precursors.[47] Li and co-workers showed that the highest sensor response for the ZnO film was achieved with 600 ppm NH_3 in air at 150 ºC (57%). The performance of the thin ZnO film was affected by NH_3 and O_2 concentration and by the temperature on the sensor response. **Figure 1.14** showed the microstructuration of the ZnO film formed post sol-gel method and the sensor response for various treatment time and NH_3 concentration.

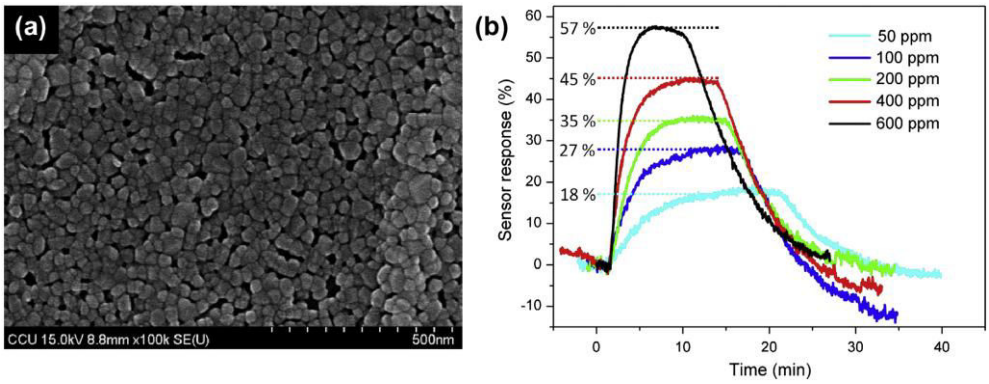

Figure 1.14. (a) SEM image of the ZnO thin film and (b) Sensor response of ZnO thin film to NH3 (50–600 ppm) at an operating temperature of 150 ºC.[47]

Mostly used techniques of deposition are spray-coating, dip-coating and spin-coating. These methods are considered fast and versatile to the production of super-wetting surfaces. Superhydrophobic surfaces were produced by dip-coating copper substrates in a solution containing $AgNO_3$ and trimethoxypropylsilane by Rangel and co-authors.[48] Indeed, superhydrophobic and superoleophobic surfaces were produced by a two-step dip-coating procedure: immersing the copper substrate in a $AgNO_3$ solution and, after that, in a solution containing 1*H*,1*H*,2*H*,2*H*-perfluorodecyltriethoxysilane. A colorful superhydrophobic and self-cleaning coating was fabricated on stainless steel by a one-step spray-coating method via

chemical reactions between inorganic salts and sodium stearate as reported by Li and co-authors (**Figure 1.15**).[49] The coating maintains excellent chemical stability under both harsh acidic and alkaline circumstances and the superhydrophobic properties are kept even after being immersed in a 3.5 wt % NaCl aqueous solution for 1 month. The coating also shows excellent resistance to corrosion.

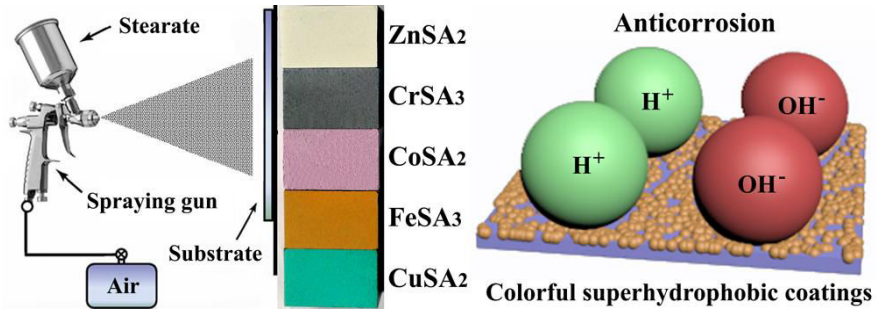

Figure 1.15. Schematic representation of the spray-coating process forming colored coatings on stainless steel substrates by spraying white, cinerous, purple, aurantium and blue stearates, respectively, and the representation of the anti-corrosive properties.[49]

1.4 ELECTROPOLYMERIZATION OF CONDUCTING POLYMERS

A famous engineering route towards to design nano and microstructured conducting polymers with a wide range of wettability is the electrochemical polymerization or electropolymerization.[50] This technique is classified as a "bottom-up" approach and presents many advantages towards the other techniques presented in *Section 1.3*. In the following, a brief introduction about conducting polymers will be presented as well as the principles of the electropolymerization technique, the mechanisms proposed for some molecules and the main factors that influence in the surface morphology and wettability.

1.4.1 Conducting polymers

The first synthesis of these organic conducting materials was performed in 1977 by Shirakawa, MacDiarmid and Heeger.[51] The researchers observed an improvement of the

electric conductivity of the polyacetylene in several orders by a simple doping with iodine vapor. Due to the polyacetylene instability in the air and hard synthesis, the demand for new conductive polymer began. The importance of this discovery was highlighted in 2000 by awarding the Nobel Prize in chemistry to the authors of this achievement.[52] Since there, the field of organic conducting polymers has attracted the interest of many academic and industrial researchers that are searching of new synthesis or manufacturing methods and potential applications.[53,54] Nowadays, the main three families of aromatic molecules which are subject of study for various researchers are polypyrrole, polyaniline and polythiophene; however, many other molecules have been discovered every day. **Scheme 1.1** shows some examples of conducting polymers.

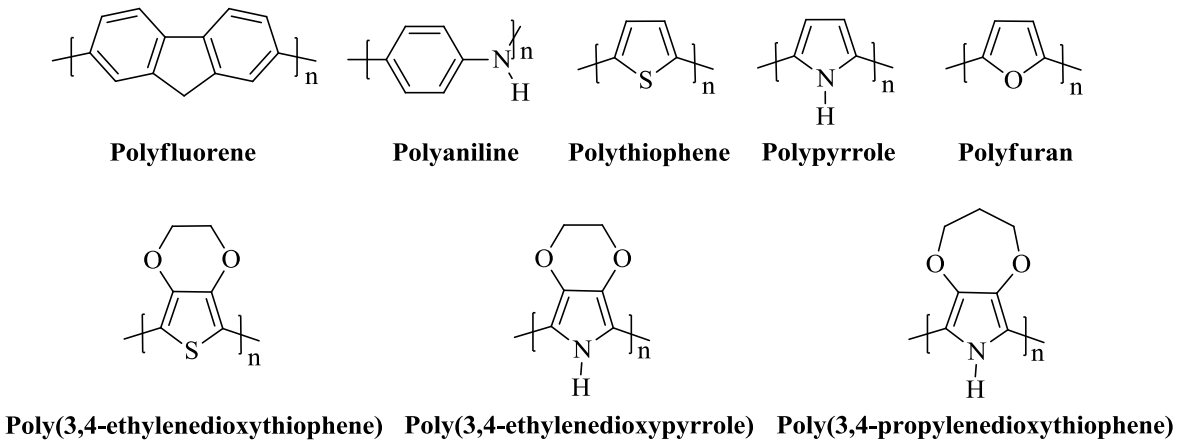

Scheme 1.1. Examples of conducting polymers.

The conducting polymers have a conjugated chain structure containing series of alternating single (σ-bonds) and double bonds (σ- and π-bonds). This configuration promotes a broad overlap between the *p*-orbitals and as a result a high degree of electronic delocalization. Additionally, this highly conjugated structure also reduces the energy gap between the several bonding and anti-bonding π orbitals (π and π^* bands) which allows easily population of the π^* band which promotes the electrical conductivity to the material (semiconductor).[51] The key to improve the electric conductivity of the conducting polymers is to introduce a dopant to produce a charge carrier along the molecular system by removing (oxidation) or by injecting (reducing) electrons.[55,56] This operation will create holes (positive charges) or electrons (negative charges) along the macromolecular chain. The nature and concentration of these dopants can significantly influence the optical and electronic properties of these materials.

Conducting polymers are unique organic materials which present many properties, such as the ability to conduct charge, good electrical and optical properties, easy synthesis and fabrication of porous and nanostructured materials.[57] They have been called significant academic and technological interest due to the combination of the electronic and optical proprieties of metals and inorganic semiconductors with the attractive properties typically associated to conventional polymers, including mechanical flexibility and low-cost production. A potential good substitute for metals and semiconductors, the conducting polymers can have their chemical, electrical and physical properties [58–60] tailored to the material specific needs or controlled through stimulation (pH, electricity, light, etc).[61–66] Recent applications for the conducting polymers are as electrochromic devices,[67–71] solar cells,[72–75] supercapacitors,[76,77] batteries,[78,79] superconductors,[80,81] etc.

In general, there are two main synthetic routes to fabricate conducting polymers: by chemical or electrochemical approaches. By chemical pathway, the reactions usually produce powdery nanomaterials which can be easily scale-up for a mass production. It is a very interesting fabrication system for mass production desired in the industry. On the other hand, the fabrication by electrochemical polymerization restricts the reactions on the surfaces of the electrodes and is useful particularly when films are desired. This is a one-step method effective to produce conducting polymeric nanomaterials with controlled morphology and properties. Our research group has been dedicated to extending and improving the performance of various conducting polymers by electrochemical polymerization due to their structuration and surface wettability.

1.4.1.1 *Pyrenes*

Pyrene was first reported by Laurent in 1837 after discovering the compound in the residue of a destructive distillation of coal tar. Since there, it has become very used in organic chemistry due to its various photophysical proprieties as reported by Duarte and Müllen.[82] Nowadays, the polypyrene is a representative π-conjugated polymer and a very interesting material for photoluminescent application due to its high fluorescence quantum yield.[83] Therefore, (oligo)polypyrenes presented higher electrical conductivity, higher thermal stability and lower toxicity than pyrene monomer. Among other distinctive properties of pyrene are their ready functionalization, solvatochromic phenomena, high propensity to form excimers which makes it very desirable for applications in photoluminescent devices and chemical sensors.[83–89]

Chhatwal and co-authors also showed the high potential application as is memory storage devices.[88,90]

Rajagopal and co-authors reported a Friedel–Crafts benzoylation of pyrene that results in the formation of green-yellow-orange luminescent crystals (**Figure 1.16**) due to the decrease in the π–π interactions (π-stacking) that caused a systematic blue-shift in the emitted light in the crystalline state.[91] The emission of pyrene monomer and (oligo)polymer is usually in the blue region,[87,92–94] but it can be also in the green region [94–96] as reported in the literature, which will normally depend of the excimer emission.

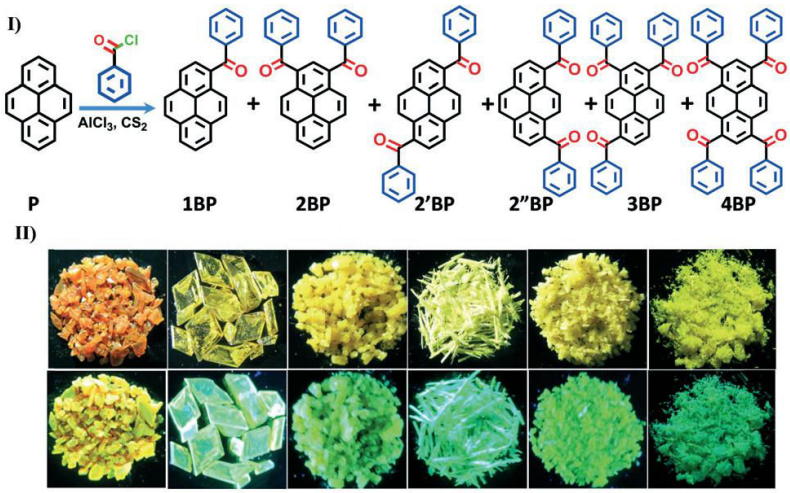

Figure 1.16. I) Molecular structures of benzoylpyrene and II) photographic images of crystals in daylight (above) and under UV illumination (below).[91]

Lu and co-workers reported the synthesis and electropolymerization of oligo(1-aminopyrene) films showing good redox activity, water solubility and enhanced fluorescence property in comparison with its monomer.[93] The film pronounced good sensitivity and fast response as fluorescent chemosensor to sense Fe(III) and Pd(II) in aqueous solution. Shi and co-authors synthesized (2-(4-(1-pyrenyl)butanoyloxy)ethyltrimethylammonium bromide) by the combination of chemical and electrochemical synthesis generating a probe with a high fluorescence quantum yield that can easily detect ultra-trace of TNT in pure or environment ground water with high sensitivity.[85]

Pyrene moiety has been called the attention of researches for their combined fluorescent and superhydrophobic properties. A fabrication of fluorescent superhydrophobic coating was presented by Xu and co-authors by the electropolymerization of polypyrene coating followed by a CVD of tetraethoxysilane (TEOS) and 1*H*,1*H*,2*H*,2*H*-perfluorooctyltriethoxysilane

(POTS).[95] The hybrid polypyrene/silica coating exhibits strong blue-green fluorescence emission derived from the excimer forms and microstructured surfaces achieving θ_{water} = 163º and α = 4º. The rough morphology and the fluorescent properties are presented in **Figure 1.17**.

Even though the pyrene derivatives present good potential for application in surface science, their use in this field remains scarce. The study of fluorescent superhydrophobic coating is usually limited to only self-assembly method and few fluorescent materials, such as quantum dots or dyes.[97–100] The restriction ways for its manufacture prevents the academic and technological advance for the preparation of robust fluorescent and superhydrophobic coating.

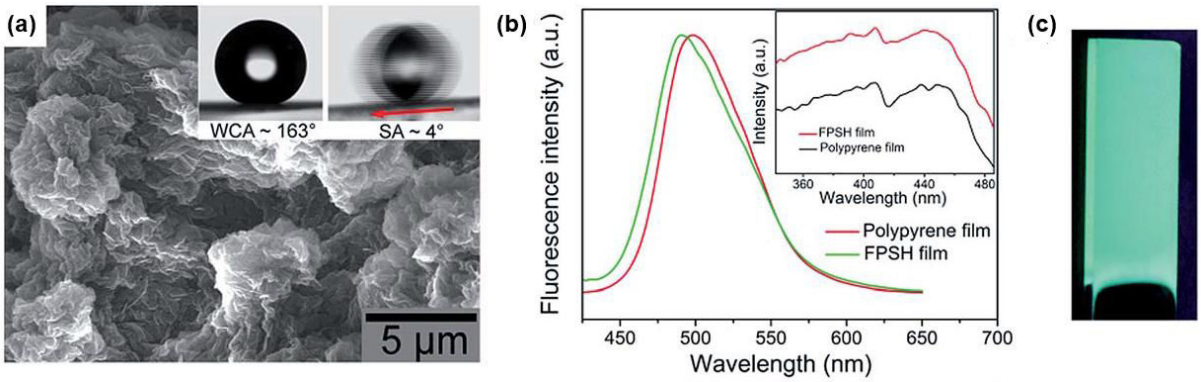

Figure 1.17. (a) SEM image of the polypyrene/silica hybrid film after electropolymerization and CVD of TEOS and POTS. Inset: the apparent (WCA) and dynamic (SA) contact angle of the studied surface. (b) Fluorescence emission spectra of the polypyrene film (λex = 408 nm, red) and polypyrene/silica (FPSH) film (λ_{ex} = 408 nm, green). Inset: the excitation spectra of the polypyrene (λ_{em} = 498.5 nm, black) and polypyrene/silica (λ_{em} = 490.5 nm) films. (c) Fluorescence photograph of the polypyrene film (blue-green fluorescence under 365 nm UV light.[95]

1.4.1.2 *Thiophenes*

One of the most studied conducting polymers is the polythiophene and its derivatives. The name of the thiophene was emerged from the combination of the words *theion* (sulfur) and *phaino* (shining) in Greek. The thiophene dated from 1883 when was discovered by Meyer who isolated the compound from the blue dye consisting of 1*H*-indole-2,3-dione (isatin) and sulfuric acid in crude benzene.[101] It is a liquid compound that is very reactive due to the high π-electron density. This molecule has been of great interest because of their high electrical

conductivity, electrochromism, high environmental and thermal stability and versatile redox properties.[102]

The thienothiophenes is a classification of fused thiophenes that have two annulated units and they are presented in four isomers: thieno[3,2-*b*]thiophene, thieno[3,4-*b*]thiophene, thieno[2,3-*b*]thiophene and thieno[3,4-*c*]thiophene. They are electron-rich structures allowing them to build conjugated and low band gap organic compounds. The fusion of three thiophene units generates the dithienothiophene which are flat and rigid molecules with delocalized system. In the following, structures that are composed for more than three thiophene units are called as thioacenes. The thienothiophenes, dithienothiophenes and thioacenes are important molecules providing interesting properties and had been calling attention not only for their versatile synthetic route but even for their application as organic materials.[103–105] The synthesis and properties of these compounds have been studied extensively and it was summarized by Cinar and Ozturk.[106]

The conjugated thiophene and its derivatives have many potential applications, such as in sensors and photovoltaic devices.[107–115] Zhao and co-authors reported the application of highly conductive doped polythiophene thin films as sensors to detect thiols and amines with low detection limit.[108] In the other hand, Cutler and co-authors reported the synthesis of polymers and copolymers of bithiophene using an electrochemical synthetic route with good photovoltaic responses in their fully reduced state when incorporated in the photoelectrochemical cells.[112] However, for the same materials in the fully oxidized state, negligible photovoltaic responses were taken. This condition is changed when the thiophene is chemically substituted with the electron withdrawing group –CN and the electron donating group $–NMe_2$ improving the observed photovoltaic response.

Thiophene derivatives also have been the subject of increased attention/research in the materials field, mainly for 3,4-ethylenedioxythiophene (EDOT), largely explored in the production of structured materials using electrospinning [116–118] and electrochemical methods [119–121] with a wide application for solar cells.[119–123] The presence of 3,4-ethylenedioxy bridge highly enriches in electron the polymerization site and also highly increases the polymer rigidity and conductivity. Recently, an electrodeposited PEDOT was post-synthetically functionalized with alkyl, aryl and perfluorinated chains by a click reaction as showed by Godeau and co-authors.[124] The surface wettability and morphology was deeply changed when the direct surface functionalization was compared with the nanoparticle-grafted surface functionalization due to the increase in the functionalizable surface area (**Figure 1.18**). The

authors also reported the use of nucleosidic linker in the post-functionalization of the surface via azido-alkyne cycloaddition reaction and by the use of Staudinger-Vilarrasa reaction to introduce various substituents as a platform to obtain parahydrophobic surfaces.[125,126] Even though they have been known and studied since a long time, more studies should be done with the thiophene main core and it derivatives because of their robust properties and extensively use.

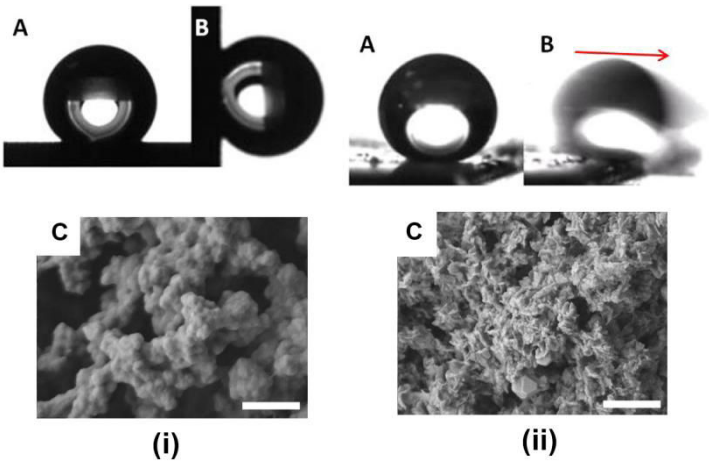

Figure 1.18. (a) Static contact angle, (b) dynamic contact angle and (c) SEM images for the surfaces (i) by a direct click chemistry reaction (parahydrophobic) and (ii) by the nanoparticle-grafted click chemistry reaction (superhydrophobic).[124]

1.4.2 Principles of electropolymerization

The electrochemical polymerization consists in a fast process that guarantees the polymerization, deposition and structuration of the film in only one-step. The principle of this method is the oxidation of the monomer in an electrochemical cell to induce the polymerization and the deposition of the film on the working electrode. The monomer, dissolved in an appropriate solvent and electrolyte, is oxidized at the surface of an electrode by application of an anodic potential. The polymerization involves a number of subsequent steps and many researchers reported different mechanisms, as described by Sabouraud and co-authors for the polypyrrole.[127] A general and representative mechanism of the electropolymerization is displayed in **Scheme 1.2**.

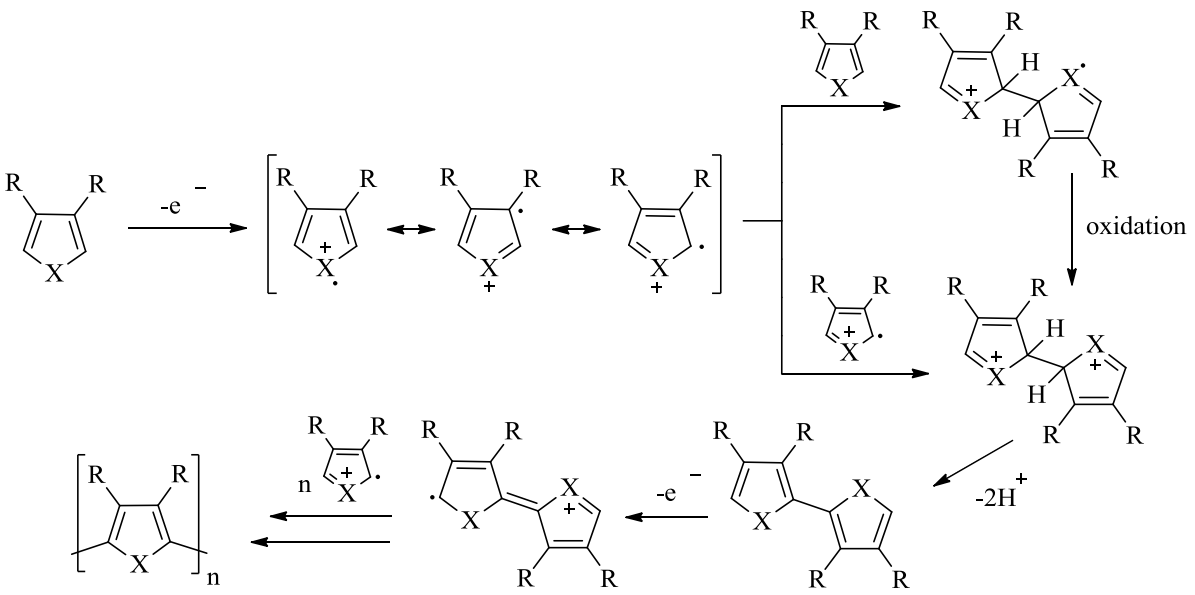

Scheme 1.2. General mechanism of electropolymerization.

The electropolymerization starts with the generation of a radical cation by the oxidation of the monomer. The coupling of two radical cations or one radical and a monomer and the successive elimination of 2 protons results in the formation of a dimer. In the sequence, the oxidation of the dimer and the sequential coupling with additional synthons (monomer, oligomer) propagates the polymeric chain growth. The termination step occurs when there are no more monomer on the media, when the polymer precipitates/deposits or due parallel reactions that cause the "death" of the active polymerization sites.[54,127]

The working electrodes can be made of various materials not easily oxidizable such as platinum, gold, glassy carbon, indium tin oxide (ITO) coated glass, nickel, stainless steel, etc. The choice of the working electrode depends mainly on the electrochemical polymerization system and the purpose of the experiments because it can influence the final properties of the deposited film, as showed by Skotheim and co-authors.[128] Indeed, the working electrode should be electrochemically stable to the applied of oxidation potential of the used monomer. Generally, the electrochemical polymerization was carried out in a three-electrode apparatus (the working electrode, the counter electrode and the reference electrode) in a one-compartment system. The counter electrode should be electrochemically inert to the use of monomers, electrolytes and solvents. The saturated calomel electrode (SCE) has been widely used as a reference electrode in aqueous and organic medium.

Nevertheless, the electropolymerization do not only provide films with controllable surface morphology and wettability as well is considerably simpler, faster and more cost-effective

technique when compared with the conventional chemical polymerization.[129] Many are the parameters that affect the electropolymerization, such as the monomer structure and concentration, the solvent, the electrolyte, the voltage, the temperature, the deposition time or method.[129–132] Indeed, this technique does not require high voltages or the use of catalyst/initiators to polymerize, being a template-free approach for the fabrication of unique surface structures.

1.4.3 Factors that influence the electropolymerization

Since 1979, when Diaz reported the first electropolymerization of pyrrole, the researchers started to search for others pathways to electropolymerize the so called conducting polymers and study which are the parameters that influence the polymerization process.[133] The electropolymerization allows obtaining materials with tunable wettability and various morphologies which are dependent of the parameters used. While many polymers present a high stability to the electrochemical parameters, others may have their morphology changed easily. Wolfs and co-authors reported the use of many supporting electrolytes and solvents in the electropolymerization of PEDOT films.[134] Structured surfaces with various shapes were obtained with high polar solvents while the less polar solvents gave smoother surfaces as showed in **Figure 1.19**. In opposition, when the supporting electrolyte was changed, no significant variation on the morphology was observed on the formed fibers structures. Although there are several works reporting how each parameter could affect the electropolymerization, the singularities of each system (specially the monomer) require a deep investigation in order to have a comprehensive evaluation concerning the influence of parameters on the process (solvent, electrochemical method, electrolyte and solvent).

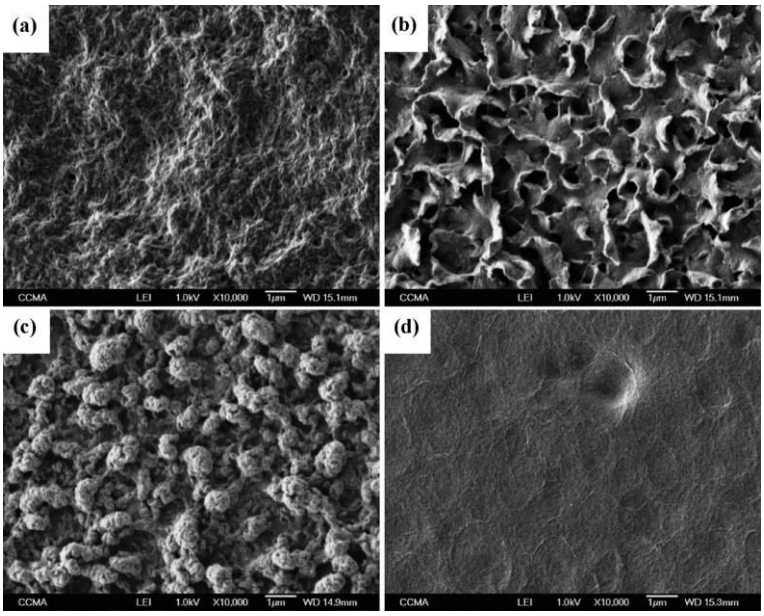

Figure 1.19. SEM images of PEDOT derivative obtained by electropolymerization in different solvents: (a) propylene carbonate, (b) benzonitrile, (c) nitrobenzene and (d) dichloromethane. Constant Potential method at 200 mC cm^{-2}, Bu_4NPF_6 as electrolyte.[134]

The choice of the supporting electrolyte is one of the most important parameters and it depends upon its solubility, degree of dissociation, conductivity, basicity and nucleophilicity and it can affect the morphology and the final properties of the deposited films.[135–138] The hydrophobic or hydrophilic nature of the electrolyte has an impact on the produced film because of the interactions between the anion and the polymer. Indeed, as higher the basicity of the anion, lower the polymer conductivity due to an increase of interactions between the positive charges of the polymer and the anion. Moreover, the anion oxidation potential should be higher than the monomer. The anion size is also an important parameter since it represents about 30% of the weight of the polymer film and it can control the microstructure and the porosity of the polymer. Lithium perchlorate electrolytes have been extensively used due their high solubility in water and acetonitrile and their high electrochemical stability.[139–141] In organic solvents, quaternary ammonium salts are common supporting electrolytes for the polymerization of conducting polymers.[142–145] Boron trifluoride diethyl etherate (BFEE) is a good supporting electrolyte used to replaced both the solvent and electrolyte for conducting polymers as reported in the literature for polypyrene polymerization [94,146] and it is often used when monomer polymerization is difficult. Shi and co-authors reported that the low ionic conductivity of pure BFEE can be increased by the addition of a small amount of water or

strong acid accelerating the polymerization rate for polythiophene and poly(*p*-phenylene) reactions.[147]

The oxidation potential used for the electropolymerization is dependent of the monomer structure and the nature of the electrolytes and solvents. For monomers with different large dense aromatic ring or electron donating groups, the oxidation potential is reduced due to the stabilization of the corresponding cation radicals. A simple example is for the benzene rings, that presents a higher oxidation potential for benzene than for naphthalene or pyrene.[148–150] Indeed, the selected electrolyte and solvent can influence in the oxidation potential acting as an electrocatalyst. The oxidation potential can also influence the film deposition: very low potentials may not achieve the oxidation of the monomer and, consequently, do not polymerize or very high potentials can lead to damage film.

Since the solubility of aromatic compounds in water is usually poor, organic solvents are more commonly used.[151–153] For polymerization reaction that proceeds via cation radical intermediates, aprotic solvents are preferably used in order to minimize the nucleophilic reactions. Among them, acetonitrile, dichloromethane and propylene carbonate have been extensively used. Poverenov and co-authors found a very significant solvent effect but a small electrolyte effect for PEDOT films prepared by electropolymerization.[154] The morphology has found to be directly related to the electrochromic properties which showed differences for using acetonitrile and propylene carbonate as solvent, such as the transparency, coloration efficacy and contrast. The choice of the solvent can even influence in the nucleation and growth mechanisms of the conducting polymers, as reported by Schrebler and co-authors for the polythiophene.[155] Indeed, acidic medium has been also used to improve the solubility and the conductivity of the electrolytes of some monomers, such as pyrrole and aniline.[152,156,157]

The electropolymerization is generally achieved by imposing a positive potential (constant potential and pulse deposition), or to cycle with a sufficiently high limit (cyclic voltammetry), or to pass an anodic current (galvanostatic deposition) through the electrolytic solution with the monomer to obtain the polymeric film. Cyclic voltammetry is a very often used method to describe the electrochemical behavior of the oxidation and reduction process. Constant potential, galvanostatic and pulse deposition methods have been utilized to describe the nucleation and growth mechanism of the oligo-polymers.[127] The progressive grow of the polymer and its properties will strongly depend on the method chosen. For example, Bellanger and co-authors have pointed out that the choice of the electrochemical method had influence in the surface oleophobicity for poly(3,4-ethylenedioxypyrrole) (PEDOP)

derivatives.[130] The electropolymerization at constant potential had lead to an oleophobic surfaces with $\theta_{hexadecane}$ = 110º due to the presence of nanoporosities on the film. However, $\theta_{hexadecane}$ = 140º had been found when the method was changed for galvanostatic and pulse deposition. Both methods are efficient to produce nanoporous surfaces which increase the oleophobicity of the films. Using these same methods, Ocón and co-authors had shown films of poly-3-methylthiophene grown as a homogeneous coating on ITO and graphite substrates for pulse deposition, while a heterogeneous structure was observed for galvanostatic method.[158]

Even though the monomer oxidation potential is independent of the pH and temperature, they influence on the behavior of the polymerization. Luo and co-authors observed an effect of temperature on the formation of the structures for thiophene derivatives. They observed a formation of nanodots structures on the surface when the electropolymerization was carried out at 25 ºC, but tubular structures when the temperature decreases to 0 ºC (**Figure 1.20**). Bazzaoui and co-authors had shown the influence of the pH on the adherence of the polypyrrole film formed.[159] When the electropolymerization was carried at acid and neutral pH, homogeneous and adherent films were formed by potentiostatic mode while for the polypyrrole coatings produced in basic pH non-adherent films were obtained.

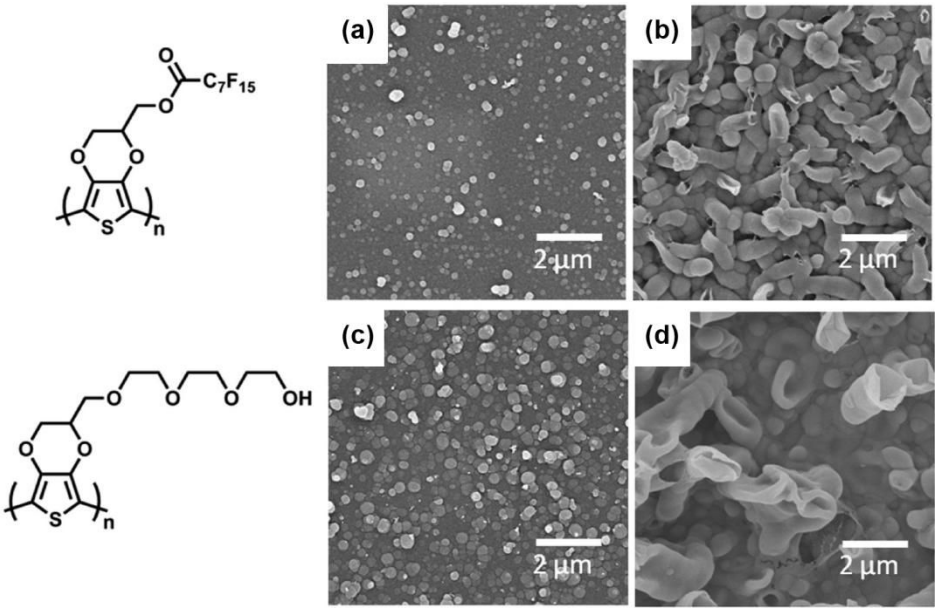

Figure 1.20. SEM images of electrodeposited PEDOT derivatives by applying a constant voltage of 1.4 V (vs Ag/Ag+) at (a-c) 25 ºC for 30 s and (b-d) 0 ºC for 90 s.[165]

In order to control the formation of surface nanostructures, the core responsible for the polymerization (such as pyrrole, thiophene, EDOT, etc) is probably the most important parameter because each molecule leads to different polymerization capacity and solubility which can highly influence the morphology. Then, the polymer can also be controlled by introducing hydrophobic/hydrophilic substituents or dopant agents.[160–162] In most of the cases, fluorocarbon or hydrocarbon chains were used to reach superhydrophobic properties.[162–164]

1.5 MICRO-NANOSTRUCTURED SURFACES AND THEIR POTENTIAL APPLICATIONS

Surfaces with special wettability and morphology have been extensively studied over the last two decades and can be now obtained using a wide range of materials and methods. Today, the study of materials with superhydrophobic properties is extensively reported both for their various wetting theories and many potential applications, such as in self-cleaning textiles, separation membranes, anti-fogging windows, anti-corrosion or anti-bacterial coatings, etc. However, the design and fabrication of surfaces that mimic the rose petal or gecko foot are also much desired. This understanding has encouraging and leading the development of sophisticated surfaces expanding its field of application. Recent advances of superhydrophobic and parahydrophobic surfaces will be present in this section as well as their potential applications.

A tungsten oxide coatings were synthesized in a few seconds by plasma assisted silanization forming a stalagmite-like self-cleaning surfaces.[166] The coating prepared by Yang and co-authors is not only superhydrophobic, but also oleophobic and exhibit multi-functionalities, such as transparency, flexibility and mechanical and thermal stability. Wong and co-authors reported the fabrication of marshmallow-like structures by spraying of a novel polyurethane-acrylic interpenetrated polymer networks suspension and fluorinated silica nanoparticles in two-step process.[167] Even over 120 cycles of abrasion tests, the surface still presented the self-cleaning behavior with $\alpha < 10^{o}$ and its morphology is stable for over 300 cyles as showed in **Figure 1.21a**. The superhydrophobic coating also presented excellent mechanical, chemical and UV resistance and can be usable for glass, wood, clay stone, paper or metals surfaces

(**Figure 1.21b-e**). The excellent mechanical properties are attributed to the soft yielding elastic deformation of the polymer texture.

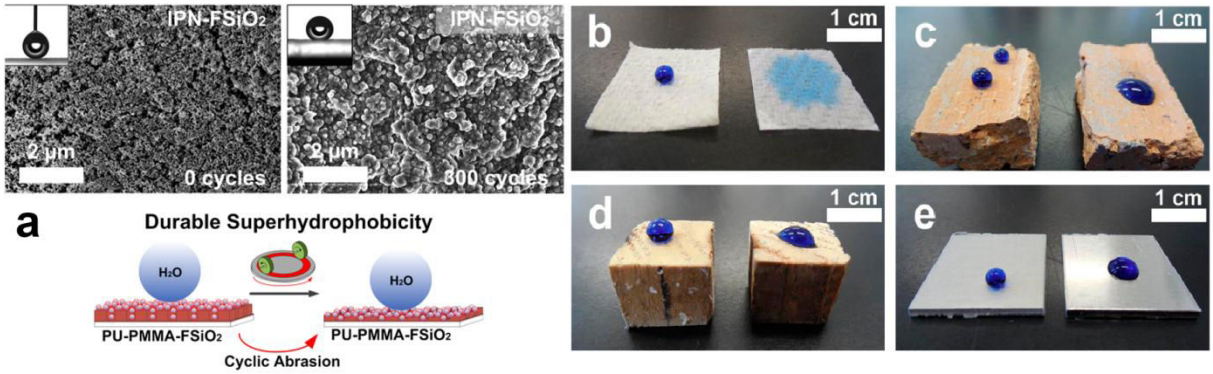

Figure 1.21. (a) SEM images of polymer (PU-PMMA-$FSiO_2$) surface before and after the abrasion test (300 cycles). PU-PMMA-$FSiO_2$ coating on a variety of substrates including (b) absorbent paper towel, (c) clay-stone, (d) wood and (e) aluminum.[167]

Different structures can lead to similar properties, such as the case of the pinecone-like structures developed by Li and co-workers.[168] By a short-time anodization process combined with a chemical modification using ethanol solution of stearic acid at room temperature, nanoflakes structures very similar to pinecones were fabricated on titanium substrate and presented excellent superhydrophobic properties under harsh conditions, such as for dirty water, tea, vinager, coffe and milk, which improve their future range of applications (**Figure 1.22**). This surface also proved to have good mechanical properties, long-term exposure to air and water jet and anti-corrosive behavior.

As well as for metals and plastic surfaces, textiles also presented superhydrophobic surfaces. Xue and co-authors fabricated a superhydrophobic and self-cleaning poly(ethylene terephthalate) (PET) textile by two-step treatment to obtain a hierarchical structure and self-cleaning behavior.[169] The PET textile surfaces were etched with sodium hydroxide yielding nanoscale pits on the microstructured textile surface. In the following, a coating with PDMS was applied with no roughening effect, only to lowering the surface energy giving the superhydrophobicity and self-cleaning behavior. The fabricated textile showed to be resistant to abrasion, UV radiation and long time laundering. Superhydrophobic and self-cleaning surfaces are the greatest desires of the academic and industrial researchers in the fabrication of nano and microstructured surfaces. In the following, it will be presented some of the desired applications to the fabrication of surfaces with hierarchical structures, such as

coatings with varied properties: anti-bacterial, anti-corrosion, anti-fouling, anti-icing, oleophobic, superhydrophobic-oleophilic, etc.

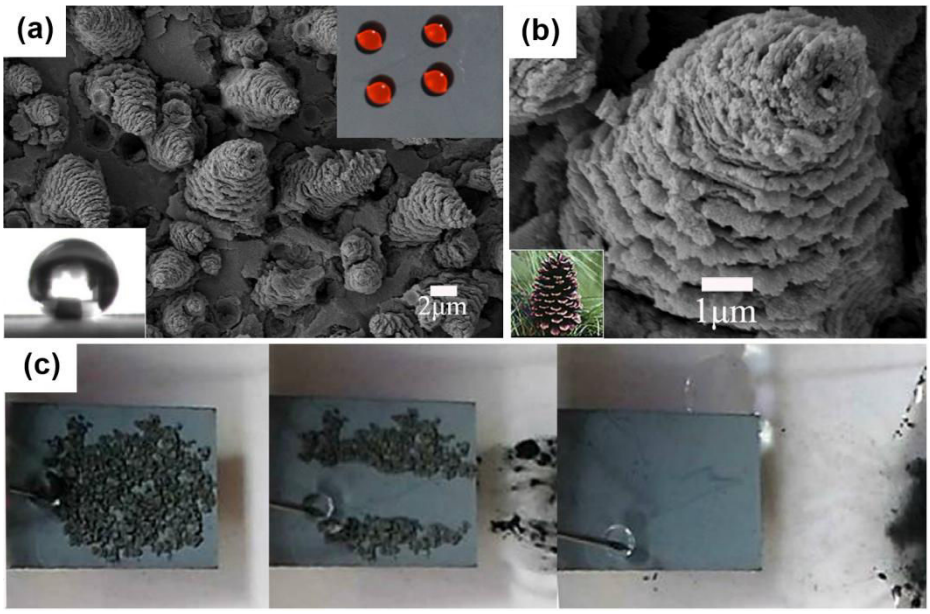

Figure 1.22. SEM images of pinecone-like structures fabricated by Li and co-workers at different magnifications: (a) 5000x and (b) 30000x and in (c) the self-cleaning effect on the surface.[168]

The creation of oil-repellent materials, or called superoleophobic surfaces, is a hot field of research for various potentials applications. However, they are extremely difficult to obtain due to the low surface tension of the oil liquids.[170–174] Remarkable works were done using stainless-steel meshes because, due to their high substrate flexibility, they are very desirable substrates for industrial applications, such as oil transportation or water-oil separation membranes. A two-steps approach was proposed by Grynyov and co-authors to prepare a superhydrophobic and superoleophobic meshes.[175] Firstly, an etching process using an aqueous solution of hydrochloric acid resulting in the creation of the nanoscale structures to the microscale existing in meshes. To enhance the hydro- and oleophobicity, a chemical treatment with perfluorononanoic acid was done. The hierarchical structure and the use of low surface energy compounds generate a self-cleaning surface for oils such as canola, castor, sesame, flax and petroleum, and superoleophobicity with very high α for turpentine, olive and silicone oil droplets. Similar properties were obtained on stainless-steel meshes via electrodeposition of conducting polymer containing low surface energy compounds.[176] Highly oleophobic properties (θ_{diiodo} = 150º and $\theta_{hexadecane}$ = 136º) were elaborated by roughening the meshes with a high deposition charge using EDOP containing an undecyl spacer, an amide

connector and a short perfluorobutyl tail. **Figure 1.23** showed the stainless steel meshes produced by Grynyov and Darmanin and the respective morphology that yield a highly oleophobic surfaces.

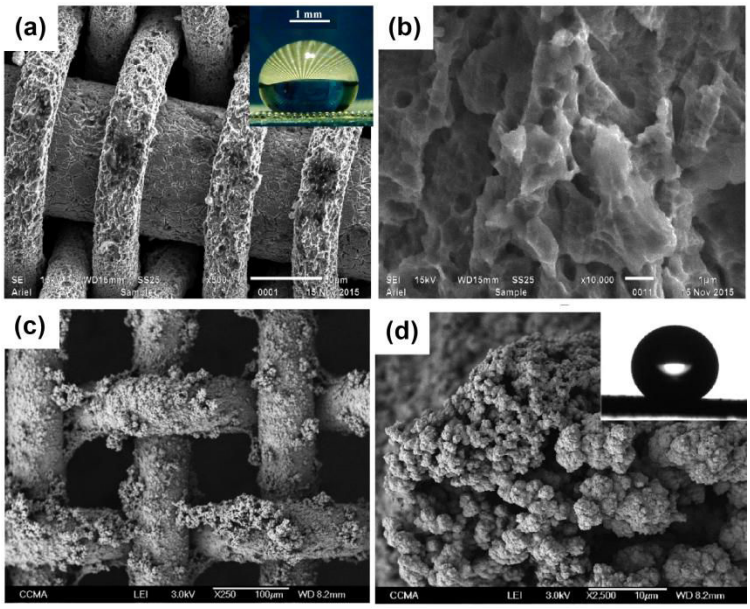

Figure 1.23. SEM images of rough stainless-steel meshes and their structures fabricated by (a-b) etching process using hydrochloric acid proposed by Grynyov and co-authors [175] and (c-d) by an electrodeposition process fluorinated EDOP proposed by Darmanin and co-authors.[176]

On the other hand, the stainless steel meshes are not only efficient to produce superoleophobic surfaces, but also superoleophilic ones.[177] Superhydrophobic nanofibers were obtained by electrodeposition of 3,4-propylenedioxythiophene (ProDOT) monomer bearing short alkyl chains with an oleophilic behavior for ethylene glycol, a liquid with an intermediate surface tension, and a superoleophilicity for very low surface tension liquids, such as sunflower oil, hexadecane, dodecane, decane, etc. Moreover, the dynamic measures showed a self-cleaning behavior, which suggests that these surfaces are good candidates to be applied as a membrane for oil/water separation. Shang and co-authors showed the fabrication of nanofibrous membrane for oil-water separation presenting superhydrophobicity and superoleophilicity.[178] The membranes were synthesized by an *in-situ* polymerization of the fluorinated polybenzoxazine incorporated silica nanoparticles functional layer on electrospun cellulose acetate nanofibers. The as-prepared surfaces presented a θ_w = 161º and θ_{oil} = 3º showing to be good candidates for industrial applications as separation membranes for water treatment and oil spin cleanup, for example. The nanofibrous structured membrane exhibited

a fast and efficient separation for oil-water mixture, as showed in **Figure 1.24**, excellent stability over a range of pH and large-scale production.

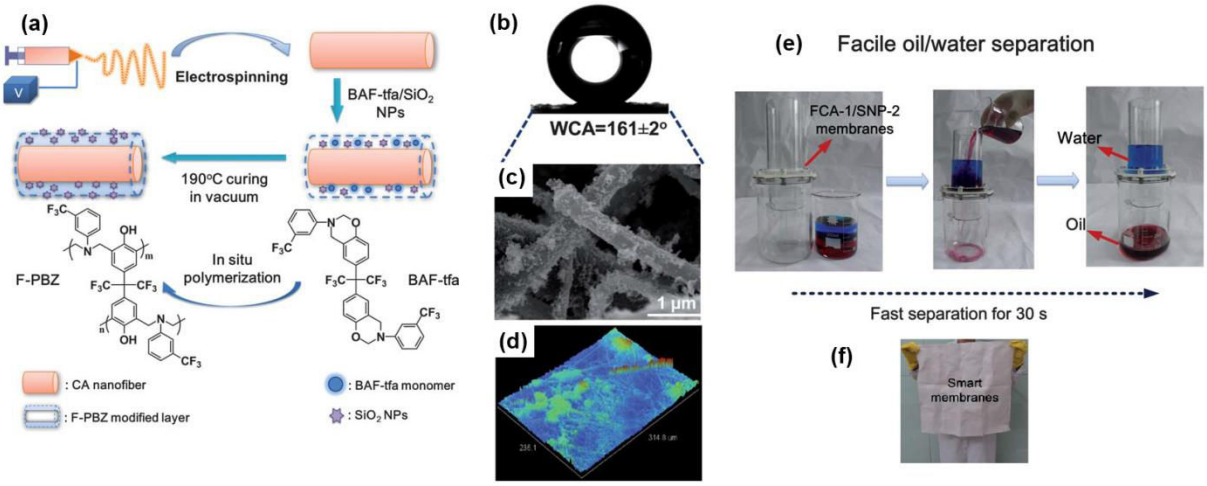

Figure 1.24. (a) Schematic representation of the in situ polymerization approach to the synthesis of fluorinated polybenzoxazine incorporated silica nanoparticles modified cellulose acetate nanofibrous membranes. (b) Water contact angle, (c) SEM image and (d) optical profilometry image for the as-prepared membrane. (e) Demonstration of the facile oil–water separation for the membranes. The water and oil were dyed by methyl blue and oil red, respectively. (f) Photograph of the large-scalable membrane (60 x 60 cm^2).[178]

One of the biggest challenges on the surface science field nowadays is the fabrication of anti-icing materials. Firstly, it was believed that was necessary to get superhydrophobicity in order to achieve anti-icing properties.[179–183] However, many researchers open this question: superhydrophobic surfaces… are they really ice repellent? Nosonovsky and Hejazi proposed a model explaining the different forces involved on the adherence of water and ice on a surface suggesting that is not always that a water repellent surface will act as an ice repellent.[184] The ice adhesion property will depend on many other factors, especially of the asperities present on surface structure. Cassie and Baxter explaining that the presence of nanoasperities or nanoroughess can generate a low water adhesion surface if the air fraction between the asperities and the surface is relevant.[7] Here, the asperities on the ice-solid interface can be the critical parameter leading to a strong ice adhesion. This theory is strongly support by many researchers. Kulinich and co-authors showed that rough surfaces can be deteriorated when submitted to icing/deicing cycles (**Figure 1.25**) in a humid atmosphere.[185] They showed that when the asperities are with the tips indented into the ice, the nanoroughness are damaged during the water solidification (icing step) and the ice melting (deicing), increasing the ice-solid contact area and decreasing the icephobicity. Similar conclusions were reported in the

works of Farhadi and Susoff.[186,187] Farther, Jung and co-authors also reported better icephobic properties for nanometer-scale smooth surfaces independent of the wettability.[188] They showed that hydrophobic surfaces really presented better resistance against the ice adhesion than hydrophilic surfaces at a same metric scale. However, hydrophilic surfaces with low roughness (1.4 – 6.0 nm) displayed considerably higher ice repellence with a greater freeze delay than hierarchically rough superhydrophobic surfaces (**Figure 1.25**). At the same time, it is not possible to affirm that superhydrophobic surfaces do not present anti-icing properties or either the nano and microstructured surfaces. Then, the fabrication of these surfaces continues a mystery: the use of compounds with low surface energy is not really necessary? Smooth surfaces are better than rough ones? What type of morphology can yield better properties to repel ice? Since anti-icing concepts are very relevant for various technical fields, such as means of transportation, cooling units, etc, it is important to study and better understand the relevance of each factor that influence the ice adhesion.

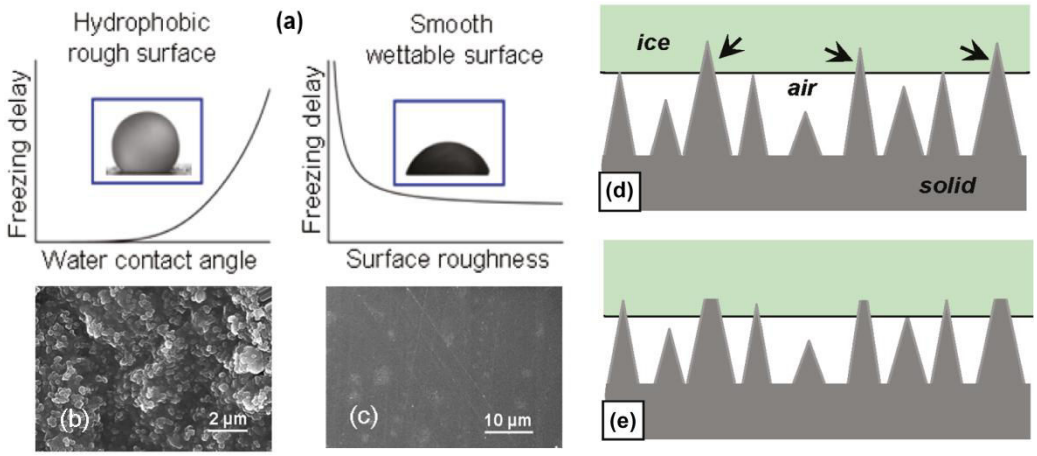

Figure 1.25. (a) Relation of the freezing delay with the surface wettability and roughness for rough and smooth surfaces. SEM images of (a) rough coating surface made with a mixture of poly(methyl methacrylate), poly(vinylidene fluoride) and Poly(tetrafluoroethylene) and (c) low roughness coating of epoxy based inorganic-organic hybrid sol-gel coating.[188] (d) and (e) are the structured surfaces during icing and deicing cycles, respectively.[185]

Momen and Farzaneh reported a multifunctional aluminium alloy substrate coated with doped-silicon aluminium oxide nanoparticles with icephobic properties.[189] The surface showed a great corrosion resistance towards to NaCl solution due to its superhydrophobic state and its interface air-solid between the pockets structures. Indeed, the ice adhesion force was found to have reduced around 5 times compared with the non-coated aluminium substrate. Here, the hierarchical structure on the surface favors to avoid the ice adhesion.

Zheng and co-authors also reported the fabrication of a superhydrophobic coating on the aluminium substrate by anodization in sulfuric acid electrolyte followed by surface modification with myristic acid yielding a hierarchical micro-nanostructure surface.[190] Merging many properties in one structured material, the surface also presented self-cleaning, anti-corrosion and anti-icing properties with an excellent weathering resistance after exposure to UV/water condensation cycles for 7 days. The corrosive properties showed to reduce in two-order of magnitude and ice adhesion strength as low as 0.065 ± 0.022 MPa was obtained for the optimized coating.

Jung and co-authors design an optical geometry to form structures from nickel to provide superhydrophobic and icephobic properties by a multi-step methodology.[181] A continuous top-down fabrication process was used: photolithography, nanoimprinting and pulse-reverse-current electrochemical deposition. Surfaces with various morphologies (bare surface, randomly nanostructured surface, an engineered nanostructured surface and an engineered hierarchical surface) were submitted to ice experiments in humid conditions for duration of 90 min. A significant decrease in the rate of ice formation was observed and ice accumulated more slowly on the hierarchical structured surface due to air present between the surface and the cavities which delays the ice nucleation and decreases the heat transfer between the droplet and the surface (**Figure 1.26**).

The surface structuration is also an important key for biological application in the surface science. To reduce or completely eliminate the extent of bacteria attachment and biofilm formation on the man-made materials have required many efforts from the academic and industrial researchers. It is known that surface chemistry plays an important influence, such as using quaternary ammonium compounds or silver particles.[191–196]

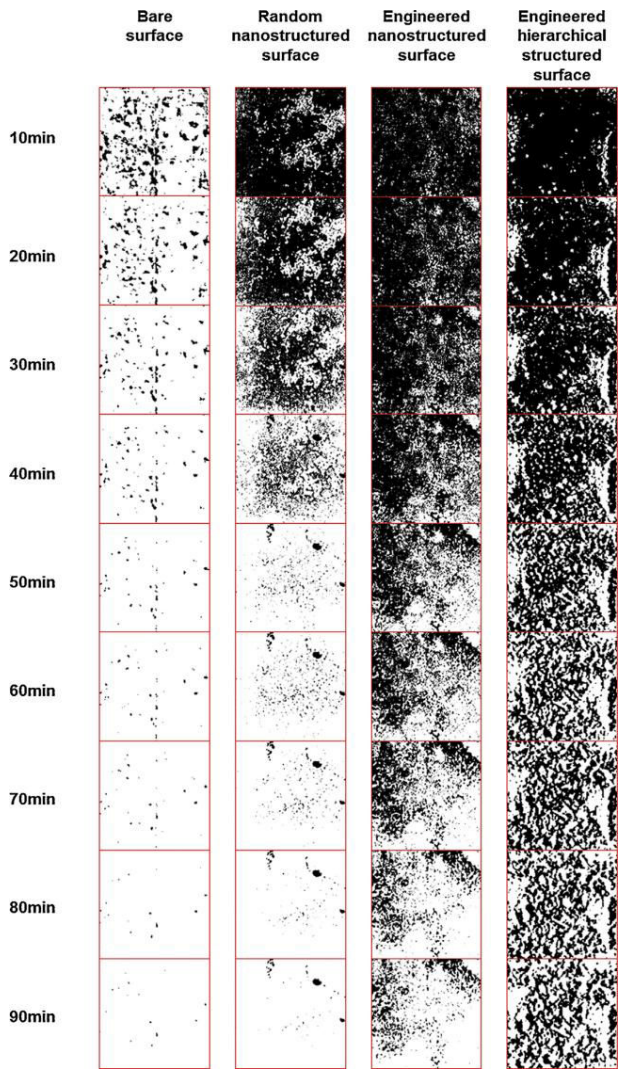

Figure 1.26. Time-lapse images of the formation of ice on the four metal surfaces. The air temperature was −10 ± 1 ºC and the surface temperature was −20 ± 1 ºC. The ice-covered area is shown as white and area without ice is shown as black.[181]

The nature already showed examples of anti-bacterial surfaces: the taro leaves and the cicada wings. Superhydrophobic, self-cleaning and anti-fouling, the nanostructures presented on the taro leaf are also highly resistant to the bacterial adhesion under completely wetting conditions.[197] In the other hand, the cicada wings are the first reported example existing naturally with a physical structure that exhibits effective bactericidal properties.[26] The nanopillars on the surface of the cicada wings are extremely efficient to kill individual *Pseudomonas aeruginosa* bacteria cells in only 3 min. This bactericidal property of the cicada wing is a physical and mechanical effect in the total with no variation when the surface chemistry was changed (a gold layer was applied on the surface with no changes on the surface roughness) (**Figure 1.27**).

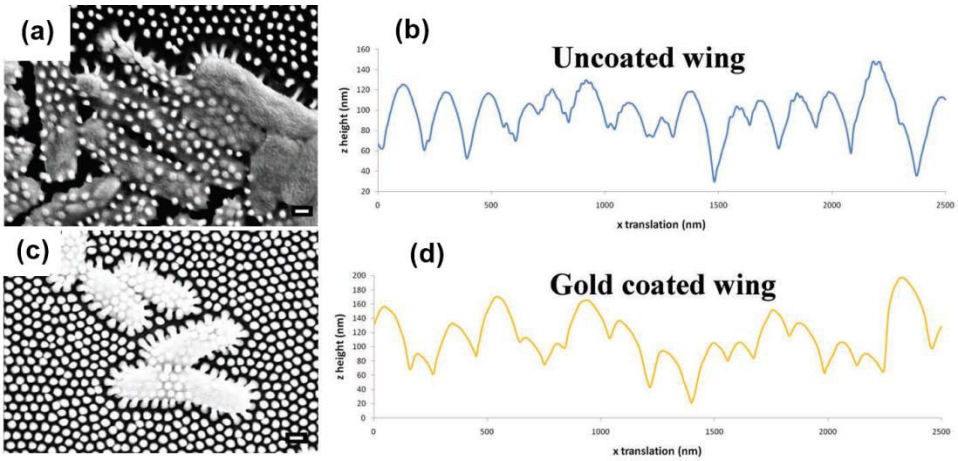

Figure 1.27. Effect of cicada wing surface structure on P. aeruginosa for (a-b) uncoated wing and (c-d) gold-coated wing. (a)-(c) shows the SEM images with nanopillar penetration on the bacterial cell and (b)-(d) the line profiles of surface topography.[26]

Many authors had already reported that the surface structure is the key parameter to reduce bacterial adhesion. Bruzaud and co-authors revealed that the bacterial adherence requires the control of surface topography using a superhydrophobic PEDOT functionalized with a fluorinated chain.[198] They showed that this property is highly associated with the water adhesion and the structures: surfaces with low water adhesion and limited crevice features provided the greatest anti-bacterial properties. A remarkable work about the influence on the ordering of the structures on the bacterial growth was done by Díaz and co-authors.[199] They showed that the bacteria grown and formed well-defined and large aggregates on randomly nanosized structures as represented in **Figure 1.28**. However, ordered engineered structure hinders the formation of aggregates as well as the bacterial alignment and the cell-to-cell sticking. Here, many of the cells are not in lateral contact with the neighboring bacteria which avoids their agglomeration and growth. Indeed, 76% of the isolated cells attached on the ordered structure surface are fitted into the trenches and aligned with them. This was the first work reporting the correlation of the bacteria cell shape and attachment with the topography of the surface.

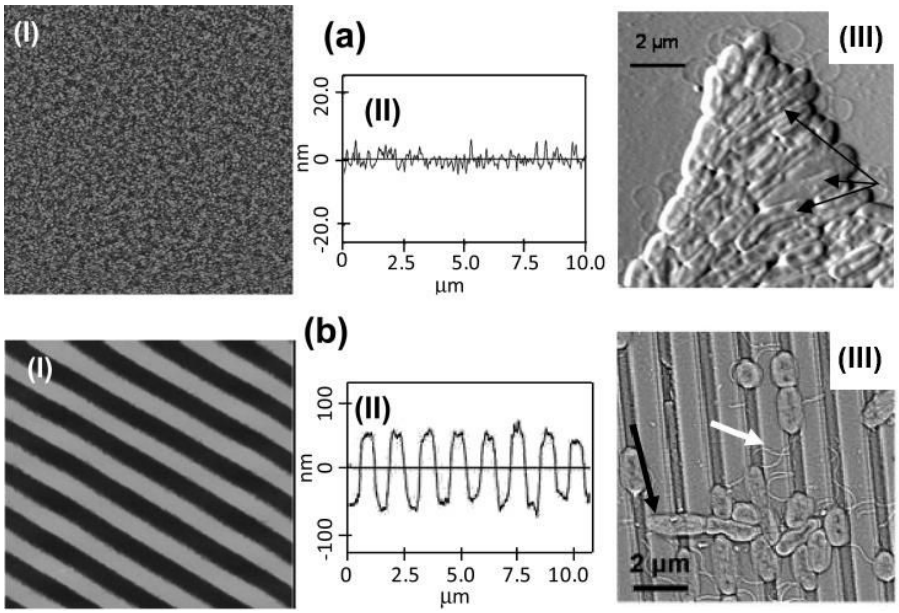

Figure 1.28. Vapor deposited surfaces at (a) randomly nanosized surface and (b) microstructured ordered surface. (I) 10 x 10 μm^2 AFM image and (II) cross section. (III) 10 x 10 μm^2 AFM image of P. fluorescens aggregates onto the analyzed substrate.[199]

It is also necessary to develop surfaces which are able to harvest water due to the scarcity of potable water in the world. Therefore, obtaining clean water is essential for the human society as well as maintaining the diversity of the fauna and flora. Countries of Middle-East and North of Africa, for example, suffer with the desertification of green areas thought several centuries. In order to find a practical and reliable method to collect water, researches are using many techniques and compounds to prepare different kind of materials that presents the proper chemical and physical parameters to attend this demand.[3,200–204] Due to their strong water adhesion, parahydrophobic surfaces with varied morphologies are quite interesting to be used as water harvesting coating surfaces.

A transparent monolayer of graphene was synthesized by multiple steps in a copper substrate by Kim and co-authors.[205] The copper foil was roughened by electroplating in sulfuric acid and copper sulfate aqueous solution at room temperature to form hierarchical surface roughness on the copper substrate. The copper surface was then thermally annealed at 850 °C in vacuum and the graphene film grown *in-situ* on the structured cooper surface by CVD in the presence of methane. A hydrophobic drape-like structure was formed with a high copper resistance to corrosion and enabling superior performance for water-harvesting applications. To demonstrate the surface performance to be applied as harvest material, an apparatus was used to measure the water condensation under humid conditions (**Figure 1.29**). The surface

was able to condensate the water vapor and start to dropwise when the water droplet achieves a specific size. The amount of condensate mass collect was 1.3 times greater for the graphene deposited on copper substrate than in the copper foil with any treatment.

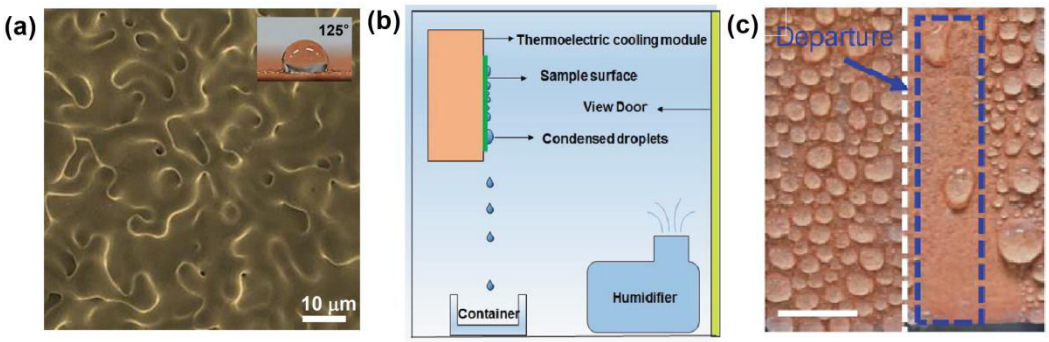

Figure 1.29. (a) SEM image of the rough drape-like monolayer of graphene deposited on copper substrate after electroplating, thermal anneling and CVD process. Inset is the contact angle of the surface. (b) Illustration of water harvesting test set-up and (c) dropwise condensation on the graphene surface.[205]

Inspired in the nature, Zhang and co-authors fabricated superhydrophobic surfaces with hydrophilic micro-sized patterns by inkjet printing method toward biomimetic fog harvesting surfaces.[206] By spin-coating, the superhydrophobic surface was prepared using a PS and silica nanoparticles forming fibers-like structures. Then, an optimized solution of dopamine was applied directly by inkjet printing to the superhydrophobic surfaces, followed by the *in-situ* polymerization, in which superhydrophilic micropatterns of polydopamine were readily obtained on the superhydrophobic surface. The micropatterned surfaces inspired in Namib Desert beetles showed enhanced water collection efficiency compared with uniform superhydrophilic and superhydrophobic. The optical and SEM images for the micropatterned superhydrophobic-superhydrophilic surface are presented in **Figure 1.30**.

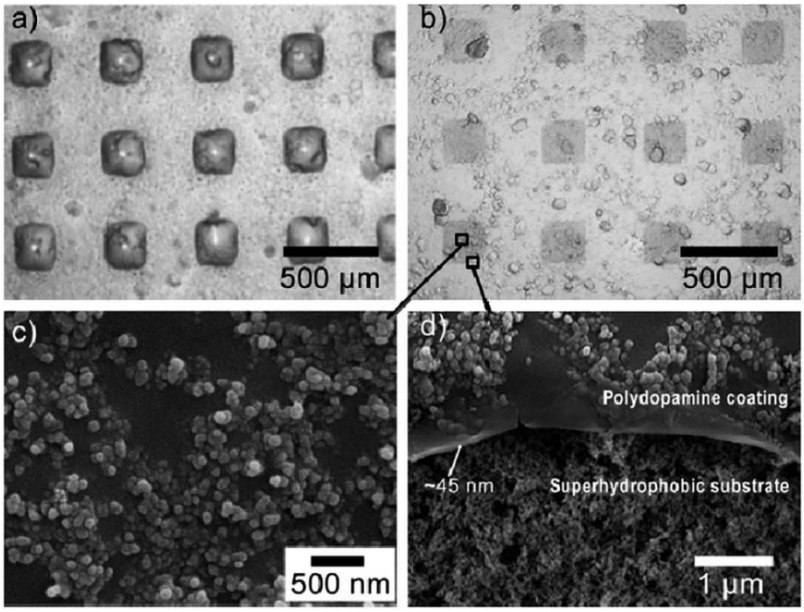

Figure 1.30. Optical microscopic image of (a) the as-printed dopamine droplet on the superhydrophobic surface and (b) of the polydopamine patterns on the surface. (c-d) SEM images of the polydopamine patterns.[206]

The research group of Prof. Jiang demonstrated a fascinating morphology of cactus-like structures using magnetic particle-assisted molding to be used as a fog collector.[207,208] To fabricate these structures, PDMS prepolymer and cobalt magnetic particles (CoMPs) through a facile approach were combining by the mechanical punching and the template dissolving technology. A schematic representation of the formation mechanism is showed in **Figure 1.31**. By regulating the weight ratio of PDMS and CoMPs, the structure of the tip could be altered under external magnetic field. The top site of the spine structures is much rougher than the bottom site, arising from the inhomogeneous distribution of CoMPs and yielding highly hydrophobic conical micro-tip arrays with a hydrophilic matrix on the base. Under an external magnetic field, static fog can be spontaneously captured and transported from the tip to the base of the spine due to the Laplace pressure difference. Indeed, the cactus spine-like structures are magnetically responsive which can be attributed to the flexibility and magnetic response properties of the PDMS embedded in CoMPs. Accompanying the horizontal movement of an external magnet, the cone arrays responded to the magnetic field by reversibly bending along the field. Once the magnet is removed, the cones will recover their original vertical positions.

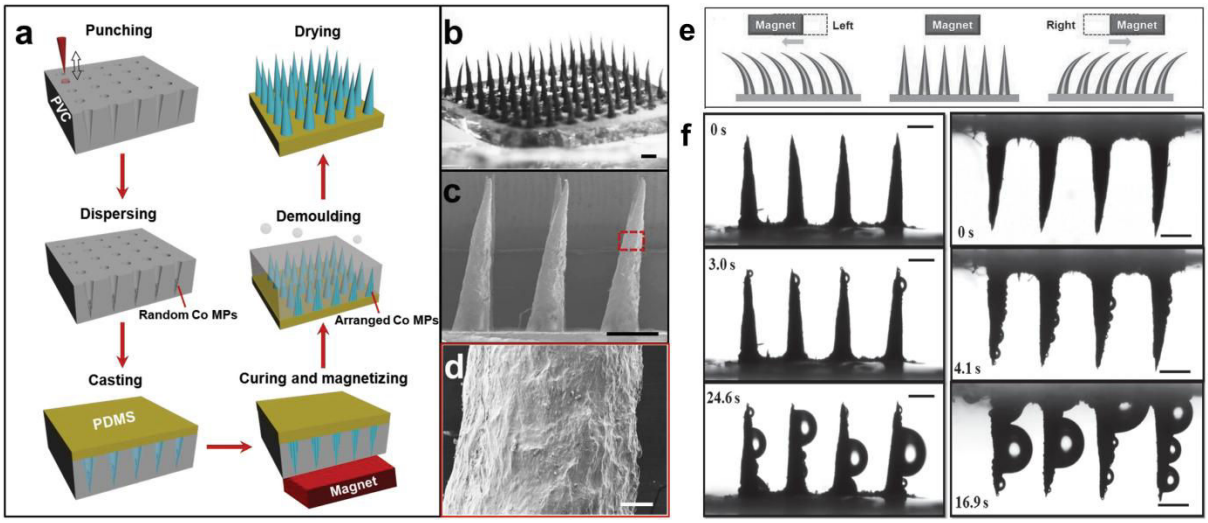

Figure 1.31. (a) Procedure to fabricate the cactus-like structures and (b-d) the corresponding optical and SEM images. Scale bars: (b-c) 1 mm and (d) 50 µm. (e) Illustration of the magnetically induced conical array responses to the magnetic field. (f) Fog collection on the cactus-like structures when the arrays are placed upwards (left) and downwards (right).Scale bars: 500 µm.[207,208]

*****

Here, in the *Chapter 1*, we focused on the presentation of the different wetting models and how the wettability can be affected. The fabulous examples of nature that inspires the researchers to mimic theses structures and properties as well as some of the methods used to fabricate them were also presented. The electropolymerization of conducting polymers was discussed, taking in account the possible factors that can affect the formation of structures and vary the wettability of the produced films. This is a versatile method that allows obtaining a wide range of structures and wettabilities in a low-cost and effective one-step process. This overview about micro and nanostructured surfaces and their potential applications showed the interest of the development of new materials for practical and useful engineering applications. Our aim is to synthesize and electropolymerize new monomers derivatives of thiophene and pyrene molecules and study their wetting behavior using the models proposed by Wenzel, Cassie-Baxter and Marmur to explain the obtained results. Indeed, the morphology structuring will be very well addressed through the analysis of microscopy.

Hereafter, *Chapter 2* will present the results concerning the electropolymerization and characterization of various thienothiophene monomers and the main parameters that affect the structure formation. A mechanism of how the structures were formed will be also proposed.

Then, *Chapter 3* will focus on the discussion about pyrene monomers and its derivatives in order to form super-wetting surfaces. Here, the superhydrophobic and parahydrophobic properties of the films allow many further studies: water adhesion, anti-bacterial properties and stimulus sensitive coating.

REFERENCES OF CHAPTER 1

(1) Darmanin, T.; Guittard, F. Recent Advances in the Potential Applications of Bioinspired Superhydrophobic Materials. *J. Mater. Chem. A.* **2014**, *2*, 16319–16359.

(2) Xue, Z.; Cao, Y.; Liu, N.; Feng, L.; Jiang, L. Special Wettable Materials for Oil/water Separation. *J. Mater. Chem. A* **2014**, *2* (8), 2445–2460.

(3) Zhu, G.; Su, Y.; Bai, P.; Chen, J.; Jing, Q.; Yang, W.; Wang, Z. L. Harvesting Water Wave Energy by Asymmetric Screening of Electrostatic Charges on a Nanostructured Hydrophobic Thin-Film Surface. *ACS Nano* **2014**, *8* (6), 6031–6037.

(4) Varanasi, K. K.; Deng, T.; Smith, J. D.; Hsu, M.; Bhate, N. Frost Formation and Ice Adhesion on Superhydrophobic Surfaces. *Appl. Phys. Lett.* **2010**, *97* (23), 234102.

(5) Young, T. An Essay on the Cohesion of Fluids. *Philos. Trans. R. Soc. London* **1805**, *95*, 65–87.

(6) Wenzel, R. N. Resistance of Solid Surfaces To Wetting By Water. *Ind. Eng. Chem.* **1936**, *28* (8), 988–994.

(7) Cassie, A. B. D.; Baxter, S. Wettability of Porous Surfaces. *Trans. Faraday Soc.* **1944**, *40* (5), 546–551.

(8) Bhushan, B.; Nosonovsky, M. *Rose Petal Effect. Encyclopedia of Nanotechnology*; Springer: Netherlands, Dordrecht, 2012.

(9) Marmur, A. Hydro- Hygro- Oleo- Omni-Phobic? Terminology of Wettability Classification. *Soft Matter* **2012**, *8*, 6867–6870.

(10) Neinhuis, C.; Barthlott, W. Characterization and Distribution of Water-Repellent, Self-Cleaning Plant Surfaces. *Ann. Bot.* **1997**, *79* (6), 667–677.

(11) Barthlott, B. W.; Schimmel, T.; Wiersch, S.; Koch, K.; Brede, M.; Barczewski, M.; Walheim, S.; Weis, A.; Kaltenmaier, A.; Leder, A.; Bohn, H. F. The Salvinia Paradox: Superhydrophobic Surfaces with Hydrophilic Pins for Air Retention Under Water. *Adv. Mater.* **2010**, *22* (21), 2325–2328.

(12) Feng, L.; Zhang, Y.; Xi, J.; Zhu, Y.; Wang, N.; Xia, F.; Jiang, L. Petal Effect: A Superhydrophobic State with High Adhesive Force. *Langmuir* **2008**, *24* (8), 4114–4119.

(13) Jin, H.; Li, Y.; Zhang, P.; Nie, S.; Gao, N. The Investigation of the Wetting Behavior on the Red Rose Petal. *Appl. Phys. Lett.* **2016**, *108* (15), 151605.

(14) Chang, F. M.; Hong, S. J.; Sheng, Y. J.; Tsao, H. K. High Contact Angle Hysteresis of Superhydrophobic Surfaces: Hydrophobic Defects. *Appl. Phys. Lett.* **2009**, *95* (6), 2012–2015.

(15) Yang, S.; Ju, J.; Qiu, Y.; He, Y.; Wang, X.; Dou, S.; Liu, K.; Jiang, L. Peanut Leaf Inspired Multifunctional Surfaces. *Small* **2014**, *10* (2), 294–299.

(16) Mele, E.; Girardo, S.; Pisignano, D. Strelitzia Reginae Leaf as a Natural Template for Anisotropic Wetting and Superhydrophobicity. *Langmuir* **2012**, *28* (11), 5312–5317.

(17) Feng, B. L.; Li, S.; Li, Y.; Li, H.; Zhang, L.; Zhai, J.; Song, Y.; Liu, B.; Jiang, L.; Zhu, D. Super-Hydrophobic Surfaces: From Natural to Artificial. *Adv. Mater.* **2002**, *14* (24), 1857–1860.

(18) Parker, A. R.; Lawrence, C. R. Water Capture by a Desert Beetle. *Nature* **2001**, *414*, 33–34.

(19) Hamlett, C. A. E.; Shirtcliffe, N. J.; Pyatt, E. B.; Newton, M. I.; Mchale, G.; Koch, K. Passive Water Control at the Surface of a Superhydrophobic Lichen. *Planta* **2011**, *234* (6), 1267–1274.

(20) Fang, Y.; Sun, G.; Cong, Q.; Chen, G.; Ren, L. Effects of Methanol on Wettability of the Non-Smooth Surface on Butterfly Wing. *J. Bionic Eng.* **2008**, *5* (2), 127–133.

(21) Yan, F.; Gang, S.; TongQing, W.; Qian, C.; LuQuanRen. Hydrophobicity Mechanism of Non-

Smooth Pattern on Surface of Butterfly Wing. *Chinese Sci. Bull.* **2007**, *52* (5), 711–716.

(22) Prum, R. O.; Quinn, T.; Torres, R. H. Anatomically Diverse Butterfly Scales All Produce Structural Colours by Coherent Scattering. *J. Exp. Biol.* **2006**, *209*, 748–765.

(23) Sun, M.; Watson, G. S.; Zheng, Y.; Watson, J. A.; Liang, A. Wetting Properties on Nanostructured Surfaces of Cicada Wings. *J. Exp. Biol.* **2009**, *212*, 3148–3155.

(24) Sun, M.; Liang, A.; Watson, G. S.; Watson, J. A.; Zheng, Y.; Ju, J.; Jiang, L. Influence of Cuticle Nanostructuring on the Wetting Behaviour/States on Cicada Wings. *PLoS One* **2012**, *7* (4), e35056.

(25) Watson, G. S.; Myhra, S.; Cribb, B. W.; Watson, J. A. Putative Functions and Functional Efficiency of Ordered Cuticular Nanoarrays on Insect Wings. *Biophys. J.* **2008**, *94* (8), 3352–3360.

(26) Ivanova, E. P.; Hasan, J.; Webb, H. K.; Truong, V. K.; Watson, G. S.; Watson, J. A.; Baulin, V. A.; Pogodin, S.; Wang, J. Y.; Tobin, M. J.; Löbbe, C.; Crawford, R. J. Natural Bactericidal Surfaces: Mechanical Rupture of Pseudomonas Aeruginosa Cells by Cicada Wings. *Small* **2012**, *8* (16), 2489–2494.

(27) Hasan, J.; Webb, H. K.; Truong, V. K.; Pogodin, S.; Baulin, V. A.; Watson, G. S.; Watson, J. A.; Crawford, R. J.; Ivanova, E. P. Selective Bactericidal Activity of Nanopatterned Superhydrophobic Cicada Psaltoda Claripennis Wing Surfaces. *Appl. Microbiol. Biotechnol.* **2013**, *97* (20), 9257–9262.

(28) Liu, K.; Du, J.; Wu, J.; Jiang, L. Superhydrophobic Gecko Feet with High Adhesive Forces towards Water and Their Bio-Inspired Materials. *Nanoscale* **2012**, *4* (3), 768.

(29) Bixler, G.; Bhushan, B. Fluid Drag Reduction and Efficient Self-Cleaning with Rice Leaf and Butterfly Wing Bioinspired Surfaces. *Nanoscale* **2013**, *5* (17), 7685–7710.

(30) Bhushan, B. Biomimetics Inspired Surfaces for Drag Reduction and Oleophobicity/philicity. *Beilstein J. Nanotechnol.* **2011**, *2*, 66–84.

(31) Bixler, G.; Bhushan, B. Biofouling: Lessons from Nature. *Philos. Transic. R. Soc. A* **2012**, *370*, 2381–2417.

(32) Dean, B.; Bhushan, B. Shark-Skin Surfaces for Fluid-Drag Reduction in Turbulent Flow: A Review. *Philos. Trans. R. Soc. A.* **2010**, *368*, 4775–4806.

(33) Cai, Y.; Lin, L.; Xue, Z.; Liu, M.; Wang, S.; Jiang, L. Filefish-Inspired Surface Design for Anisotropic Underwater Oleophobicity. *Adv. Funct. Mater.* **2014**, *24* (6), 809–816.

(34) Mijatovic, D.; Eijkel, J. C. T.; Van den Berg, A. Technologies for Nanofluidic Systems: Top-down vs. Bottom-up-a Review. *Lab Chip* **2005**, *5* (5), 492–500.

(35) Choi, H.; Choo, S.; Shin, J.; Kim, K.-I.; Lee, H. Fabrication of Superhydrophobic and Oleophobic Surfaces with Overhang Structure by Reverse Nanoimprint Lithography. *J. Phys. Chem. C* **2013**, *117*, 24354−24359.

(36) Hanarp, P.; Sutherland, D. S.; Gold, J.; Kasemo, B. Control of Nanoparticle Film Structure for Colloidal Lithography. *Colloids Surf. A.* **2003**, *214*, 23–36.

(37) Lee, D. Y.; Lee, D. H.; Lee, S. G.; Cho, K. Hierarchical Gecko-Inspired Nanohairs with a High Aspect Ratio Induced by Nanoyielding. *Soft Matter* **2012**, *8*, 4905–4910.

(38) Salapare III, H.; Blantocas, G. Q.; Rivera, W. L.; Ong, V. A.; Hipolito, R. S.; Ramos, H. J. Anti-Bacterial Property of Hydrogen-Ion and Oxygen-Ion Treated. *Plasma Fusion Res.* **2011**, *6*, 2406043.

(39) Salapare III, H.; Suarez, B. A. T.; Cosiñero, H. S. O.; Bacaoco, M. Y.; Ramos, H. J. Irradiation of Poly(Tetrafluoroethylene) Surfaces by CF_4 Plasma to Achieve Robust Superhydrophobic and Enhanced Oleophilic Properties for Biological Applications. *Mater. Sci. Eng. C* **2015**, *46*, 270–275.

(40) Zhao, Y.; Ibrahim, M.; Li, W.; Wu, G.; Wang, C.; Zheng, Y.; Yeung, K. W. K.; Chu, P. K. Enhanced Antimicrobial Properties, Cytocompatibility, and Corrosion Resistance of Plasma-Modified Biodegradable Magnesium Alloys. *Acta Biomater.* **2014**, *10*, 544–556.

(41) Siqueira, N. M.; Garcia, K. C.; Bussamara, R.; Both, F. S.; Vainstein, M. H.; Soares, R. M. D. Poly(Lactic Acid)/chitosan Fiber Mats: Investigation of Effects of the Support on Lipase Immobilization. *Int. J. Biol. Macromol.* **2015**, *72*, 998–1004.

(42) Yu, H.; Jia, Y.; Yao, C.; Lu, Y. PCL/PEG Core/sheath Fibers with Controlled Drug Release Rate Fabricated on the Basis of a Novel Combined Technique. *Int. J. Pharm.* **2014**, *469*, 17–22.

(43) Lin, W.-H.; Chen, T.-H.; Chang, J.-K.; Taur, J.-I.; Lo, Y.-Y.; Lee, W.-L.; Chang, C.-S.; Su, W.-B.; Wu, C.-I. A Direct and Polymer-Free Method for Transferring Graphene Grown by Chemical Vapor Deposition to Any Substrate. *ACS Nano* **2014**, *8* (2), 1784–1791.

(44) Wang, X.; Feng, H.; Wu, Y.; Jiao, L. Controlled Synthesis of Highly Crystalline MoS_2 Flakes by Chemical Vapor Deposition. *J. Am. Chem. Soc.* **2013**, *135*, 5304–5307.

(45) Thongsuriwong, K.; Amornpitoksuk, P.; Suwanboon, S. Structure, Morphology, Photocatalytic and Antibacterial Activities of ZnO Thin Films Prepared by Sol–Gel Dip-Coating Method. *Adv. Powder Technol.* **2013**, *24*, 275–280.

(46) Li, H.; Hao, Y.; Lu, H.; Liang, L.; Wang, Y.; Qiu, J.; Shi, X.; Wang, Y.; Yao, J. A Systematic Study on Visible-Light N-Doped TiO_2 Photocatalyst Obtained from Ethylenediamine by Sol – Gel Method. *Appl. Surf. Sci.* **2015**, *344*, 112–118.

(47) Li, C.-F.; Hsu, C.-Y.; Li, Y.-Y. NH_3 Sensing Properties of ZnO Thin Films Prepared via Sol – Gel Method. *J. Alloys Compd.* **2014**, *606*, 27–31.

(48) Rangel, T. C.; Michels, A. F.; Weibel, D. E. Superomniphobic and Easily Repairable Coatings on Copper Substrates Based on Simple Immersion or Spray Processes. *Langmuir* **2015**, *31*, 3465–3472.

(49) Li, J.; Wu, R.; Jing, Z.; Yan, L.; Zha, F.; Lei, Z. One-Step Spray-Coating Process for the Fabrication of Colorful Superhydrophobic Coatings with Excellent Corrosion Resistance. *Langmuir* **2015**, *31*, 10702–10707.

(50) Darmanin, T.; Guittard, F. Wettability of Conducting Polymers: From Superhydrophilicity to Superoleophobicity. *Prog. Polym. Sci.* **2014**, *39* (4), 656–682.

(51) Shirakawa, H.; Louis, E.; MacDiarmid, A.; Chiang, C.; Heeger, A. Synthesis of Electrically Conducting Organic Polymers: Halogen Derivatives of Polyacetylene, (CH)x. *J. Chem. Soc. Chem. Commun.* **1977**, 24, 578–580.

(52) https://www.nobelprize.org/nobel_prizes/chemistry/laureates/2000/.

(53) Jang, J. Conducting Polymer Nanomaterials and Their Applications. *Adv. Polym. Sci.* **2006**, *199* (1), 189–259.

(54) Li, C.; Bai, H.; Shi, G. Conducting Polymer Nanomaterials: Electrosynthesis and Applications. *Chem. Soc. Rev.* **2009**, *38* (8), 2397–2409.

(55) Wallace, G.; Spinks, G. Conducting Polymers – Bridging the Bionic Interface. *Soft Matter* **2007**, *3* (6), 665–671.

(56) Bredas, J. L.; Street, G. B. Polarons, Bipolarons, and Solitons in Conducting Polymers. *Acc. Chem. Res.* **1985**, *18* (10), 309–315.

(57) Balint, R.; Cassidy, N. J.; Cartmell, S. H. Conductive Polymers: Towards a Smart Biomaterial for Tissue Engineering. *Acta Biomater.* **2014**, *10* (6), 2341–2353.

(58) Raghava, K.; Sin, B. C.; Ryu, K. S.; Kim, J.-C.; Chung, H.; Lee, Y. Conducting Polymer Functionalized Multi-Walled Carbon Nanotubes with Noble Metal Nanoparticles: Synthesis, Morphological Characteristics and Electrical Properties. *Synth. Met.* **2009**, *159* (7–8), 595–603.

(59) Abidian, M. R.; Corey, J. M.; Kipke, D. R.; Martin, D. C. Conducting-Polymer Nanotubes Improve Electrical Properties, Mechanical Adhesion, Neural Attachment, and Neurite Outgrowth of Neural Electrodes. *Small* **2010**, *6* (3), 421–429.

(60) Fujimoto, C. H.; Hickner, M. A.; Cornelius, C. J.; Loy, D. A. Ionomeric Poly(phenylene) Prepared by Diels-Alder Polymerization: Synthesis and Physical Properties of a Novel Polyelectrolyte. *Macromolecules* **2005**, *38*, 5010–5016.

(61) Ramanathan, K.; Bangar, M. A.; Yun, M.; Chen, W.; Myung, N. V; Mulchandani, A. Bioaffinity Sensing Using Biologically Functionalized Conducting-Polymer Nanowire. *J. Am. Chem. Soc.* **2005**, *127*, 496–497.

(62) Joshi, A.; Gangal, S. A.; Gupta, S. K. Chemical Ammonia Sensing Properties of Polypyrrole Thin Films at Room Temperature. *Sens. Actuators B.* **2011**, *156* (2), 938–942.

(63) Xu, L.; Chen, W.; Mulchandani, A.; Yan, Y. Reversible Conversion of Conducting Polymer Films from Superhydrophobic to Superhydrophilic. *Angew. Chemie* **2005**, *44* (37), 6009–6012.

(64) Rahman, A.; Kwon, N.; Won, M.; Choe, E. S.; Shim, Y. Functionalized Conducting Polymer as an Enzyme-Immobilizing Substrate: An Amperometric Glutamate Microbiosensor for in Vivo Measurements. *Anal. Chem.* **2005**, *77* (15), 4854–4860.

(65) Prabhakaran, M. P.; Ghasemi-Mobarakeh, L.; Jin, G.; Ramakrishna, S. Electrospun Conducting Polymer Nanofibers and Electrical Stimulation of Nerve Stem Cells. *J. Biosci. Bioeng.* **2011**, *112* (5), 501–507.

(66) Fujii, B. S.; Read, E. S.; Binks, B. P.; Armes, S. P. Stimulus-Responsive Emulsifiers Based on Nanocomposite Microgel Particles. *Adv. Mater.* **2005**, *17* (8), 1014–1018.

(67) Chang, K.; Wang, H. P.; Wu, T.-Y.; Sun, W. Optical and Electrochromic Characterizations of Four 2,5-Dithienylpyrrole-Based Conducting Polymer Films. *Electrochim. Acta* **2014**, *119*, 225–235.

(68) Tarkuc, S.; Sahmetlioglu, E.; Tanyeli, C.; Akhmedov, I. M.; Toppare, L. A Soluble Conducting Polymer : 1-Phenyl-2,5-Di(2-Thienyl)-1*H*-Pyrrole and Its Electrochromic Application. *Electrochim. Acta* **2006**, *51*, 5412–5419.

(69) Tarkuc, S.; Sahmetlioglu, E.; Tanyeli, C.; Akhmedov, I. M.; Toppare, L. Electrochromic Properties of a Soluble Conducting Polymer of 1-Benzyl-2,5-Di(thiophene-2-Yl)-1H-Pyrrole. *Sens. Actuators B.* **2007**, *121*, 622–628.

(70) Sahin, E.; Sahmetlioglu, E.; Akhmedov, I.; Tanyeli, C.; Toppare, L. Synthesis and Characterization of a New Soluble Conducting Polymer and Its Electrochromic Devices. *Org. Electron.* **2006**, *7*, 351–362.

(71) Mortimer, R. J.; Dyer, A. L.; Reynolds, J. R. Electrochromic Organic and Polymeric Materials for Display Applications. *Displays* **2006**, *27*, 2–18.

(72) Chen, C.; Dou, L.; Zhu, R.; Chung, C.; Song, T.; Zheng, Y. B.; Hawks, S.; Li, G.; Weiss, P.; Yang, Y. Visibly Transparent Polymer Solar Cells Produced by Solution Processing. *ACS Nano* **2012**, *6* (8), 7185–7190.

(73) Li, G.; Zhu, R.; Yang, Y. Polymer Solar Cells. *Nat. Photonics* **2012**, *6*, 153–161.

(74) Wu, Z.; Sun, C.; Dong, S.; Jiang, X.; Wu, S.; Wu, H.; Yip, H.; Huang, F.; Cao, Y. N-Type Water/Alcohol-Soluble Naphthalene Diimide-Based Conjugated Polymers for High-Performance Polymer Solar Cells. *J. Am. Chemiscal Soc.* **2016**, *138* (6), 2004–2013.

(75) Chen, J.; Cui, C.; Li, Y.; Zhou, L.; Ou, Q.; Li, C.; Li, Y.; Tang, J.-X. Single-Junction Polymer Solar Cells Exceeding 10 % Power Conversion Efficiency. *Adv. Mater.* **2015**, *27*, 1035–1041.

(76) Qu, G.; Cheng, J.; Li, X.; Yuan, D.; Chen, P.; Chen, X.; Wang, B.; Peng, H. A Fiber Supercapacitor with High Energy Density Based on Hollow Graphene/Conducting Polymer Fiber Electrode. *Adv. Mater.* **2016**, *28*, 3646–3652.

(77) Wang, K.; Wu, H.; Meng, Y.; Wei, Z. Conducting Polymer Nanowire Arrays for High Performance Supercapacitors. *Small* **2014**, *10* (1), 14–31.

(78) Li, W.; Chou, S.; Wang, J.; Wang, J.; Gu, Q.; Liu, H.; Dou, S. Multifunctional Conducing Polymer Coated $Na_{1+x}MnFe(CN)_6$ Cathode for Sodium-Ion Batteries with Superior Performance via a Facile and One-Step Chemistry Approach. *Nano Energy* **2015**, *13*, 200–207.

(79) Wang, J.; Lu, L.; Shi, D.; Tandiono, R.; Wang, Z.; Konstantinov, K.; Liu, H. A Conductive Polypyrrole-Coated , Sulfur–Carbon Nanotube Composite for Use in Lithium–Sulfur Batteries. *ChemPlusChem* **2013**, *78*, 318–324.

(80) Snook, G. A.; Kao, P.; Best, A. S. Conducting-Polymer-Based Supercapacitor Devices and Electrodes. *J. Power Sources* **2011**, *196* (1), 1–12.

(81) Gómez, H.; Ram, M. K.; Alvi, F.; Villalba, P.; Lee, E.; Kumar, A. Graphene-Conducting Polymer Nanocomposite as Novel Electrode for Supercapacitors. *J. Power Sources* **2011**, *196* (8), 4102–4108.

(82) Figueira-Duarte, T. M.; Mullen, K. Pyrene-Based Materials for Organic Electronics. *Chem. Rev.* **2011**, *111* (11), 7260–7314.

(83) Birks, J. B.; Christophorou, L. G. Excimer Fluorescence Spectra of Pyrene Derivatives. *Spectrochim. Acta* **1963**, *19* (2), 401–410.

(84) Kalyanasundaram, K.; Thomas, J. K. Environmental Effects on Vibronic Band Intensities in Pyrene Monomer Fluorescence and Their Application in Studies of Micellar Systems. *J. Am. Chem. Soc.* **1977**, *99* (7), 2039–2044.

(85) Chen, Y.; Bai, H.; Chen, Q.; Li, C.; Shi, G. A Water-Soluble Cationic Oligopyrene Derivative: Spectroscopic Studies and Sensing Applications. *Sens. Actuators B.* **2009**, *138*, 563–571.

(86) Haddad, R.; Holzinger, M.; Maaref, A.; Cosnier, S. Pyrene Functionalized Single-Walled Carbon Nanotubes as Precursors for High Performance Biosensors. *Electrochim. Acta* **2010**, *55*, 7800–7803.

(87) Qin, L.; Lu, B.; Xu, J.; Zhang, G.; Zhang, S. Novel Functionalized Conjugated Polypyrene with Polyacrylate: Synthesis, Electrochemistry, Luminescence, and Chemical Sensing Properties. *RSC Adv.* **2014**, *4*, 28368–28376.

(88) Chhatwal, M.; Kumar, A.; Gupta, R. D.; Awasthi, S. K. A Pyrene-Based Electropolymerized Film as a Solid-State Platform for Multi-Bit Memory Storage and Fluorescence Sensing of Nitroaromatics in Aqueous Solutions. *J. Mater. Chem. C* **2016**, *4*, 4129–4133.

(89) Costa, T.; Seixas De Melo, J.; Burrows, H. D. Fluorescence Behavior of a Pyrene-End-Capped Poly(Ethylene Oxide) in Organic Solvents and in Dioxane-Water Mixtures. *J. Phys. Chem. B* **2009**, *113* (3), 618–626.

(90) Chhatwal, M.; Kumar, A.; Awasthi, S. K.; Zharnikov, M.; Gupta, R. D. An Electroactive Metallo−Polypyrene Film As A Molecular Scaffold For Multi-State Volatile Memory Devices. *J. Phys. Chem. C* **2016**, *120*, 2335–2342.

(91) Rajagopal, S.; Reddy, S.; Hariharan, M. Crystallization Induced Green-Yellow-Orange Emitters Based on Benzoylpyrenes. *CrystEngComm* **2016**, *18* (27), 5089–5094.

(92) Rawe, B. W.; Brown, C. M.; MacKinnon, M. R.; Patrick, B. O.; Bodwell, G. J.; Gates, D. P. A C-Pyrenyl Poly(methylenephosphine): Oxidation "Turns On" Blue Photoluminescence in Solution and the Solid State. *Organometallics* **2017**, 36 (14), 2520–2526.

(93) Lu, B.; Zhen, S.; Zhao, L.; Zhang, G.; Mo, D.; Xu, J. A Novel Solution-Processable Amino-Group-Substituted Oligopyrene: Synthesis, Electropolymerization, Properties, and Application in Fl Uorescent Chemosensor. *Synth. Met.* **2014**, *198*, 155–160.

(94) Lu, B.; Xu, J.; Fan, C.; Jiang, F.; Miao, H. Facile Electrosynthesis of Nitro-Group-Substituted Oligopyrene with Bicolored Emission. *Electrochim. Acta* **2008**, *54* (2), 334–340.

(95) Xu, L.; Tong, F.; Lu, X.; Lu, K.; Lu, Q. Multifunctional Polypyrene/Silica Hybrid Coatings with Stable Excimer Fluorescence and Robust Superhydrophobicity Derived from Electrodeposited Polypyrene Films. *J. Mater. Chem. C* **2015**, *3*, 2086–2092.

(96) Xu, L.; Zhao, J.; Liu, R.; Liu, H.; Liu, J.; Wang, H. Electrosyntheses and Characterizations of Novel Electrochromic and Fluorescent Copolymers Based on 2,2-Bithiophene and Pyrene. *Electrochim. Acta* **2010**, *55* (28), 8855–8862.

(97) Hou, L.; Wang, C.; Chen, L.; Chen, S. Multiple-Structured Nanocrystals towards Bifunctional Photoluminescent-Superhydrophobic Surfaces. *J. Mater. Chem.* **2010**, *20* (19), 3863–3868.

(98) Hong, J.; Bae, W. K.; Lee, H.; Oh, S.; Char, K.; Caruso, F.; Cho, J. Tunable Superhydrophobic and Optical Properties of Colloidal Films Coated with Block Copolymer Micelles/Micelle Multilayers. *Adv. Mater.* **2007**, *19* (24), 4364–4369.

(99) Yang, S.; Wang, L.; Wang, C.-F.; Chen, L.; Chen, S. Superhydrophobic Thermoplastic Polyurethane Films with Transparent/Fluorescent Performance. *Langmuir* **2010**, *26* (23), 18454–18458.

(100) Yang, S.; Zhou, C.; Liu, J.; Yu, M.; Zheng, J. One-Step Interfacial Synthesis and Assembly of Ultrathin Luminescent AuNPs/Silica Membranes. *Adv. Mater.* **2012**, *24* (24), 3218–3222.

(101) Meyer, V. Ueber Den Begleiter Dee Bensole Im Steinkohlentheer. *Eur. J. Inorg. Chem.* **1883**, *16* (1), 1465–1478.

(102) Jaymand, M.; Hatamzadeh, M.; Omidi, Y. Modification of Polythiophene by the Incorporation of Processable Polymeric Chains: Recent Progress in Synthesis and Applications. *Prog. Polym. Sci.* **2015**, *47*, 26–69.

(103) Roncali, J. Conjugated Poly(Thiophenes): Synthesis, Functionalization, and Applications. *Chem. Rev.* **1992**, *92* (4), 711–738.

(104) Dikcal, F.; Ozturk, T.; Cinar, M. E. Fused Thiophenes: An Overview of the Computational Investigations. *Org. Commun.* **2017**, *10* (2), 56–71.

(105) Skabara, P. J.; Perepichka, I. F.; Perepichka, D. F. Handbook of Thiophene-Based Materials: Applications in Organic Electronics and Photonics, 2 Volume Set. London; 2009.

(106) Cinar, M. E.; Ozturk, T. Thienothiophenes, Dithienothiophenes, and Thienoacenes: Syntheses, Oligomers, Polymers, and Properties. *Chem. Rev.* **2015**, *115* (9), 3036–3140.

(107) Navale, S. T.; Mane, A. T.; Khuspe, G. D.; Chougule, M. A.; Patil, V. B. Room Temperature NO2 Sensing Properties of Polythiophene Films. *Synth. Met.* **2014**, *195* (2), 228–233.

(108) Zhao, D.; Li, L.; Niu, W.; Chen, S. Chemical Highly Conductive Polythiophene Films Doped with Chloroauric Acid for Dual-Mode Sensing of Volatile Organic Amines and Thiols. *Sens. Actuators B* **2017**, *243*, 380–387.

(109) Bai, S.; Guo, J.; Sun, J.; Tang, P.; Chen, A.; Luo, R.; Li, D. Enhancement of NO_2-Sensing Performance at Room Temperature by Graphene-Modified Polythiophene. *Ind. Eng. Chem. Res.* **2016**, *55* (19), 5788–5794.

(110) Chandra, M. R.; Redyy, P. S. P.; Rao, T. S.; Pammi, S. V. N.; Kumar, K. S.; Babu, K. V.; Kumar, C. K.; Hemalatha, K. P. J. Enhanced Visible-Light Photocatalysis and Gas Sensor Properties of Polythiophene Supported Tin Doped Titanium Nanocomposite. *J. Phys. Chem. Solids* **2017**, *105*, 99–105.

(111) Li, X.; Li, J.; Wang, H.; Li, R.; Ma, H.; Du, B.; Wei, Q. An Electrochemiluminescence Sensor for Bromate Assay Based on a New Cationic Polythiophene Derivative. *Anal. Chim. Acta* **2014**, *852*, 69–73.

(112) Cutler, C. A.; Burrell, A. K.; Officer, D. L.; Too, C. O.; Wallace, G. G. Effect of Electron Withdrawing or Donating Substituents on the Photovoltaic Performance of Polythiophenes. *Synth. Met.* **2002**, *128* (1), 35–42.

(113) Mehmood, U.; Al-Ahmed, A.; Hussein, I. A. Review on Recent Advances in Polythiophene Based Photovoltaic Devices. *Renew. Sustain. Energy Rev.* **2016**, *57*, 550–561.
(114) Jo, J. W.; Jung, J. W.; Wang, H.-W.; Kim, P.; Russell, T. P.; Jo, W. H. Fluorination of Polythiophene Derivatives for High Performance Organic Photovoltaics. *Chem. Mater.* **2014**, *26* (14), 4214−4220.
(115) Jiao, N.; He, D.; Qian, L.; Lei, Z.; Ding, L. Lock-up Function of Fluorine Enhances Photovoltaic Performance of Polythiophene. *Sci. China Chem.* **2017**, *60* (2), 251–256.
(116) Laforgue, A.; Robitaille, L. Production of Conductive PEDOT Nanofibers by the Combination of Electrospinning and Vapor-Phase Polymerization. *Macromolecules* **2010**, *43* (9), 4194–4200.
(117) Liu, N.; Fang, G.; Wan, J.; Zhou, H.; Long, H.; Zhao, X. Electrospun PEDOT:PSS–PVA Nanofiber Based Ultrahigh-Strain Sensors with Controllable Electrical Conductivity. *J. Mater. Chem.* **2011**, *21* (47), 18962.
(118) Chang, H. C.; Sun, T.; Sultana, N.; Lim, M. M.; Khan, T. H.; Ismail, A. F. Conductive PEDOT:PSS Coated Polylactide (PLA) and Poly(3-Hydroxybutyrate-Co-3-Hydroxyvalerate) (PHBV) Electrospun Membranes: Fabrication and Characterization. *Mater. Sci. Eng. C* **2016**, *61*, 396–410.
(119) Zhang, J.; Li, X.; Guo, W.; Hreid, T.; Hou, J.; Su, H.; Yuan, Z. Electropolymerization of a Poly(3,4-Ethylenedioxythiophene) and Functionalized, Multi-Walled, Carbon Nanotubes Counter Electrode for Dye-Sensitized Solar Cells and Characterization of Its Performance. *Electrochim. Acta* **2011**, *56* (9), 3147–3152.
(120) Xiao, Y.; Wu, J.; Yue, G.; Lin, J.; Huang, M.; Lan, Z.; Fan, L. Electrodeposition of High Performance PEDOT/Ti Counter Electrodes on Ti Meshes for Large-Area Flexible Dye-Sensitized Solar Cells. *Electrochim. Acta* **2012**, *85*, 432–437.
(121) Xiao, Y. M.; Lin, J. Y.; Wu, J. H.; Tai, S. Y.; Yue, G. T. Pulse Potentiostatic Electropolymerization of High Performance PEDOT Counter Electrodes for Pt-Free Dye-Sensitized Solar Cells. *Electrochim. Acta* **2012**, *83*, 221–226.
(122) Zhang, J.; Pazoki, M.; Simiyu, J.; Johansson, M. B.; Cheung, O.; Häggman, L.; Johansson, E. M. J.; Vlachopoulos, N.; Hagfeldt, A.; Boschloo, G. The Effect of Mesoporous TiO_2 Pore Size on the Performance of Solid-State Dye Sensitized Solar Cells Based on Photoelectrochemically Polymerized Poly(3,4-Ethylenedioxythiophene) Hole Conductor. *Electrochim. Acta* **2016**, *210*, 23–31.
(123) Lin, J.; Wang, W.; Chou, S. Flexible Carbon Nanotube/polypropylene Composite Plate Decorated with Poly(3,4-Ethylenedioxythiophene) as Efficient Counter Electrodes for Dye-Sensitized Solar Cells. *J. Power Sources* **2015**, *282*, 348–357.
(124) Godeau, G.; Szczepanski, C. R.; Darmanin, T.; Guittard, F. Nanoparticle Covered Surfaces: An Efficient Way to Enhance Superhydrophobic Properties. *Mater. Des.* **2016**, *92*, 911–918.
(125) Godeau, G.; Guittard, F.; Darmanin, T. Nucleoside Surfaces as a Platform for the Control of Surface Hydrophobicity. *RSC Adv.* **2016**, *6*, 62471–62477.
(126) Godeau, G.; Darmanin, T.; Guittard, F. Staudinger Vilarassa Reaction: A Powerful Tool for Surface Modification and Superhydrophobic Properties. *J. Colloid Interface Sci.* **2015**, *457*, 72–77.
(127) Sabouraud, G.; Sadki, S.; Brodie, N. The Mechanisms of Pyrrole Electropolymerization. *Chem. Soc. Rev.* **2000**, *29* (5), 283–293.
(128) Prejza, J.; Lundström, I.; Skotheim, T. Electropolymerization of Pyrrole in the Presence of Fluoborate. *J. Electrochem. Soc.* **1982**, *129* (8), 1685–1689.
(129) Darmanin, T.; De Givenchy, E. T.; Amigoni, S.; Guittard, F. Superhydrophobic Surfaces by

Electrochemical Processes. *Adv. Mater.* **2013**, *25* (10), 1378–1394.
(130) Bellanger, H.; Darmanin, T.; Taffin de Givenchy, E.; Guittard, F. Influence of Intrinsic Oleophobicity and Surface Structuration on the Superoleophobic Properties of PEDOP Films Bearing Two Fluorinated Tails. *J. Mater. Chem. A* **2013**, *1* (8), 2896.
(131) Karami, H.; Asadi, M. G.; Mansoori, M. Pulse Electropolymerization and the Characterization of Polyaniline Nanofibers. *Electrochim. Acta* **2012**, *61*, 154–164.
(132) Çağlar, A.; Cengiz, U.; Yıldırım, M.; Kaya, İ. Effect of Deposition Charges on the Wettability Performance of Electrochromic Polymers. *Appl. Surf. Sci.* **2015**, *331*, 262–270.
(133) Diaz, A. F.; Kanazawa, K. K. Electrochemical Polymerization of Pyrrole. *J. Chem. Soc. Chem. Commun.* **1979**, *0* (14), 635–636.
(134) Wolfs, M.; Darmanin, T.; Guittard, F. Versatile Superhydrophobic Surfaces from a Bioinspired Approach. *Macromolecules* **2011**, *44*, 9286–9294.
(135) Iroh, J.; Wood, G. A. Effect of Electrolytes on the Kinects and Mechanism of the Electropolymerization of Pyrrole on to Carbon Fibers. *Eur. Polym. J.* **1997**, *33* (1), 107–114.
(136) Lu, B.; Zhen, S.; Ming, S.; Xu, J.; Zhao, G. Effect of Electrolytes on the Electropolymerization and Optoelectronic Properties of Poly(3- Methylselenophene). *RSC Adv.* **2015**, *5* (86), 70649–70660.
(137) Demoustier-Champagne, S.; Stavaux, P. Effect of Electrolyte Concentration and Nature on the Electropolymerized Polypyrrole Nanotubules. *Chem. Mater.* **1999**, *11*, (3), 829–834.
(138) Li, Y.; Yang, J. Effect of Electrolyte Concentration on the Properties of the Electropolymerized Polypyrrole Films. *J. Appl. Polym. Sci.* **1997**, *65*, 2739–2744.
(139) Asami, R.; Atobe, M.; Fuchigami, T. Electropolymerization of an Immiscible Monomer in Aqueous Electrolytes Using Acoustic Emulsification. *J. Am. Chem. Soc.* **2005**, *127* (38), 13160–13161.
(140) Zhou, D.; Zhou, R.; Chen, C.; Yee, W.-A.; Kong, J.; Ding, G.; Lu, X. Non-Volatile Polymer Electrolyte Based on Poly(Propylene Carbonate), Ionic Liquid and Lithium Perchlorate for Electrochromic Devices. *J. Phys. Chem. B* **2013**, *117* (25), 7783–7789.
(141) Hwang, B.-J.; Santhanam, R.; Wu, C.-R.; Tsai, Y.-W. Nucleation and Growth Mechanism for the Electropolymerization of Aniline in Trifluoroacetic Acid/lithium Perchlorate/propylene Carbonate Medium. *J. Solid State Electrochem.* **2003**, *7* (10), 678–683.
(142) Ak, M.; Sulak, M.; Kurtay, G.; Güllü, M.; Toppare, L. Synthesis and Electropolymerization of 1,2-Bis(Thiophen-3-Ylmethoxy) Benzene and Its Electrochromic Properties and Electrochromic Device Application. *Solid State Sci.* **2010**, *12* (7), 1199–1204.
(143) Agrawal, V.; Shahjad; Bhardwaj, D.; Bhargav, R.; Sharma, G. D.; Bhardwaj, R. K.; Patra, A.; Chand, S. Morphology and Doping Level of Electropolymerized Biselenophene-Flanked 3,4-Ethylenedioxythiophene Polymer: Effect of Solvents and Electrolytes. *Electrochim. Acta* **2016**, *192*, 52–60.
(144) Duran, B.; Çakmakcı, I.; Bereket, G. Role of Supporting Electrolyte on the Corrosion Performance of Poly (Carbazole) Films Deposited on Stainless Steel. *Corros. Sci.* **2013**, *77*, 194–201.
(145) Gupta, B.; Singh, A. K.; Prakash, R. Electrolyte Effects on Various Properties of Polycarbazole. *Thin Solid Films* **2010**, *519* (3), 1016–1019.
(146) Xie, X.; Lei, W.; Liu, X.; Hao, Q.; Xia, M.; Wang, F.; Si, W. Facile Electrosynthsis of Poly(pyrene-1-Sulfonic Acid Sodium Salt) Film: A Good Candidate for Blue Light-Emitting Diodes Applications. *Mater. Lett.* **2011**, *65* (8), 1234–1237.
(147) Shi, G.; Li, C.; Liang, Y. High-Strength Conducting Polymers Prepared by Electrochemical Polymerization in Boron Trifluoride Diethyl Etherate Solution. *Adv. Mater.* **1999**, *11* (13),

1145–1146.
(148) Li, C.; Chen, F.; Shi, G.; Xu, J.; Xu, Z. Electrosynthesis of Free-Standing Poly(Para-Phenylene) Films in Mixed Electrolytes of Boron Trifluoride Diethyl Etherate and Trifluoroacetic Acid on Stainless Steel. *J. Appl. Polym. Sci.* **2002**, *83*, 2462–2466.
(149) Huang, Z.; Qu, L.; Shi, G.; Hong, X. Electrochemical Polymerization of Naphthalene in the Electrolyte of Boron Trifluoride Diethyl Etherate Containing Trifluoroacetic Acid and Polyethylene Glycol Oligomer. *J. Electroanal. Chem.* **2003**, *556*, 159–165.
(150) Lu, G.; Shi, G. Electrochemical Polymerization of Pyrene in the Electrolyte of Boron Trifluoride Diethyl Etherate Containing Trifluoroacetic Acid and Polyethylene Glycol Oligomer. *J. Electroanal. Chem.* **2006**, *586* (2), 154–160.
(151) Li, C.; Imae, T. Electrochemical and Optical Properties of the Poly(3,4-Ethylenedioxythiophene) Film Electropolymerized in an Aqueous Sodium Dodecyl Sulfate and Lithium Tetrafluoroborate Medium. *Macromolecules* **2004**, *37* (7), 2411–2416.
(152) Aeiyach, S.; Lacaze, P. C. Electropolymerization of Benzene and Biphenyl in Organic Media: Influence of Different Parameters (Solvent, Water, Acidity, Salt) on the Formation of Polyparaphenylene Films (PPP). *J. Polym. Sci. Part A Polym. Chem.* **1989**, *27*, 515–526.
(153) Ouyang, J.; Li, Y. Effect of Electrolyte Solvent on the Conductivity and Structure of as-Prepared Polypyrrole Films. *Polymer.* **1997**, *38* (8), 1971–1976.
(154) Poverenov, E.; Li, M.; Bitler, A.; Bendikov, M. Major Effect of Electropolymerization Solvent on Morphology and Electrochromic Properties of PEDOT Films. *Chem. Mater.* **2010**, *22* (13), 4019–4025.
(155) Valle, M. A.; Cury, P.; Schrebler, R. Solvent Effect on the Nucleation and Growth Mechanisms of Poly(thiophene). *Electrochim. Acta* **2002**, *48* (4), 397–405.
(156) Fusalba, F.; Bélanger, D. Electropolymerization of Polypyrrole and Polyaniline - Polypyrrole from Organic Acidic Medium. *J. Phys. Chem. B* **1999**, *103* (42), 9044–9054.
(157) Martyak, N. M.; Mcandrew, P.; Mccaskie, J. E.; Dijon, J. Electrochemical Polymerization of Aniline from an Oxalic Acid Medium. *Prog. Org. Coatings* **2002**, *45* (1), 23–32.
(158) Ocón, P.; Herrasti, P.; Rojas, S. Galvanostatic and Pulse Potential Synthesis of Poly-3-Methylthiophene. Polymer as Catalytic Support. *Polymer.* **2001**, *42* (6), 2439–2448.
(159) Martins, J. I.; Bazzaoui, M.; Reis, T. C.; Costa, S. C.; Nunes, M. C.; Martins, L.; Bazzaoui, E. A. The Effect of pH on the Pyrrole Electropolymerization on Iron in Malate Aqueous Solutions. *Prog. Org. Coatings* **2009**, *65*, 62–70.
(160) Taleb, S.; Darmanin, T.; Guittard, F. Elaboration of Voltage and Ion Exchange Stimuli-Responsive Conducting Polymers with Selective Switchable Liquid-Repellency. *ACS Appl. Mater. Interfaces* **2014**, *6* (10), 7953–7960.
(161) Mortier, C.; Darmanin, T.; Guittard, F. 3,4-Ethylenedioxypyrrole (EDOP) Monomers with Aromatic Substituents for Parahydrophobic Surfaces by Electropolymerization. *Macromolecules* **2015**, *48* (15), 5188–5195.
(162) El-Maiss, J.; Darmanin, T.; Guittard, F. Controlling Electrodeposited Conducting Polymer Nanostructures with the Number and the Length of Fluorinated Chains for Adjusting Superhydrophobic Properties and Adhesion. *RSC Adv.* **2015**, *5* (47), 37196–37205.
(163) Wolfs, M.; Darmanin, T.; Guittard, F. Analogy of Morphology in Electrodeposited Hydrocarbon and Fluorocarbon Polymers. *RSC Adv.* **2012**, *3* (2), 647–652.
(164) Cheng, X.; Zhao, J.; Sun, H.; Fu, Y.; Cui, C.; Zhang, X. Effect of Substituents on Electrochemical and Optical Properties of Thienyl-Derivatized Polypyrenes. *J. Electroanal. Chem.* **2013**, *690*, 60–67.
(165) Luo, S.-C.; Sekine, J.; Zhu, B.; Zhao, H.; Nakao, A.; Yu, H. Polydioxythiophene Nanodots,

Nonowires, Nano-Networks, and Tubular Structures: The Effect of Functional Groups and Temperature in Template-Free Electropolymerization. *ACS Nano* **2012**, *6* (4), 3018–3026.

(166) Yang, C.; Chuang, S.-I.; Lo, Y.-H.; Cheng, H.-M.; Duh, J.-G.; Chen, P.-Y. Stalagmite-like Self-Cleaning Surfaces Prepared by Silanization of Plasma-Assisted Metal-Oxide Nanostructures. *J. Mater. Chem. A.* **2016**, *4*, 3406–3414.

(167) Wong, W. S. Y.; Stachurski, Z. H.; Nisbet, D. R.; Tricoli, A. Ultra-Durable and Transparent Self-Cleaning Surfaces by Large-Scale Self-Assembly of Hierarchical Interpenetrated Polymer Networks. *Appl. Mater. Interfaces* **2016**, *8* (21), 13615–13623.

(168) Li, S.-Y.; Li, Y.; Wang, J.; Nan, Y.-G.; Ma, B.-H.; Liu, Z.-L.; Gu, J.-X. Fabrication of Pinecone-like Structure Superhydrophobic Surface on Titanium Substrate and Its Self-Cleaning Property. *Chem. Eng. J.* **2016**, *290*, 82–90.

(169) Xue, C.-H.; Li, Y.-R.; Zhang, P.; Ma, J.-Z.; Jia, S.-T. Washable and Wear-Resistant Superhydrophobic Surfaces with Self-Cleaning Property by Chemical Etching of Fibers and Hydrophobization. *ACS Appl. Mater. Interfaces* **2014**, *6* (13), 10153–10161.

(170) Lakshmi, R. V; Bharathidasan, T.; Bera, P.; Basu, B. J. Fabrication of Superhydrophobic and Oleophobic Sol – Gel Nanocomposite Coating. *Surf. Coat. Technol.* **2012**, *206*, 3888–3894.

(171) Cao, L.; Gao, D. Transparent Superhydrophobic and Highly Oleophobic Coatings. *Faraday Discuss.* **2010**, *146*, 57–65.

(172) Howarter, J. A.; Genson, K. L.; Youngblood, P. Wetting Behavior of Oleophobic Polymer Coatings Synthesized from Fluorosurfactant-Macromers. *ACS Appl. Mater. Interfaces* **2011**, *3*, 2022–2030.

(173) Basu, B. J.; Kumar, V. D.; Anandan, C. Surface Studies on Superhydrophobic and Oleophobic Polydimethylsiloxane –Silica Nanocomposite Coating System. *Appl. Surf. Sci.* **2012**, *261*, 807–814.

(174) Coclite, A. M.; Shi, Y.; Gleason, K. K. Grafted Crystalline Poly-Perfluoroacrylate Structures for Superhydrophobic and Oleophobic Functional Coatings. *Adv. Mater.* **2012**, *24*, 4534–4539.

(175) Grynyov, R.; Bormashenko, E.; Whyman, G.; Bormashenko, Y.; Musin, A.; Pogreb, R.; Starostin, A.; Valtsifer, V.; Strelnikov, V.; Schechter, A.; Kolagatla, S. Superoleophobic Surfaces Obtained via Hierarchical Metallic Meshes. *Langmuir* **2016**, *32* (17), 4134–4140.

(176) Darmanin, T.; Tarrade, J.; Celia, E.; Guittard, F. Superoleophobic Meshes with High Adhesion by Electrodeposition of Conducting Polymer Containing Short Perfluorobutyl Chains. *J. Phys. Chem. C* **2014**, *118* (4), 2052–2057.

(177) Darmanin, T.; Guittard, F. Homogeneous Growth of Conducting Polymer Nanofibers by Electrodeposition for Superhydrophobic and Superoleophilic Stainless. *RSC Adv.* **2014**, *4*, 50401–50405.

(178) Shang, Y.; Si, Y.; Raza, A.; Yang, L.; Mao, X.; Ding, B.; Yu, J. An in Situ Polymerization Approach for the Synthesis of Superhydrophobic and Superoleophilic Nanofibrous Membranes for Oil–water Separation. *Nanoscale* **2012**, *4*, 7847–7854.

(179) Zuo, Z.; Liao, R.; Guo, C.; Yuan, Y.; Zhao, X.; Zhuang, A.; Zhang, Y. Fabrication and Anti-Icing Property of Coral-like Superhydrophobic Aluminum Surface. *Appl. Surf. Sci.* **2015**, *331*, 132–139.

(180) Li, Y.; Luo, C.; Li, X.; Zhang, K.; Zhao, Y.; Zhu, K.; Yuan, X. Submicron/Nano-Structured Icephobic Surfaces Made from Fluorinated Polymethylsiloxane and Octavinyl-POSS. *Appl. Surf. Sci.* **2016**, *360*, 113–120.

(181) Jung, M.; Kim, T.; Kim, H.; Shin, R.; Lee, J.; Lee, J.; Lee, J.; Kang, S. Design and Fabrication of a Large-Area Superhydrophobic Metal Surface with Anti-Icing Properties Engineered Using a Top-down Approach. *Appl. Surf. Sci.* **2015**, *351*, 920–926.

(182) Wang, N.; Xiong, D.; Li, M.; Deng, Y.; Shi, Y.; Wang, K. Superhydrophobic Surface on Steel Substrate and Its Anti-Icing Property in Condensing Conditions. *Appl. Surf. Sci.* **2015**, *355*, 226–232.

(183) He, M.; Wang, J.; Li, H.; Song, Y. Super-Hydrophobic Surfaces to Condensed Micro-Droplets at Temperatures below the Freezing Point Retard Ice/frost Formation. *Soft Matter* **2011**, *7*, 3993–4000.

(184) Nosonovsky, M.; Hejazi, V. Why Superhydrophobic Surfaces Are Not Always Icephobic. *ACS Nano* **2012**, *6* (10), 8488–8491.

(185) Kulinich, S. A.; Farhadi, S.; Nose, K.; Du, X. W. Superhydrophobic Surfaces: Are They Really Ice-Repellent? *Langmuir* **2011**, *27* (1), 25–29.

(186) Farhadi, S.; Farzaneh, M.; Kulinich, S. A. Anti-Icing Performance of Superhydrophobic Surfaces. *Appl. Surf. Sci.* **2011**, *257* (14), 6264–6269.

(187) Susoff, M.; Siegmann, K.; Pfaffenroth, C.; Hirayama, M. Evaluation of Icephobic Coatings — Screening of Different Coatings and Influence of Roughness. *Appl. Surf. Sci.* **2013**, *282*, 870–879.

(188) Jung, S.; Dorrestijn, M.; Raps, D.; Das, A.; Megaridis, C. M.; Poulikakos, D. Are Superhydrophobic Surfaces Best for Icephobicity? *Langmuir* **2011**, *27* (6), 3059–3066.

(189) Momen, G.; Farzaneh, M. Facile Approach in the Development of Icephobic Hierarchically Textured Coatings as Corrosion Barrier. *Appl. Surf. Sci.* **2014**, *299*, 41–46.

(190) Zheng, S.; Li, C.; Fu, Q.; Hu, W.; Xiang, T.; Wang, Q.; Du, M.; Liu, X.; Chen, Z. Development of Stable Superhydrophobic Coatings on Aluminum Surface for Corrosion-Resistant, Self-Cleaning, and Anti-Icing Applications. *Mater. Desing* **2016**, *93*, 261–270.

(191) Thebault, P.; Taffin de Givenchy, E.; Levy, R.; Vandenberghe, Y.; Guittard, F.; Géribaldi, S. Contact-Active Microbicidal Gold Surfaces Using Immobilization of Quaternary Ammonium Thiol Derivatives. *Eur. J. Med. Chem.* **2009**, *44* (10), 4227–4234.

(192) Caillier, L.; de Givenchy, E. T.; Levy, R.; Vandenberghe, Y.; Géribaldi, S.; Guittard, F. Synthesis and Antimicrobial Properties of Polymerizable Quaternary Ammoniums. *Eur. J. Med. Chem.* **2009**, *44* (8), 3201–3208.

(193) Thebault, P.; Givenchy, E. T. d; Géribaldi, S.; Levy, R.; Vandenberghe, Y.; Guittard, F. Surface and Antimicrobial Properties of Semi-Fluorinated Quaternary Ammonium Thiol Surfactants Potentially Usable for Self-Assembled Monolayers. *J. Fluor. Chem.* **2010**, *131* (5), 592–596.

(194) Shin, K. R.; Kim, Y. S.; Kim, G. W.; Yang, H. W.; Gun Ko, Y.; Shin, D. H. Effects of Concentration of Ag Nanoparticles on Surface Structure and in Vitro Biological Responses of Oxide Layer on Pure Titanium via Plasma Electrolytic Oxidation. *Appl. Surf. Sci.* **2015**, *347*, 574–582.

(195) Huang, L.; Zhao, S.; Wang, Z.; Wu, J.; Wang, J.; Wang, S. In Situ Immobilization of Silver Nanoparticles for Improving Permeability, Antifouling and Anti-Bacterial Properties of Ultra Filtration Membrane. *J. Memb. Sci.* **2016**, *499*, 269–281.

(196) Xu, T.; Wu, L.; Yu, Y.; Li, W.; Zhi, J. Synthesis and Characterization of Diamond – Silver Composite with Anti-Bacterial Property. *Mater. Lett.* **2014**, *114*, 92–95.

(197) Ma, J.; Sun, Y.; Gleichauf, K.; Lou, J.; Li, Q. Nanostructure on Taro Leaves Resists Fouling by Colloids and Bacteria under Submerged Conditions. *Langmuir* **2011**, *27* (16), 10035–10040.

(198) Bruzaud, J.; Tarrade, J.; Celia, E.; Darmanin, T.; Taf, E.; Givenchy, D.; Guittard, F.; Herry, J.; Guilbaud, M.; Bellon-fontaine, M. The Design of Superhydrophobic Stainless Steel Surfaces by Controlling Nanostructures: A Key Parameter to Reduce the Implantation of Pathogenic Bacteria. *Mater. Sci. Eng. C* **2017**, *73*, 40–47.

(199) Díaz, C.; Schilardi, P. L.; Salvarezza, R. C.; Lorenzo de Mele, M. F. Nano/Microscale Order Affects the Early Stages of Biofilm Formation on Metal Surfaces. *Langmuir* **2007**, *23* (22), 11206–11210.

(200) Lin, Z.-H.; Cheng, G.; Lee, S.; Pradel, K. C.; Wang, Z. L. Harvesting Water Drop Energy by a Sequential Contact-Electrification and Electrostatic-Induction Process. *Adv. Mater.* **2014**, *26*, 4690–4696.

(201) Kato, S.; Yamada, K.; Nishide, T. Water Harvesting Capability of Petal-Effect Hafnia Films and Hydrophilic-Hydrophobic Patterned Films. *J. Ceram. Soc. Japan* **2015**, *123* (2), 73–78.

(202) Zhu, H.; Guo, Z. Hybrid Engineered Materials with High Water-Collecting Efficiency Inspired by Namib Desert Beetles. *Chem. Commun.* **2016**, *52*, 6809–6812.

(203) Zhu, H.; Yang, F.; Li, J.; Guo, Z. High-Efficiency Water Collection on Biomimetic Material with Superwettable Patterns. *Chem. Commun.* **2016**, *52* (84), 12415–12417.

(204) Wang, Y.; Zhang, L.; Wu, J.; Hedhili, M. N.; Wang, P. A Facile Strategy for the Fabrication of a Bioinspired Hydrophilic–Superhydrophobic Patterned Surface for Highly Efficient Fog-Harvesting. *J. Mater. Chem. A* **2015**, *3*, 18963–18969.

(205) Kim, G.-T.; Gim, S.-J.; Cho, S.-M.; Koratkar, N.; Oh, I.-K. Wetting-Transparent Graphene Films for Hydrophobic Water-Harvesting Surfaces. *Adv. Mater.* **2014**, *26*, 5166–5172.

(206) Zhang, L.; Wu, J.; Hedhili, M. N.; Yang, X.; Wang, P. Inkjet Printing for Direct Micropatterning of a Superhydrophobic Surface: Toward Biomimetic Fog Harvesting Surfaces. *J. Mater. Chem. A.* **2015**, *3*, 2844–2852.

(207) Cao, M.; Ju, J.; Li, K.; Dou, S.; Liu, K.; Jiang, L. Facile and Large-Scale Fabrication of a Cactus-Inspired Continuous Fog Collector. *Adv. Funct. Mater.* **2014**, *24*, 3235–3240.

(208) Peng, Y.; He, Y.; Yang, S.; Ben, S.; Cao, M.; Li, K.; Liu, K.; Jiang, L. Magnetically Induced Fog Harvesting via Flexible Conical Arrays. *Adv. Funct. Mater.* **2015**, *25*, 5967–5971.

CHAPTER 2

Thienothiophenes: hydrophobicity and water adhesion

This chapter is dedicated to the discussion of the electrochemical polymerization of various thienothiophene monomers (differing by core and type of substituted chains) and their efficacy to form nanotubular structures. Previous work on this electropolymerizable core using 3,4-naphthalenedioxthiophene derivatives (NaphDOT) have shown interesting results towards the surface morphology.[1] The process to obtain nanotubes without hard templates is extremely rare in the literature.[2–11] Here, we will first report an electrochemical study for five thienothiophene derivatives differing by the momomer core following the study about the influence of electropolymerization method and electrolyte. A discussion about the mechanism concerning the nanotubes formation as well as the surface wettability will be also presented. In a second step, we will show the influence of the type and the size of the grafted chain in a thienothiophene series (thieno[3,4-*b*]thiophene). The discussion will be also focused on the surface morphology and wettability for 12 synthesized molecules.

2.1 STUDY THE EFFECT OF THE AROMATIC CORE

It is already known that the monomer core plays an important role in the final surface structure due to the differences in the steric hindrance of each molecule, the polymer rigidity and conductivity. Many are the works reporting the use of aromatic cores, such as thiophenes,[12–14] indoles,[15] pyrroles,[16,17] anilines,[18–20] for example, yielding surfaces with various morphologies. Indeed, the monomer will also define which solvent will be used to polymerize. At this way, the solvent used is a main parameter that governs the surface morphology because of the differences in the solubility of the oligomers formed in the first instance.[21] Most of electrochemical polymerizations are carried out in organic media because of the good solubility of the monomers, especially if substituents are present. Aprotic solvents with poor nucleophilic character and exceptional electrochemical stability, such as acetonitrile and dichloromethane, are preferably used.

In this first work, five thienothiophene derivatives (**Scheme 2.1**) are tested as monomers: thieno[2,3-*b*]thiophene (Thienothiophene-1), thieno[3,2-*b*]thiophene (Thienothiophene-2), 2,2′-bithieno[3,2-*b*]thiophene (Thienothiophene-3), dithieno[3,2-*b*:2′,3′-*d*]thiophene

(Thienothiophene-4) and naphtho[1,2-*b*:5,6-*b*′]dithiophene (Thienothiophene-5). The monomers were purchased from Sigma-Aldrich and were used without any previous purification. We report the influence of the monomer, the electrodeposition method and electrolyte on the surface structure and hydrophobicity.

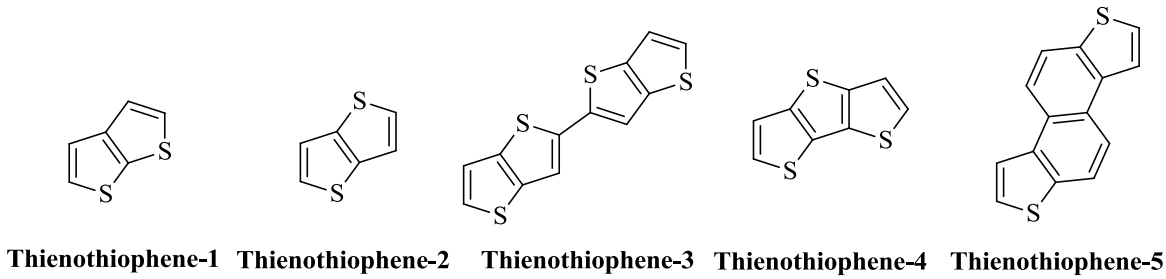

Scheme 2.1. Monomers studied in this work.

2.1.1 Influence of the Electrochemical Method

During the electrochemical polymerization, it is known that conducting polymers can self-organize at the surface of the electrode forming various structures. The morphology can directly influence the surface wettability and, consequently, the potential applications of the surface. To polymerize, it is enough to apply a sufficiently stimulus, which will depend on the electrochemical method used, for the film of the corresponding polymer to progressively grow at the electrode surface. Therefore, the morphology of the polymer film depends on the applied electrochemical method during the electropolymerization. With this aim, here we study the influence of four electrochemical methods (cyclic voltammetry, constant potential, galvanostatic deposition and pulse deposition) on the surface wettability and morphology of the thienothiophenes presented in **Scheme 2.1**. More specifically, we will focus on the formation of nanotubes and discuss the differences in the surface morphology with the electrochemical methods. A detailed electropolymerization procedure as well as the surface characterization analysis for the whole thesis is given in ***Annex A2*** and ***Annex A3***, respectively.

2.1.1.1 *Cyclic Voltammetry*

Firstly, the electropolymerization of the thienothiophenes was carried in a solution of 0.1 M of tetrabutylammonium perchlorate (Bu_4NClO_4) in 10 mL of anhydrous dichloromethane with 0.01 M of each monomer. The cyclic voltammetry was used to determine the monomer oxidation potential (E^{ox}) by a single potential scan (2.34 - 2.76 V). The polymers were electrodeposited by scanning from -1 V to a potential slightly lower to the monomer oxidation potential, called the working potential, E^{w} (2.06 - 2.46 V). The complete data of E^{ox} and E^{w} is presented in the ***Table A2.1***. This is the first method to be presented because it is a fundamental tool for monitoring the polymer growth and the effect of the monomer core by the voltammograms curves.

The cyclic voltammograms are displayed in **Figure 2.1**. Thienothiophene-3 and Thienothiophene-4 polymerize perfectly and the cyclic voltammograms present several oxidation and reduction peaks. A high and relatively constant amount of polymer is also deposited after each scan. By contrast, with Thienothiophene-1, Thienothiophene-2 and Thienothiophene-5, the amount of polymer deposited is much lower. It is not surprising that Thienothiophene-3 and Thienothiophene-4 polymerize more than the other ones because there are at least two important parameters that can explain this: first of all, the monomers polymerize well if the density of radicals formed at the polymerization sites after monomer oxidation is important. Usually donating effects favor the polymerization and reversely. Second, the polymer rigidity is another extremely important parameter in order to highly enhance the polymer conductivity and polymer chain length.

However, a very intense peak at about -0.5 V was observed during the back scans. This peak is very important for the formation of nanotubes, because it may correspond to the decomposition potential of acidic water $2\ H_2O \rightarrow 2\ H_2(g) + O_2\ (g)$ and as a consequence the formation of gas bubbles. Another possibility is that the H^+ released during electropolymerization leads to H_2, but this is less probable because tetrabutylammonium ion can be considered H^+ ions scavenger [22]. The mechanism of formation of nanotubes will be studied later. Hence, Thienothiophene-1, Thienothiophene-2 and Thienothiophene-5 seem to be the most appropriate monomers for the formation of nanotubes.

The stability of the polymeric films was also studied by cyclic voltammetry in order to observe the polymer mass loss during the electrochemical process. The evaluation was done in a free-polymer solution using a surface polymerized after 3 deposition scans. **Figure 2.2**

show that PThienothiophene-1 and PThienothiophene-2 present a larger polymer loss in the first scans which is not so huge in the next scans. In this way, they present a good stability in comparison with the others polymers. For PThienothiophene-3, PThienothiophene-4 and PThienothiophene-5 the polymer loss is much more intense and increase after each scan.

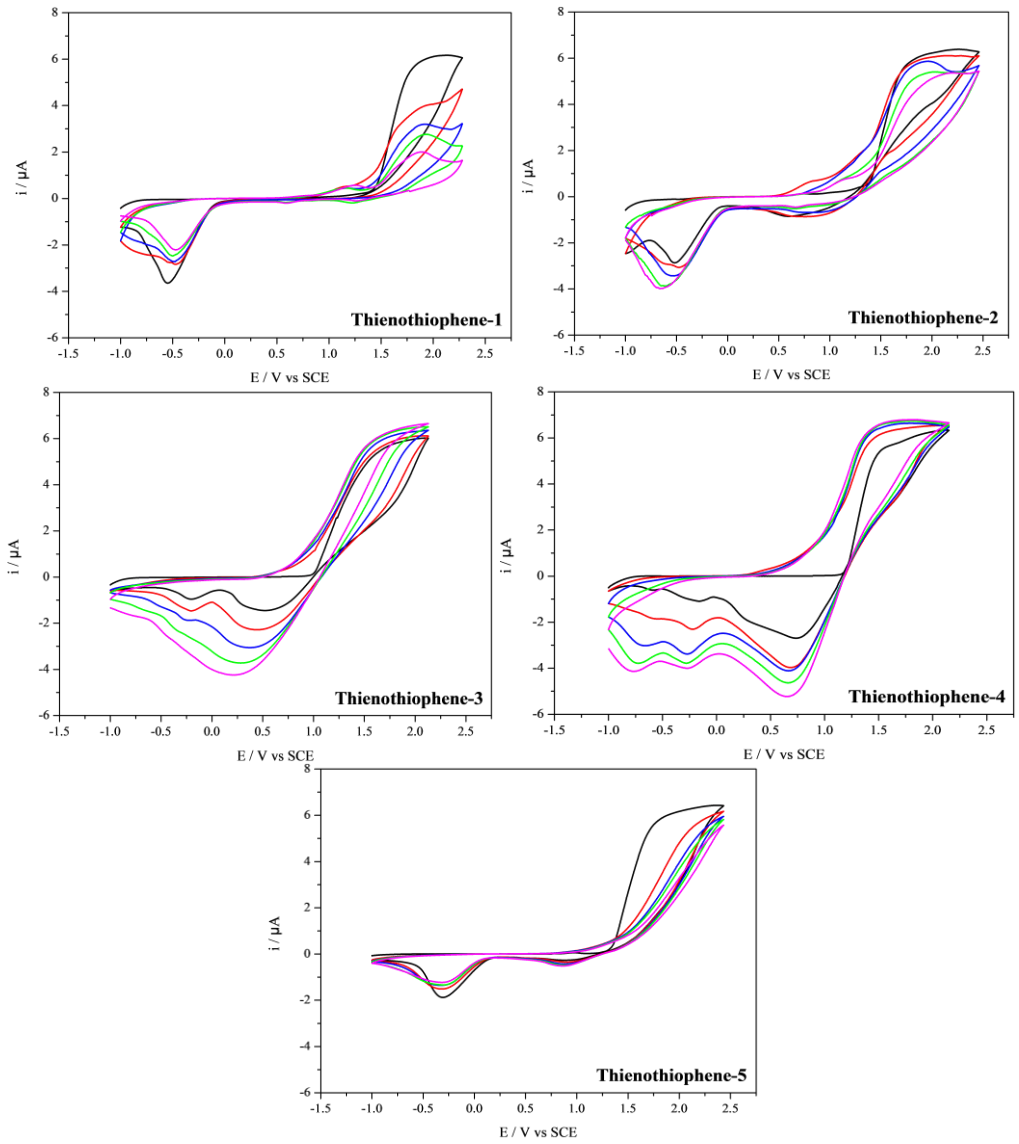

Figure 2.1. Cyclic voltammograms of the thienothiophene monomers in 0.1 M Bu_4NClO_4/dichloromethane at a scan rate of 20 mV s^{-1}. Black line: scan 1, red line: scan 2, blue line: scan 3, green line: scan 4, magenta line: scan 5.

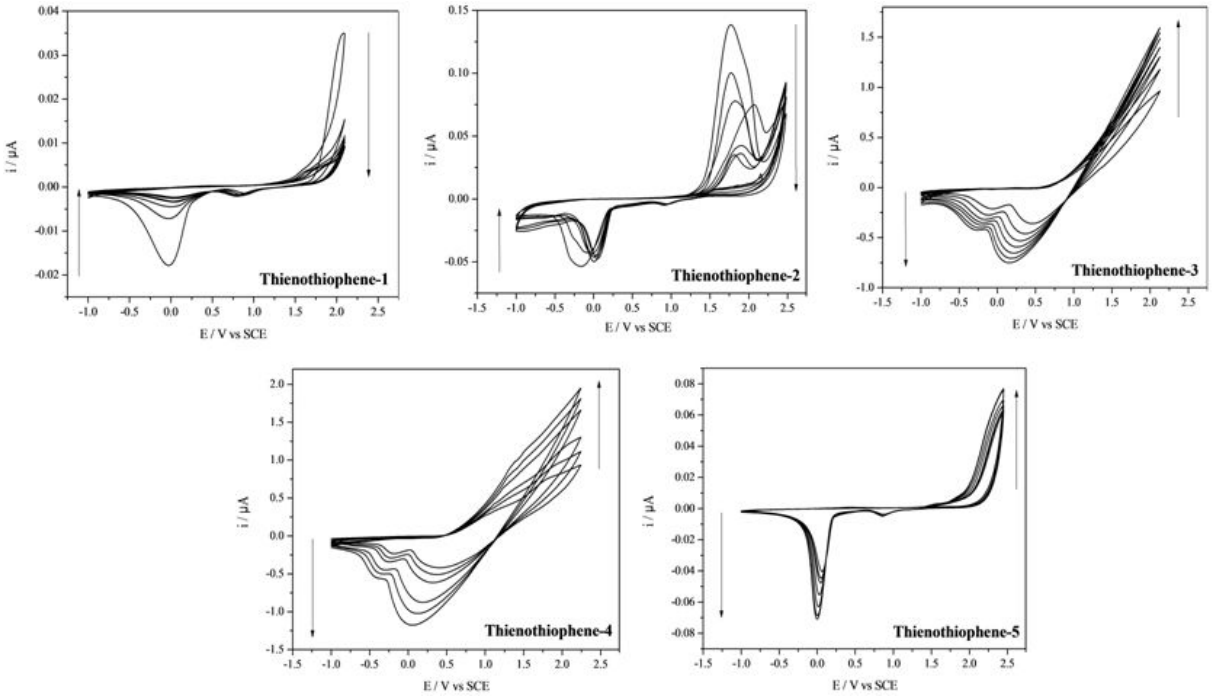

Figure 2.2. Cyclic voltammograms (6 scans at 20 mV s^{-1}) for the thienothiophene monomers after electrodeposition of 3 scans. Solution of 0.1 M Bu_4NClO_4/dichloromethane.

The SEM images for 3 depositions scans are given in **Figure 2.3**. First of all, the electropolymerization of Thienothiophene-3, Thienothiophene-4 and Thienothiophene-5 induces the agglomeration of nanostructures forming extremely rough surfaces. The nanostructures consist in nanofibers for Thienothiophene-3, mixtures of nanofibers and nanosheets for Thienothiophene-4 and mixtures of nanofibers and spherical nanoparticles for Thienothiophene-5. In contrast, large nanotubes are obtained with Thienothiophene-1 and Thienothiophene-2, where the top of the nanotubes is closed with Thienothiophene-1 and open with Thienothiophene-2. Hence, as showed by the voltammograms in **Figure 2.1**, Thienothiophene-1 and Thienothiophene-2 are excellent monomers for the formation of nanotubes. The SEM images of Thienothiophene-1 and Thienothiophene-2 confirm the importance of the presence of the peak corresponding to the formation of gas bubbles during the electropolymerization, but the absence of nanotubes with Thienothiophene-5 also confirms the importance of the monomer structure in the nanotube formation.

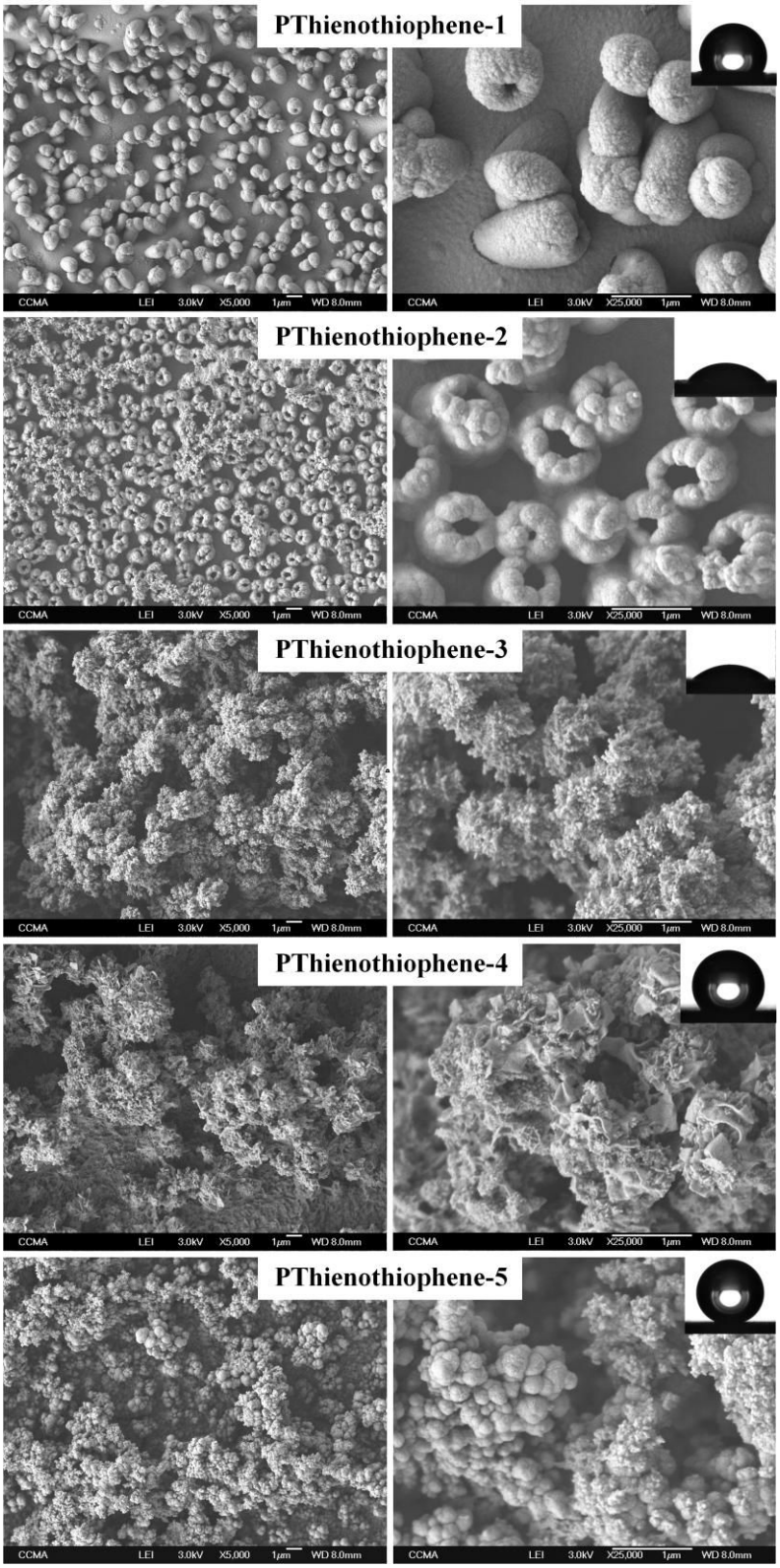

Figure 2.3. SEM images of the polymers electrodeposited by cyclic voltammetry (3 scans) in a 0.1 M solution of Bu_4NClO_4/dichloromethane. Magnifications: 5000x and 25000x.

A possible explanation for the different structures obtained for the polymers is the monomer structure and the number of polymerizable sites of each. As Thienothiophene-1 and Thienothiophene-2 are small and less complex structures, thus the polymerization proceeds more organized and aligned, which could favor the formation of nanotubes. In opposition, Thienothiophene-3, Thienothiophene-4 and Thienothiophene-5 are more complex and voluminous structures, which induce a higher steric hindrance during the polymerization and favor the formation of large and spaced agglomerates on the surface. Indeed, the monomer or the corresponding polymer has to be able to stabilize the gas bubbles during the polymerization to allow nanotube formation. These results confirm the importance of the monomer core in the morphology and, consequently, in the surface wettability of the polymer film.

The surface roughness and the θ_w are also available in **Table 2.1**. For most of the surfaces, θ_w achieves its highest value after 1 deposition scans and starts to decreases as the number of deposition scans increases because the surfaces become too rough, which favors the Wenzel state. For the surfaces with nanotubes obtained with Thienothiophene-2, the highest θ_w (= 150.7°) are obtained with a very high water adhesion (α > 90º). When the number of deposition scans increases, the surfaces become more hydrophilic, as well as for Thienothiophene-3. However, after the formation of rough nanotubes with Thienothiophene-1, the wettability remains almost the same even with increased number of deposition scans, as well as seen for PThienothiophenes-4. In opposition, PThienothiophene-5 presents a high θ_w for reduced deposition scans with a non-sticky behavior after 3 scans, but a superhydrophilicity was observed for higher number of deposition scans due to the increase of the surface roughness. In summary, these polymers are parahydrophobic (α > 90º), except for PThienothiophene-5 which presents a low water adhesion (H = 12 and α = 11º) after 3 scans. **Figure 2.4** shows the dynamic properties for the polymeric surfaces gathering the predominant parahydrophobic behavior for the thienothiophene films and the unique superhydrophobic surface for PThienothiophene-5 after 3 deposition scans. Moreover, all the surfaces are completely oleophilic using diiodomethane and hexadecane independently of the number of deposition scans, which suggest a potential application in oil/water membrane separation.

Table 2.1. Apparent contact angles of water (θ_w) and roughness data as a function of the polymer and the number of deposition scans. Polymerization at 0.1 M solution Bu_4NClO_4/dichloromethane.

Polymer	Number of deposition scans	Ra [µm]	Rq [µm]	θ_w [deg]
PThienothiophene-1	1	0.4	0.7	122.4
	3	1.4	2.8	114.6
	5	2.2	3.9	108.1
PThienothiophene-2	1	1.3	2.9	150.7
	3	6.1	9.3	36.2
	5	5.4	8.5	44.5
PThienothiophene-3	1	2.8	4.2	149.0
	3	6.9	9.7	23.7
	5	9.9	13.1	0
PThienothiophene-4	1	3.6	6.2	144.5
	3	8.9	12.6	136.6
	5	12.0	16.2	133.8
PThienothiophene-5	1	2.3	3.6	146.4
	3	2.3	3.7	153.3
	5	7.2	10.7	0

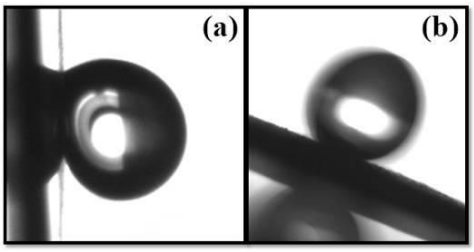

Figure 2.4. Water droplet images for (a) PThienothiophene-2 after 1 scan and (b) PThienothiophene-5 after 3 scans showing a sticky and non-sticky behavior, respectively. Polymerization at 0.1 M solution Bu_4NClO_4/dichloromethane.

To better analyze the wettability behavior of the nanotubes, **Figure 2.5** shows the SEM images of PThienothiophene-1 and PThienothiophene-2 for different number of scans. It should be noted that even presenting lower density of agglomerates and a reduced amount of structures, the nanotubes in PThienothiophene-1 remain with the top closed even when the number of deposition scans increases. This should keep the wettability of the surface constant as the number of deposition scans increases. The lower θ_w showed on **Table 2.1** for PThienothiophene-1 after 1 scan can be explained by both low density of nanotubes and its low roughness. Indeed, the diameter of the nanotubes do not show a significant change when

the number of deposition scans increases. This is not surprising since the peak at about -0.5 V (**Figure 2.1**) concerning the formation of gas bubbles showed a decrease in it intensity during the scans. An opposite behavior was found for PThienothiophene-2. The nanotubes showed the top closed after 1 scan, but when the number of scans increases, their top start to open. The porosity also highly increases with the number of scans as well as the diameter of the nanotubes. This is expected because the reduction of H^+ into H_2 takes place during each scan when the potential is close to -0.5 V and showed a significant increase. Hence, the presence of surface porosity can have a negative effect on θ_w, even if the surface with Thienothiophene-2 presents rough structures. The effect of porosity on water wettability can be seen in the inset water drop pictures in **Figure 2.5**.

In order to better control the formation of nanotubes, the thienothiophenes were also polymerized using other electrochemical methods: constant potential, galvanostatic deposition and square pulse deposition. These methods will be presented in the next topics.

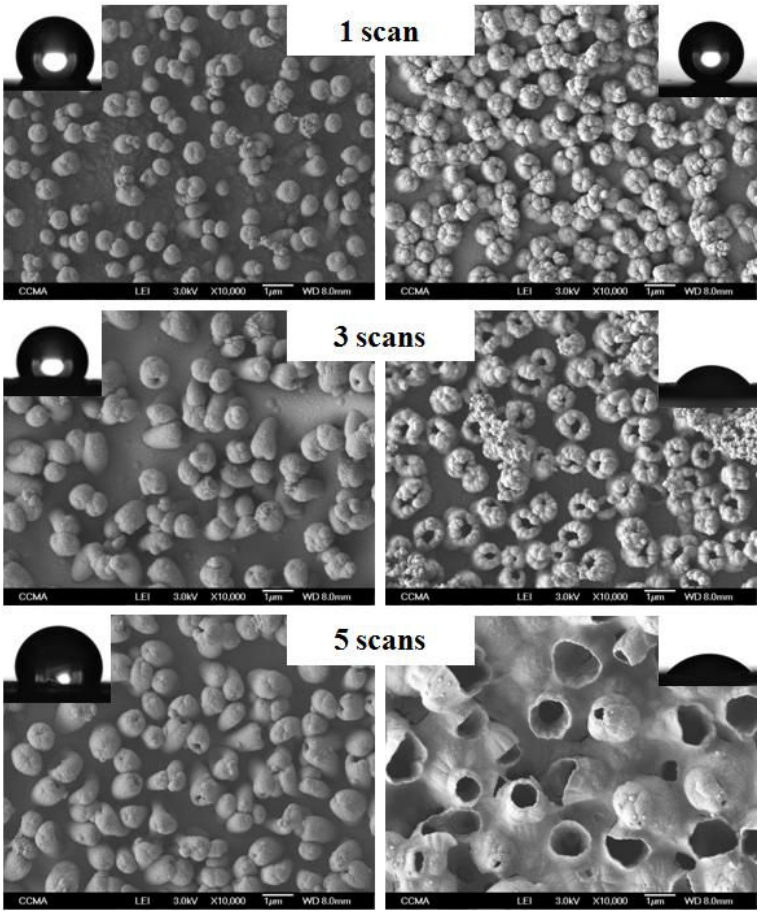

Figure 2.5. SEM images of PThienothiophene-1 (left) and PThienothiophene-2 (right) electrodeposited by cyclic voltammetry in Bu_4NClO_4/dichloromethane for different number of scans.

2.1.1.2 *Constant Potential*

Potentiostatic techniques, such as constant potential and galvanostatic deposition, are commonly used to investigate the nucleation mechanism and the polymer growth.[23] Here, the thickness of the deposited polymer can be controlled by the delivered charge density. This technique is highly used to fabricate parahydrophobic and superhydrophobic surfaces using conducting polymers.[24–28] The monomer was electrochemically polymerized by a constant potential (E^w of each monomer) using different deposition charges (Qs) from 12.5 to 400 mC cm^{-2} in order to visualize the changes in the surface structures at different stages. The films were prepared in the following conditions: 0.01 M of each monomer in a 0.1 M solution of Bu_4NClO_4 and anhydrous dichloromethane.

To better understand the behavior behind the formation and grow of nanotubes, SEM images of PThienothiophene-2 are displayed in **Figure 2.6**. The roughness and wettability data are shown in **Table 2.2**. All the nanoseeds are formed in the first instance of the electropolymerization. Indeed, it shows that for Qs = 12.5 mC cm^{-2}, all the surface structures are nanoporous with the diameter ∅ ≈ 120-130 nm and the height ≈ 100 nm. Here, the surface is parahydrophobic with θ_w = 118.7°. Then, as Qs increases from 12.5 to 50 mC cm^{-2}, the diameter and the height of the surface structures also increase, but the number of surface structures presenting their top open decreases. This number is about 100% for Qs = 12.5 mC cm^{-2}, 50% for Qs = 50 mC cm^{-2} and 0% for Qs = 100 mC cm^{-2}, which induces a decrease in θ_w. From Qs = 50 mC cm^{-2}, the height of the structures remains quite constant, but their top begin to close which explains the decrease in θ_w. As the deposition charge increases, a new layer of polymer is deposited on the surface covering the nanotubes. Hence, few structures can be identified after high deposition charges.

The SEM images for the PThienothiophenes 1, 3, 4 and 5 are shown in **Figure 2.7** and the roughness and wettability data also in **Table 2.2**. For PThinothiophene-1, the nanoseeds are also formed in the first instance and the morphology is quite similar to that formed by cyclic voltammetry after 1 deposition scan. Since a larger amount of nanoseeds were presented for 12.5 mC cm^{-2}, the morphology of the surface is very different for Qs > 50 mC cm^{-2} from the obtained by cyclic voltammetry. A cauliflower-like structure can be observed for Qs > 100 mC cm^{-2}. The diameter of the structures also augments with the increase in the applied charge: at Qs = 50 mC cm^{-2} the diameter is ∅ ≈ 350 nm, at Qs = 100 mC cm^{-2} is ∅ ≈ 500 nm

and at Qs = 400 mC cm^{-2} is ∅ ≈ 750 nm. However, it is important to notice that the top of the structures remains closed for all the Qs applied as observed for cyclic voltammetry. A decrease in ~ 60º was observed in Qs from 50 to 100 mC cm^{-2} due to the changes in the morphology.

The type of structures did not change significantly when the electrochemical method was changed for the PThienothiophenes 3, 4 and 5. A mixture of nanospheres with nanofibers and nanosheets can be seen for these polymers. Here, it is clear that Thienothiophenes 3, 4 and 5 are not favorable to form nanotubes on the surface probably due to the size and molecular arrangements of the monomers. Indeed, they may present different planarity and rigidity from Thienothiophenes 1 and 2. The roughness showed to be higher for PThienothiophene-4 as well as showed by cyclic voltammetry and the wettability follow the same tendency for both electrochemical methods.

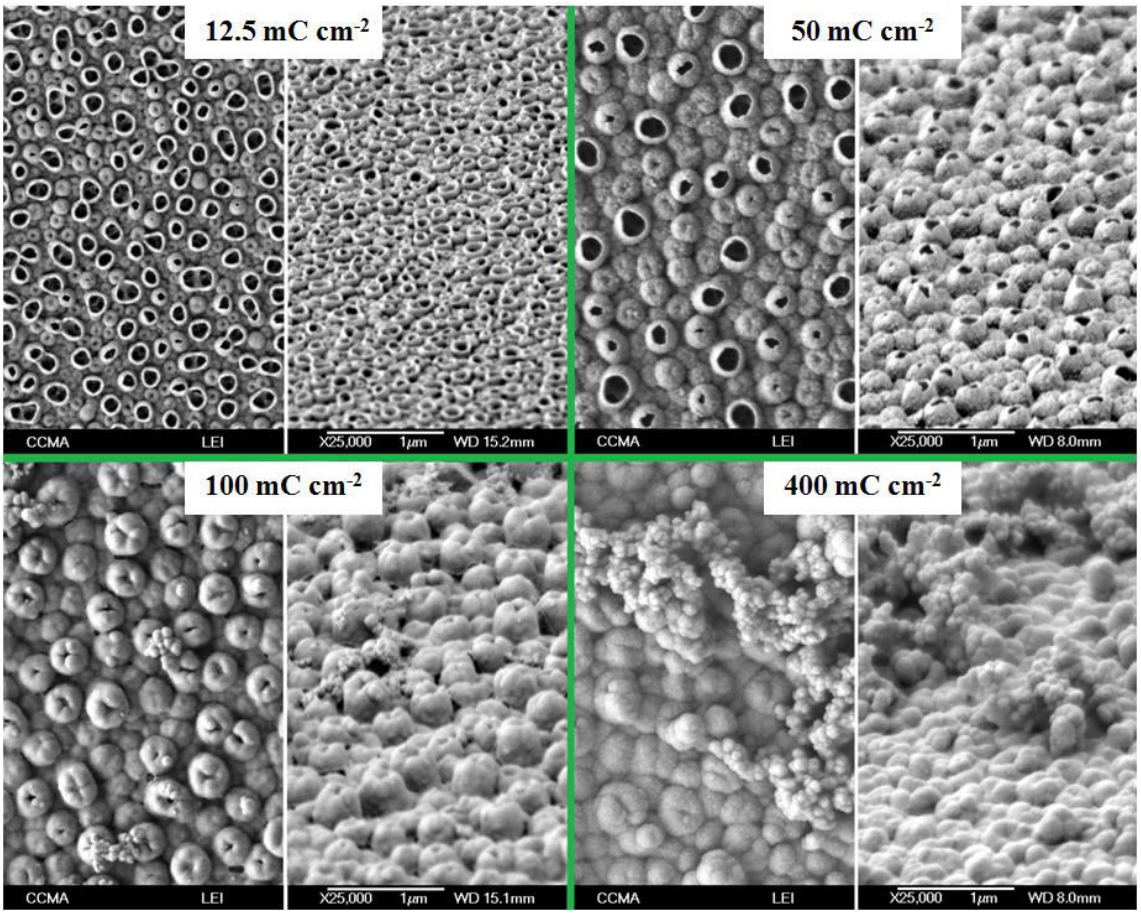

Figure 2.6. SEM images (flat and inclined at 60°) of PThienothiophene-2 electrodeposited at constant potential using different deposition charges. Polymerization at 0.1 M solution Bu_4NClO_4/dichloromethane.

Table 2.2. Apparent contact angles of water (θ_w) and roughness data as a function of the polymer and the deposition charge (Qs). Polymerization at 0.1 M solution Bu_4NClO_4/dichloromethane.

Polymer	Qs [mC cm^{-2}]	Ra [nm]	Rq [nm]	θ_w [deg]
PThienothiophene-1	12.5	8.2	10.6	112.9
	25	7.6	9.8	120.3
	50	10.2	13.0	111.5
	100	19.1	24.5	66.0
	200	77.7	100.6	61.8
	400	83.6	107.8	67.5
PThienothiophene-2	12.5	6.4	8.3	118.7
	25	7.9	11.1	116.1
	50	37.1	47.6	38.4
	100	69.4	88.1	64.3
	200	190.7	264.0	0
	400	170.1	271.1	0
PThienothiophene-3	12.5	44.7	64.3	85.3
	25	77.0	229.2	106.4
	50	241.5	1540.0	120.0
	100	2333.3	7533.3	40.8
	200	5767.0	12800.0	44.2
	400	7320.0	14633.0	0
PThienothiophene-4	12.5	10.6	15.6	88.7
	25	11.8	15.4	77.0
	50	156.1	465.1	63.1
	100	441.2	2166.7	42.6
	200	7533.3	14766.7	41.4
	400	10533.3	17833.3	0
PThienothiophene-5	12.5	42.8	73.0	100.7
	25	43.1	54.5	113.3
	50	227.3	298.4	112.1
	100	403.4	862.1	79.7
	200	5433.3	11100.0	108.4
	400	3256.7	7866.7	43.1

In conclusion, both monomers Thienothiophene-1 and Thienothiophene-2 showed to be favorable to the formation of nanotubes. However, since the formation of nanotubes for Thienothiophene-2 seems to be more versatile with the size, porosity and form of the structures, the sequence of this work will be presented using this monomer for the next studies.

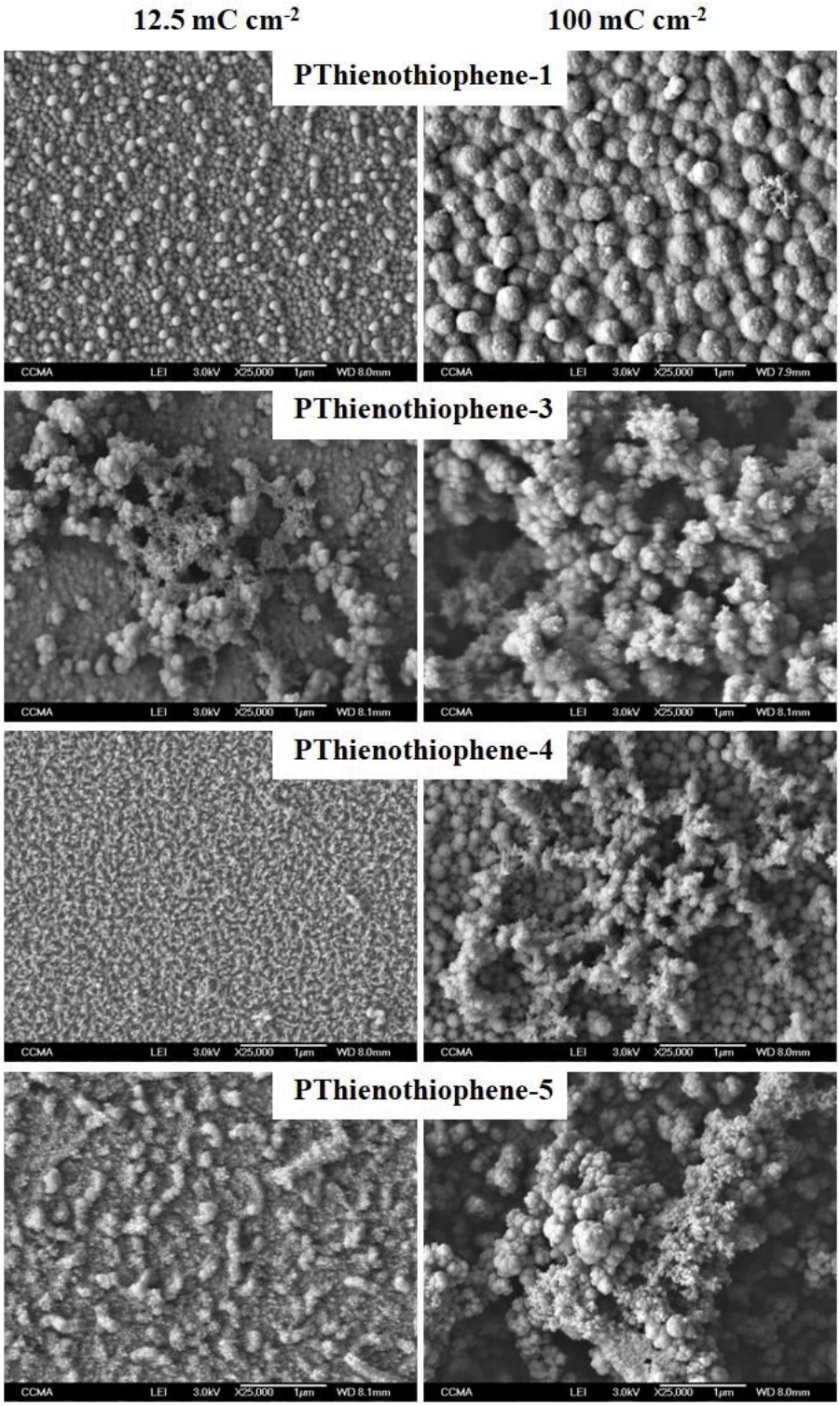

Figure 2.7. SEM images of the polymers electrodeposited by constant potential as function of the deposition charge (Qs) in a 0.1 M solution of Bu_4NClO_4/dichloromethane.

2.1.1.3 *Galvanostatic deposition*

As well as constant potential, galvanostatic deposition is used for control the nucleation and chain propagation of the polymer. Many researches showed the nucleation and growth mechanisms for metals, such as copper, lithium and tin, for example, but few works were found with conducting polymers.[6,29–31] Here, the polymerization was carried out using galvanostatic method by applying different and constants current densities to reach an appropriate potential for the deposition in a specific interval of time. Five currents (0.1, 0.5, 1, 5 and 10 mA) were used in five deposition times (10, 20, 40, 80 and 160 s) in order to study their influence in the polymer growth and structuration in a solution of 0.1 M of Bu_4NClO_4 in anhydrous dichloromethane. For this method, only Thienothiophene-2 (thieno[3,2-*b*]thiophene) was used to polymerize.

Figure 2.8 shows the SEM images for PThienothiophene-2 for the five currents after 20 and 80 s of deposition. As the current density increase, the amount of structures on the surfaces and their size also increase. Moreover, the morphology seems to change in the same direction with the increase in the deposition time. For low current densities, nanoseeds are formed after 20 s which enable the growth of nanotubes and nanospheres for 0.1 and 0.5 mA, respectively, when the deposition time increases to 80 s. For 1 mA, it is clear the formation of nanotubes (∅ = 0.2 µm) after 20 s of deposition time. However, they have grown and formed flower-like structures (∅ = 0.5 µm) after 80 s of deposition. In opposition to the nanotubes, surfaces deposited using 5 mA present ordered nanodomes with almost no changes in their morphology when the deposition time increases. Rough structures can be seen for 10 mA for both 20 s and 80 s. The hollow structures formed applying high current density presented their top closed and had grown assuming a shape similar to tree-like and cauliflower-like structures. This behavior happens when the electropolymerization is carried out under harsh conditions allowing a rapid grow of the top closed tubes in tree-like or cauliflower-like structures, as showed by constant potential. For the surfaces produced with high current densities, the formation of new seeds while electropolymerization progress is not clearly observed. However, the growth of the structures occurs for all the current densities and deposition times. Inclined SEM images (60°) for the surfaces of 0.1, 1 and 10 mA at 80 s are presented in **Figure 2.9**.

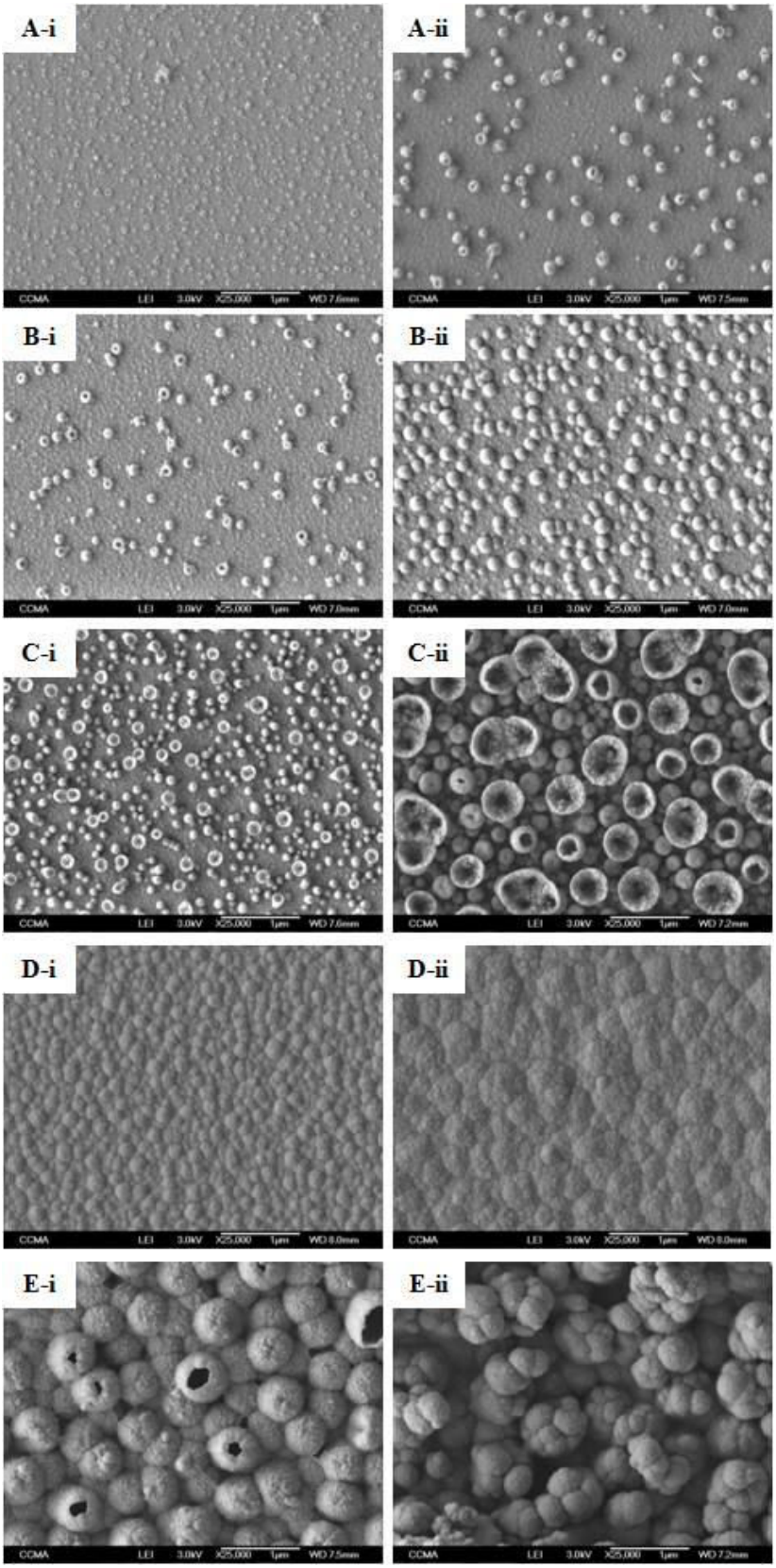

Figure 2.8. SEM images of PThienothiophene-2 electropolymerized by galvanostatic method during i) 20 s and ii) 80 s for the current densities: A) 0.1, B) 0.5, C) 1.0, D) 5.0 and E) 10.0 mA. Polymerization at 0.1 M solution Bu_4NClO_4/dichloromethane.

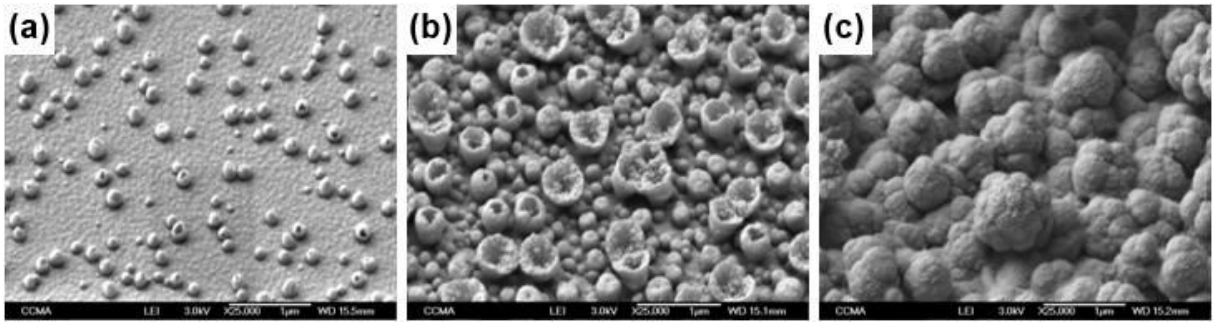

Figure 2.9. SEM images after substrate inclination of 60º of PThienothiophene-2 polymerized by galvanostatic method during 80 s for the current densities: a) 0.1, b) 1 and c) 10 mA. Polymerization at 0.1 M solution Bu_4NClO_4/dichloromethane.

By analyzing the inclined images, it is clear the surface growth and structuration as function of current density:

- at 0.1 mA → few nanotubes dispersed on the surface (Fig 3a);
- at 1 mA → very large capsules with top open (Fig 3b);
- at 10 mA → formation of cauliflower-like structures (Fig 3c);

Hence, the growth of the tubular structures is not cylindrical-like, but spherical. As the polymerization proceeds, the polymer growth around the gas bubbles leading to open capsules and at the end similar to cauliflower-like structures.

The profilometry results are presented in **Table 2.3**. The roughness is approximately constant for 0.1 and 0.5 mA, yielding very smooth surfaces. For 1 and 5 mA an increase was observed for deposition time over 80 s. Meanwhile, for 10 mA, the polymeric surfaces presented an important increase in the roughness with the deposition time, showing that the control of the current density is very important in order to study the growing of the structures. These results are in agreement with the SEM images showing that the roughness of the polymeric films increase with the deposition time and with the current density.

The apparent contact angle measurements for the polymers electrodeposited by galvanostatic method are presented in **Figure 2.10**. In general, the surfaces presented a hydrophilic behavior. For a current density of 0.1 mA, the wettability does not show a significant variation (θ_w ~ 80º) with the deposition time because the current density applied is very low. Hydrophobic surfaces were only obtained to 1 mA at short deposition time. However, as the deposition time increases, a hydrophilic behavior was assumed again. For surfaces with a current density > 0.5 mA, the θ_w tend to decrease with the deposition time and the current density. The roughness plays a significant effect on the wettability results for the galvanostatic surfaces.

Table 2.3. Roughness data for PThienothiophene-2 electropolymerized by galvanostatic method as function of the current density (mA) and the deposition time (s). Polymerization at 0.1 M solution Bu_4NClO_4/dichloromethane.

Deposition time (s)	Ra (nm)					Rq (nm)				
	Current density (mA)									
	0.1	0.5	1.0	5.0	10.0	0.1	0.5	1.0	5.0	10.0
10	10.7	9.0	9.2	9.7	37.5	16.0	13.3	13.3	15.9	50.6
20	9.7	9.3	8.5	9.3	39.7	14.1	12.8	11.7	12.3	56.9
40	10.3	9.1	9.0	13.3	216.6	18.8	12.5	12.0	13.3	1580.0
80	9.2	10.4	35.6	18.8	344.2	12.8	15.6	47.7	27.5	3138.0
160	11.3	8.4	90.1	512.4	1139.8	21.8	21.0	118.7	2746.2	8134.0

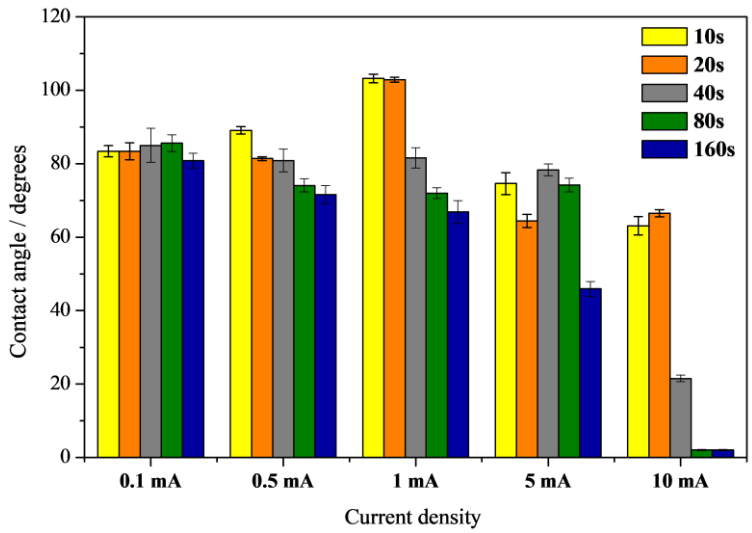

Figure 2.10. Apparent contact angle for water (θ_w) for PThienothiophene-2 electropolymerized by galvanostatic method as function of the current density (mA) and the deposition time (s). Polymerization at 0.1 M solution Bu_4NClO_4/dichloromethane.

The behavior observed by profilometry and wettability measurements suggests that the deposition time does not show a significant impact on the θ_w and the roughness for low current densities. However, for surfaces prepared with a current density higher than 1 mA, a huge variation could be observed for long deposition times (usually t > 40 s). Thus, it indicates that for galvanostatic method, as much as the current density and/or the deposition time increase, the deposition tends to be more significant for the properties here studied. Similar results were found for Hanan Teller and co-workers in the study of the nucleation and growth mechanism of formed tin structures.[30] They observed that the increasing in the

deposition time leads to a further nucleation and growing of branched dendrites. But the growing of the structures is clear to be affected when the intensity of the current density increase. In opposition for the results obtained with the thienothiophenes, Allen Pei and co-workers showed a decrease in the nuclei size when the current density increases for lithium metals.[29] This will depend of the type of material and electrodeposition parameters used.

2.1.1.4 *Square Pulse deposition*

Electropolymerization by square pulse method refers to a deposition where the potential or the current density is rapidly alternated between two values. It consists in a series of pulses of equal duration and/or amplitude where each pulse consists of an "on" time during which an anodic potential is applied and an "off" time during which a cathodic potential is applied. In order to evaluate the differences in the morphology and wettability, polymeric films were deposited by pulse potentiostatic method using the following cycles: 5 and 10 s at 2.46 V (polymerization time, t_p) and 2 s at -1 V (relaxing time, t_r). A representative scheme of the pulse polymerization is given in ***Figure A2.1***. The t_r was chosen in relation to the two t_p used, which should be less than t_p due to the possible delay time in starting the polymerization.[32] At t_p = 5 s, it was performed cycles of 4 and 16 repetitions, and for t_p = 10 s, cycles of 2 and 8 repetitions, to mimic the deposition time used to prepare the surfaces by galvanostatic method (20 and 80 s, respectively).

Figure 2.11 shows the SEM images for these surfaces. For t_p = 5 s, nanodomes structures were obtained after 4 cycles (t = 20 s) and some tubes with ∅ = 0.6 µm were obtained after 16 cycles (t = 80 s). Spheres with a micrometer size were formed for surfaces prepared using a t_p = 10 s for both repetitions cycles. However, for the longer deposition times, structures similar to the tree-like shape were found. The roughness results presented in **Table 2.4** are in agreement with the SEM images, showing that rougher surfaces are obtained for longer deposition times. In **Figure 2.12**, the wettability results showed a hydrophobic behavior (θ_w ~ 100º) for all surfaces prepared by pulse potentiostatic method independent of the t_p and the number of polymerization cycles. Here, the roughness did not have any influence. The conditions used to polymerize by pulse method seem to be not so harsh when compared with the galvanostatic method since no variation on the θ_w in **Figure 2.12**. A possible explanation is related to t_r which occurs at intervals of each 5 or 10 s and takes place during 2 s in the

polymerization cycle. The t_r in pulse deposition is the main parameter that affect the mechanism of particle growth.[32] Consequently, the t_r does not favor the formation of structures as compared with the surfaces obtained by the other methods, specially for galvanostatic deposition that uses the same deposition time, which presented a larger amount of structures on the surface.

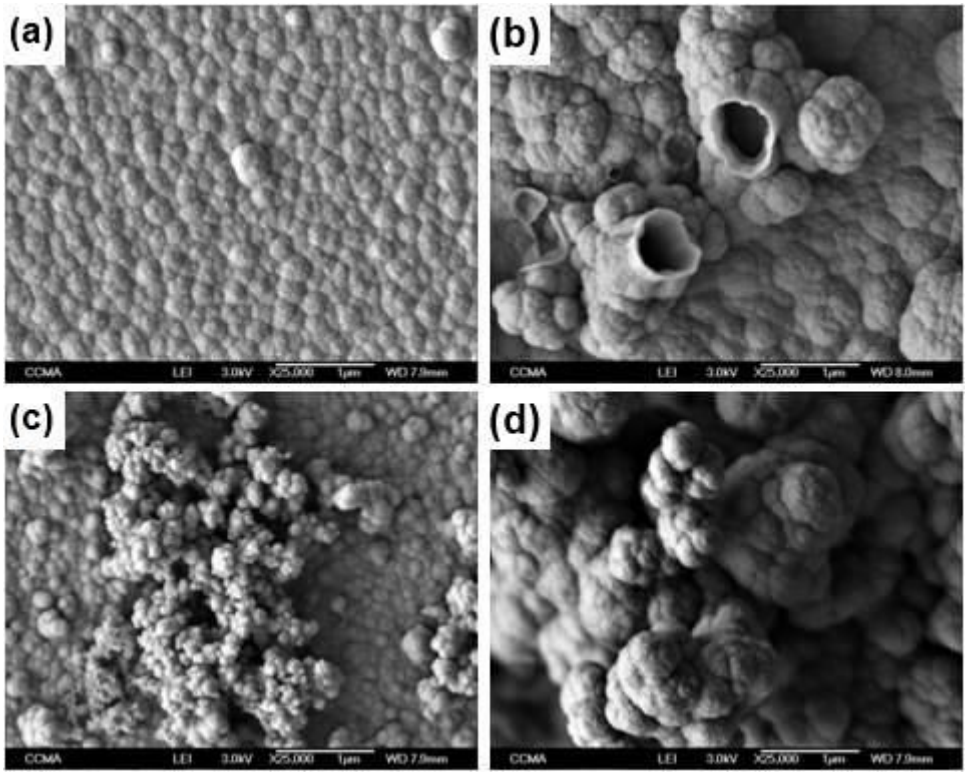

Figure 2.11. SEM images of PThienothiophene-2 electropolymerized by pulse deposition method at t_p = 5 s for a repetition of a) 4x (20 s) and b) 16x (80 s) and at t_p = 10 s for c) 2x (20 s) and d) 8x (80 s). Polymerization at 0.1 M solution of Bu_4NClO_4/dichloromethane. Relaxing time (t_r) = 2 s.

Table 2.4. Roughness data for PThienothiophene-2 electropolymerized by pulse deposition method as function of the polymerization time (t_p) and the number of repetitions/deposition time (s). Polymerization at 0.1 M solution of Bu_4NClO_4/dichloromethane. Relaxing time (t_r) = 2 s.

Polymerization time (t_p)	Repetition	Ra (nm)	Rq (nm)
5 s	4 x (= 20 s)	7.9	10.4
	16 x (= 80 s)	315.4	731.9
10 s	2 x (= 20 s)	80.2	657.2
	8 x (= 80 s)	358.9	1190.0

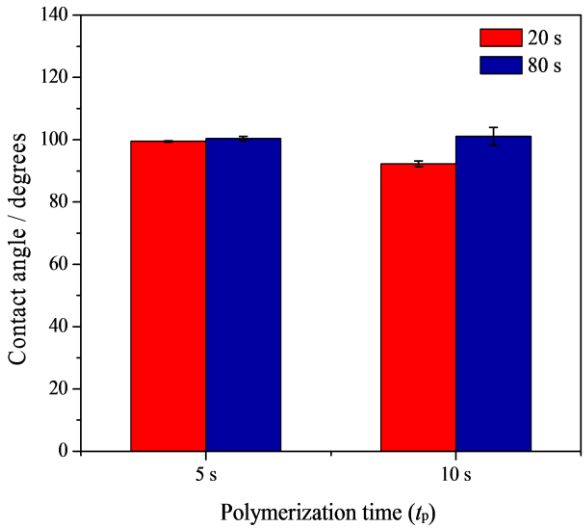

Figure 2.12. Apparent contact angle for water (θ_w) for PThienothiophene-2 electropolymerized by pulse deposition method as function of the polymerization time (t_p) and the deposition time (s). Polymerization at 0.1 M solution of Bu_4NClO_4/dichloromethane. Relaxing time (t_r) = 2 s.

Using t_p = 5 s, more repetition cycles (1, 8, 12, 20, 24, 28 and 32) were done in order to better understand the conditions of polymerization and how they can affect the surface structure and wettability. These results are presented in **Figure 2.13** and shows that the surfaces are hydrophobic (θ_w ~100º) for number of cycles increasing up to 24. Otherwise, for higher repetition cycles, θ_w drastically decreases which can be explained by the increase in roughness. In general, the roughness increases exponentially from cycle 1 to cycle 32. A limit between the surface wettability and roughness was achieved in 24 cycles where was obtained a hydrophobic surface with Ra ~ 1 µm. With higher number of repetition cycles, the roughness measures increased up to 4 µm decreasing θ_w to ~ 20º. These results showed that the increase in the roughness strongly impacts the surface wettability.

In comparison with the other methods which presented surfaces very structured, the surfaces produced by pulse deposition showed some differences during the polymerization process. The non-ordered structures for t_p = 10 s and the absence of structures for t_p = 5 s after 4 repetition cycles may be a consequence of the t_r which induces a pause in the polymerization. During the t_r = 2 s, the nucleation stops and restart in the new cycle. No references were found to indicate if the polymer growth also pauses during the t_r, but with the SEM images it seems to be more significant than the nucleation for pulse deposition surfaces. One possible explanation is the delay which may occur in restart the nucleation when the potential is applied during the t_p.

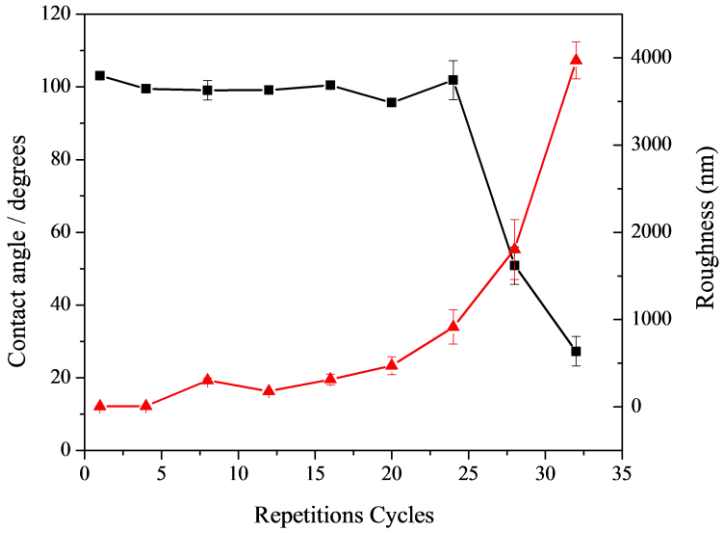

Figure 2.13. Apparent contact angle for water (θ_w) *vs* roughness data for PThienothiophene-2 electropolymerized by pulse deposition method as function of the repetition cycles at t_p = 5 s and t_r = 2 s. Polymerization at 0.1 M solution of Bu_4NClO_4/dichloromethane.

2.1.2. Influence of the Electrolyte

The choice of the electrolyte depends upon its solubility, degree of dissociation, nucleophilicity and its interaction with the monomer.[33] Quaternary ammonium salts are commonly used as electrolyte for the electropolymerization of conducting polymers and show good solubility in organic solvents and high electrochemical stability. A first work in our research group showed the huge influence of the electrolyte in the surface wettability and roughness of PEDOT surfaces.[34] Smooth and structured surfaces could be obtained by electropolymerization of thiophene derivative using eight different electrolytes.[1]

In this topic, two other electrolytes were tested to investigate their effect on the surface structures: tetrabutylammonium tetrafluoroborate (Bu_4NBF_4) and tetrabutylammonium hexafluorophosphate (Bu_4NPF_6). The electropolymerization was carried out using 0.1 M solution of anhydrous dichloromethane/electrolyte by constant potential and cyclic voltammetry because they showed the best results for the nanotubes formation. The SEM images for the polymer films made by constant potential are shown in **Figures 2.14** and **2.15** and the surface wettability and roughness in **Table 2.5**.

Using Bu_4NBF_4 as electrolyte, all the nanoseeds are formed in the first instance of the electropolymerization as observed with Bu_4NClO_4 by constant potential (**Figure 2.14**). Indeed, for Qs = 12.5 mC cm^{-2}, all the surface structures are nanoporous. Additionally, their ∅ ≈ 50-60 nm and height ≈ 100 nm are lower compared with those observed using

Bu_4NClO_4, which leads also to higher θ_w (126.0°). As Qs increases from 12.5 to 100 mC cm^{-2}, the diameter and the height of the surface structures increase, but the number of structures having their top open decreases and θ_w does not significantly change. For Qs = 100 mC cm^{-2} the height of the nanoplots is higher than that with Bu_4NClO_4. By contrast, for Qs > 100 mC cm^{-2}, the surface structures highly change from nanoplots to tree-like structures with a high increase of θ_w up to 137.9°. It is also possible to see the huge difference in the roughness for the high deposition charges. The tree-like structures formed yield a roughness 18 times higher than the roughness of the nanoseeds observed with Bu_4NClO_4 as electrolyte. Using Bu_4NBF_4, the structuration still clearly observed on the surface in opposition to the totally covered surface obtained using Bu_4NClO_4, after a charge of 400 mC cm^{-2} was applied.

Using Bu_4NPF_6 as electrolyte (**Figure 2.15**), the results are relatively similar than those observed with Bu_4NBF_4, but the porous structures close much faster between Qs = 12.5 and 25 mC cm^{-2}. Indeed, the tree-like structures are formed quickly (Qs = 50 mC cm^{-2}) than the surfaces produced with Bu_4NBF_4 (Qs = 100 mC cm^{-2}). However, the tree-like structures obtained after 400 mC cm^{-2} of imposed charge using Bu_4NPF_6 present almost the same roughness and height than those using Bu_4NBF_4, but a lower θ_w. This is the first time that it is reported the possibility to obtain not only arrays of nanotubes but also tree-like structures with a high θ_w and high water adhesion.

Table 2.5. Apparent contact angles for water (θ_w) and roughness data for PThienothiophene-2 electropolymerized by constant potential as a function of the electrolyte and the deposition charge. Polymerization at 0.1 M solution electrolyte/dichloromethane.

Electrolyte	Qs [mC cm^{-2}]	Ra [nm]	Rq [nm]	θ_w [deg]
Bu_4NBF_4	12.5	6.6	8.4	126.0
	25	7.0	9.9	126.4
	50	11.9	15.0	125.5
	100	30.0	38.2	126.7
	200	593.6	1046.3	137.9
	400	3137.3	4733.3	137.6
Bu_4NPF_6	12.5	7.1	9.1	119.7
	25	7.7	9.5	120.6
	50	23.8	30.0	121.8
	100	82.7	107.2	123.4
	200	323.2	503.1	123.5
	400	3436.7	5453.3	115.8

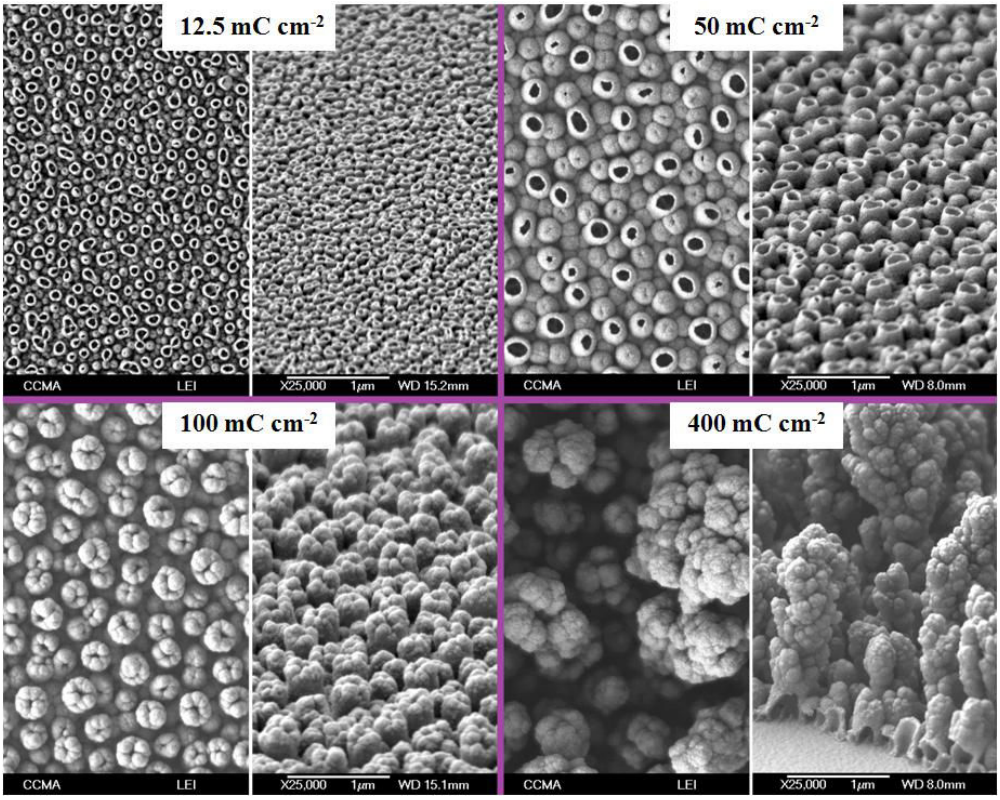

Figure 2.14. SEM images (flat and inclined at 60°) of PThienothiophene-2 electrodeposited at constant potential using different deposition charges in a solution 0.1 M Bu_4NBF_4/dichloromethane

.

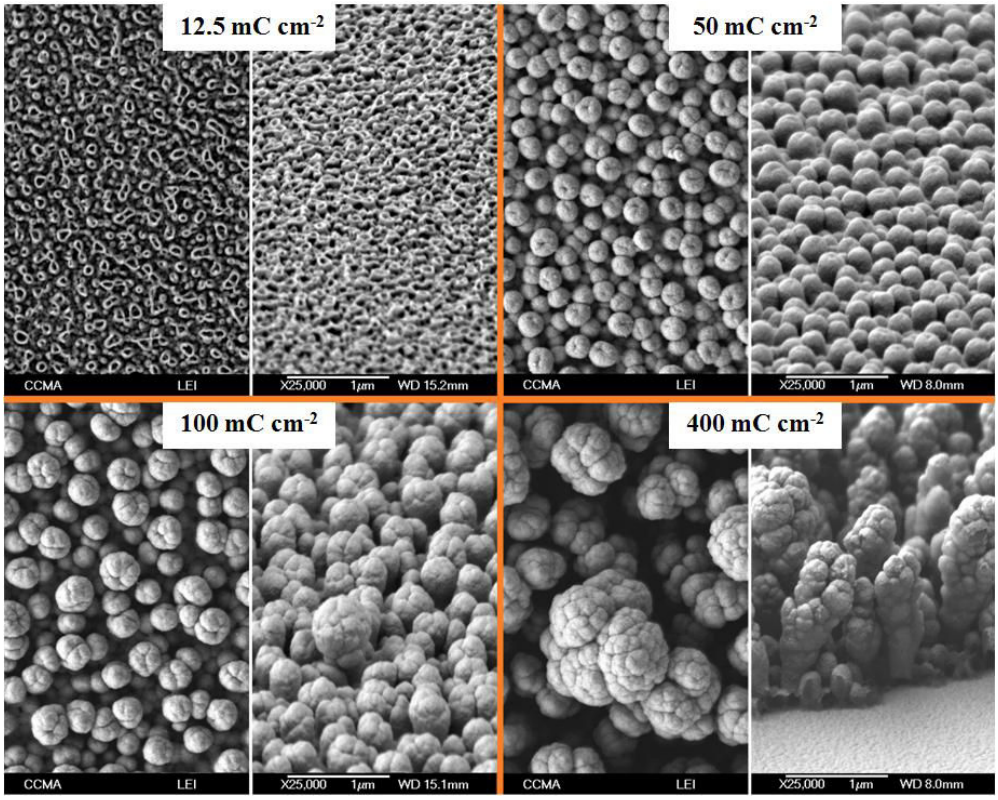

Figure 2.15. SEM images (flat and inclined at 60°) of PThienothiophene-2 electrodeposited at constant potential using different deposition charges in a solution 0.1 M Bu_4NPF_6/dichloromethane.

Tree-like structures are also obtained by cyclic voltammetry since the first scan using Bu_4NBF_4 and Bu_4NPF_6 as electrolytes (**Figure 2.16**). The surfaces present similar roughness with those obtained using Bu_4NClO_4, but, in opposition, an improvement in the wettability properties was achieved (**Table 2.6**). Indeed, highly hydrophobic surfaces were obtained with high water adhesion for both electrolytes by cyclic voltammetry, yielding parahydrophobic surfaces. It is commonly observed that structures similar to nanotubes or with a tree-like shape shown high water adhesion. Generally, the water penetrates in the space between the structures, but not inside them. In addition, as observed for constant potential, the growth of the structures is faster for Bu_4NPF_6 than for Bu_4NBF_4 as showed in the first deposition scan. However, since a large range of potential is used, it is difficult to control the amount of polymer deposited on the surface. Hence, the polymer growth is easily handled using the constant potential method than cyclic voltammetry. Nevertheless, both methods are effective to produce nanotubes and tree-like structures using this monomer.

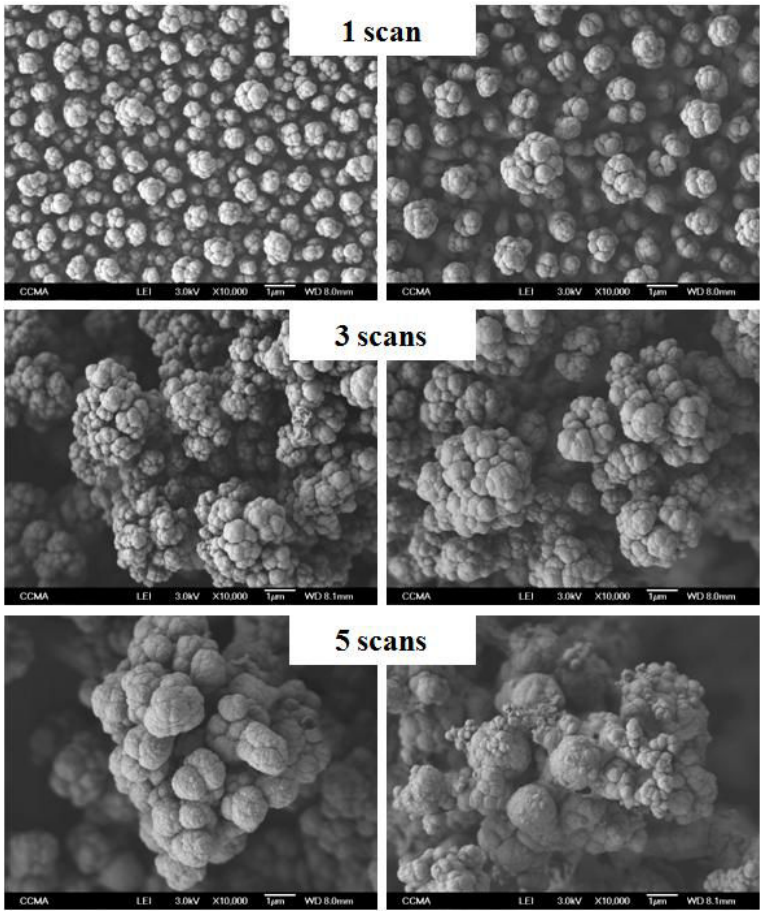

Figure 2.16. SEM images of PThienothiophene-2 electrodeposited at cyclic voltammetry using Bu_4NBF_4 (left) and Bu_4NPF_6 (right) as an electrolyte in solution 0.1 M of electrolyte/dichloromethane.

Table 2.6. Apparent contact angles for water (θ_w) and roughness data for PThienothiophene-2 electropolymerized by cyclic voltammetry as a function of the electrolyte and the number of scans. Polymerization at 0.1 M solution electrolyte/dichloromethane.

Electrolyte	Number of deposition scans	Ra [µm]	Rq [µm]	θ_w [deg]
Bu_4NBF_4	1	1,7	2,9	136,8
	3	6,3	7,9	146,8
	5	6,0	8,0	74,6
Bu_4NPF_6	1	1,9	2,9	129,5
	3	9,8	12,2	140,5
	5	18,2	22,0	142,1

2.1.3 Discussion about the mechanism of porous structures formation

Here, it is clear that the formation of porous structures is due to the formation of gas bubbles during the electropolymerization process. Several authors already reported the formation of porous structures during the electropolymerization of pyrrole in water and using surfactants.[7–9] They observed that O_2 and H_2 bubbles can be formed from water following the used potentials during the electropolymerization process. In our work, anhydrous dichloromethane is used as solvent but it is impossible to remove completely "trace" water. For example, it is known that trace water can be absorbed on glass substrates and indeed we used a glass electrochemical cell and also a glass electrode (SCE) for our experiments. Otherwise, H_2 bubbles may also be formed from H^+ ions released during the electropolymerization process.

In order to evaluate the effects of either water or H^+ ions, firstly 0.5 % of water was added in the experiments. Because the solubility of water in dichloromethane is extremely low, the concentration could not be higher. It was observed an increase of the porosity of the structures both by cyclic voltammetry and at constant potential (**Figure 2.17**). For example, at constant potential and after adding 0.5 % of water, the diameter of the nanoporosities increases from 120-130 nm to 180-200 nm for Qs = 12.5 mC cm^{-2} and from 180-200 nm to 310-330 nm for Qs = 50 mC cm^{-2}. Moreover, the number of structures having their top open is also more important. Indeed, the nanotubes formed by cyclic voltammetry present a $\varnothing \approx 0.5$ µm and after the addition of 0.5% of water, $1 < \varnothing < 5$ µm. It seems that the water content plays a very important role on the formation of surfaces structures.

In order to evaluate also the effect of H^+ ions, 1 % $HClO_4$ (70 % in water) was used. Here, we clearly see in the SEM images (**Figure 2.18**) that the presence of H^+ ions has a negative impact for the formation of porous structures, both by cyclic voltammetry and constant potential. For example, at constant potential only some nanorings are observed for Qs = 12.5 mC cm^{-2}. For higher Qs, spherical nanoparticles were formed on the surface. The same morphological behavior was observed by cyclic voltammetry.

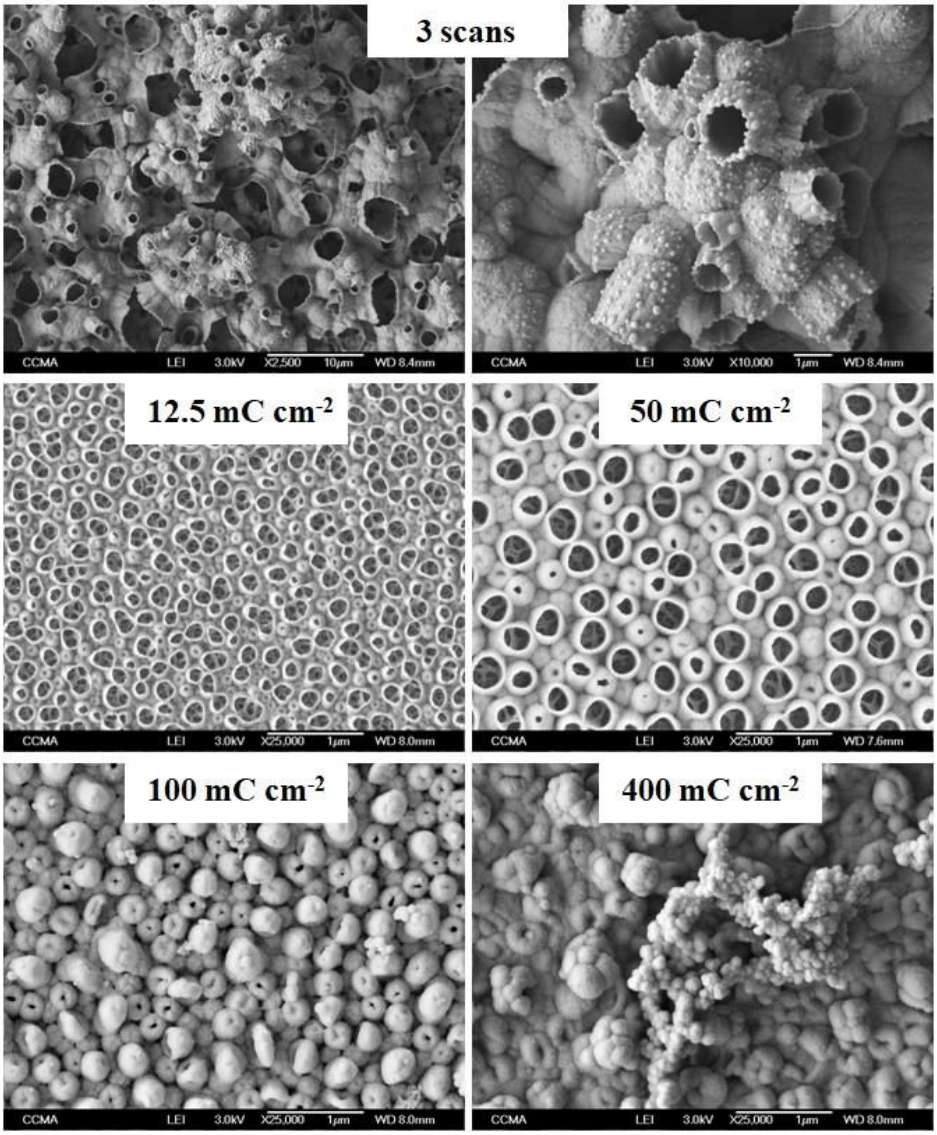

Figure 2.17. SEM images of PThienothiophene-2 electrodeposited by cyclic voltammetry (3 scans) and by constant potential in Bu_4NClO_4/dichloromethane + 0.5 % water.

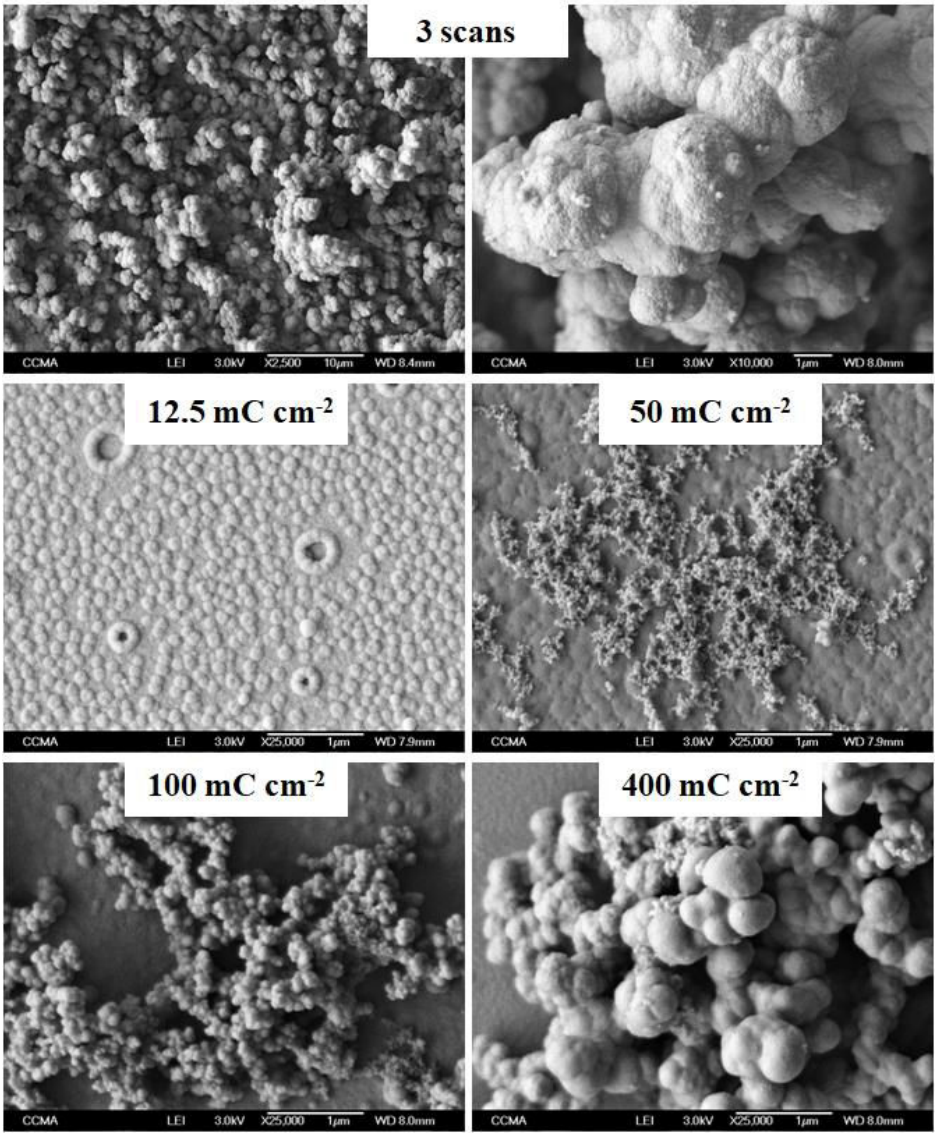

Figure 2.18. SEM images of PThienothiophene-2 electrodeposited by cyclic voltammetry (3 scans) and by constant potential in Bu_4NClO_4/dichloromethane + 1 % $HClO_4$.

Hence, we can now conclude that it is well the water content, which acts on the structure porosity and not the H^+ ions. The mechanism proposed for the nanotubes formation is the following:

- At high potential around 2.0–2.5 V *vs* SCE (at cyclic voltammetry, constant potential, galvanostatic deposition and pulse deposition):

  $$\mathbf{n\ Monomer \rightarrow Polymer + 2\ ne^- + 2\ nH^+}$$

  $$\mathbf{2\ H_2O \rightarrow O_2\ (bubbles) + 4\ H^+ + 4\ e^-}$$

- At low potential around -0.5 V *vs* SCE (only by cyclic voltammetry and pulse deposition):

  $$\mathbf{2\ H^+ + 2\ e^- \rightarrow H_2\ (bubbles)}$$

At constant potential, the porous structures are highly ordered because the polymerization and the formation of O_2 bubbles occurred at the same time. Only trace water can explain the formation of gas bubbles at constant potential. This is also the case by galvanostatic deposition.

As a consequence, it is not surprising to have increased density of porous structures by cyclic voltammetry and pulse deposition than at constant potential and galvanostatic deposition because both O_2 and H_2 bubbles could be produced if the potential range is sufficiently important. In opposition, only O_2 bubbles could be produced at constant potential and galvanostatic deposition. By cyclic voltammetry, the structures are more porous, but disordered because of the evolution of H_2 bubbles which can also damage the polymer films already formed. However, by pulse deposition method the porous structures can only be formed at high potentials during the oxidation of the monomer. During the t_r, a potential of -1 V is applied which is lower than the potential where occurs the formation of H_2 bubbles (around -0.5 V). The formless structures produced by pulse deposition can be explained by the instantaneous application of the high pulse potential (t_p) or low pulse potential (t_r) which differs from cyclic voltammetry by scanning a range of potential (from -1 V to 2.46 V).

In order to characterize these surfaces, the wettability and roughness data are presented in **Tables 2.7** and **2.8**. The nanotubes formed by the addition of 0.5% and 1 % $HClO_4$ showed that both method or solvent have a significant influence not only in the morphology, but also in wetting behavior.

Table 2.7. Apparent contact angles for water (θ_w) and roughness data for PThienothiophene-2 electropolymerized by cyclic voltammetry as a function of the solvent and the number of scans. Polymerization at 0.1 M solution Bu_4NClO_4/solvent.

Electrolyte	Number of deposition scans	Ra [nm]	Rq [nm]	θ_w [deg]
DCM + 0.5% water	1	380.0	1300.0	126.6
	3	9700.0	16500.0	65.5
	5	7500.0	13500.0	38.9
DCM + 0.5% $HClO_4$	1	708.0	3130.0	110.3
	3	7603.3	12740.0	103.0
	5	8956.7	14400.0	67.1

Table 2.8. Apparent contact angles for water (θ_w) and roughness data for PThienothiophene-2 electropolymerized by constant potential as a function of the solvent and the deposition charge. Polymerization at 0.1 M solution Bu_4NClO_4/solvent.

Polymer	Qs [mC cm^{-2}]	Ra [nm]	Rq [nm]	θ_w [deg]
DCM + 0.5% water	12.5	8.4	10.6	123.0
	25	9.1	11.4	120.1
	50	22.2	30.7	26.3
	100	69.7	90.1	27.9
	200	357.6	1200.0	19.4
	400	454.3	2600.0	15.7
DCM + 0.5% $HClO_4$	12.5	13.4	28.7	82.2
	25	17.0	46.9	72.7
	50	29.7	49.5	0.0
	100	97.0	274.1	0.0
	200	74.9	496.3	0.0
	400	2936.7	8656.7	0.0

2.1.4 Discussion about the wettability results

To understand the wetting behavior obtained for the surfaces, the apparent contact angles for smooth surfaces of the same polymer, also called the Young angle (θ^Y), were studied. To probe this, analogue smooth surfaces for the thienothiophene monomers were formed at a constant potential and using low deposition charge (1 mC cm^{-2}) followed by a reduction step using cyclic voltammetry from 1.5 V to -1 V.

Roughness measurements were presented in **Table 2.9** and confirm their ultra-low roughness (Ra = 6.3 – 6.6 nm). **Table 2.9** also showed the wettability results for thienothiophene the analogous smooth surfaces. These θ^Y_w showed that all the polymers are intrinsically hydrophilic with $\theta^Y_w << 90°$. Moreover, θ^Y_w is quite similar for all the studied polymers (65-75°). Two models are often used to explain the wetting properties of rough surfaces using the θ^Y: Wenzel and Cassie-Baxter.[35,36] To follow Wenzel equation, the roughness parameter r increases θ only if $\theta^Y > 90º$ (intrinsically hydrophobic materials) but decreases θ if $\theta^Y < 90º$ (intrinsically hydrophilic materials). However, using the Cassie-Baxter equation is possible to increase θ if $\theta^Y < 90º$. The Cassie-Baxter equation can predict extremely high θ with low adhesion (superhydrophobic properties) if the air fraction is extremely important, but also extremely high adhesion (parahydrophobic properties) if the solid fraction is more important.

Table 2.9. Apparent contact angles of water (θ_w) and roughness data for the smooth corresponding polymers. Polymerization at 0.1 M solution Bu_4NClO_4/dichloromethane.

Polymer	Ra [nm]	θ^Y_w [deg]	θ^Y_{diodo} [deg]	θ^Y_{hexa} [deg]	γ_{SV} [mN m^{-1}]	γ^D_{SV} [mN m^{-1}]	γ^P_{SV} [mN m^{-1}]
PThienothiophene-1	6.5	66.7	23.4	0	46.5	36.5	10.0
PThienothiophene-2	6.5	70.4	27.1	0	44.3	35.9	8.3
PThienothiophene-3	6.3	73.1	27.5	0	43.0	35.9	7.1
PThienothiophene-4	6.6	67.2	25.0	0	46.1	36.3	9.8
PThienothiophene-5	6.4	67.3	23.6	0	46.2	36.5	9.7

Hence, the parahydrophobic properties of the nanotubes can be explained by the presence of a composite interface. As the polymer is intrinsically hydrophilic, the water droplet should penetrate into the spaces between the nanotubes (Wenzel state) which highly increases the water adhesion, but not penetrate inside the nanotubes (Cassie-Baxter state), as shown in **Figure 2.19**. As a consequence, it is easy to demonstrate that the parahydrophobic properties are highly dependent on the diameter and height of the nanotubes as well as the distance between them. The parahydrophobic properties of the tree-like structures can also be explained if the fractal roughness of the structures impedes their full wetting. In consequence, the Wenzel equation predicts the superhydrophilic and hydrophilic properties by galvanostatic when the water droplet penetrates into the surface roughness leading to a large solid-liquid interface. By contrast, the hydrophobic properties of the surfaces produced by pulse deposition can be explained by the presence of a composite state, because when the surface wet, water partially penetrates between the structures, but not into them.

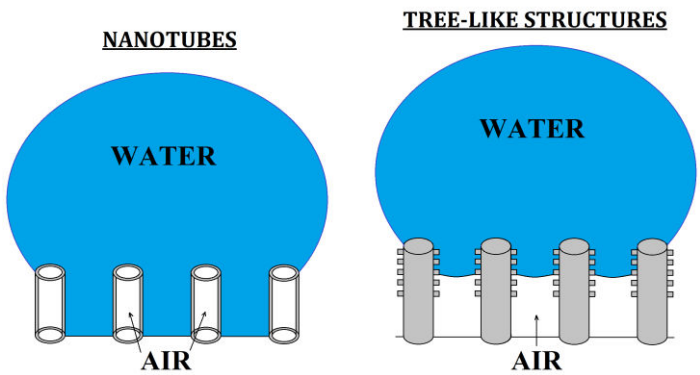

Figure 2.19. Schematic representation of a water droplet deposited on intrinsically hydrophilic nanotubes and tree-like structures.

2.2 STUDY THE EFFECT OF THE SUBTITUENTS

This section is dedicated for the discussion about the influence of the introduction of different families of substituents in thienothiophene core. The incorporation of substituents with different surface energies on the monomer before the electropolymerization is a way to achieve a range of surface wettability and varied morphologies. Bellanger et al showed that the use of dodecyl spacers between the EDOP core and the fluorinated substituents yield surfaces with superhydrophobic and highly oleophobic properties.[28] Using the same monomer core, parahydrophobic surfaces were achieved with a very different morphology when aromatic substituents were used.[37] Using ProDOT as a model core, different wettabilities and surface roughness were also reported.[14,38,39] Alkyl and aromatic chains were grafted in 3,4-phenylenedioxythiophene (PhEDOT) and showed a huge impact in the morphology yielding very smooth or completely structured surfaces by electropolymerization process.[40] The introduction of different substituents can lead to the formation of a wide range of wettability and morphology interfering in the final properties of the surfaces.

In this section, we will present the synthesis of 12 monomers derived from thieno[3,4-*b*]thiophene. The choice of this monomer core was made in order to find a favorable synthetic route to obtain a library of thienothiophene derivatives containing different substituents. Indeed, we searched in the literature for a monomer core as close as possible of thieno[2,3-*b*]thiophene and thieno[3,2-*b*]thiophene, the monomers which yield the best results concerning about the formation of nanotubes and their wetting and morphological properties presented in the first part of this chapter (*Section 2.1*). We found in the literature the possibility to synthesize thieno[3,4-*b*]thiophene, the third thienothiophene analogous, with the introduction of different substituents. The monomers synthesized in this section are summarized in **Scheme 2.2**. They were polymerized via the same electrochemical process and their surface wettability and morphology were investigated. The results are detailed in the following parts.

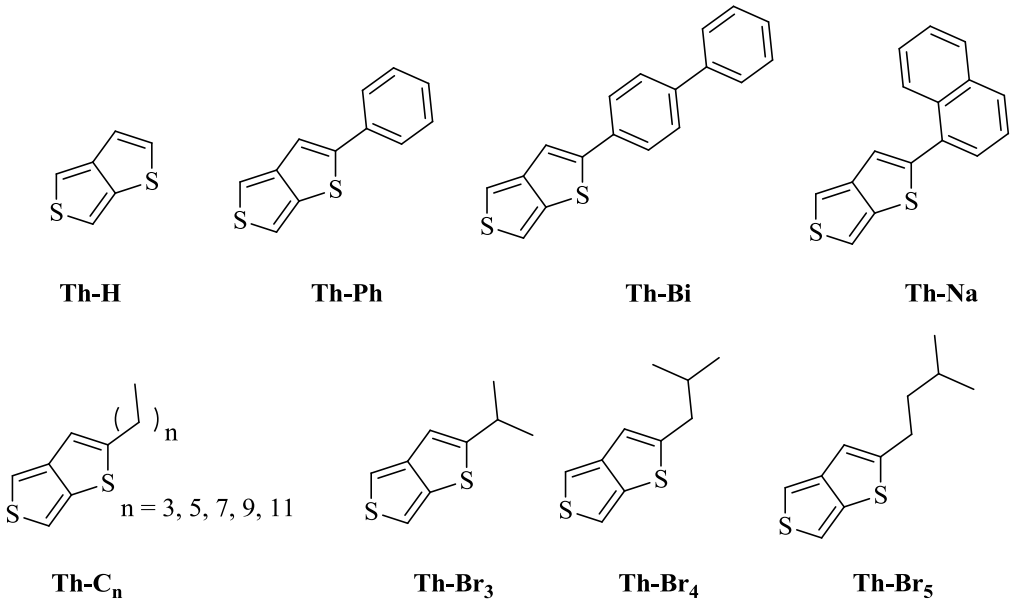

Scheme 2.2. Monomers synthesized and studied in this section.

2.2.1 Monomer Synthesis

The synthesis of the thieno[3,4-*b*]thiophene derived monomers was adapted from procedures reported in the literature.[41–43] The monomers were synthesized by a two-steps synthesis starting from a Sonogashira coupling followed by a second step of cyclization (**Scheme 2.3**). The detailed procedure and the monomers characterization by proton and carbon NMR spectroscopy (^{1}H and ^{13}C NMR) are reported in the ***Annex A1.1***.

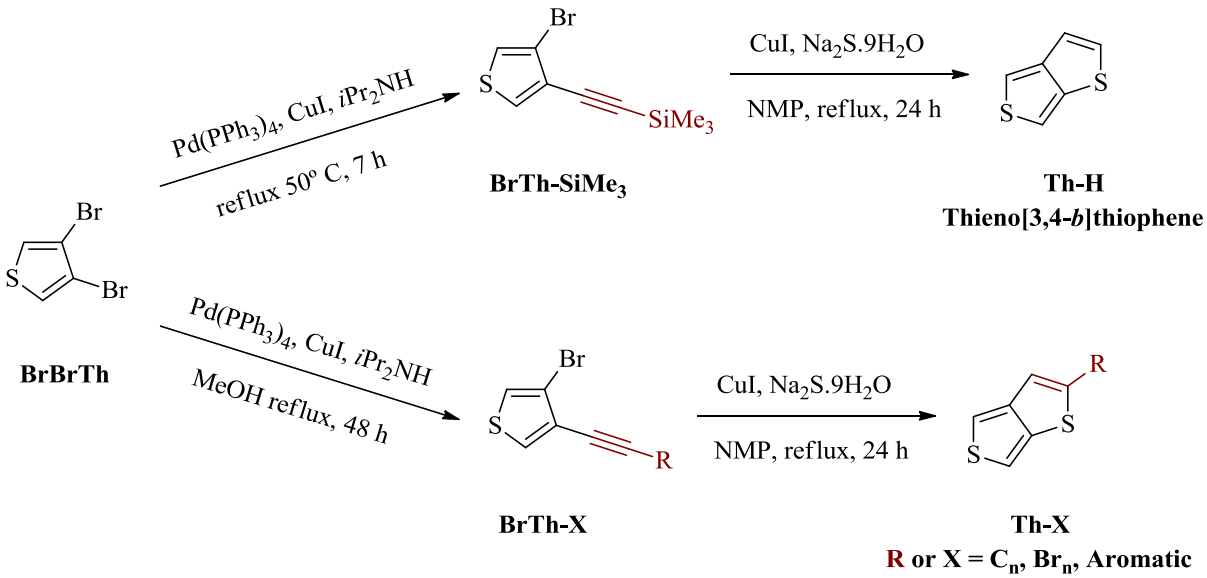

Scheme 2.3. Synthesis pathway to the thieno[3,4-*b*]thiophene derivatives.

2.2.2 Electrochemical Polymerization and Surface Characterization

After synthesis, each monomer was polymerized by cyclic voltammetry in a 0.1 M solution of Bu_4NClO_4 in anhydrous dichloromethane at 20 mV s^{-1}. This method was chosen because yield surfaces with good wetting properties and it was favorable to form nanotubes. Indeed, this method allows the study of the electrochemical properties of each monomer which showed to be important to understand the mechanism of nanotube formation.

The cyclic voltammograms are displayed in **Figure 2.20**. All the thienothiophenes polymerized perfectly presenting clear oxidation and reduction peaks. Several oxidation and reduction peaks were observed during the polymerization of monomers bearing the longer alkyl chains and aromatic substituents. Despite of, all the voltammograms indicate a significant polymer growth throughout the electropolymerization. However, these peaks are reduced after the first deposition scan for the aromatic monomers Th-Na and Th-Bi which reveal a reduced polymer growth compared with the others. These results are expected because the aromatic substituents can highly reduce the electronic availability and as a consequence limit the polymerization. They also induce high steric hindrance.

A peak at around -0.5 V in the back scan was also observed for all the voltammograms. As explained before, this peak may indicate the formation of H_2 from trace water during the electropolymerization which has been shown to possible lead to the nanotubes formation. Throughout the electropolymerization by cyclic voltammetry, gas bubbles were formed and act as a template to form the nanotubes on the surface during both high and low potential. However, the formation of nanotubular structures is also highly dependent of the monomer used which should be able to stabilize the gas bubbles formed during the electropolymerization.

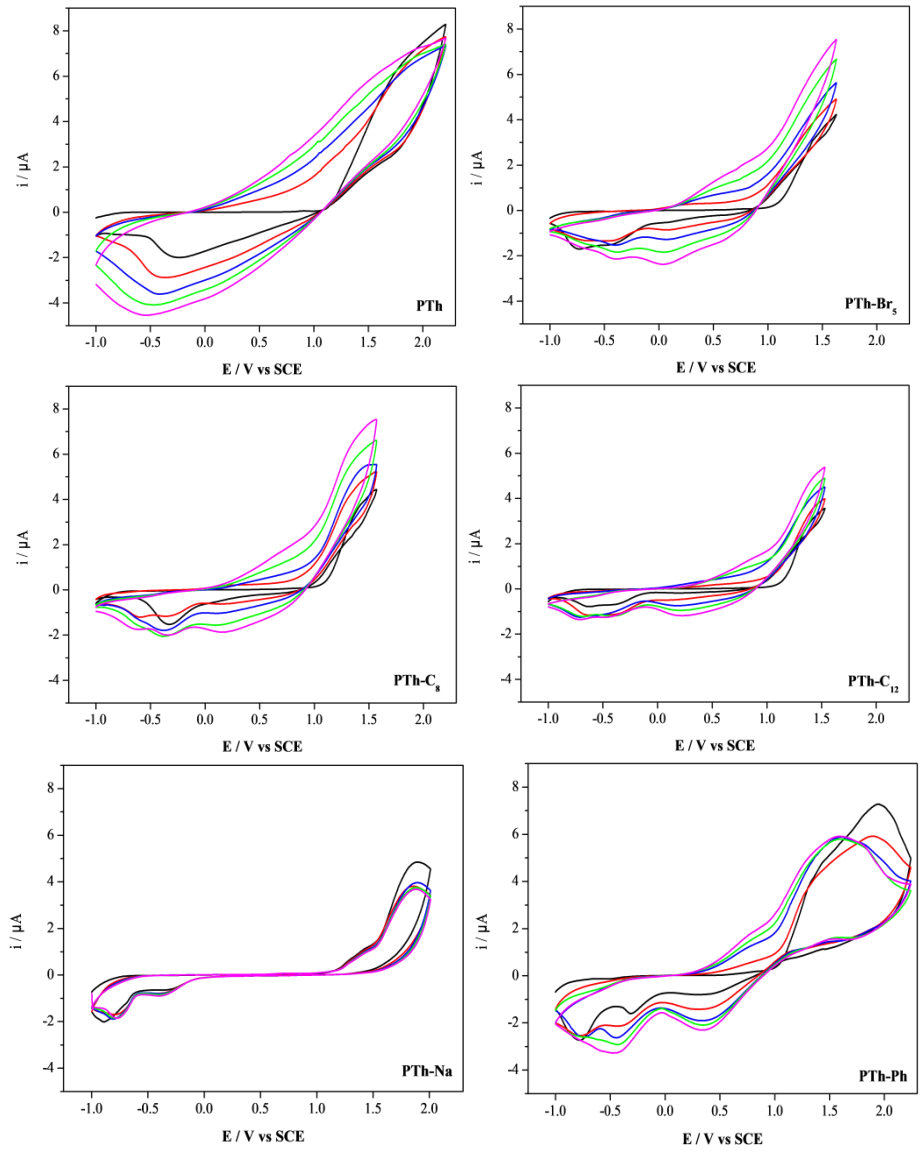

Figure 2.20. Cyclic voltammograms of the thienothiophene derived monomers in 0.1 M Bu_4NClO_4/ dichloromethane at a scan rate of 20 mV s^{-1}. Scan 1 = black line, Scan 2 = red line, Scan 3 = blue line, Scan 4 = green line and Scan 5 = magenta line.

These results are all supported by the SEM images collected of these surfaces (**Figures 2.21** and **2.22**). The morphology of PTh-H is mainly composed by spherical particles (∅ = 1 – 1.5 µm) and it is very similar to the morphology found for PThienothiophene-5 as show **Figure 2.3**. The thienothiophene cores showed to be very versatile yielding different surface structures depending on the monomer rigidity and the solubility.

For the molecules grafted with the linear alkyl chain, few and dispersed nanotubes (∅ = 1 µm) were observed on the surface for PTh-C_4. Upon a closer observation, PTh-C_6 showed few and very slight beginning of nanotubes formation by the appearance of some concave

structures which may indicate the presence of gas bubbles during the polymerization. However, as the alkyl substituent increase in length, rough surfaces are obtained, but with no structuration. Only after a further increase in the alkyl chain to PTh-C_{12}, extremely large wrinkles are observed. A possible explanation is the solubility of the polymer that may be lower for Th-C_{12} than for Th-C_{10} and Th-C_8.

Regarding the structures of the monomers with the branched alkyl chain in **Figure 2.22**, very different results can be seen. All the polymer surfaces presented higher structuration comparing to those formed with linear alkyl chain. For the shortest branched chain, PTh-Br_3, a sphere-like structure, similar to PTh-H, was observed, although with smaller particle sizes (∅ ~ 0.3 µm). Increasing the chain length, prominent differences are observed. For PTh-Br_4, large and well ordered spheres with ∅ = 2 µm were formed while for PTh-Br_5 hollow spheres could be seen. It seems that in a first instance, spheres similar to those present in the surface of PTh-Br_4 were formed for PTh-Br_5 during the electropolymerization; however, they seem to wither with the progress of the reaction. This process could have happened during the polymerization (oxidation and/or reduction step) or even when the sample was removed from the electrochemical cell (and consequently, from the solution).

Looking upon the aromatic-substituted monomers in **Figure 2.22**, highly interesting structures are observed. While for the phenyl-substituent the surface is mainly composed by spheres, nanotubes with ∅ = 0.5 µm were formed using the naphthyl-substituted monomer (PTh-Na). It is not surprising to yield nanotubes structures using this aryl group. In the literature, Szczepanski and co-authors also showed that naphthyl-substituent is favorable to form nanotubes on the structures even using different electropolymerization conditions.[40] They presented the synthesis and electropolymerization of various PhEDOT derivatives yielding different types of structures and this aromatic group was the unique to afford the formation of nanotubular structures. Here, quite similar structure of PTh-Na was obtained for PTh-Bi, with a couple of hollow nanotubes. These structures may also have wilted during the electropolymerization process. The absence of nanotubes in many surfaces highlighted the importance of the monomer structure in the electropolymerization process.

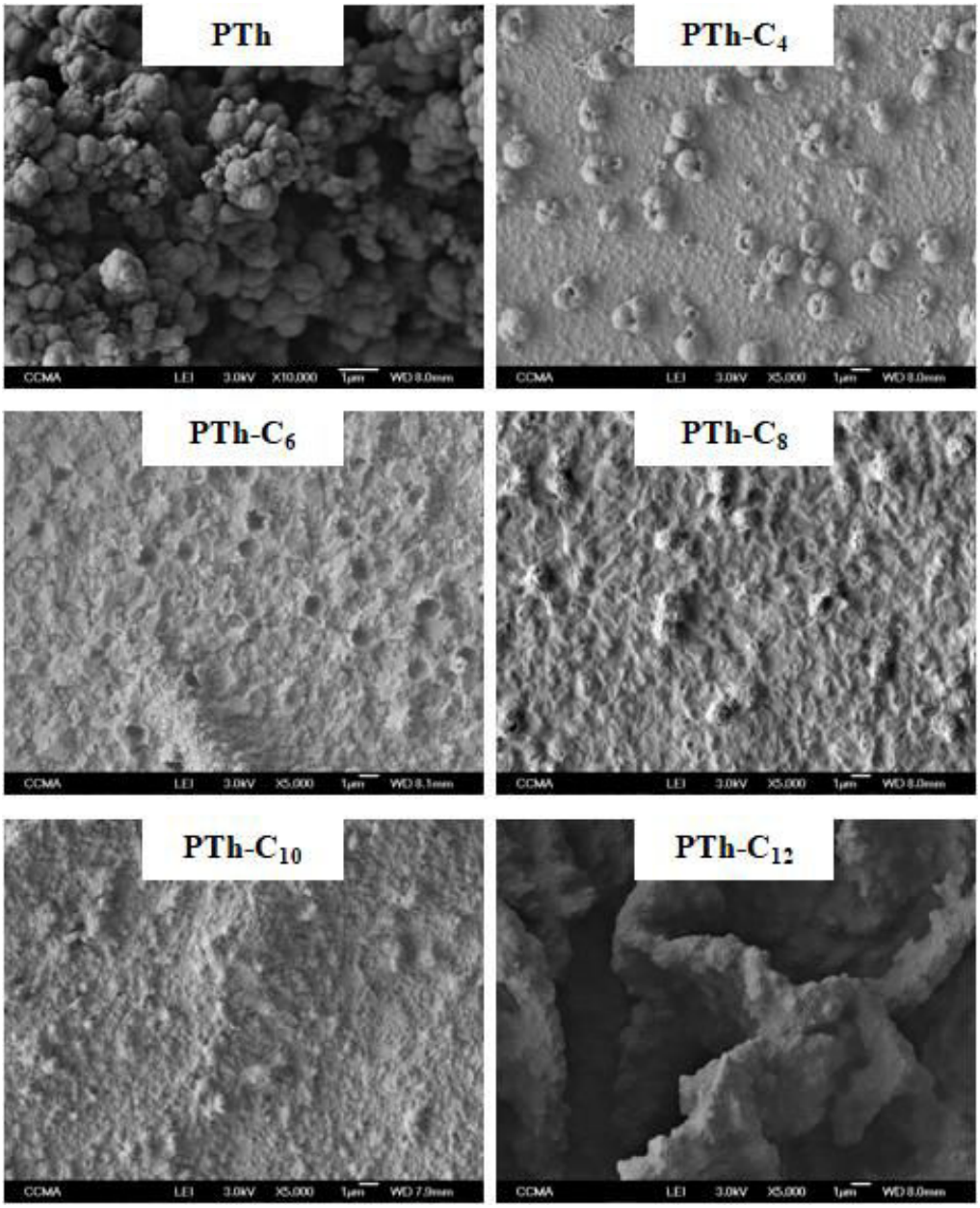

Figure 2.21. SEM images of the PTh-H and the linear-substituent polythienothiophenes electrodeposited by cyclic voltammetry (3 scans) in a 0.1 M solution of Bu_4NClO_4/dichloromethane.

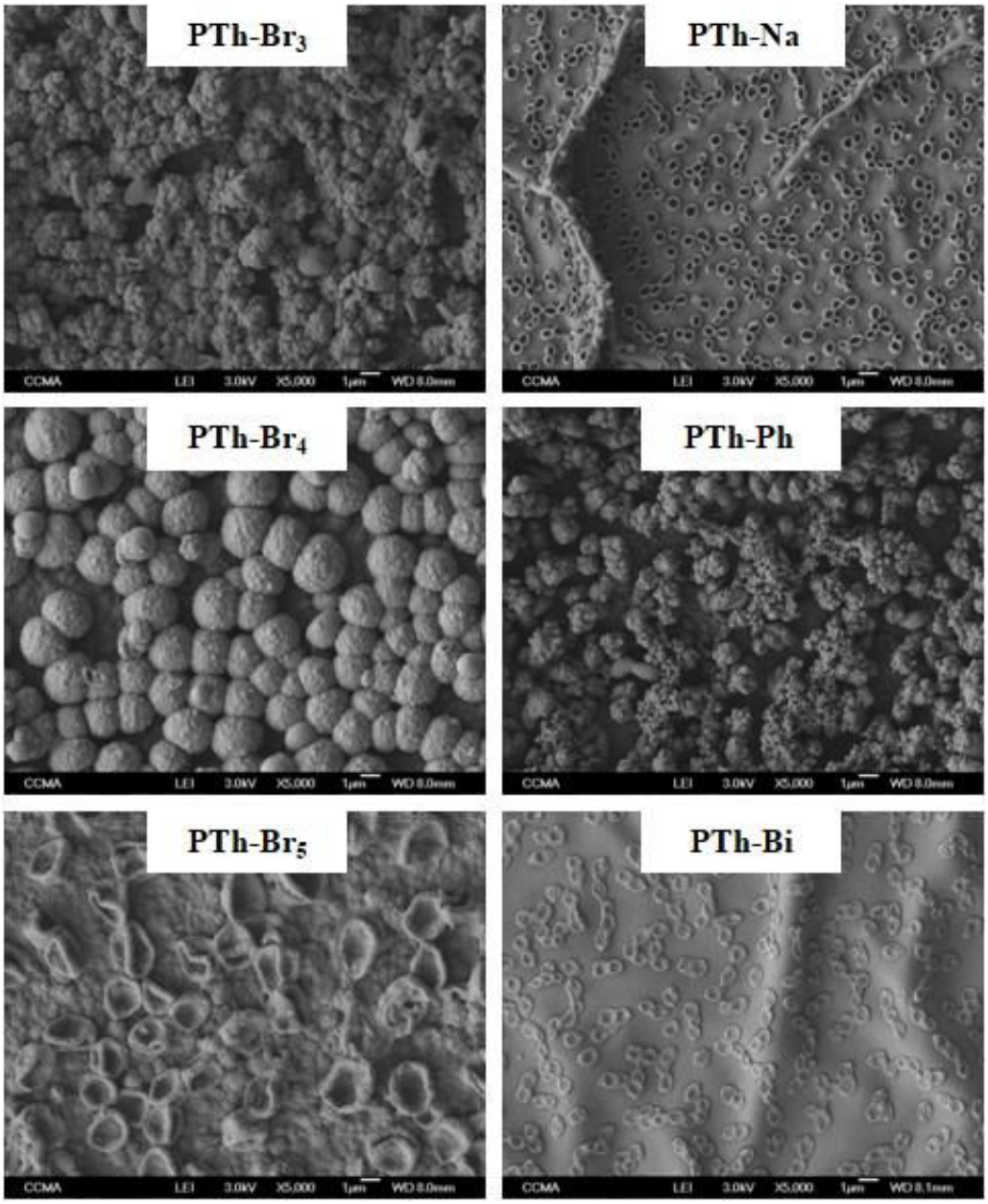

Figure 2.22. SEM images of the branched- and aromatic-substituent polythienothiophenes electrodeposited by cyclic voltammetry (3 scans) in a 0.1 M solution of Bu_4NClO_4/dichloromethane.

Figure 2.23 shows the evolution of the morphology of PTh-Na surfaces after 1, 3 and 5 deposition scans from different perspectives (flat and inclined surfaces). In these images, it is very clear the formation of nanotubes after the electropolymerization independently of the number of scans. Upon a closer observation, a slight decrease in the density of nanotubes was observed on the surface increased the number of scans. Indeed, a slight increase in the porosity of nanotubes was observed when the number of deposition scans increases to 3 and 5. The porosity increased from ∅ ~ 0.4 µm after 1 deposition scan to ∅ ~ 0.6 µm and ∅ ~ 0.7

µm after 3 and 5 deposition scans, respectively. However, the number of deposition scans does not influence the thickness of the shell structure as well as the shape of the tubes. All deposition scans showed well-defined and distributed top open nanotubes on the surface. Indeed, the height of the nanotubes does not change significantly with the number of scans.

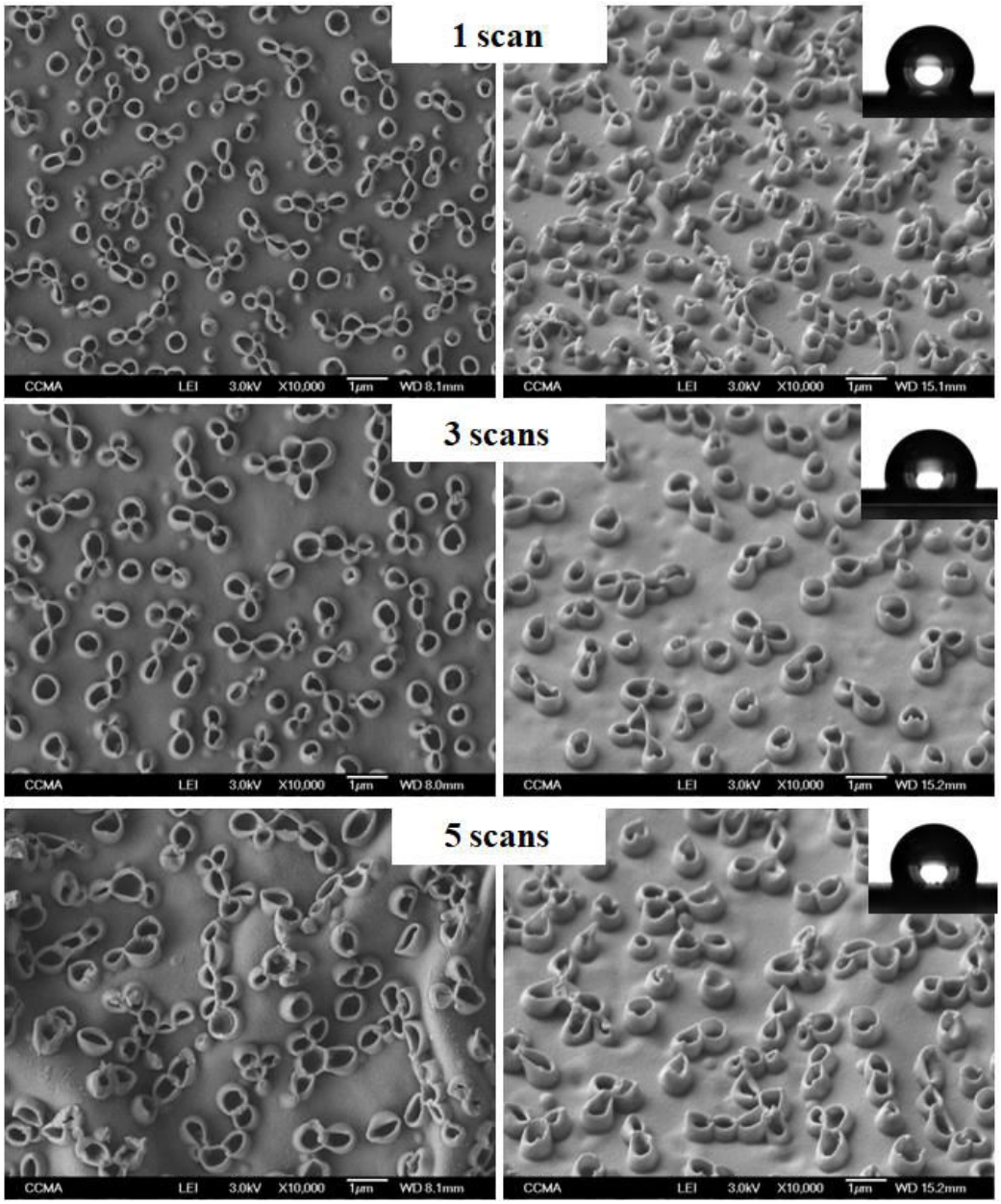

Figure 2.23. SEM images (flat and inclined at 45º) of PTh-Na electrodeposited by cyclic voltammetry in Bu_4NClO_4/dichloromethane for different number of scans.

The roughness data is presented in **Table 2.10**. Many correlations can be done with the SEM images. As a tendency, rougher surfaces are obtained with the increasing in number of scans. Additionally, the surface roughness seems to be similar in each family of monomers (aryl,

linear and branched alkyl chains). The PTh-H presents the highest roughness for all the thienothiophenes studied here while the two aromatic-substituted PTh-Na and PTh-Bi presented the lowest measures. This result for the aromatic-substituents was already expected due to the voltammograms in **Figure 2.20** which showed a reduction in the oxidation and reduction peaks after the first scan. It induces a decrease of the polymer growth during the electropolymerization process and, consequently, a lower roughness.

The surface wettability was also evaluated and these results are also shown in **Table 2.10**. As observed for the roughness data, the group of families also presented a similar wettability of their parents with few exceptions. Generally, the surfaces showed a hydrophobic behavior. PTh-H showed the greatest θ_w after 3 deposition scans for all the polymers studied in this section. The linear alkyl chains showed a θ_w ~ 110 – 140º with a highest θ_w for the shortest alkyl chain lengths. Indeed, 3 deposition scans presented the highest θ_w for PTh-C_4 and PTh-C_6 surfaces while for PTh-C_8, PTh-C_{10} and PTh-C_{12} θ_w decreases with the number of scans due to the increase in the surface roughness. For the aromatic and branched substituents, similar water wettability was observed. Nevertheless, PTh-Na showed a slight decrease in θ_w with higher number of scans due to the increase of the nanotubes porosity. The wettability is governed normally by two parameters: chemical composition and surface roughness. For the PTh-Na is the second parameter that affect the water wettability.

Using diiodomethane as a probe liquid, it is not surprising to get surfaces totally wet for the electrodeposited thienothiophenes such as obtained for PTh-H and the molecules containing aromatic substituents. The spherical structures mainly formed for PTh-H and the nanotubes by the PTh-Na, for example, promote the presence of air inside these structures, which may be replaced when in contact with diiodomethane due to it higher density. This behavior leads to an increase in the surface wettability and it was also observed for the thienothiophenes presented in *Section 2.1* of this chapter. This phenomena was already reported for the PhEDOT derivatives, for example.[40] However, in opposition to all other studies using thiophenes derivatives in surface science, for branched and linear alkyl chains it was possible the measure the oleo-wetting properties. An oleophilic behavior was observed for almost all the surfaces. It is clear the decrease of the θ_{diiodo} with the number of scans for the three branched-substituents due to the changes in the morphology. For PTh-Br_3, the presence of spherical nanoparticles favors the surface to become wet as already observed for other monomers yielding similar structures.[27] However, for the linear alkyl chains the wettability is

quite similar independently of the number of scans and higher θ_{diiodo} were found for longer alkyl chains. For PTh-C_{12} after 5 deposition scans, an oleophobic behavior was reached with θ_{diiodo} ~ 95º.

The wetting properties can be better explained by considering the inherent hydrophobicity/hydrophilicity of each polymer by the evaluation of the analogous smooth surfaces given by the θ^Y. The characterization of the smooth surfaces and the surface energy data are presented in **Table 2.11** and the comparison between the wettability of the smooth and the structured surfaces is given in **Figure 2.24**. All the monomers form very smooth surfaces as indicated by the roughness data (Ra = 7.1 – 9.6 nm). PTh-H showed to be the most hydrophilic polymer (θ^Y = 73º) and the θ^Y is in agreement with the data for the other thienothiophene cores presenting θ^Y = 67 – 73º (**Table 2.9**). With the introduction of different families of substituents, an increase in the θ^Y was obtained, but in general all presented θ^Y < 90º. In opposition, PTh-C_{12} and PTh-Bi are considered intrinsically hydrophobic due to θ^Y > 90º for the alkyl chain and θ^Y ~ 90º for the aromatic chain. It should be noted that all the polymers are intrinsically oleophilic as θ^Y_{diiodo} < 90º in all cases. The polymerization of PTh-Br_3 and PTh-H yield the most dramatic changes in θ_w from the inherent θ^Y, increasing θ_w in ~ 70º each surface due to the surface structuring as shown in **Figure 2.24**. PTh-C_{12} showed the lowest difference between the smooth and structured surfaces after 1 and 3 scans (~ 5º -13º). These molecules with long apolar alkyl chains are known to have very high θ^Y. In opposition of all polymers, PTh-Br_5 showed a negative effect of the morphology on the wetting results, since $\theta^Y > \theta_W$.

Hence, the wettability of the surfaces most likely follows a combination of both Wenzel and Cassie-Baxter regimes due to parahydrophobic surfaces obtained for the thienothiophenes. The water droplet should penetrate in the spaces between the structures (nanotubes or nanospheres) following the Wenzel regime. This process increases the water adhesion between the liquid and solid interface. However, the water droplets should not penetrate inside the structures as predict Cassie-Baxter, leading to a composite parahydrophobic state as represented in **Figure 2.19**.

Table 2.10. Apparent contact angles of water (θ_w) and roughness data as a function of the polymer and the number of deposition scans of the substituent-derivatives of thienothiophenes. Polymerization at 0.1 M solution Bu_4NClO_4/dichloromethane.

Polymer	Number of deposition scans	Ra [nm]	Rq [nm]	θ_{water} [deg]	θ_{diiodo} [deg]
PTh	1	647.1	2030.0	122.0	0
	3	7983.3	12886.7	142.5	0
	5	13965.0	18925.0	141.5	0
PTh-C_4	1	10.2	19.9	83.8	45.4
	3	1208.0	2595.0	124.5	53.1
	5	3390.0	4536.7	121.7	49.7
PTh-C_6	1	23.1	31.1	98.1	55.6
	3	449.9	1670.0	138.8	69.8
	5	2565.0	4420.0	134.2	81.4
PTh-C_8	1	63.5	90.8	131.2	68.0
	3	1023.2	1890.0	109.8	68.9
	5	1021.5	2222.3	108.4	71.4
PTh-C_{10}	1	111.6	194.0	134.1	88.6
	3	1906.7	4126.7	121.0	69.3
	5	5450.0	10633.3	101.1	66.5
PTh-C_{12}	1	404.1	1393.6	127.7	77.5
	3	4306.0	8626.0	110.2	75.2
	5	5370.0	99767.0	101.0	94.9
PTh-Br_3	1	201.1	254.8	120.0	19.0
	3	5586.7	10043.3	137.3	0
	5	9073.3	14000.0	148.3	0
PTh-Br_4	1	104.5	122.9	128.3	48.7
	3	3805.0	6562.0	140.1	42.5
	5	10000.0	14500.0	123.5	0
PTh-Br_5	1	285.6	1090.0	136.1	84.1
	3	4658.0	8070.0	111.8	47.2
	5	2020.0	4903.3	76.8	22.5
PTh-Na	1	60.9	76.8	113.8	0
	3	306.4	700.6	104.8	0
	5	657.4	1310.0	107.8	0
PTh-Ph	1	2070.0	4880.0	130.5	0
	3	4942.0	8606.0	130.8	0
	5	7910.0	11503.3	151.0	0
PTh-Bi	1	48.9	84.7	115.8	0
	3	212.9	457.7	133.6	25.7
	5	1171.3	2173.3	103.1	30.0

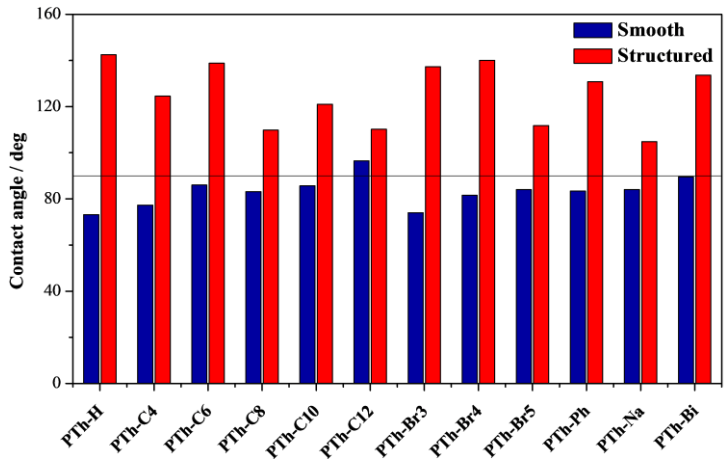

Figure 2.24. Comparison between the apparent contact angles of water for smooth and structured (3 deposition scans) surfaces for the substituent-derivatives of thienothiophenes. Polymerization at 0.1 M Bu_4NClO_4/dichloromethane. Solid line: 90º.

The surface energy data presented in **Table 2.11** are in agreement with the results discussed for the smooth surfaces. The highest surface tension was found for PTh-H which presented the lowest θ^Y. Taking these data upon closer inspection, PTh-H, PTh-C_4 and PTh-Br_3 showed a higher polar component which could be explained by the absence or presence of short alkyl chain, respectively. In opposition, an ultra-low polar component was obtained for PTh-C_{12} due to the use of a long alkyl chain (γ^D_{SV} = 30.9 mN m$^-$1 and γ^P_{SV} = 0.8 mN m^{-1}). Nevertheless, all the polymers presented a very similar apolar component (γ^D_{SV} ~ 30 - 34 mN m^{-1}).

Table 2.11. Apparent contact angles of water (θ_w) and roughness data for the smooth corresponding polymers of the substituent-derivatives of thienothiophenes. Polymerization at 0.1 M solution Bu_4NClO_4/dichloromethane.

Smooth Polymer	Ra [nm]	θ_w [deg]	θ_{diiodo} [deg]	θ_{hexa} [deg]	γ_{SV} [mN m^{-1}]	γ^D_{SV} [mN m^{-1}]	γ^P_{SV} [mN m^{-1}]
PTh	9.1	73.2	37.4	0	41.6	33.9	7.7
PTh-C_4	8.1	77.3	49.6	0	37.6	30.9	6.7
PTh-C_6	8.5	86.0	51.8	0	33.8	30.4	3.4
PTh-C_8	7.1	83.1	51.8	0	34.8	30.4	4.4
PTh-C_{10}	9.3	85.7	43.1	0	35.7	32.6	3.1
PTh-C_{12}	9.0	96.5	49.9	0	31.7	30.9	0.8
PTh-Br_3	9.4	74.0	43.1	0	40.8	32.6	8.2
PTh-Br_4	9.2	81.5	40.2	0	37.6	33.3	4.3
PTh-Br_5	9.0	84.0	43.2	0	36.2	32.6	3.6
PTh-Na	9.6	84.0	39.3	0	36.9	33.5	3.4
PTh-Ph	9.2	83.4	38.0	0	37.3	33.8	3.5
PTh-Bi	9.1	89.5	45.0	0	34.2	32.1	2.1

2.3 GENERAL DISCUSSION

Here, we showed the possibility to obtain not only arrays of nanotubes, but also tree-like structures, nanospheres and cauliflower-like structures with high water adhesion using thienothiophene derivatives in organic solvent (dichloromethane) and without any surfactants. The formation of nanotubes is due to the stabilization by the polymer of gas bubbles (O_2 and/or H_2 depending on the electropolymerization method) produced *in-situ* during electropolymerization process. We also demonstrated that the water content plays an important role even if it is not the unique parameter.

Many types of structures were obtained employing different thienothiophenes cores by cyclic voltammetry, such as nanotubes, nanofibers, nanospheres and nanosheets. We showed that the electrochemical parameters are extremely important to control the type of nanostructure. The method chosen plays an important role on the nanotubes formation. By cyclic voltammetry as electropolymerization method, the amount of released gas was found to be much higher, although the electropolymerization at constant potential allows an easier control of the nanotube formation. By galvanostatic method, nanotubes, nanodomes and flower-like structures could be formed differing by the current density applied. In opposition, by pulse deposition various structures are formed. It is also possible to form nanotubes, but they are not well-ordered and distributed around the surfaces when compared with the other methods. The changes observed in morphology and mainly in wettability can be explained by the mechanisms of nucleation and particle growth which are more affected in pulse method than in the other methods. Moreover, it was also possible to obtain arrays of tree-like structures at high deposition charges displaying extremely high water adhesion with high θ_w by both constant potential and by cyclic voltammetry using different electrolytes.

Monomers derived from thienothiophene bearing linear, branched and aromatic substituents were successfully synthesized by a two-steps synthesis and electropolymerized yielding unique structures. Once more, nanotubes were formed for a monomer bearing a naphthyl-substituent showing that the number of scans does not have a huge influence on their size and porosity as showed for thieno[3,2-*b*]thiophene, a similar monomer. Parahydrophobic properties were found for all the surfaces independently of the substituent used.

REFERENCES OF CHAPTER 2

(1) Darmanin, T.; Laugier, J. P.; Orange, F.; Guittard, F. Influence of the Monomer Structure and Electrochemical Parameters on the Formation of Nanotubes with Parahydrophobic Properties (High Water Adhesion) by a Templateless Electropolymerization Process. *J. Colloid Interface Sci.* **2016**, *466*, 413–424.

(2) Liu, H.; Zhai, J.; Jiang, L. Wetting and Anti-Wetting on Aligned Carbon Nanotube Films. *Soft Matter* **2006**, *2* (10), 811–821.

(3) Perebeinos, V.; Tersoff, J. Wetting Transition for Carbon Nanotube Arrays under Metal Contacts. *Phys. Rev. Lett.* **2015**, *114* (8), 85501.

(4) Ozden, S.; Ge, L.; Narayanan, T. N.; Hart, A. H. C.; Yang, H.; Sridhar, S.; Vajtai, R.; Ajayan, P. M. Anisotropically Functionalized Carbon Nanotube Array Based Hygroscopic Scaffolds. *ACS Appl. Mater. Interfaces* **2014**, *6* (13), 10608–10613.

(5) Chen, X.; Kong, L.; Dong, D.; Yang, G.; Yu, L.; Chen, J.; Zhang, P. Synthesis and Characterization of Superhydrophobic Functionalized $Cu(OH)_2$ Nanotube Arrays on Copper Foil. *Appl. Surf. Sci.* **2009**, *255* (7), 4015–4019.

(6) Xiao, A.; Zhou, S.; Zuo, C.; Zhuan, Y.; Ding, X. Improved Electrochemical Performances of CuO Nanotube Array Prepared via Electrodeposition as Anode for Lithium Ion Battery. *Mater. Res. Bull.* **2015**, *70*, 795–798.

(7) Qu, L.; Shi, G.; Yuan, J.; Han, G.; Chen, F. Preparation of Polypyrrole Microstructures by Direct Electrochemical Oxidation of Pyrrole in an Aqueous Solution of Camphorsulfonic Acid. *J. Electroanal. Chem.* **2004**, *561*, 149–156.

(8) Yuan, J.; Qu, L.; Zhang, D.; Shi, G. Linear Arrangements of Polypyrrole Microcontainers. *Chem. Commun.* **2004**, 8, 994–995.

(9) Qu, L.; Shi, G.; Chen, F.; Zhang, J. Electrochemical Growth of Polypyrrole Microcontainers. *Macromolecules* **2003**, *36* (4), 1063–1067.

(10) Parakhonskiy, B.; Andreeva, D.; Helmuth, M.; Shchukin, D. G. Hollow Polypyrrole Containers with Regulated Uptake/Release Properties. *Langmuir* **2009**, *25* (8), 4780–4786.

(11) Parakhonskiy, B.; Shchukin, D. Polypyrrole Microcontainers: Electrochemical Synthesis and Characterization. *Langmuir* **2015**, *31* (33), 9214–9218.

(12) Najafisayar, P.; Bahrololoom, M. E. The Effect of Pulse Electropolymerization on the Electrochemical Properties of Polythiophene Films. *Electrochim. Acta* **2013**, *114*, 462–473.

(13) Wolfs, M.; Darmanin, T.; Guittard, F. Effect of Hydrocarbon Chain Branching in the Elaboration of Superhydrophobic Materials by Electrodeposition of Conducting Polymers. *Surf. Coatings Technol.* **2014**, *259*, 594–598.

(14) Darmanin, T.; Mortier, C.; Eastoe, J.; Sagisaka, M.; Guittard, F. Sticky Superhydrophobic Hard Nanofibers from Soft Matter. *RSC Adv.* **2014**, *4*, 35708–35716.

(15) Zhang, W. Poly(Indole-5-Carboxylic Acid)-Functionalized ZnO Nanocomposite for Electrochemical DNA Hybridization Detection. *J. Solid State Electrochem.* **2016**, *20*, 499–506.

(16) Grzeszczuk, M.; Ozsakarya, R. Surface Morphology and Corresponding Electrochemistry of Polypyrrole Films Electrodeposited Using a Water Miscible Ionic Liquid. *RSC Adv.* **2014**, *4* (42), 22214–22223.

(17) Mortier, C.; Darmanin, T.; Guittard, F. 3,4-Dialkoxypyrrole for the Formation of Bioinspired Rose Petal-like Substrates with High Water Adhesion. *Langmuir* **2016**, *32* (47), 12476–12487.

(18) Zhou, H.; Chen, Æ. H.; Luo, Æ. S. The Effect of the Polyaniline Morphology on the Performance of Polyaniline Supercapacitors. *J. Solid State Electrochem.* **2005**, *9* (8), 574–580.
(19) Kuang, H.; Cao, Q.; Wang, X.; Jing, B.; Wang, Q.; Zhou, L. Influence of the Reaction Temperature on Polyaniline Morphology and Evaluation of Their Performance as Supercapacitor Electrode. *J. Appl. Polym. Sci.* **2013**, *130* (5), 3753–3758.
(20) Zhou, Q.; Li, Y.; Huang, L.; Li, C.; Shi, G. Three-Dimensional Porous Graphene/polyaniline Composites for High-Rate Electrochemical Capacitors. *J. Mater. Chem. A.* **2014**, *2*, 17489–17494.
(21) Poverenov, E.; Li, M.; Bitler, A.; Bendikov, M. Major Effect of Electropolymerization Solvent on Morphology and Electrochromic Properties of PEDOT Films. *Chem. Mater.* **2010**, *22* (13), 4019–4025.
(22) Darmanin, T.; Guittard, F. Templateless Electrodeposition of Conducting Polymer Nanotubes on Mesh Substrates for High Water Adhesion. *Nano-Struct. Nano-Objects* **2016**, *7*, 64–68.
(23) Sabouraud, G.; Sadki, S.; Brodie, N. The Mechanisms of Pyrrole Electropolymerization. *Chem. Soc. Rev.* **2000**, *29* (5), 283–293.
(24) Darmanin, T.; Guittard, F. Highly Hydrophobic Films with Various Adhesion by Electrodeposition of poly(3,4-Bis(alkoxy)thiophene)s. *Soft Matter* **2013**, *9* (5), 1500–1505.
(25) Darmanin, T.; Guittard, F. Superoleophobic Surfaces with Short Fluorinated Chains? *Soft Matter* **2013**, *9* (25), 5982.
(26) Pringle, J. M.; Armel, V.; Macfarlane, D. R. Electrodeposited PEDOT-on-Plastic Cathodes for Dye-Sensitized Solar Cells. *Chem. Commun.* **2010**, *46* (29), 5367–5369.
(27) Szczepanski, C. R.; Darmanin, T.; Guittard, F. Using Poly(3,4-Ethylenedioxythiophene) Containing a Carbamate Linker as a Platform to Develop Electrodeposited Surfaces with Tunable Wettability and Adhesion. *RSC Adv.* **2015**, *5* (109), 89407–89414.
(28) Bellanger, H.; Darmanin, T.; de Givenchy, E. T.; Guittard, F. Influence of Long Alkyl Spacers in the Elaboration of Superoleophobic Surfaces with Short Fluorinated Chains. *RSC Adv.* **2013**, *3* (16), 5556.
(29) Pei, A.; Zheng, G.; Shi, F.; Li, Y.; Cui, Y. Nanoscale Nucleation and Growth of Electrodeposited Lithium Metal. *Nano Lett.* **2017**, *17*, 1132–1139.
(30) Teller, H.; Ohanona, S.; Kashyap, D.; Schechter, A. Morphological Study of Branched Sn Structure Formed under Selected Electrochemical Conditions. *J. Mater. Sci.* **2016**, *51* (18), 8471–8483.
(31) Pérez-Fernández, B.; Martín-Yerga, D.; Costa-García, A. Galvanostatic Electrodeposition of Copper Nanoparticles on Screen-Printed Carbon Electrodes and Their Application for Reducing Sugars Determination. *Talanta* **2017**, *175*, 108–113.
(32) Karami, H.; Asadi, M. G.; Mansoori, M. Pulse Electropolymerization and the Characterization of Polyaniline Nanofibers. *Electrochim. Acta* **2012**, *61*, 154–164.
(33) Li, C.; Bai, H.; Shi, G. Conducting Polymer Nanomaterials: Electrosynthesis and Applications. *Chem. Soc. Rev.* **2009**, *38* (8), 2397–2409.
(34) Wolfs, M.; Darmanin, T.; Guittard, F. Versatile Superhydrophobic Surfaces from a Bioinspired Approach. *Macromolecules* **2011**, *44*, 9286–9294.
(35) Wenzel, R. N. Resistance of Solid Surfaces To Wetting By Water. *Ind. Eng. Chem.* **1936**, *28* (8), 988–994.
(36) Cassie, A. B. D.; Baxter, S. Wettability of Porous Surfaces. *Trans. Faraday Soc.* **1944**, *40* (5), 546–551.
(37) Mortier, C.; Darmanin, T.; Guittard, F. 3,4-Ethylenedioxypyrrole (EDOP) Monomers with Aromatic Substituents for Parahydrophobic Surfaces by Electropolymerization.

Macromolecules **2015**, *48* (15), 5188–5195.

(38) El-Maiss, J.; Darmanin, T.; Guittard, F. Controlling Electrodeposited Conducting Polymer Nanostructures with the Number and the Length of Fluorinated Chains for Adjusting Superhydrophobic Properties and Adhesion. *RSC Adv.* **2015**, *5* (47), 37196–37205.

(39) Godeau, G.; Darmanin, T.; Guittard, F. Superhydrophobic/highly Oleophobic Surfaces Based on Poly(3,4-Propylenedioxythiophene) Surface Post-Functionalization. *J. Polym. Res.* **2016**, *23* (4), 81.

(40) Szczepanski, C. R.; M'Jid, I.; Darmanin, T.; Godeau, G.; Guittard, F. A Template-Free Approach to Nanotube-Decorated Polymer Surfaces Using 3,4-Phenylenedioxythiophene (PhEDOT) Monomers. *J. Mater. Chem. A* **2016**, *4* (44), 17308–17323.

(41) Patra, A.; Wijsboom, Y. H.; Leitus, G.; Bendikov, M. Tuning the Band Gap of Low-Band-Gap Polyselenophenes and Polythiophenes: The Effect of the Heteroatom. *Chem. Mater.* **2011**, *23* (12), 896–906.

(42) Bae, W. J.; Scilla, C.; Duzhko, V. V.; Ho Jo, W.; Coughlin, E. B. Synthesis and Photophysical Properties of Soluble Low-Bandgap Thienothiophene Polymers with Various Alkyl Side-Chain Lengths. *J. Polym. Sci. Part A Polym. Chem.* **2011**, *49* (15), 3260–3271.

(43) Homyak, P. D.; Tinkham, J.; Lahti, P. M.; Coughlin, E. B. Thieno [3,4-*b*] Thiophene Acceptors with Alkyl, Aryl, Perfluoroalkyl, and Perfluorophenyl Pendants for Donor − Acceptor Low Bandgap Polymers. *Macromolecules* **2013**, *46*, 8873–8881.

CHAPTER 3
Pyrenes: superhydrophobicity, fluorescence and anti-bioadhesion

As showed in *Chapter 2*, one of the most important parameter to change the surface morphology was the polymerizable core used for the electrodeposition. However, the morphology is one of the two parameters that can affect the surface wettability.[1] Indeed, other important parameters to improve the wettability include the length and the nature of the substituent chain, the presence of connector or spacer, the nature of the heteroatoms in the polymerizable core, etc.

In this *Chapter 3* we will focus the discussion on the pyrene moiety which has been calling the attention of the researches due to its fluorescence and superhydrophobic properties.[2] The aim here is to obtain surfaces with high θ_w and sticky and/or non-sticky behavior. Since is already known the fluorescence property of pyrene, a brief study explaining the differences in absorption and emission for the pyrene derivatives will be presented. In addition, taking advantage about the superhydrophobic and parahydrophobic behavior from the polypyrene surfaces, some analyses for potential applications were done. The bacterial resistance of three polymeric films was evaluated using two bacterial strains: *Staphylococcus aureus* and *Pseudomonas aeruginosa*. Copolymers made by electropolymerization were also an alternative to obtain pH-sensitive surfaces by a simple basic and acid treatment. In the end, also using pyrene copolymer surfaces, we presented a new method to measure the water adhesion of sticky and non-sticky surfaces by an ejection test using a catapult apparatus.

3.1 INFLUENCE OF NON-FLUORINATED CHAINS

As already showed in *Chapter 2*, the monomer substituent has a huge impact in the surface wettability and morphology. In this section we will present the results concerning the synthesis and electropolymerization of pyrene monomers bearing non-fluorinated substituents and their surface characterization. The use of linear and branched hydrocarbon chains already showed potential results to obtain superhydrophobic and parahydrophobic surfaces with a wide range of water adhesion.[3–5] In addition, the use of other substituents, such as adamantyl,

phenyl and glycol groups, will be also used to study their influence in the surface wettability and morphology of the polypyrene surfaces. **Scheme 3.1** shows the monomers synthesized and studied in this section.

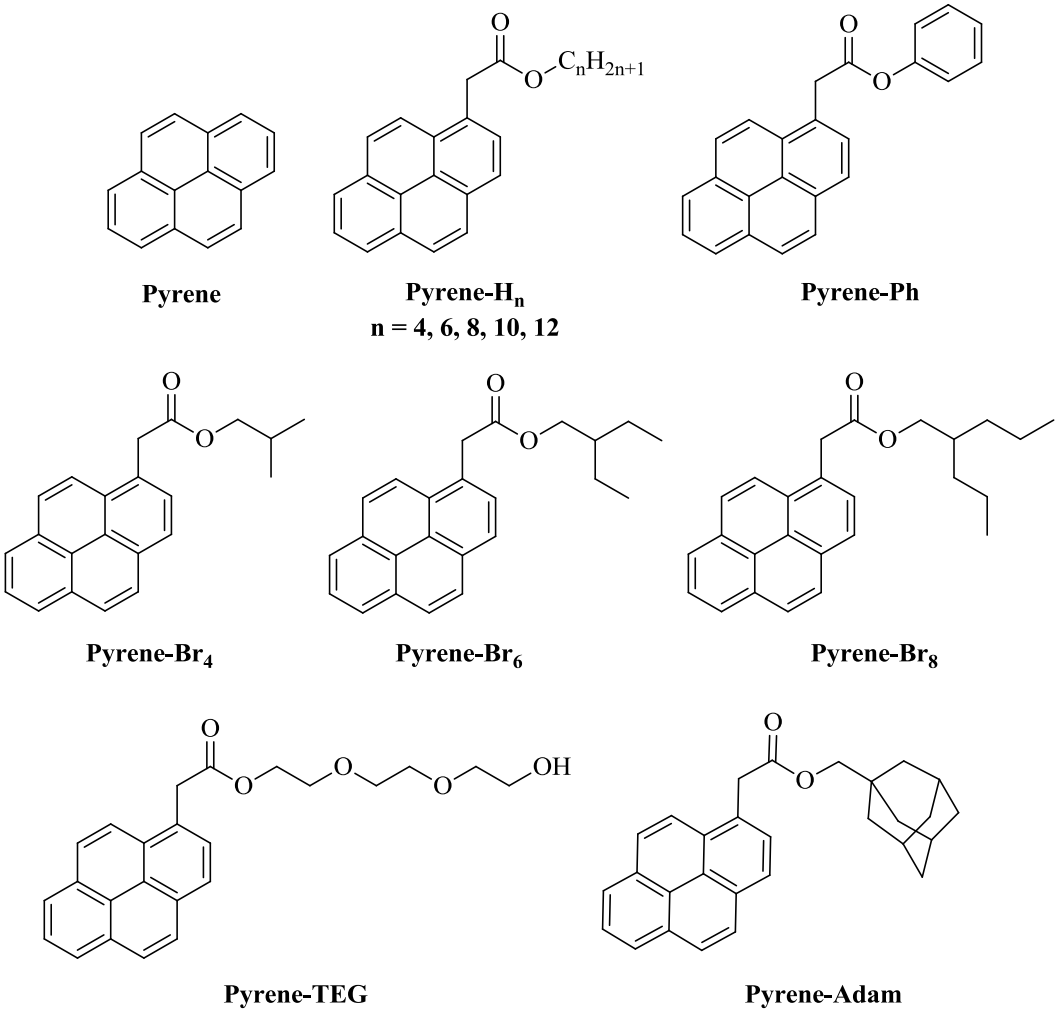

Scheme 3.1. Original non-fluorinated monomers synthesized and studied in this section.

3.1.1 Monomer Synthesis

The monomers were synthesized by an esterification reaction starting from 1-pyreneacetic acid (Py-COOH) and the corresponding alcohol in anhydrous dichloromethane using of *N*-(3-dimethylaminopropyl)-*N'*-ethylcarbodiimide hydrochloride (EDC), 4-(dimethylamino)pyridine (DMAP) and triethylamine (TEA) (**Scheme 3.2**). The reaction was followed by a purification step by column chromatography using silica gel (eluent:

dichloromethane:cyclohexane 1:1). The detailed procedure and the monomers characterization by proton and carbon NMR (^{1}H and ^{13}C NMR) are showed in ***Annex A1.2.1***. The pyrene (Py) monomer was purchased by Sigma Aldrich and was used with any previous purification.

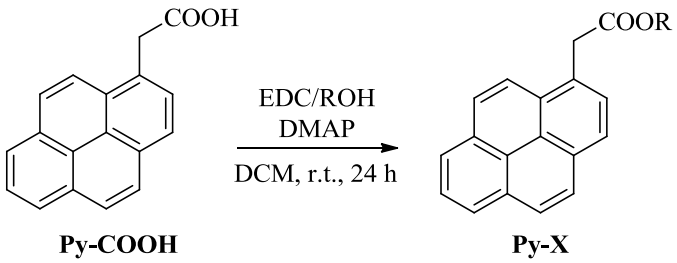

Scheme 3.2. Synthesis pathway to the non-fluorinated pyrenes studied.

3.1.2 Electrochemical Polymerization and Surface Characterization

In order to produce highly homogeneous polymer films, the cyclic voltammetry was used as deposition method and surfaces were produced by 1, 3 and 5 deposition scans. A solution of 0.1 M of Bu_4NClO_4 in anhydrous acetonitrile and 0.01 M of each monomer was used to polymerize at a scan rate of 20 mV s^{-1}. The E^{ox} was found by a single potential scan (1.58 – 1.67 V) and the polymers were electrodeposited from -0.7 V to E^{w} (1.50 – 1.58 V). The complete data is summarized in ***Table A2.4***.

Cyclic voltammograms of the non-fluorinated pyrenes are displayed in **Figure 3.1**. They show that the deposited film decreases with the number of scans. As already explained, many are the parameters that can affect the polymerization, such as the monomer planarity, rigidity, polymer conductivity, steric hindrance, etc. Here, the monomers Py-Adam, Py-Ph and Py-TEG showed to be more sensitive to the polymerization parameters than the branched and linear hydrocarbon chains. These results are not surprising since the monomers presented different arrangements. Linear and branched alkyl substituents are chains that extend their length away in one direction. In opposition, adamantyl- and phenyl-substituents are located directly next to the polymerizable core and all their volume may generate a higher spatial impediment throughout the polymerization. On the other hand, Py-TEG is a very long chain, similar to Py-H_{10} and Py-H_{12}, but the presence of the heteroatom affect the polymerization in a different way compared with the others.

For all the curves, the oxidation and reduction potentials of the corresponding polymers are very close to that of the monomers indicating that the polymer chain lengths are very short. The GPC data given in **Table 3.1** show that the polymerization degree of the polymers is extremely low (< 2.5), which means that the films are composed especially of monomers, dimers and trimers. Moreover, monomers and dimers are especially present with adamantyl-substituent while dimers and trimers are especially present with decyl and phenyl groups. These data are in agreement with the results presented in the cyclic voltammetry curves showing a lower polymer growth for Py-Adam monomer. Due to the multiple polymerization sites of pyrene and the presence of a substituent, many different dimers and trimers can be formed during polymerization. These results are in complete agreement with the literature.[2,6] Xu and co-workers showed that the electropolymerization of non-substituted pyrene in the same conditions gives oligomers of only 6–11 units.[2] In agreement, Chen and co-workers obtained an average repeat unit of 4 when the monomer (2-(4-(1-pyrenyl)butanoyloxy)ethyltrimethylammonium bromide) was polymerized by a combination of chemical and electrochemical methods.[6] Hence, it is not surprising to find that the substitution of pyrene with voluminous substituents reduces the polymer chain length to only some units. Even that the pyrene films are not more than few oligomers, to simplify the terminology in this work, the pyrene films will be called as polymer films.

It is surprising that oligomers of only few units are sufficiently insoluble to deposit as film, but can be explained by the fact of the pyrene moiety has not a high solubility in acetonitrile. Moreover, pyrene is known to induce extremely strong π-stacking interactions, which also self-assemblies and may highly decrease polymer solubility.[7–9]

Table 3.1. Data of non-fluorinated polymer chain length obtained by GPC. Polymerization in 0.1 M Bu_4NClO_4/acetonitrile. Number of scans: 3.

Polymer	Mn	Mw	Polymerization Degree
PPy-H_{10}	953	2195	2.38
PPy-Ph	714	1665	2.12
PPy-Adam	555	1079	1.41

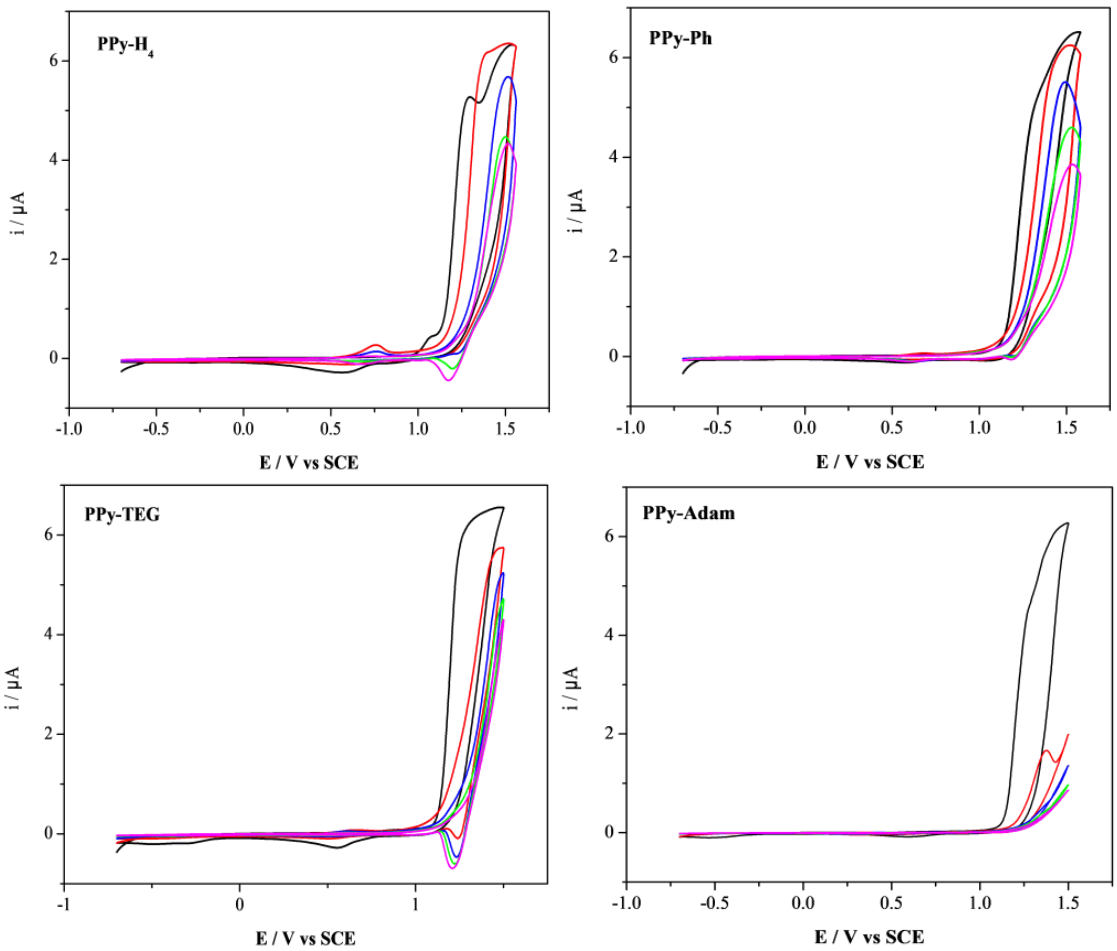

Figure 3.1. Cyclic voltammograms of the non-fluorinated pyrene monomers in 0.1 M Bu_4NClO_4/ acetonitrile at a scan rate of 20 mV s^{-1}. Black line: scan 1, red line: scan 2, blue line: scan 3, green line: scan 4, magenta line: scan 5**.**

The polymers were characterized by infrared (IR) spectroscopy using reflectance mode. The IR spectra are displayed in **Figure 3.2** in which the most intense peaks are highlighted. In all the polymers, a peak around 1740 cm^{-1} is observed which is characteristic of the presence of the ester group and at around 1000-1200 cm^{-1} several peaks characteristics from C–O stretching. Otherwise, for PPy-Adam, PPy-TEG and for linear and branched alkyl pyrenes are clear the presence of peaks at around 2800-3000 cm^{-1} attributed to the stretching of C–H and at around 850 cm^{-1} characteristic from C–H bending. A large peak around 3400 cm^{-1} attributed to the stretching of O–H is also present in the spectrum of PPy-TEG. The spectra also display a peak at 1632 cm^{-1} attributed to the stretching of C=C in the benzene units which is clearer in PPy-Ph.

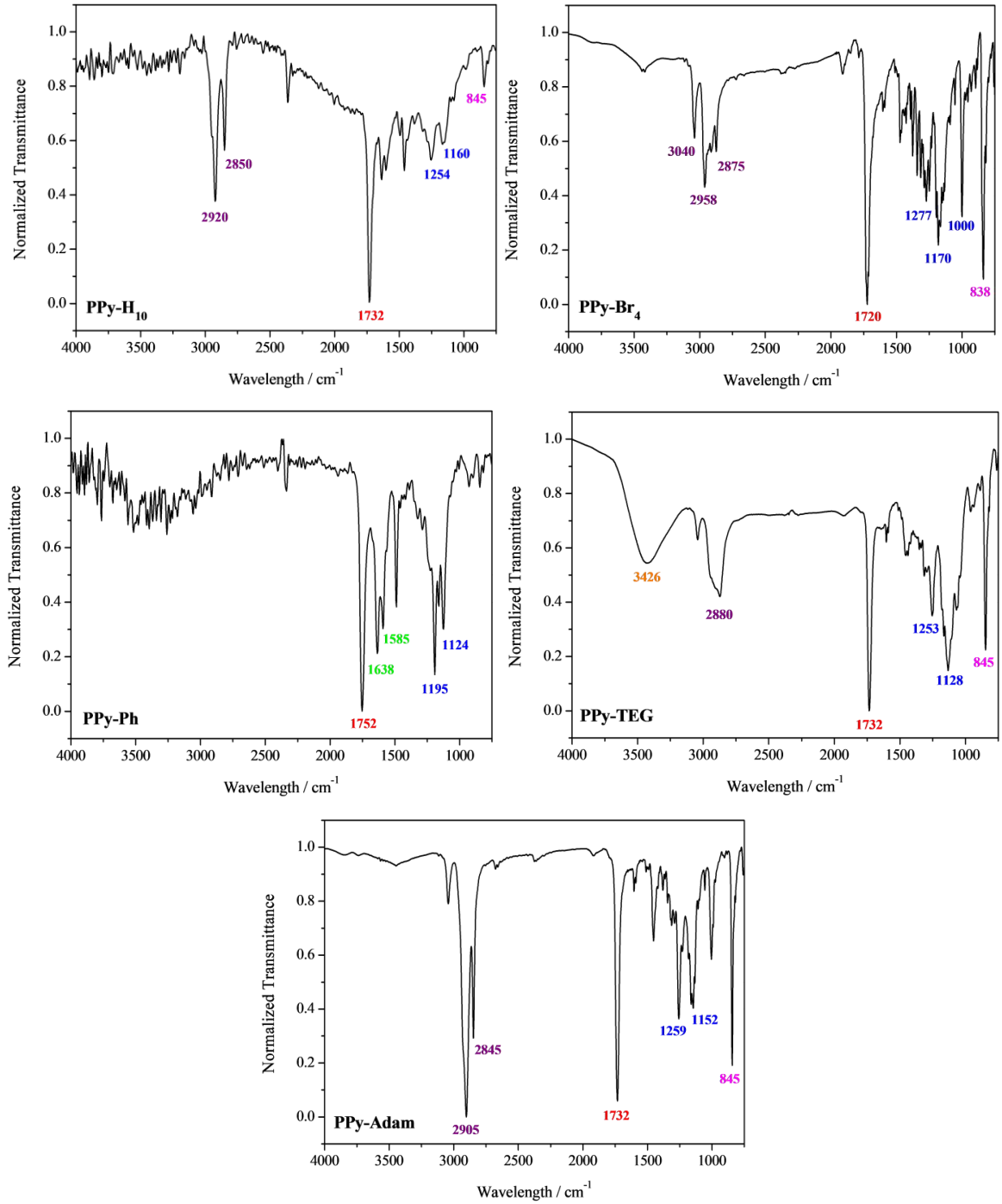

Figure 3.2. IR spectra of the non-fluorinated polypyrenes in 0.1 M Bu_4NClO_4/anhydrous acetonitrile at a scan rate of 20 mV s^{-1}. Number of scans: 5.

The surface morphology of each polymer after 3 deposition scans is given in **Figure 3.3** and **Figure 3.4** and the surface roughness is gathered in **Table 3.2**. The SEM images show that PPy is composed of flower-like microstructures inducing the higher roughness of all the

studied polymers. This result is in agreement with the literature where a similar methodology was used to electrodeposite polypyrene surface.[2]

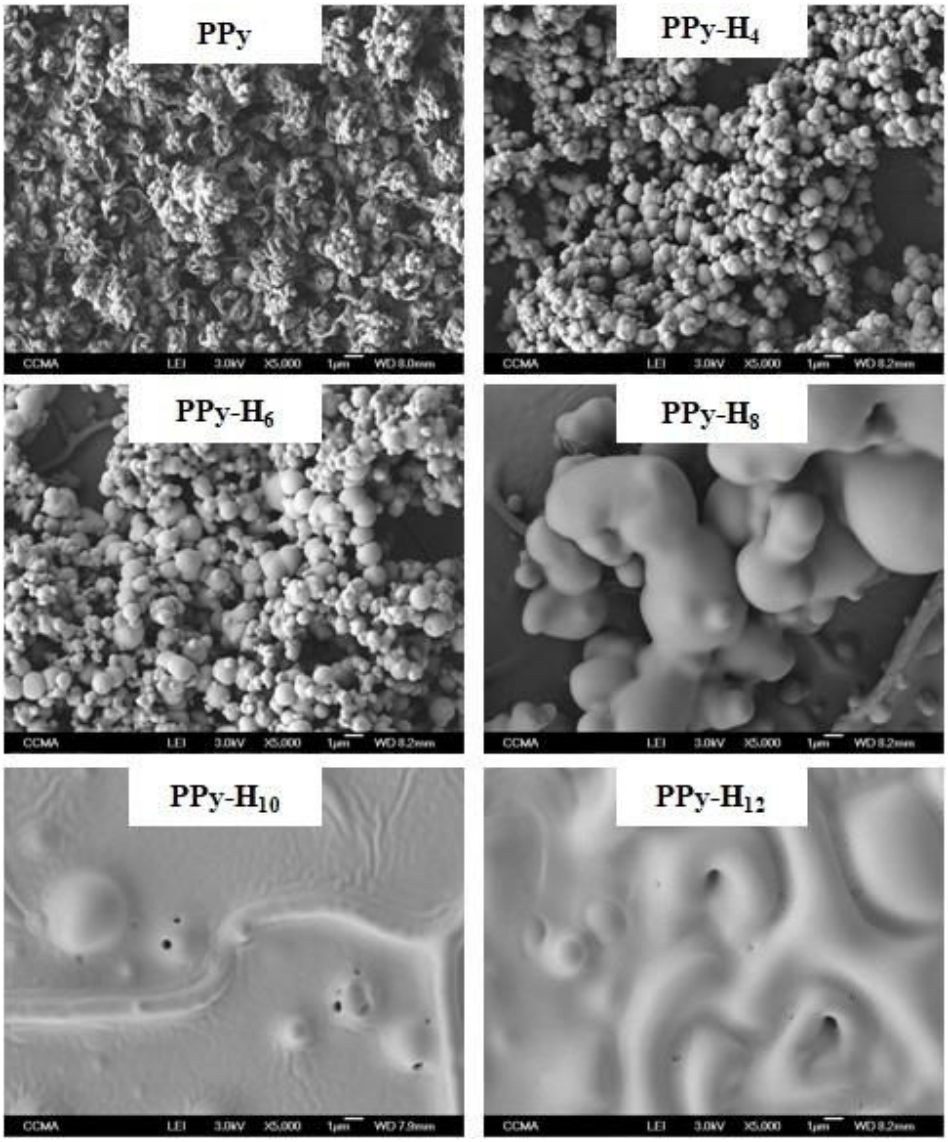

Figure 3.3. SEM images of the non-substituted and hydrocarbon polymers electrodeposited by cyclic voltammetry (3 scans) in a 0.1 M solution of Bu_4NClO_4/acetonitrile. Magnifications: 5000x.

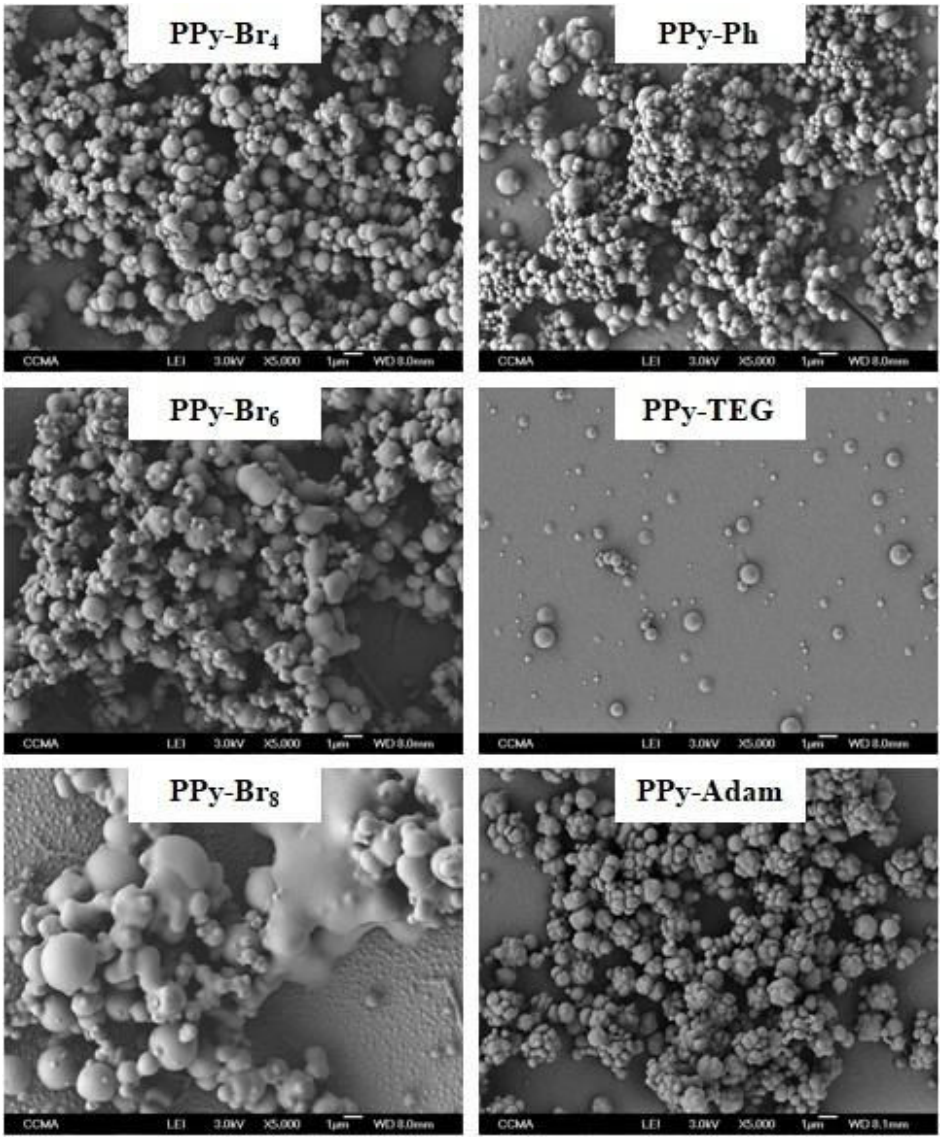

Figure 3.4. SEM images of the branched hydrocarbons, phenyl-, glycol- and adamantyl-subtstituent in polymers electrodeposited by cyclic voltammetry (3 scans) in a 0.1 M solution of Bu_4NClO_4/acetonitrile. Magnifications: 5000x.

The influence of the alkyl chain length on the surface morphology was found to be considerable important. While less structured surfaces were obtained using long alkyl chains (PPy-H_{12} and PPy-H_{10}), well defined spherical particles were obtained with shorter alkyl chains (PPy-H_8, PPy-H_6 and PPy-H_4). Upon closer inspection to SEM images, it is observed that the particles size increases as the alkyl chain increases. The diameter of the particles is about ∅ ≈ 0.8 µm for PPy-H_4, ∅ ≈ 1.2 µm for PPy-H_6, ∅ > 4 µm for PPy-H_8, ∅ > 6 µm for PPy-H_{10} and ∅ > 10 µm for PPy-H_{12}. It is clear that for polymers where number of carbons is > 8, the nanospheres become large aggregates of microparticles loosing the defined form of

the spherical structures generating a surface less structured than for shorter alkyl chains. For the branched-substituted polymers, a similar behavior was observed comparing to the polypyrenes containing linear alkyl chains with equivalent number of carbons.

Usually, the morphology of electrodeposited polymers was found to be highly dependent on the solubility of the oligomers formed in the first instance of the electropolymerization. However, due to the lower polymerization degree, the stability and morphology of the polypyrene films is believed to be governed by the π-stacking interactions between the pyrene units during the polymerization, which decreases their solubility, leading to the polymer precipitation and deposition. Here, the size of the substituents will influence the molecules interactions and, consequently, their solubility and deposition

These results were confirmed by roughness measurements, as shown in **Table 3.2**. Generally, the roughness increased with the number of scan for the polymer surfaces. The mean arithmetic surface roughness (Ra) of PPyrene-H_{12} and PPyrene-H_{10} slightly increased between 1 and 3 deposition scans and remained similar for higher number of scans. Here, the increase can be explained by the presence of large wrinkles observed in these films. By contrast, the increase in Ra of PPyrene-H_8, PPyrene-H_6 and PPyrene-H_4 was extremely important and the roughness showed to be 6 times bigger than for the pyrenes containing longer alkyl chains. Even that the PPy-Adam and PPy-Ph showed a well-defined particles and very structured surfaces, the maximum Ra achieved was ≈ 540 nm for these polymers. Indeed, the non-substituted PPy showed the higher roughness parameters while the PPy-TEG the lowest ones for the non-flourinated pyrenes studied.

The contact angle measured for different probe liquids (water, diiodomethane and hexadecane) are also gathered in **Table 3.2**. For PPy-H_{12} and PPy-H_{10} the contact angles of the three probe liquids were similar whatever the number of deposition scans. This can be easily explained by the smoothness of the polymer films, which is not significantly affected by the number of deposition scans. These two polymers were slightly hydrophobic ($\theta_w \approx 90º$) and superoleophilic ($\theta_{hexa} \approx 0º$). By contrast, for PPy-H_8, PPy-H_6 and PPy-H_4, the contact angles of the probe liquids varied with the number of deposition scans. More precisely, the water contact angles often increased while decreased for diiodomethane as the number of deposition scans increased. This is because the electrodeposition of PPy-H_8, PPy-H_6 and PPy-H_4 induced the formation of spherical particles and the surface wettability was highly affected by the roughness. For short alkyl chains, similarities were found once again for the linear and branched-substituents. The first deposition scan showed the lowest θ_w, but the highest θ_{diiodo}

for the branched alkyl chains. For 3 and 5 deposition scans, very high θ_w were obtained but with very high water adhesion. A maximum value of θ_w = 132.4º was reached for PPy-Br_4 and θ_w = 112.2º for PPy-H_6. Here, the polymers are extremely rough explaining the high θ_w. Hydrophobic properties were obtained with a sticky behavior for PPy-Ph and PPy-Adam. The presence of rough structures has a negative impact in the wettability using diiodomethane and hexadecane as probe liquids when compared with PPy-TEG which is a smooth surface. PPy-Adam presented a higher θ_w at 3 deposition scans and PPy-Ph at 5 deposition scans, both due to higher roughness. For PPy-TEG, no significant changes were observed with the number of scans. These polymers are significatively less hydrophobic because they are much less structured (PPy-TEG) and the substituent is less hydrophobic (PPy-Ph, PPy-Adam and PPy-TEG) than the alkyl-substituted pyrenes.

Moreover, the dynamic contact angle measurements revealed the sticking behavior of all the surfaces. Water droplets were deposited on each surface and it remained stuck even after surface inclination of 90º. In opposition for all the substituted pyrenes, PPy presented a superhydrophobic behavior with a very high θ_w and very low water adhesion (very low both H and α) for 3 and 5 deposition scans.

Table 3.2. Apparent and dynamic contact angles and roughness data as a function of the polymer and the number of deposition scans of the non-fluorinated polypyrenes. Polymerization at 0.1 M solution Bu_4NClO_4/acetonitrile.

Polymer	Number of deposition scans	Ra [nm]	Rq [nm]	θ_{water} [deg]	H_{water}	α_{water}	θ_{diiodo} [deg]	θ_{hexa} [deg]
PPy	1	135	210	133.5	Sticky		0	0
	3	4000	5900	153.3	0.7	8.0	0	0
	5	6200	8900	152.1	0.7	6.0	0	0
PPy-H_{12}	1	125	170	94.1	-	-	48.9	0
	3	450	700	90.7	-	-	52.6	0
	5	390	550	93.1	-	-	45.9	0
PPy-H_{10}	1	135	210	88.1	-	-	33.5	0
	3	350	710	91.0	-	-	34.1	0
	5	410	670	99.7	-	-	39.2	0
PPy-H_8	1	650	400	90.7	-	-	20.5	0
	3	1890	3400	106.7	-	-	0	0
	5	2750	5150	97.7	-	-	0	0
PPy-H_6	1	630	1100	84.0	-	-	13.6	0
	3	1860	2780	110.5	-	-	0	0
	5	1720	2800	112.2	-	-	0	0
PPy-H_4	1	25	120	77.6	-	-	0	0
	3	1640	2640	103.7	-	-	0	0
	5	480	1920	111.8	-	-	0	0
PPy-Br_8	1	240	440	94.0	-	-	19.0	0
	3	480	1150	103.3	-	-	0	0
	5	1240	2300	108.5	-	-	0	0
PPy-Br_6	1	90	450	89.2	-	-	16.0	0
	3	1600	2050	129.8	-	-	0	0
	5	1670	2120	128.8	-	-	0	0
PPy-Br_4	1	20	30	83.0	-	-	23.7	0
	3	2075	2800	132.4	-	-	0	0
	5	2900	3450	132.4	-	-	18.1	0
PPy-Ph	1	140	380	85.2	-	-	0	0
	3	360	640	91.2	-	-	0	0
	5	520	870	105.7	-	-	0	0
PPy-TEG	1	20	50	57.4	-	-	28.5	0
	3	35	60	61.5	-	-	27.6	0
	5	40	70	62.8	-	-	30.6	0
PPy-Adam	1	75	160	98.1	-	-	0	0
	3	550	935	113.2	-	-	13.2	0
	5	85	200	94.2	-	-	0	0

Comparing the structured surfaces with the smooth ones, **Figure 3.5** shows the results of θ_w after 3 deposition scans versus the smooth θ^Y. These θ^Y and their respective surface tension are also given in **Table 3.3**. All the polymers here are intrinsically hydrophilic ($\theta^Y_w < 90º$) and oleophilic ($\theta^Y_{diiodo} < 90º$ and $\theta^Y_{hexa} < 90º$) and the influence of the alkyl chain length on θ^Y was found to be not very important. The most hydrophilic polymers are PPy-TEG (θ^Y_w = 71.4º) and PPy-Adam (θ^Y_w = 73.0º) and the less hydrophilic is PPy-H_{12} (θ^Y_w = 88.3º) and PPy-H_{10} (θ^Y_w = 85.8º). The surface structures showed a negative impact in the wettability using diiodomethane as a probe liquid for alkyl pyrenes when n < 8. Since PPy-H_{10} and PPy-H_{12} are quite smooth, no changes were observed for all the probe liquids. The most dramatic changes in θ_w from the inherent θ^Y are from PPy, PPy-Br_6, PPy-Br_4 and PPy-Adam. Indeed, PPy-TEG showed a negative impact of the roughness added on the structured surface which can indicate a high porosity of the polymeric layer formed during the electropolymerization. The decrease in the surface oleophobicity can be explained by the Wenzel equation, but the increase in surface hydrophobicity can be just explained by the Cassie-Baxter equation.[10,11] A liquid droplet in the "Cassie-Baxter state" enters in only some parts of the surface roughness. The presence of air between the liquid droplet and the surface induces also the formation of a liquid vapor-interface. In the case of our structured surfaces, their high adhesion (sticking behavior) shows that the air fraction is relatively low and the surface can be classified as parahydrophobic.[12]

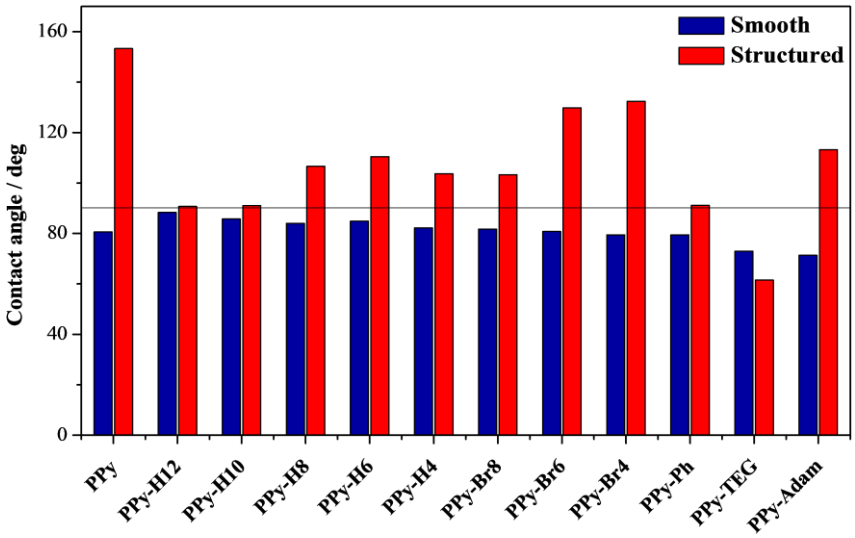

Figure 3.5. Comparison between the apparent contact angles of water for smooth and structured (3 deposition scans) surfaces for the non-fluorinated polymers. Polymerization at 0.1 M Bu_4NClO_4/acetonitrile. Solid line: 90º.

Table 3.3. Apparent contact angles of water (θ_w) and roughness data for the smooth corresponding polymers of the non-fluorinated pyrenes. Polymerization at 0.1 M solution Bu_4NClO_4/acetonitrile.

Smooth Polymer	Ra [nm]	θ_w [deg]	θ_{diiodo} [deg]	θ_{hexa} [deg]	γ_{SV} [mN m^{-1}]	γ^D_{SV} [mN m^{-1}]	γ^P_{SV} [mN m^{-1}]
PPy	11.0	80.6	29.6	11.5	39.4	35.2	4.2
PPy-H_{12}	9.3	88.3	32.6	0	36.8	34.9	1.9
PPy-H_{10}	10.0	85.8	32.7	0	37.5	34.9	2.6
PPy-H_8	8.9	84.0	21.6	0	39.4	36.6	2.8
PPy-H_6	9.4	84.9	33.2	0	37.7	34.8	2.9
PPy-H_4	9.3	82.2	38.4	0	37.7	33.7	4.0
PPy-Br_8	8.8	81.8	31.8	0	38.9	35.1	3.8
PPy-Br_6	8.2	80.8	31.5	0	39.3	35.1	4.2
PPy-Br_4	9.2	79.5	36.2	0	39.0	34.2	4.9
PPy-Ph	9.5	79.5	33.9	0	39.4	34.7	4.7
PPy-TEG	8.2	71.4	31.4	0	43.3	35.2	8.1
PPy-Adam	8.5	73.0	33.9	0	42.2	34.7	7.5

The surface tension data presented in **Table 3.3** showed the higher polar components to PPy-TEG and PPy-Adam also leading to a higher surface energy. The lower polar component was found for PPy-H_{12} as already expect due to the longer alkyl chain. No significant differences were observed for the apolar components of the smooth surfaces.

3.2 INFLUENCE OF FLUORINATED CHAINS

The last section had shown that non-fluorinated substituents are capable to form highly hydrophobic surfaces with a wide range of morphology. However, no superhydrophocity was obtained with the substituted pyrenes until this moment. The aim in this section is to describe the polymerization and characterization of fluorinated pyrenes in order to obtain polymers with superhydrophobic properties. As showed in the literature, different properties can be obtained using different chains achieving sticky and non-sticky behaviors.[13,14] To this end, fluoroalkyl chains differing by their size (n = 4, 6 and 8 carbons on the fluorinated chain) were used to evaluate their final properties. Indeed, the linker which connects the pyrene moiety to the fluorinated chain was also studied. Here, six different linkers were used: ester (Py-OF_n), thioester (Py-SF_n), amide (Py-NF_n), carbamate (Py-NOF_n), thiocarbamate (Py-NSF_n) and urea (Py-NNF_n). It will be evaluated the impact in surface wettability and

morphology of the use of different heteroatoms on the linkers of the fluorinated chain. The monomers studied in this section are summarized in **Scheme 3.3**.

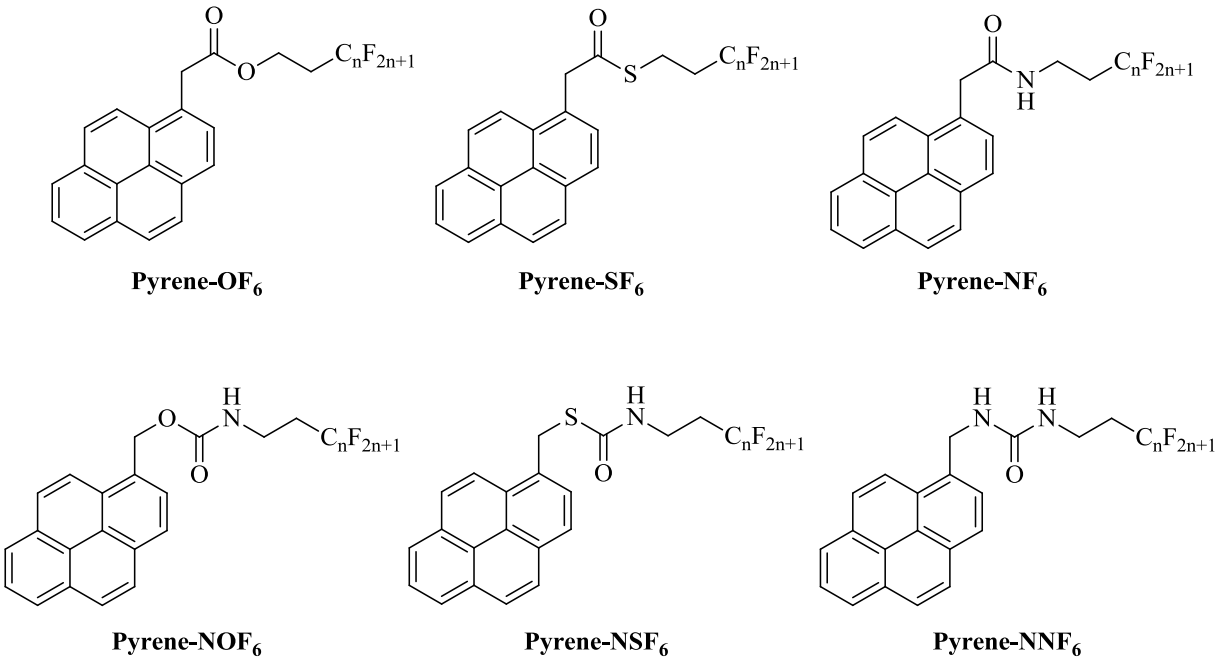

Scheme 3.3. Original fluorinated monomers synthesized and studied in this Section.

3.2.1 Monomer Synthesis

The synthesis of pyrene monomers bearing ester, thioester and amide were performed by the coupling between 1-pyrene acetic acid and the corresponding fluorinated alcohol, thiol and amine, respectively, in anhydrous dichloromethane using EDC as coupling agent in presence of DMAP and TEA (**Scheme 3.4**). The series of pyrene monomers containing carbamate, thiocarbamate and urea linkers was synthesized as reported in **Scheme 3.5** based on the nucleophilic addition of modified pyrenes containing alcohol, thiol and amine groups with fluorinated isocyanates in presence of TEA as a base. The detailed procedure and the monomer characterization by proton, fluorine and carbon NMR (^{1}H, ^{19}F and ^{13}C NMR) are shown in ***Annex A1.2.2***.

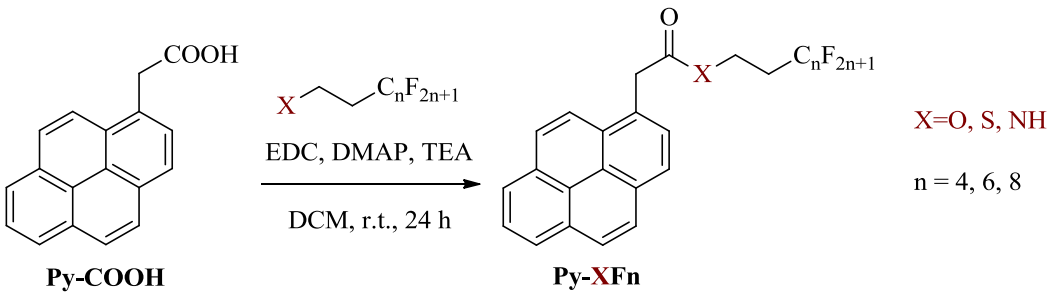

Scheme 3.4. Synthesis pathway to the fluorinated pyrenes studied bearing ester, thioester and amide linkers.

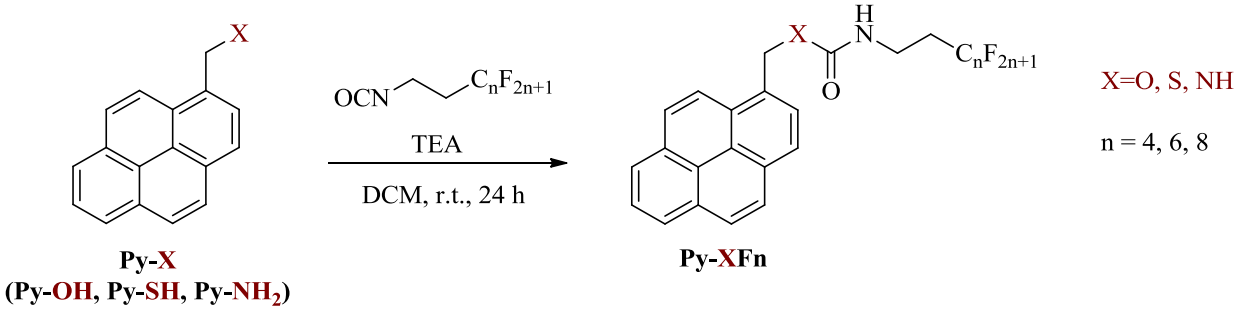

Scheme 3.5. Synthesis pathway to the fluorinated pyrenes studied bearing carbamate, thiocarbamate and urea linkers.

3.2.2 Electrochemical Polymerization and Surface Characterization

The electrochemical polymerization was carried out by cyclic voltammetry using a solution of 0.1 M of Bu_4NClO_4 in anhydrous acetonitrile and 0.01 M of each monomer. The polymers were electrodeposited by 1, 3 and 5 deposition scans from -0.7 V to E^w (1.40 – 1.59 V) at a scan rate of 20 mV s^{-1}. The E^{ox} was found from 1.46 – 1.65 V and the complete data is gathered in ***Table A2.5***.

The cyclic voltammograms displayed in **Figure 3.6** show that the oxidation and reduction potentials of the corresponding polymers are very close to that of the monomers which indicates that the polymer chain lengths are also very short, in a similar manner as for the non-fluorinated pyrenes. To confirm this data, GPC analysis were done with PPy-OF_6 and PPy-OF_8 and the results are presented in **Table 3.4**. The data for PPy-OF_4 is not presented because the polymer film was not soluble in the tested solvents. These data show an extremely low polymerization degree for both polymers (<1.4) showing that the films were

composed mainly by monomers and dimers. In comparison with the non-fluorinated polymers, it is expected to find a lower polymerization degree with the fluorinated chains due the higher steric hindrance and lower solubility of the fluorinated monomers. It is also important to notice that with the increase of the fluorinated chain, a decrease in the polymer growth was observed both by cyclic voltammetry curves and GPC data. Indeed, a decrease in the polymer growth was also observed with the number of scans.

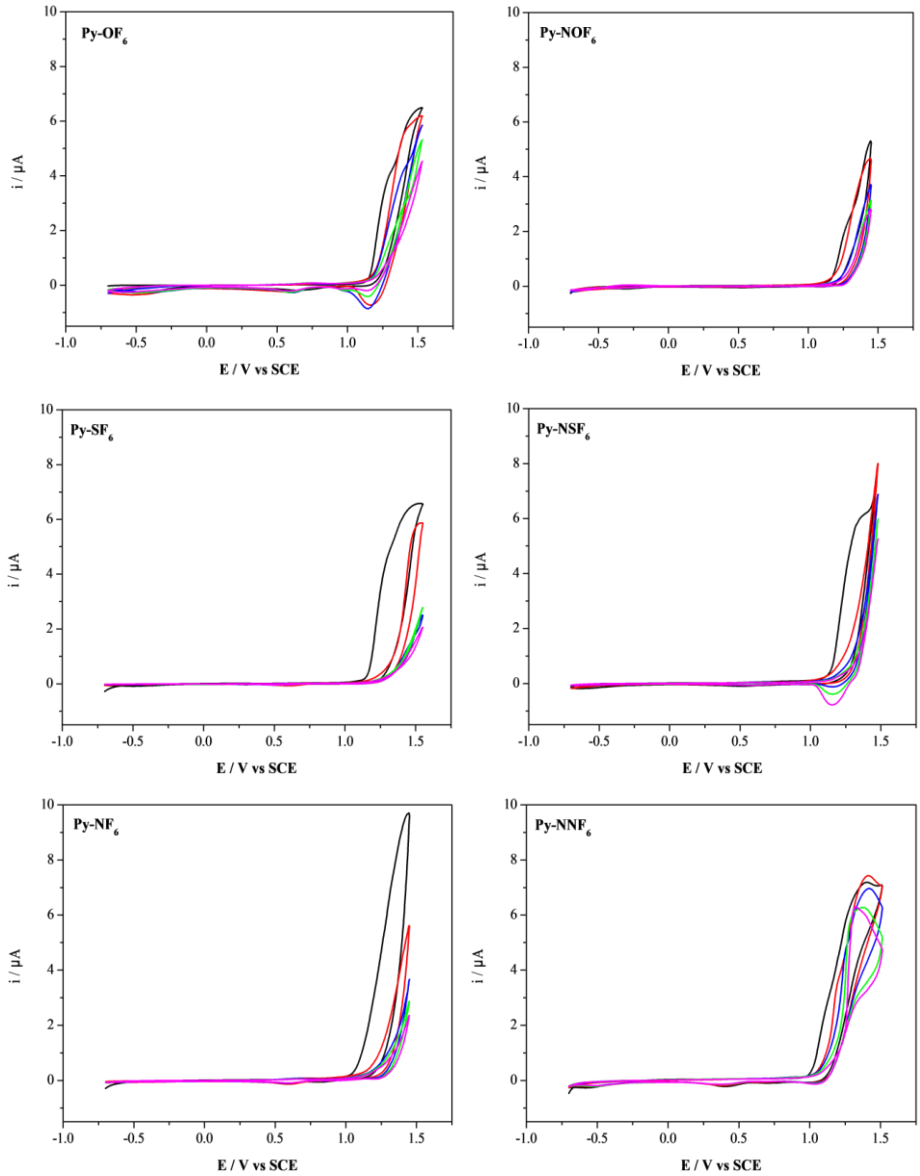

Figure 3.6. Cyclic voltammograms of the fluorinated pyrene monomers in 0.1 M Bu_4NClO_4/anhydrous acetonitrile at a scan rate of 20 mV s^{-1}. Black line: scan 1, red line: scan 2, blue line: scan 3, green line: scan 4, magenta line: scan 5.

Table 3.4. Data of fluorinated polymer chain length obtained by GPC. Polymerization in 0.1 M Bu_4NClO_4/acetonitrile. Number of scans: 3.

Polymer	Mn	Mw	Polymerization Degree
PPy-OF$_6$	814	1831	1.34
PPy-OF$_8$	894	1869	1.27

The ester, carbamate and thiocarbamate series of polypyrenes showed similar characteristics for the electropolymerization. A constant deposition of the polymer film with a gradual reduction of the oxidation peaks was noticed. For the thioester and amide series, a drastic reduction after the first scans was observed suggesting a reduction on the thickness of the deposited polymer layer. Differing from the other pyrenes, for urea series the oxidation and reduction peaks of the monomers and the corresponding polymers are further away from each other. Indeed, the urea linker induced higher intermolecular interactions which can decrease the substituent flexibility and mobility and may also decrease the steric hindrance. It is known that long fluorinated chains can induce two different effects in the polymerization: first, it can increase the steric hindrance due to the increase in the substituent chain; and second, it can decrease the steric hindrance due to the decrease in the substituent mobility.[15,16]

Figure 3.7 displayed some examples of IR spectra for the non-fluorinated pyrenes. Similarly to the non-fluorinated pyrenes, the IR spectra showed the characteristics peaks from C=O and C–H in around 1700 and 845 cm^{-1}, respectively. The position of the peaks of the carbonyl groups is lightly shifted due to the use of different linkers. The nature of the linker and the presence of different intermolecular interactions on the polymer films may influence the energy of carbonyl stretching. No influence in the frequency of C=O stretching was observed with the size of the fluorinated chains. The peaks around 1100-1300 cm^{-1} are attributed to the stretching of C–F present in these pyrenes. For the amide, carbamate, thiocarbamate and urea series, a peak at around 3300 cm^{-1} is attributed to the N–H stretching.

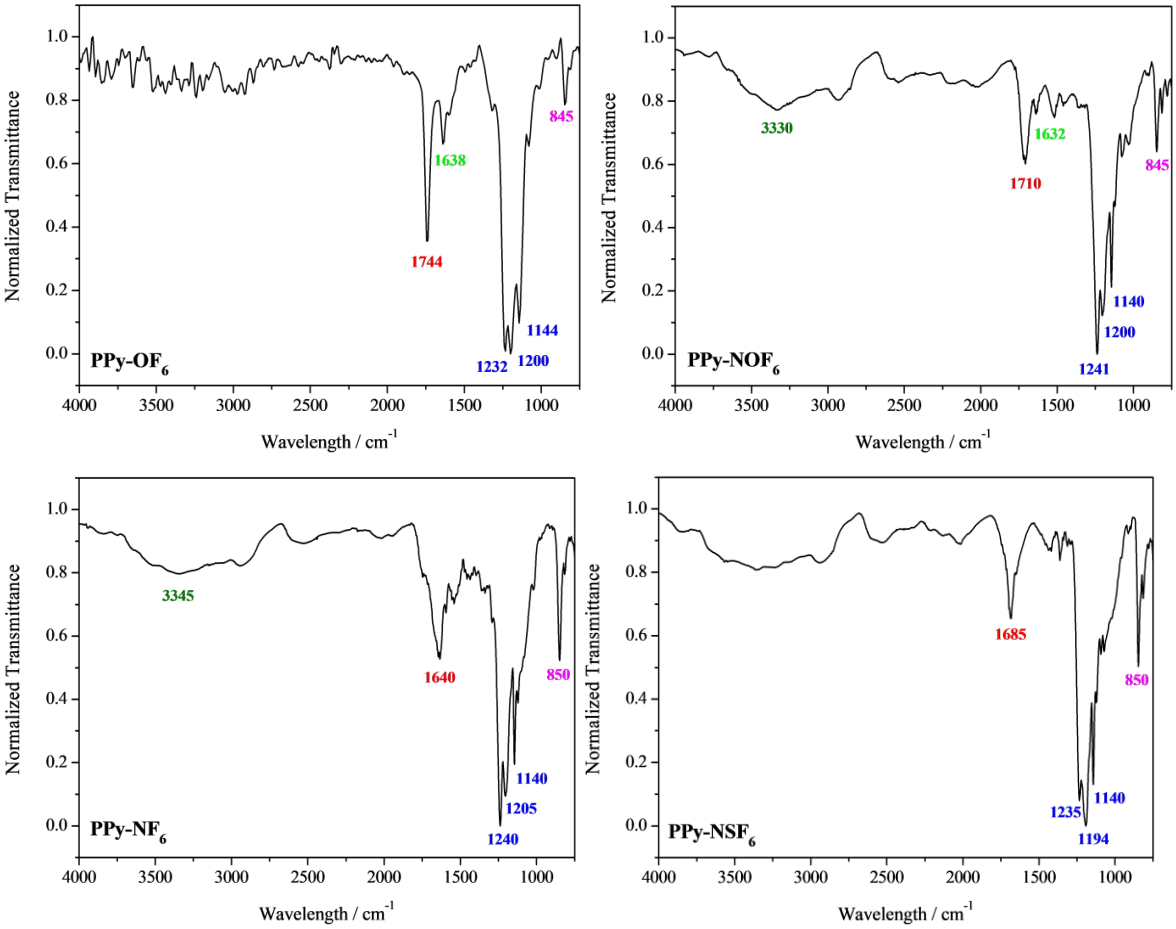

Figure 3.7. IR spectra of the fluorinated polypyrenes in 0.1 M Bu_4NClO_4/acetonitrile at a scan rate of 20 mV s^{-1}. Number of scans: 5.

The SEM images and the roughness data are given in **Figure 3.8** and **Table 3.5** for the ester, thioester and amide series and in **Figure 3.9** and **Table 3.6** for the carbamate, thiocarbamate and urea series. As showed for the non-fluorinated molecules, the polymerization of substituted pyrenes induces a deposition of spherical particles of different sizes. A clear trend of decreasing roughness with the increase of the fluorinated chain is observed for the ester, thioester, carbamate and thiocarbamate series. Regarding the nano-particle size for PPy-NSF_n series, for example, the diameter decreased with the number of carbons: ∅ ≈ 800 nm for n = 4, ∅ ≈ 500 nm for n = 6 and ∅ ≈ 350 nm for n = 8.

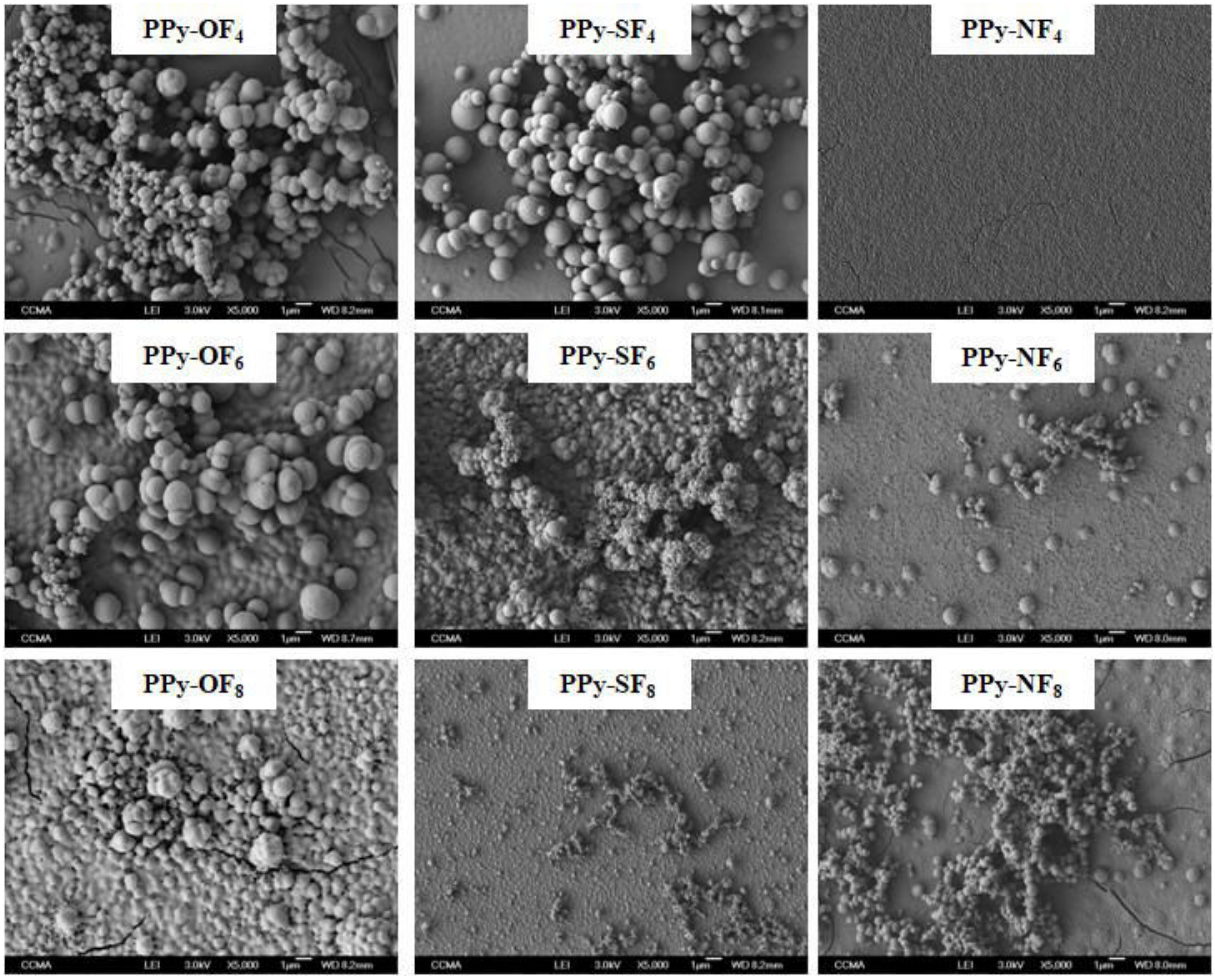

Figure 3.8. SEM images of the fluorinated polymers (ester, thioester and amide) electrodeposited by cyclic voltammetry (3 scans) in a 0.1 M solution of Bu_4NClO_4/acetonitrile. Magnifications: 5000x.

On surfaces with short fluorinated chains, the nanospheres are more defined and in a bigger amount compared with the longer fluorinated chains. In opposition, the deposition of Py-NF_n and Py-NNF_n form relatively smooth surfaces with nano-scale topography. This result is not surprising since the monomers containing amide and urea moieties are more polar and, in consequence, more soluble generating surfaces smoother and/or less structured.

Generally, in the case of the fluorinated pyrenes, the surface of the spherical particles are not smooth, but nanostructured. Indeed, it is known that a dual-scale surface roughness can have a high impact on the superhydrophobic properties and can highly reduce the contact angle hysteresis [17]. The summary of the mean apparent contact angles (θ) of liquids differing by their surface tension (water, diiodomethane and hexadecane), the hysteresis (H) and sliding angles (α) is given in **Table 3.5** and **Table 3.6**.

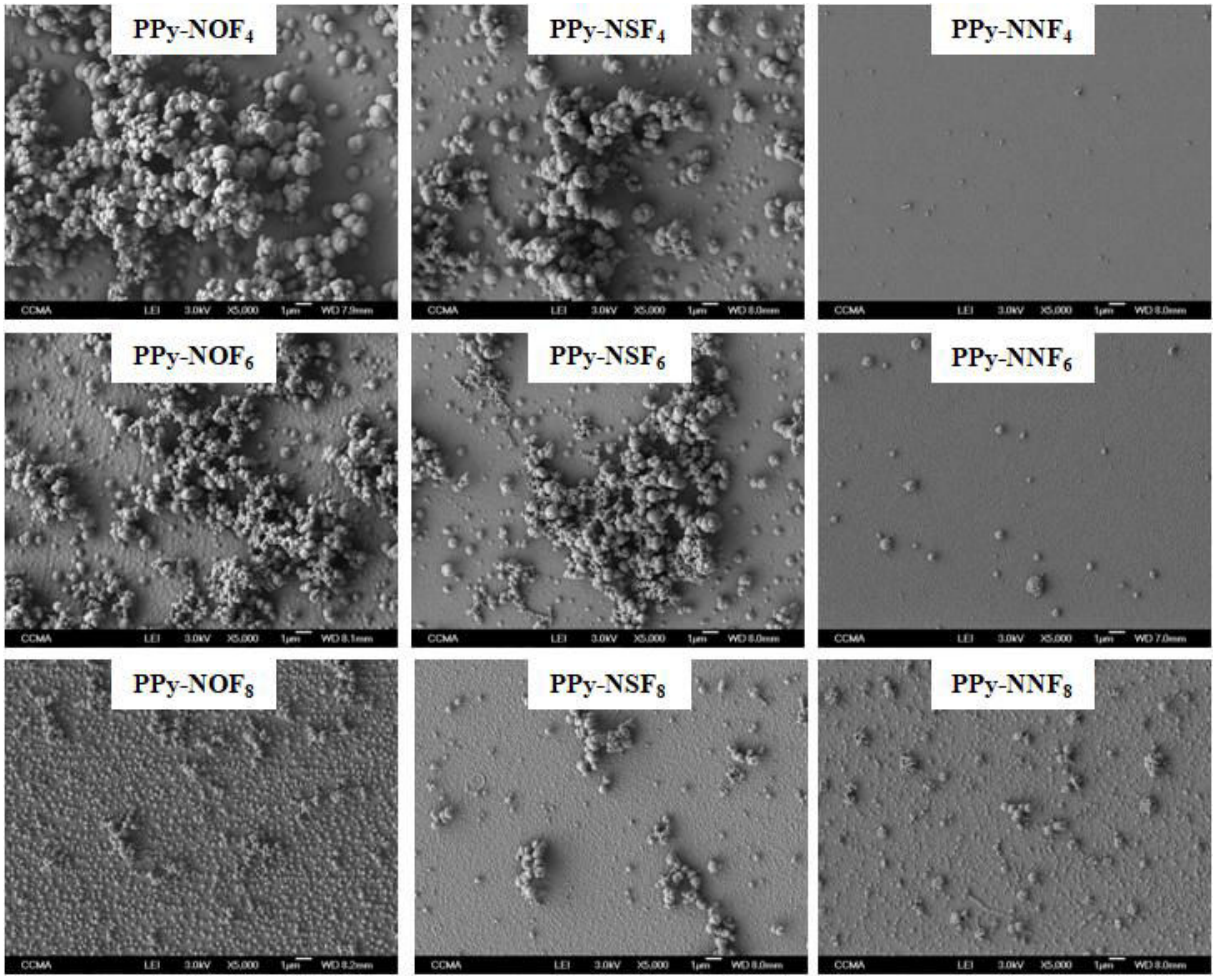

Figure 3.9. SEM images of the fluorinated polymers (carbamate, thiocarbamate and urea) electrodeposited by cyclic voltammetry (3 scans) in a 0.1 M solution of Bu_4NClO_4/acetonitrile. Magnifications: 5000x.

Superhydrophobic properties with very low H and α were obtained for PPy-OF_n and PPy-NOF_n series and for PPy-SF_n and PPy-NSF_n when n < 8. Here, the increase on the fluorinated chain from n = 6 to n = 8 decreased θ_w may be due to the formation of less structured surfaces as showed by the SEM images. The superhydrophobicity can be explained by the presence of micro and nanostructures observed on these polymer films. The surfaces composed by polymers with amide and urea linker presented high θ_w, but also high H and α. Regarding PPy-NF_n series, the most hydrophobic surface was obtained for 3 deposition scans independently of the size of the chain due to their morphology. A superhydrophobic surface using urea linker was only obtained for 5 deposition scans with the longer fluorinated chain. This behavior can be explained due to the use of long fluorinated chain and the longer deposition scans yielding to rougher surface for PPy-NNF_n series even if Ra = 46 nm. It is

already expected that the amide and urea series showed the less hydrophobic surfaces because of their polarity and consequently formation of less structured surfaces.

Table 3.5. Apparent and dynamic contact angles and roughness data as a function of the polymer and the number of deposition scans of the fluorinated polypyrenes bearing ester, thioester and amide linkers. Polymerization at 0.1 M solution Bu_4NClO_4/acetonitrile.

Polymer	Number of deposition scans	Ra [nm]	Rq [nm]	θ_{water} [deg]	H_{water}	α_{water}	θ_{diiodo} [deg]	θ_{hexa} [deg]
PPy-OF$_8$	1	60	105	125.0	Sticky		130.6	91.2
	3	180	290	157.8	1.5	2.0	130.0	97.5
	5	250	365	156.3	16.0	15.2	131.0	85.6
PPy-OF$_6$	1	45	115	136.5	Sticky		103.0	74.6
	3	580	1030	159.4	1.1	1.1	137.8	93.3
	5	1150	2000	160.0	0.9	1.0	135.8	95.0
PPy-OF$_4$	1	65	180	116.4	Sticky		85.2	49.3
	3	460	970	157.6	4.1	3.8	105.7	43.2
	5	630	1080	155.9	29.7	21.6	108.8	36.8
PPy-SF$_8$	1	16.7	32.2	128.9			103.5	72.3
	3	34.6	66.1	127.1	Sticky		100.9	74.9
	5	26.2	44.5	122.0			99.3	73.4
PPy-SF$_6$	1	149.5	355.3	155.6	36.5	19.7	118.8	82.1
	3	583.6	1588.0	157.8	0.5	1.0	144.2	123.6
	5	849.1	2230.0	156.0	0.6	1.0	147.6	113.3
PPy-SF$_4$	1	23.2	38.7	109.7	Sticky		82.6	55.7
	3	136.7	3700.0	154.5	1.6	9.7	100.8	58.0
	5	525.5	3000.0	127.3	Sticky		97.0	57.6
PPy-NF$_8$	1	22.3	36.7	118.1			97.7	66.1
	3	81.2	731.8	151.4	Sticky		112.1	61.4
	5	111.4	444.7	140.8			105.9	76.0
PPy-NF$_6$	1	15.9	25.9	124.6			109.0	79.0
	3	85.6	170.8	130.7	Sticky		103.1	72.8
	5	79.4	200.4	118.0			92.7	75.8
PPy-NF$_4$	1	7.6	10.5	99.7			77.0	45.9
	3	10.2	13.0	116.4	Sticky		102.6	59.1
	5	53.8	68.2	109.0			95.1	60.9

Table 3.6. Apparent and dynamic contact angles and roughness data as a function of the polymer and the number of deposition scans of the fluorinated polypyrenes bearing carbamate, thiocarbamate and urea linkers. Polymerization at 0.1 M solution Bu_4NClO_4/acetonitrile.

Polymer	Number of deposition scans	Ra [nm]	Rq [nm]	θ_{water} [deg]	H_{water}	α_{water}	θ_{diiodo} [deg]	θ_{hexa} [deg]
PPy-NOF$_8$	1	36.3	67.9	132.6	Sticky		108.5	79.1
	3	63.8	122.6	157.7	4.3	5.2	140.4	104.3
	5	75.3	129.5	157.4	2.1	3.2	148.4	103.4
PPy-NOF$_6$	1	35.5	75.6	124.9	Sticky		109.4	75.9
	3	316.4	1433.3	156.7	1.7	2.4	150.3	106.0
	5	447.1	1853.3	157.6	1.4	3.2	147.9	86.9
PPy-NOF$_4$	1	74.0	756.8	123.2	Sticky		97.5	58.7
	3	1400.0	3900.0	156.0	3.2	2.3	146.9	72.7
	5	2500.0	4900.0	156.8	4.5	2.6	147.8	66.1
PPy-NSF$_8$	1	17.0	38.3	122.2			94.2	67.2
	3	26.5	46.6	119.5	Sticky		98.4	65.8
	5	30.6	55.8	123.6			103.2	68.5
PPy-NSF$_6$	1	14.0	28.1	121.2	Sticky		97.3	59.1
	3	96.4	153.0	126.9	Sticky		101.7	67.0
	5	69.7	149.9	153.0	2.0	7.0	115.1	64.3
PPy-NSF$_4$	1	16.4	26.4	108.8	Sticky		87.5	40.5
	3	197.2	593.8	155.7	1.0	2.0	110.9	55.1
	5	311.9	817.7	155.1	Sticky		123.6	68.7
PPy-NNF$_8$	1	12.5	25.2	116.5	Sticky		97.6	75.8
	3	17.9	38.7	126.8	Sticky		113.4	91.0
	5	46.0	88.3	155.6	3.0	6.0	132.6	95.7
PPy-NNF$_6$	1	7.1	10.1	109.7			94.0	66.0
	3	9.2	14.6	111.1	Sticky		95.4	72.3
	5	25.4	36.5	122.6			100.3	75.7
PPy-NNF$_4$	1	7.5	9.6	107.0			87.4	61.6
	3	10.4	13.7	108.1	Sticky		91.2	59.8
	5	7.0	8.9	105.1			87.5	58.4

It is not surprising that the surfaces which presented best hydrophobicity will also be the most oleophobic. The carbamate series presented the best oleophobicity for both liquids, achieving the superoleophobicity for diiodomethane (θ_{diiodo} = 150.3º) and highly oleophobic properties for hexadecane (θ_{hexa} = 106º) due to the surface structure and the use of low surface energy compound. **Figure 3.10** shows the images of the water droplets of water, diiodomethane and hexadecane for the PPy-NOF$_6$. As expected, PPy-OF$_n$ series is also highly oleophobic for

diiodomethane and in the limit between oleophilicity and oleophobicity using hexadecane. Therefore, PPy-SF_n, PPy-NF_n, PPy-NSF_n and PPy-NNF_n are oleophobic and oleophilic for diiodomethane and hexadecane, respectively.

Figure 3.10. Picture of the droplets deposited on PPy-NOF_6 surfaces with all probe liquids. Polymerization in solution of 0.1 M Bu_4NClO_4/acetonitrile.

From these results, it can be seen that the heteroatom (O, S and N) which connect the linker with the pyrene unit does greatly impact in the wetting behavior. While for polymers using thioester, thiocarbamate, amide or urea linkers a wide range of wettability was obtained for water- and oleo-phobicity, for the ester and carbamate series a suitable superhydrophobicity and highly oleophobicity was obtained from 3 deposition scans.

To give a better explanation on the effects of the surface structures on the surface hydrophobicity and oleophobicity, the θ^Y were also evaluated. Smooth surfaces were prepared with Ra = 6.8 – 10.0 nm and the full data is given in **Table 3.7**. PPy-OF_n and PPy-SF_n (for n = 6 or 8) are intrinsically hydrophobic which may explain the higher wetting properties for the structured polymers and a slight hydrophilicity was found for n = 4. However, for the monomers with amide, carbamate, thiocarbamate and urea, an intrinsically hydrophilic behavior was observed ($\theta^Y_w < 90º$). This behavior may be explained by the presence of N-H bonds which favors the affinity with water. Here, even with long fluorinated chains that present very low surface energy, the presence of N-H bonds showed a strong influence on the wettability due to their high polarity. This result is supported by the literature where monomers derived from thiophenes containing a carbamate linker showed $\theta^Y_w < 90º$ which were attributed by the high polarity of the linker group.[18] **Figure 3.11** shows that the series with ester, thioester, carbamate and thiocarbamate linkers presented a higher improvement in their hydrophobicity compared with the amide and urea linker due to their lower polarity. Analyzing the interaction between the smooth surfaces and liquids with lower surface tension,

we observed no significant changes for θ^{Y}_{diiodo} and very low θ^{Y}_{hexa}. The most intrinsically oleophobic is PPy-SF_8 showing θ^{Y}_{diiodo} = 62.3º and θ^{Y}_{hexa} = 26.3º.

Hence, most of the results obtained with water cannot be explained with the Wenzel equation. In the case of oils such as diiodomethane, a slight increase of θ^{Y} is observed for the fluorinated polypyrenes even if they are highly oleophilic. As proposed by Marmur, a parahydrophobic surface is able to trap a high amount of air inducing a high increase in θ even if θ^{Y} < 90º. This can explain the surfaces with a sticky behavior (PPy-NF_n and PPy-NNF_n series). In the case of the superhydrophobic surfaces (high θ and low H and α), the presence of a dual-scale surface roughness allows to trap a high amount of air between the different liquids and the surface as described by the Cassie-Baxter equation. The surface energy data presented in **Table 3.7** showed a lower polar component for Py-OF_n and Py-SF_n which can explain their highest θ^{Y}_{w}. For the other polymers no significant changes were observed.

Table 3.7. Apparent contact angles and roughness data for the smooth corresponding polymers of the non-fluorinated pyrenes. Polymerization at 0.1 M solution Bu_4NClO_4/acetonitrile.

Smooth Polymer	Ra [nm]	θ_w [deg]	θ_{diiodo} [deg]	θ_{hexa} [deg]	γ_{SV} [mN m^{-1}]	γ^{D}_{SV} [mN m^{-1}]	γ^{P}_{SV} [mN m^{-1}]
PPy-OF_8	9.7	92.8	59.2	18.9	29.6	27.6	2.0
PPy-OF_6	9.8	90.2	43.4	15.8	33.9	32.0	1.9
PPy-OF_4	10.0	85.7	36.7	9.9	36.7	33.9	2.8
PPy-SF_8	9.9	97.1	62.3	26.3	27.3	26.0	1.3
PPy-SF_6	9.3	95.6	56.6	19.8	29.5	28.2	1.3
PPy-SF_4	7.0	87.8	44.7	11.7	34.7	32.2	2.5
PPy-NF_8	8.7	89.3	55.3	13.0	31.7	29.0	2.7
PPy-NF_6	7.3	82.5	46.9	11.0	35.8	31.4	4.4
PPy-NF_4	6.8	86.6	33.0	9.8	37.2	34.8	2.4
PPy-NOF_8	8.1	84.4	45.9	0	34.9	31.1	3.8
PPy-NOF_6	8.6	85.0	47.9	0	34.9	31.4	3.5
PPy-NOF_4	8.3	83.6	44.4	0	36.1	32.3	3.8
PPy-NSF_8	8.6	78.4	43.2	0	38.3	32.6	5.7
PPy-NSF_6	8.6	84.2	39.0	0	36.9	33.6	3.3
PPy-NSF_4	8.1	81.9	36.4	0	38.1	34.1	4.0
PPy-NNF_8	8.6	83.2	37.3	0	37.5	33.9	3.6
PPy-NNF_6	8.5	83.7	41.1	0	36.7	33.1	3.6
PPy-NNF_4	8.3	82.1	43.6	0	36.8	32.5	4.3

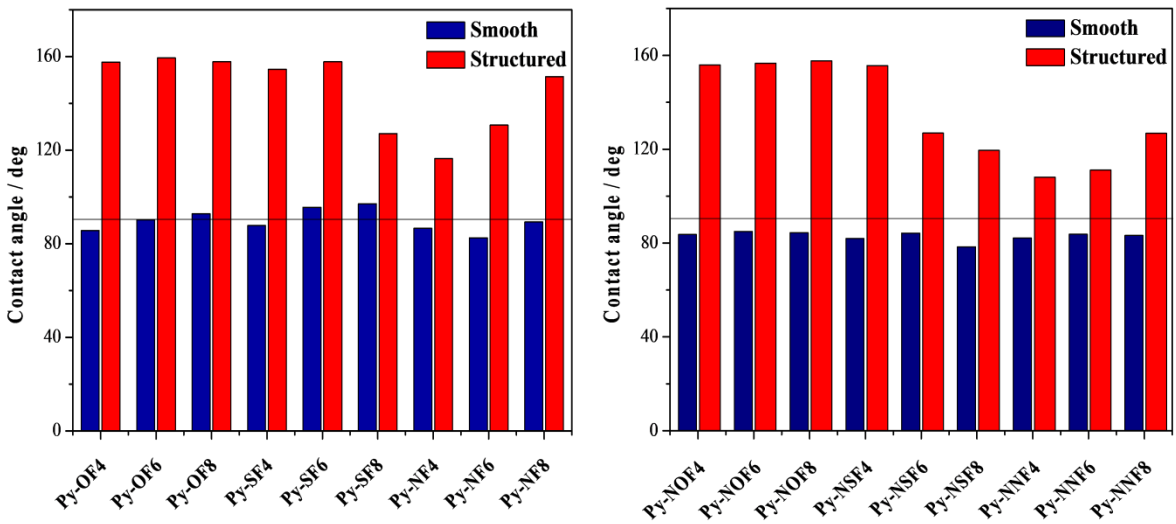

Figure 3.11. Comparison between the apparent contact angles of water for smooth and structured (3 deposition scans) surfaces for the fluorinated polymers. Polymerization at 0.1 M Bu_4NClO_4/acetonitrile. Solid line: 90º.

3.3 INFLUENCE OF THE PARAMETERS OF ELECTROPOLYMERIZATION

Previously in *Chapter 2*, it was shown that the electrochemical parameters play an important role on the final properties of the polymer films affecting the surface wettability and morphology. Here we briefly investigate the influence of the electrolyte, solvent and electrodeposition method on the electropolymerization of a fluorinated pyrene monomer (Py-OF_6). Eight different electrolytes have been tested as well as two solvents and two deposition methods.

3.3.1 Influence of the Electrolyte

Firstly, the monomers were electropolymerized in ITO plates by cyclic voltammetry from -0.7 V to the E^w (***Table A2.6***) using the solution 0.1 M with different electrolytes in anhydrous acetonitrile. Here, eight different electrolytes were tested: Bu_4NClO_4, Bu_4NBF_4, Bu_4NPF_6, tetrabutylammonium bis(trifluoromethane) sulfonimide (Bu_4NTf_2N), tetrabutylammonium trifluoromethanesulfonate ($Bu_4NCF_3SO_3$), tetrabutylammonium perfluorobutanesulfonate ($Bu_4NC_4F_9SO_3$), lithium perchlorate ($LiClO_4$), lithium bis(trifluoromethane) sulfonimide

($LiTf_2N$). Whatever the electrolyte, the cyclic voltammetry curves showed that the oxidation and reduction potentials of the resulting conducting polymers are very close to that of the monomers confirming that the polymer chain length is extremely short. No significant changes were observed for the different electrolytes.

SEM images as a function of the electrolyte are given in **Figure 3.12**. The surface morphologies are similar whatever the electrolyte and the structure consists on large microspheres of micron size, even if the electrolyte affects the spheres surface roughness (**Table 3.8**). The electrolytes Bu_4NClO_4, $Bu_4NCF_3SO_3$, $Bu_4NC_4F_9SO_3$ and $LiClO_4$ give rougher surfaces. It is already know that ClO_4^- and fluorinated counterions tend to generate surfaces with a very high roughness, as showed in the literature.[5] However, the action of the electrolyte will depend of the monomer used to polymerize and the interactions between them. Nevertheless, all the microspheres present a quite similar nanoroughness, which is extremely interesting for enhancing the hydrophobic properties.[19,20]

Usually, the use of different electrolytes can provide surfaces with distinct morphologies if the electrolyte plays an important factor on the polymer solubility. This is not the case here because the polymers are extremely insoluble whatever the electrolyte used due to the fluorinated chains and the strong π-stacking interactions on pyrene moieties. Moreover, the fact to obtain always spherical particles whatever the electrolyte used also confirms the high polymer insolubility, as observed with other conducting polymers with long fluorinated or hydrocarbon chains previously.[3]

The θ for the probe liquids are also given in **Table 3.8**. Two deposition scans are necessary to obtain superhydrophobic properties with ultra-low water adhesion whatever the electrolyte by the deposition on ITO plates. However, some variation can be observed on the dynamic components for the surfaces deposited by 1 scan. The lowest water adhesion was found for Bu_4NTf_2N and $LiTf_2N$ and a sticky behavior for $Bu_4NCF_3SO_3$ and $Bu_4NC_4F_9SO_3$. The highest oleophobic properties with θ_{hexa} = 118.7° were obtained with $LiTf_2N$. The droplets images for this surface are showed in **Figure 3.13**. The influence of the electrolyte on the surface hydrophobicity and oleophobicity is not significant, which confirms the observations done by SEM.

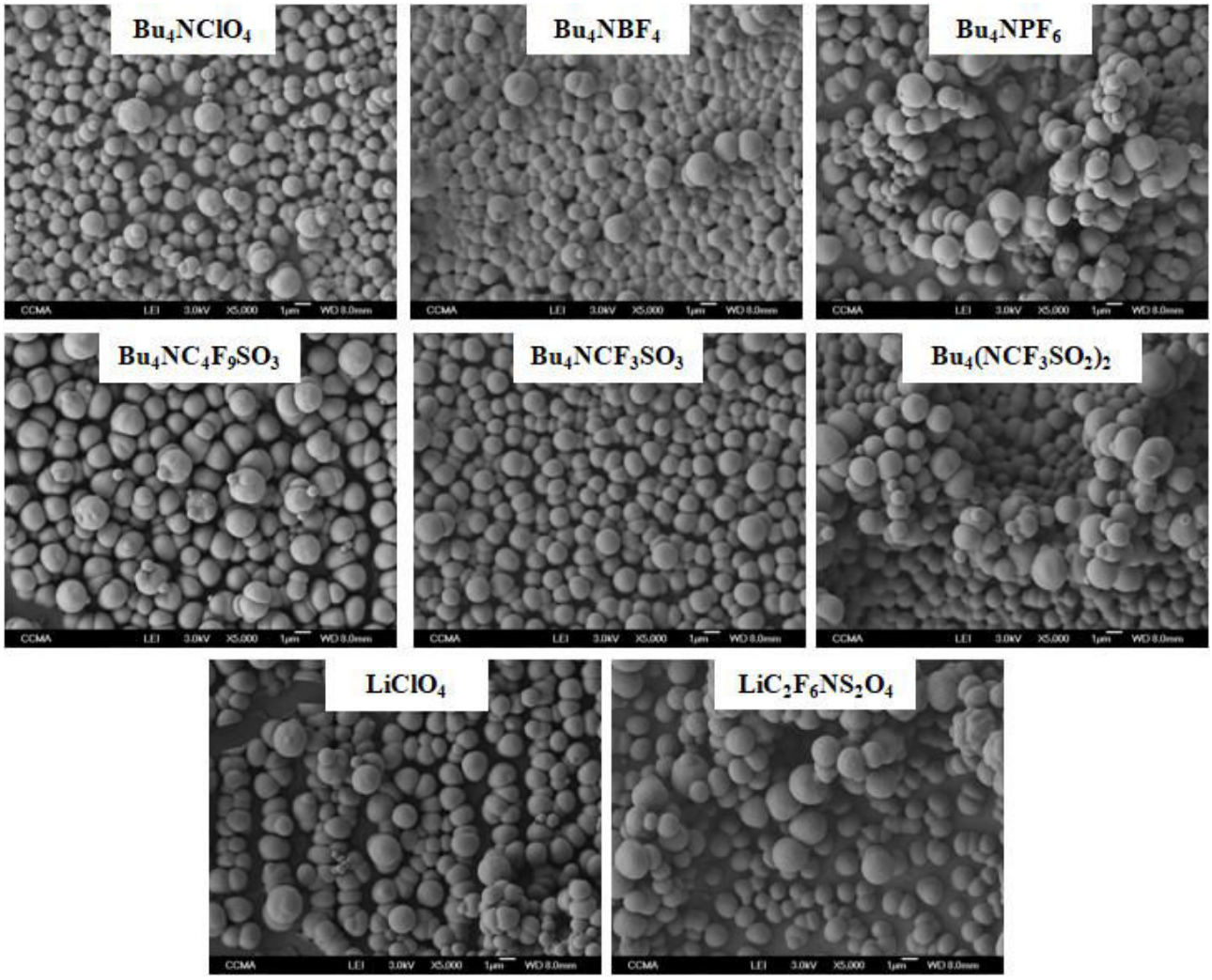

Figure 3.12. SEM images of PPy-OF_6 electrodeposited using different electrolytes in solution 0.1 M electrolyte/acetonitrile. (Magnification of X5000; Number of scans: 2; ITO plates).

Figure 3.13. Picture of the droplets deposited on PPy-OF_6 surfaces with all probe liquids using $LiTf_2N$ as an electrolyte in solution 0.1 M electrolyte/acetonitrile.

Table 3.8. Apparent and dynamic contact angles and roughness data of the probe liquids as function of electrolyte and the number of deposition scans for PPy-OF_6 surfaces. Polymerization in solution 0.1 M of electrolyte/acetonitrile. Deposition on ITO plates.

Electrolyte	Number of deposition scans	Ra [µm]	Rq [µm]	θ_{water} [deg]	H_{water}	α_{water}	θ_{diiodo} [deg]	θ_{hexa} [deg]
Bu_4NClO_4	1	1.1	2.5	153.2	7.0	7.9	126.3	96.2
	2	3.8	5.9	155.9	1.3	2.0	137.8	107.5
Bu_4NBF_4	1	0.6	0.8	153.3	8.3	15.1	107.4	50.9
	2	2.4	4.1	155.5	0.8	2.4	127.0	78.8
Bu_4NPF_6	1	0.3	0.6	154.3	18.0	24.9	111.9	71.6
	2	2.8	5.2	156.7	0.2	4.1	137.0	79.3
Bu_4NTf_2N	1	0.3	0.6	155.2	0.5	7.5	120.5	68.9
	2	4.5	7.3	153.5	0.2	3.4	137.4	71.4
$Bu_4NCF_3SO_3$	1	6.3	10.7	142.8	sticky	sticky	113.9	61.4
	2	10.1	16.2	154.0	0.2	5.1	120.4	70.8
$Bu_4NC_4F_9SO_3$	1	2.7	5.2	146.7	sticky	sticky	121.4	71.7
	2	10.7	16.1	153.1	0.6	8.4	128.0	79.2
$LiClO_4$	1	6.4	10.3	152.6	33.0	61.2	118.9	71.3
	2	14.4	21.4	154.7	0.5	4.7	127.6	76.1
$LiTf_2N$	1	0.5	1.4	153.1	0.3	5.4	120.1	65.1
	2	4.4	7.9	153.1	0.1	1.7	143.0	118.7

3.3.2 Influence of the Electrochemical Method

Electropolymerization experiments were also performed in order to find the optimal conditions by depositions at constant potential and using different deposition charges (Qs from 12.5 to 400 mC cm^{-2}) using Bu_4NClO_4 as an electrolyte. SEM images are given in **Figure 3.14** and the roughness and water contact angles in **Table 3.9**. The surface morphology is close to that obtained by cyclic voltammetry, but the size of the microspheres is much lower. Indeed, they increased from ∅ ≈ 0.25 µm for Qs = 12.5 mC cm^{-2} to ∅ ≈ 1 µm for Qs = 200 mC cm^{-2}, while the size was ∅ ≈ 1 µm after 2 deposition scans by cyclic voltammetry in ITO plates. The structuration of the polymer also increased with the charge, but was much lower than by cyclic voltammetry. With only 1 scan was obtained almost the same roughness of the surfaces over 200 mC cm^{-2}. A θ_w > 150º was achieved for Qs > 100 mC cm^{-2}, but the water droplets maintained the spherical shape when the surface is turned 90º,

showing a sticky behavior. Indeed, high oleophobicity for diiodomethane can be achieved for surfaces Qs > 25 mC cm^{-2}.

However, when a second step using cyclic voltammetry was done, the polymers were obtained in the reduced state (undoped state) and differences in the static and dynamic wettability could be seen. Higher contact angles are achieved for all Qs with a superhydrophobic state for Qs > 50 mC cm^{-2} due to the reduction step where the counterions are removed from the surface increasing it hydrophobicity. No variations were observed on the morphologies after the reduction step showing that the changes on the hydrophobicity are not due to removal the counterion. Also, no significant changes were observed in the wettability for the other probe liquids (diiodomethane and hexadecane). The smooth surfaces confirm this result as presented in **Table 3.10**. The results show that θ^{Y}_{w} for PPy-OF_6 in the reduced state are in the limit between hydrophobicity and hydrophilicity and for PPy-OF_6 in the oxidized state is hydrophilic. Indeed, even no significant differences are found in the apolar components of the reduced and oxidized polymers, the polar components showed quite different surface energies confirming our hypothesis about the doped and undoped states. Hence, by imposed potential method, the same potential is applied for all the depositions, which leads to a better control of the polymer growth by varying Qs. However, with cyclic voltammetry, greater wetting properties are obtained for all the probe liquids and also better dynamic components. By this method, a superhydrophobic and highly oleophobic behavior was found for the surfaces prepared with only 1 scan using Bu_4NClO_4 as an electrolyte.

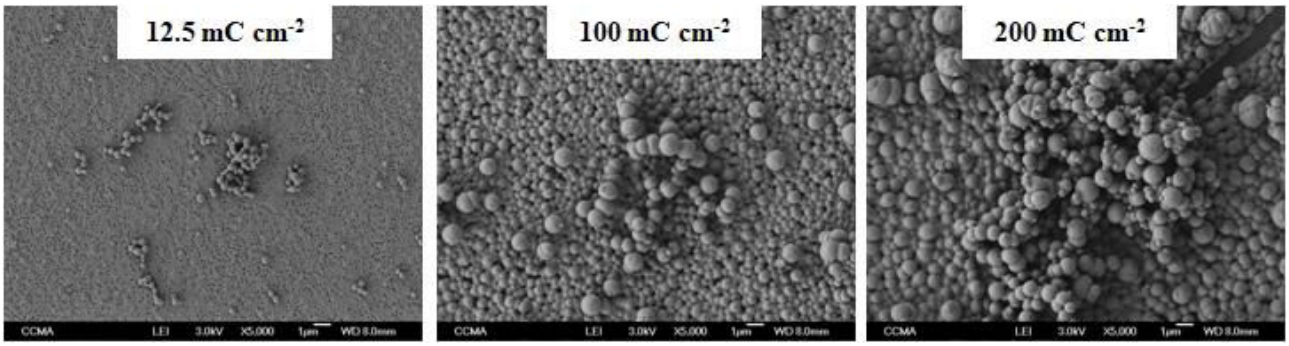

Figure 3.14. SEM images of PPy-OF_6 electrodeposited using different Qs by constant potential in solution 0.1 M Bu_4NClO_4/acetonitrile. Deposition on ITO plates.

Table 3.9. Apparent and dynamic contact angles and roughness data as function of the deposition charge for PPy-OF_6 surfaces in the oxidized state (by constant potential) and in the reduced state (by constant potential followed by cyclic voltammetry). Polymerization in solution 0.1 M of Bu_4NClO_4/acetonitrile. Deposition on ITO plates.

	Qs [mC cm^{-2}]	Ra [µm]	Rq [µm]	θ_{water} [deg]	H_{water}	α_{water}	θ_{diiodo} [deg]	θ_{hexa} [deg]
Oxidized state	12.5	0.1	0.2	127.1	sticky		86.0	76.6
	25	0.1	0.1	142.2	sticky		114.0	83.8
	50	0.2	0.4	138.7	sticky		116.8	72.4
	100	0.4	0.6	151.6	sticky		115.6	65.0
	200	1.4	3.0	153.1	sticky		107.7	71.2
	400	3.4	6.5	151.7	sticky		120.2	77.1
Reduced state	12.5	0.1	0.2	135.7	sticky		114.9	42.8
	25	0.1	0.3	143.6	sticky		120.1	55.1
	50	0.2	0.6	156.9	0.3	6.0	132.5	64.3
	100	0.3	1.1	156.3	1.0	7.0	136.2	88.4
	200	0.3	0.8	156.2	2.5	8.6	129.3	82.1
	400	0.3	0.7	156.0	0.5	7.6	128.4	79.1

Table 3.10. Apparent contact angles and roughness data for the smooth corresponding polymers of PPy-OF_6 in the oxidized and reduced state. Polymerization at 0.1 M solution Bu_4NClO_4/acetonitrile. Deposition on ITO plates.

	Ra [nm]	θ_w [deg]	θ_{diiodo} [deg]	θ_{hexa} [deg]	γ_{SV} [mN m^{-1}]	γ^D_{SV} [mN m^{-1}]	γ^P_{SV} [mN m^{-1}]
Oxidized state	8.9	78.5	39.1	27.8	36.0	28.6	7.4
Reduced state	9.8	90.2	43.2	15.8	33.1	30.6	2.5

3.3.3 Influence of the Solvent

Other experiments were also performed with Bu_4NClO_4 using dichloromethane as a solvent. The SEM images in **Figure 3.14** showed that the polymerization also leads to the formation of some spherical particles, but they were less well defined than the ones with acetonitrile. Some big cracks were also observed on the surface due to the fast evaporation of dichloromethane, which can lead to a lower θ_w, as showed in **Table 3.11**. Moreover, the use of a less polar solvent increases the solubility of these polymers during the polymerization leading to a formation of less structured surfaces and less defined particles. For these reasons,

the highest θ_w obtained using dichloromethane as a solvent is 130.8º after 3 scans. These results of wettability are expected and they are in agreement with the resulting surface morphology.

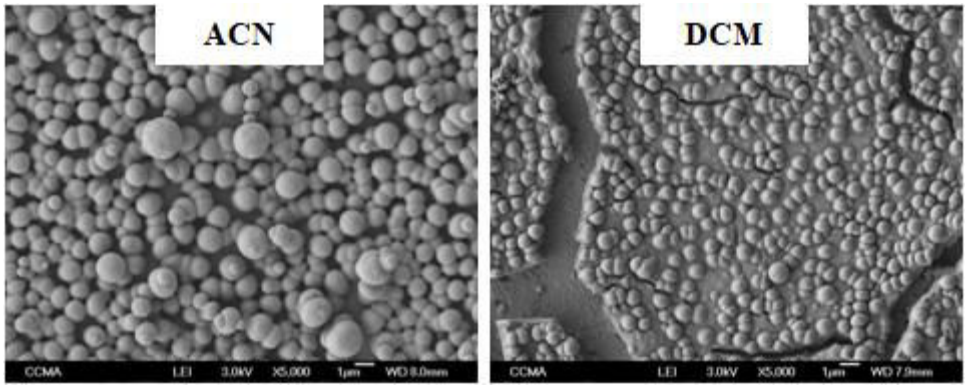

Figure 3.15. SEM images of PPy-OF_6 electrodeposited using dichloromethane as a solvent in solution with 0.1 M of Bu_4NClO_4. Deposition on ITO plates. Number of scans: 3. ACN = Acetonitrile, DCM = Dichloromethane.

Table 3.11. Apparent and dynamic contact angles and roughness data as function of the number of deposition scans and the solvent for PPy-OF_6 surfaces. Polymerization at 0.1 M solution Bu_4NClO_4/solvent. Deposition on ITO plates.

Solvent	Number of deposition scans	Ra [µm]	Rq [µm]	θ_{water} [deg]	H_{water}	α_{water}	θ_{diiodo} [deg]	θ_{hexa} [deg]
DCM	1	0.2	0.3	111.3	sticky		80.3	47.2
	3	0.7	1.6	130.8	sticky		107.2	45.9
	5	2.2	4.5	127.0	sticky		114.3	42.1
ACN	1	1.1	2.5	153.2	7.0	7.9	126.3	96.2
	3	4.8	7.1	155.9	3.8	5.3	145.8	110.3
	5	6.2	10.5	155.6	10.3	8.1	142.4	107.0

In conclusion, we showed that the surface roughness at both a micro and a nanoscale can be controlled with many parameters such as the electrolyte, the solvent and the deposition method. The hydrophobicity and water adhesion showed to have a significant impact when the solvent and the electrochemical method changed, respectively. However, the polypyrene surface showed to present the same range of wettability and quite similar structures through the electropolymerization sign different electrolytes.

3.4 FLUORESCENCE PROPERTIES

As presented in *Chapter 1*, pyrene monomer has calling attention for their unique fluorescent properties. It is known that the absorption and emission may be affected by the polymerization method and the functionalization on the monomer unit. Here we will present the results concerning the fluorescence properties for the pyrene derivatives (monomers and polymer films) presented in the *Sections 3.1* and *3.2* and how the substituents grafted on the monomer can affect them. This work was performed in collaboration with the MS Gabriela Morán Cruz, Dr. Xiao Xie and Prof. Rachel Méallet-Renault from the Université Paris-Saclay (Institut des Sciences Moléculaires d'Orsay - ISMO), in Orsay, France. The experimental procedure is described in ***Annex A3.1.3*** for the monomers and ***Annex A3.2.6*** for the polypyrene films.

3.4.1 Spectroscopic Properties of Pyrene Monomers

The absorption and fluorescence emission spectra of the non-substituted pyrene monomer in aerated dichloromethane solution are typical of what was expected.[21] However, both absorption and fluorescence emission spectra for the substituted pyrene monomers show a bathochromic shift compared to the non-substituted pyrene. The length and the chemical composition of the grafted chains do not affect the position or shape of the absorption bands. The maximum absorption wavelength was shifted by 7 nm whatever the functional group is. The shift does not seem to depend upon the length or the nature of atoms present on the substituent. As shown by Konishi and co-workers, it is likely that the methylene group which is connected to the aromatic ring controls the red shift in the absorption band.[22] Indeed, a red shift is also observed for all the emission spectra of pyrene derivatives which also might come from the additional chains grafted on the pyrene monomer.

3.4.2 Spectroscopic Properties of Pyrene Polymers

The pyrene polymers present different absorption and emission spectra compared with the corresponding monomers. **Figure 3.16** depicts the UV-vis absorption and fluorescence emission spectra for PPy and PPy-Ph. While the pyrene monomers display structured

absorption spectra, pyrene polymers exhibit a broad structureless spectral shape and a large red-shift compared to the respective monomers. The pyrene monomer characteristic spectral shape is no longer seen and such information tends to show that oligomerization occurs, also confirmed by the GPC data showed previously. The broadness of the band may suggest that several species such as aggregates exist. All the derivatives also possess one single structureless and red shifted emission band (λ_{em} = 472 - 515 nm) differently from their parent monomers (**Table 3.12**). This behavior is characteristic of an excimer emission of pyrene.[23] Indeed, usually the fluorescence spectrum of pyrene in concentrated solution consists of two distinct components, a band in the violet range with fine vibrational structure (monomer emission), and a blue-green band (λ_{em} = 482 nm) which is broad and structureless (excimer, i.e excited state dimer formed by a monomer in the ground state and a monomer in the excited state). At high concentration and in the crystalline state the fluorescence is almost exclusively from the excimer but no corresponding changes occur in the absorption spectrum with increase in concentration. In our case, the absorption spectra from monomer to polymer are drastically changed whereas the emission of monomer cannot be observed and an excimer-like emission is observed.

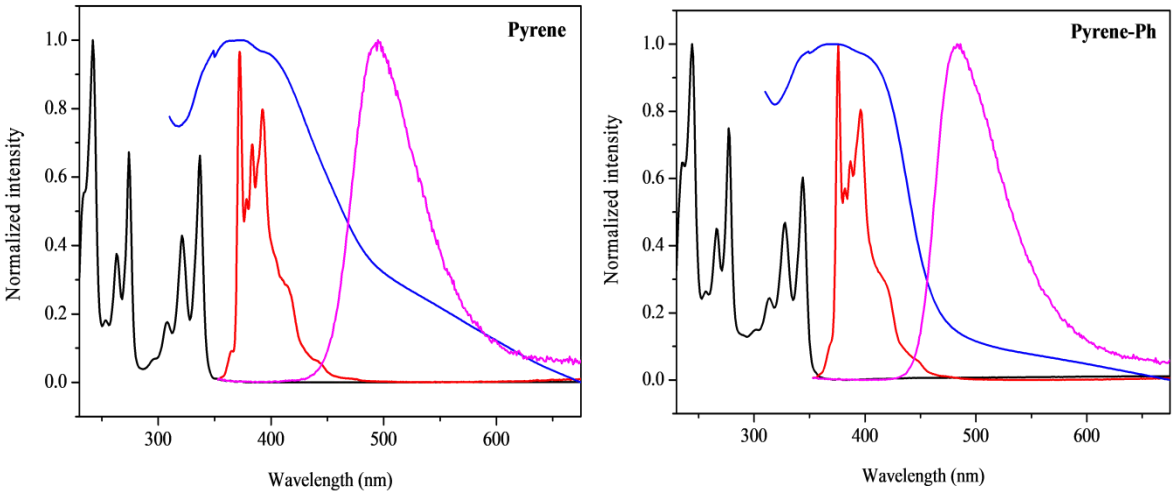

Figure 3.16. Absorption and emission spectra (normalization to 1 at the maximum intensity of every spectrum) for the non-substituted pyrene (Py) and Py-Ph. Absorption spectra of the monomers in DCM (black lines), emission spectra of the monomers in DCM with λ_{ex} = 343 nm (red lines), absorption spectra of the polymers (blue lines), emission spectra of the polymers with λ_{ex} = 343 nm (magenta lines). Polymerization in solution 0.1 M Bu_4NClO_4/acetonitrile. Number of scans: 2. Deposition in ITO plates.

Table 3.12. Spectroscopic Parameters of Pyrene Derivatives Polymers. Polymerization in solution 0.1 M Bu_4NClO_4/acetonitrile. Number of scans: 2. Deposition in ITO plates.

Polymer	$\lambda_{abs,max}$ [nm]	$\lambda_{em,max}$ [nm]
PPy	376	498
PPy-H_{12}	376	485
PPy-H_{10}	358	494
PPy-H_8	382	505
PPy-H_6	361	503
PPy-H_4	360	495
PPy-Br_8	375	478
PPy-Br_6	375	485
PPy-Br_4	361	489
PPy-Ph	367	488
PPy-TEG	358	X
PPy-OF_8	349	475
PPy-OF_6	370	478
PPy-OF_4	360	487
PPy-SF_6	370	482
PPy-NF_6	371	500
PPy-NOF_6	366	500

Note: For the polymer films PPy-NSF_6 and PPy-NNF_6, no data was obtained.

Looking for the emission spectra (**Figure 3.17**), it appears that fluorinated oligomers have a slightly blue-shifted emission compared to alkyl oligomers (same chain length). It is known that the fluorinated pyrenes have a spacer of 2 carbons between the fluorinated chain and the pyrene moiety, but no significant differences were observed in the absorption and emission spectra when the size of the fluorinated chain increases for comparison. A difference also arises from branched to linear form containing the same number of carbons: oligomers with linear chain show a red-shifted emission compared to branched oligomers. Moreover looking at band shape and full-width at half-maximum, for a given chain length, branched oligomers always show thinner emission bands compared to linear ones. Both observations are consistent with differences in aggregation or relative interactions or even due to different proportion concerning oligomers with distinct sizes. Indeed, in branched oligomers one may assume that steric hindrance is higher than in linear ones (for a given chain length), thus aggregation or interaction between oligomers is less in branched chains than in linear ones. If interaction or aggregation state increases with a linear chain then a red-shift and broadening of the band is expected.

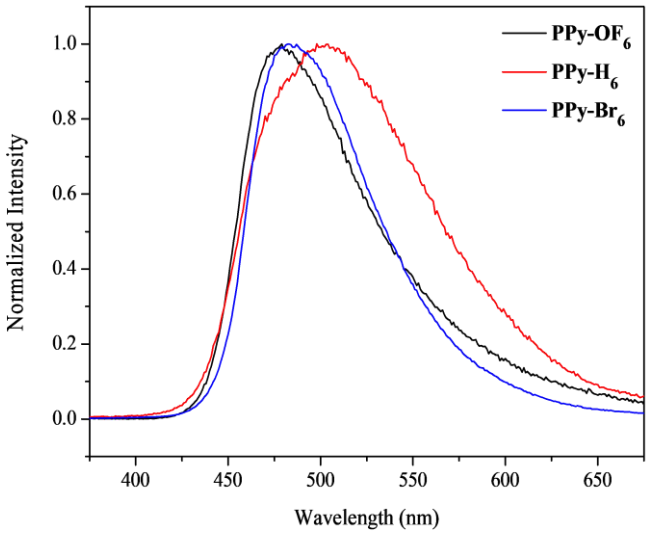

Figure 3.17. Emission spectra for the polypyrene films with number of carbons = 6. Polymerization in solution 0.1 M Bu_4NClO_4/acetonitrile. Number of scans: 2. Deposition in ITO plates.

Moreover, examples of fluorescence and transmission confocal images in **Figure 3.18** show all the polymer films emitted in the green region. Indeed, the fluorescence intensity of the spherical particles formed on the surface are much stronger compared with places that have less polymer. As the number of scans increases we observe also an increase in the fluorescence intensity. In fluorescence and transmission confocal microscopy, we were able to observe the aggregates formed using branched and linear alkyl chains as well as the smooth films produced by PPy-TEG and pyrene bearing long linear chains. The fluorescence confocal images well corroborate the SEM images and similar topographies are observed whatever the sample is.

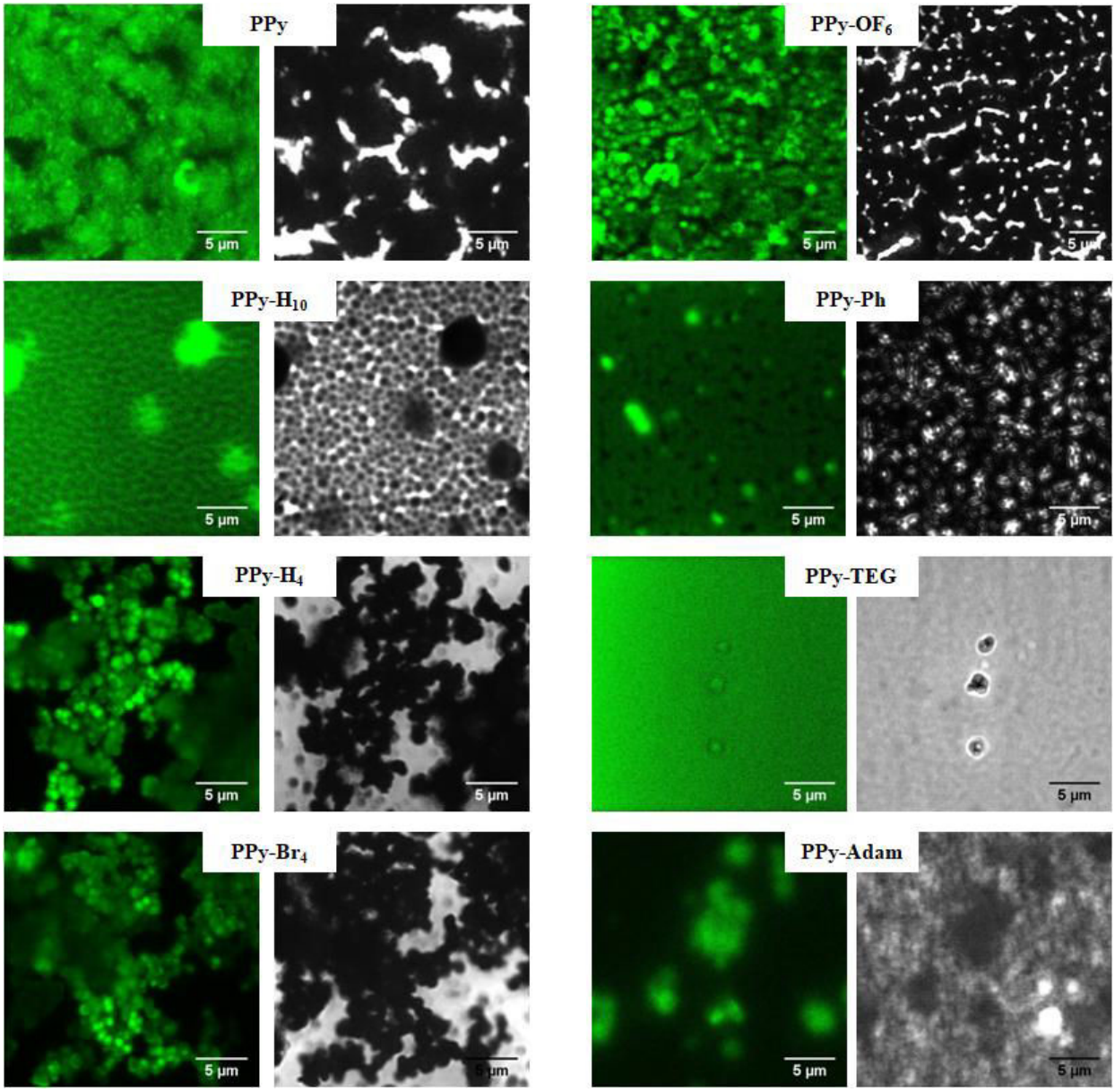

Figure 3.18. Confocal fluorescence microscopy of polypyrene films: fluorescence mode (left) and transmission mode (right). Polymerization in solution 0.1 M Bu_4NClO_4/acetonitrile. Number of scans: 2. Deposition in ITO plates.

3.5 ANTI-BACTERIAL PROPERTIES

By taking advantage of the versatile properties of polypyrene films, bacterial interaction tests were performed under different conditions for the following polymers: PPy-OF_6, PPy-H_4 and PPy-Br_4. It is known that superhydrophobic surfaces provide good bacterial-resistance due to the presence of air inside the surface roughness and for this purpose the fluorinated pyrene was used.[24–27] Indeed, PPy-OF_6 showed a

superhydrophobic behavior with a very low water adhesion (H = 1° and α = 1°) with good stability towards the electrochemical parameters as showed in *Section 3.3*. Therefore, non-fluorinated polymers can also provide a reduction on bacterial adhesion as showed by Bruzaud and co-authors.[28] For this purpose, PPy-H_4 and PPy-Br_4 were used for this study. Then, the aim here was to evaluate the influence of the surface chemistry, morphology and wettability of these polymer films under two different bacteria strains (Gram-positive and Gram-negative). *Staphylococcus aureus* is a Gram-positive bacteria in the form of a *coccus* with a diameter of 0.5 – 1 µm while *Pseudomonas aeruginosa* is a *bacillus* and Gram-negative bacteria with a diameter of 1 – 2 µm. Both *S. aureus* and *P. aeruginosa* have been recognized among the most frequent cause of biofilm-associated infections and recently included by the World Health Organization in the list of the most critical multidrug resistant bacteria considered as particular threat in hospitals.[29] For this reason, they were chosen as representative for this study. The detailed procedure for the bio-experiments is described in ***Annex A3.3***. This work was done in collaboration with the MS Gabriela Morán Cruz and Prof. Rachel Méallet-Renault from the Université Paris-Saclay (Institut des Sciences Moléculaires d'Orsay - ISMO), in Orsay, France.

The bacterial interaction on the films was tested by static incubation for 2 h (bacterial adhesion) and 24 h (biofilm formation) with the two bacterial stains (*S. aureus* and *P. aeruginosa*). The quantitative results presented correspond to zoom 1 which represents a larger area of analysis while the confocal images were presented for zoom 3 to provide better observation. A reduction on the bacterial adhesion was obtained for all the polypyrenes compared with the glass control for both strains studied as shown in **Figure 3.19**. The fluorinated and non-fluorinated polymer films showed a reduction on the bacterial adhesion of 90% and 30%, respectively, as compared to the glass control for *S. aureus* strain. For *P. aeruginosa*, the percentage of bacteria coverage (%cover) on the surface is 11% for PPy-OF_6, 7% for PPy-H_4 and 9% for PPy-Br_4, reducing in ~70% the bacterial adhesion towards the control. These results showed a significant reduction of the bacterial adhesion on polypyrene films independent of the substituent. After longer time of incubation, the biofilm formation could be evaluated. **Figure 3.19** shows that for *S. aureus* the %cover on the surface is ~90% for the glass control whereas for PPy-OF_6 is 1%, for PPy-H_4 is 5% and for PPy-Br_4 is 6%. Similar results were obtained for *P. aeruginosa*: a %cover is ~90% for the glass control and ~9% for the polypyrenes. Since biofilm formation is considered a major hazard because (i) is irreversible, and

(ii) it can promote further infections by the detachment of new bacteria capable to spread and continue the colonization cycle [30], it is necessary to find new materials in order to prevent it. Here we demonstrate that even if the bacterial adhesion is not completely avoided, it does not necessarily lead to biofilm formation. These results show promising potential polymer films for the fluorinated and non fluorinated pyrenes against biofilm formation and subsequent antimicrobial resistance. Even exhibiting few differences in the %cover for the bacterial adhesion and the biofilm formation, all the polymers tested here are capable to avoid the bacteria interaction.

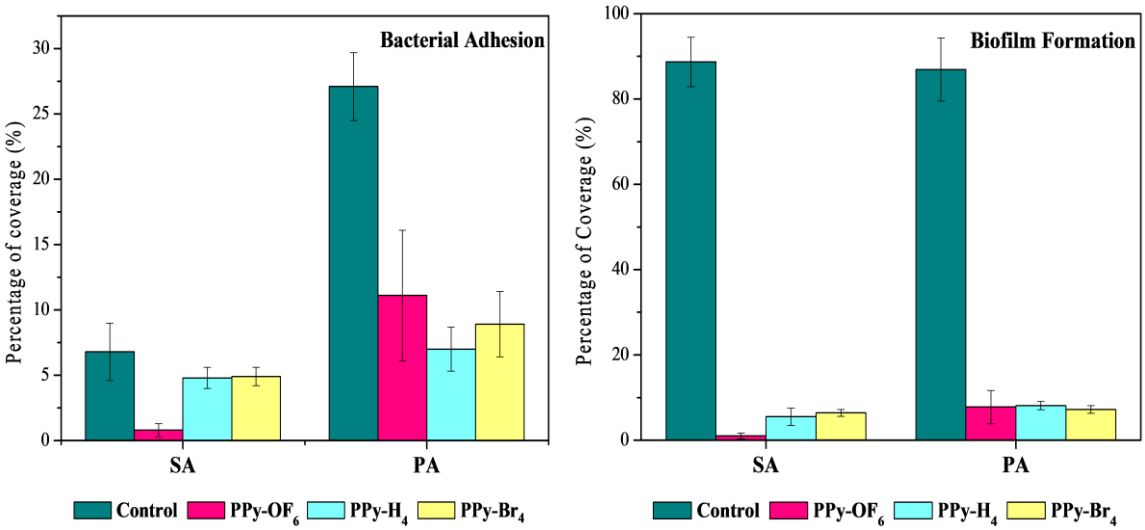

Figure 3.19. Average percentage of coverage (%cover) after incubation of 2 h (bacterial adhesion) and 24 h (biofilm formation) for *S. aureus* (SA) and *P. aeruginosa* (PA) for the polypyrene surfaces and glass control.

These results are supported by the confocal images in **Figure 3.20** and **Figure 3.21**. The adhesive behaviors of *S. aureus* and *P. aeruginosa* were different, which might be explained by the bacterial structure. For *S. aureus*, the surface morphology has a huge influence in the bacterial adhesion as well as the wettability. Since PPy-OF_6 present good polymer coverage (see fluorescence images) and hierarchical structure with the presence of trapped air between the microstructures (Cassie-Baxter state), it seems to be more effective to avoid the bacterial attachment than the surfaces in the composite state, as for the PPy-H_4 and PPy-Br_4. Indeed, the higher heterogeneity of the polymer coverage and higher thickness (~15 µm for PPy-OF_6 and ~40 µm for PPy-H_4) for the non-fluorinated polymers contributes to get more bacteria attached showing an

increase in 60% in bacterial coverage compared with the fluorinated polymer after 2h of incubation. Valle and co-authors reported similar results for *S. aureus* in a modified polystyrene surface where the microstructures topography favors the adherence of *S. aureus* whereas nano-microstructures reduced it.[31]

Looking forwards to *P. aeruginosa* results, no significant differences were found for the bacterial interaction for the three polymers in both incubation times. This can be due to the fact that *P. aeruginosa* has bigger size than *S. aureus*, which hinders the high dependence of the polymer structures. Indeed, the higher %cover for both bacterial adhesion and biofilm formation for *P. aeruginosa* than for *S. aureus* can be explained by the presence of appendages which favors the adhesion of *P. aeruginosa* on surfaces in general.

Herein, the morphology of the polypyrenes surfaces allows a mechanical anchoring between the bacteria and the structure. It is clear that this connection is generally a physical engagement when no higher %cover of biofilm is formed on the surface for a long incubation time. In the literature is reported many studies where the morphology is the main responsible for the bacterial avoiding,[32–34] including a natural example of the cicada wings.[35,36] Indeed, the high hydrophobicity of the polypyrene surfaces favors the repellence of the bacteria attachment for both strains. However, for *S. aureus* strain, the superhydrophobic behavior of the fluorinated polymer favors bacterial repellence when compared with the hydrophobic non-fluorinated pyrenes.

The toxicity of the polymer films was determined by the ratio of each dye (SYTOX® Red/FM®5-95) for the PPy-OF_6 surface. Most of the bacteria observed on the glass control and the fluorinated surface were viable. Less than 0.5% of dead bacteria were found suggesting a non-toxicity of PPy-OF_6 films as well as the glass control.

To summarize, the bacterial adhesion was reduced between 60-90% for the fluorinated polymer and between 30-70% for the non fluorinated polymers for both bacterial strains, having comparable repellent efficiency effect with previously reported superhydrophobic surfaces (reduction of bacterial adhesion of 50-90%).[37,38] Although bacterial adhesion was not completely avoided, biofilm formation was totally prevented by reducing the %cover of the polypyrene films in 90-99% in *P. aeruginosa* and *S. aureus*, respectively. It demonstrates the capability of polypyrene films in being highly efficient against biofilm formation even if some bacteria can be adhered.

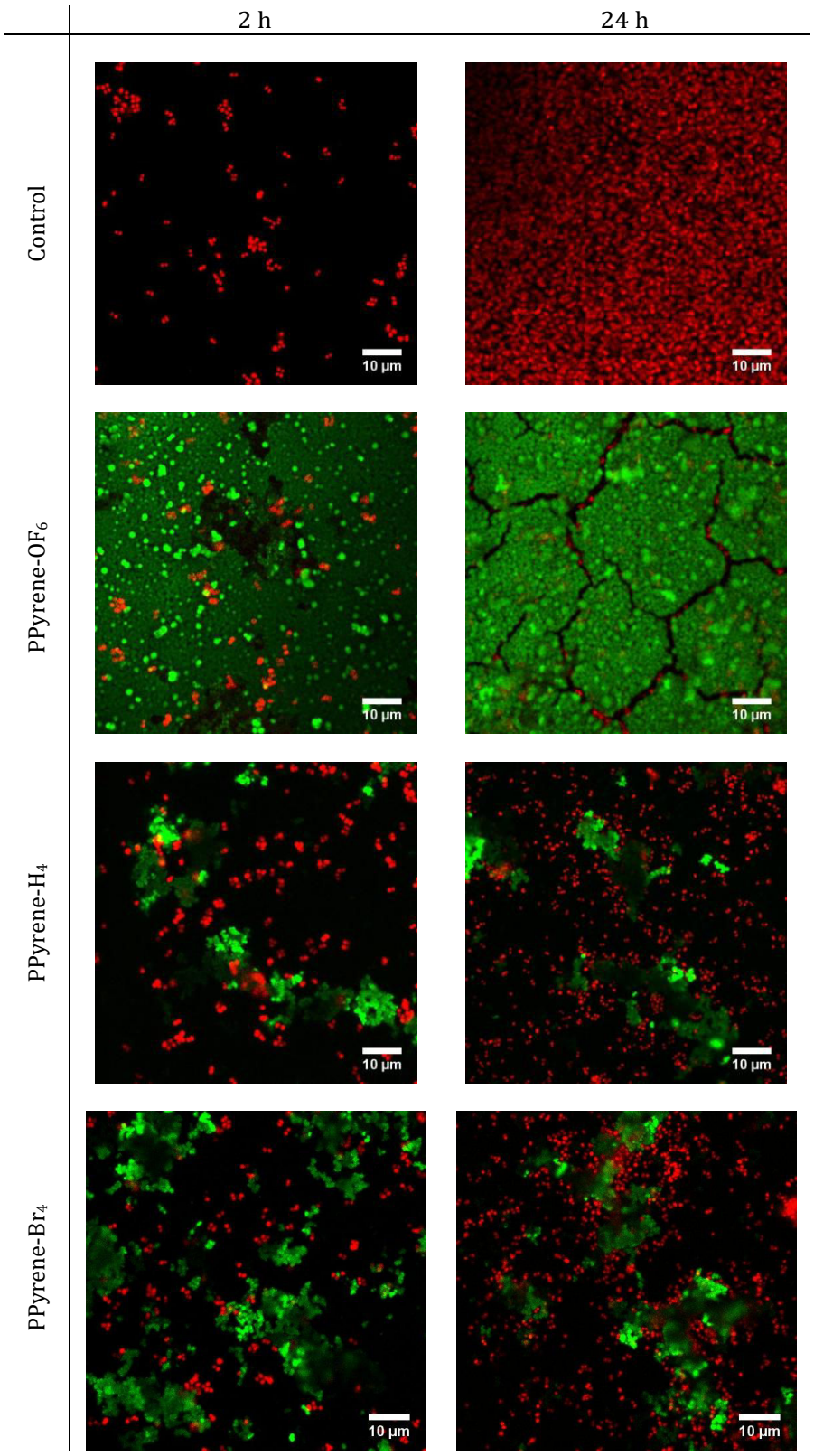

Figure 3.20. Fluorescence imaging of the surfaces after 2 h and 24 h incubation of *S. aureus*. The surrounding medium is an aqueous saline (150 mM) solution. Images taken at zoom 3. Polymer marked in green channel and bacteria (FM®5-95 dye for PPy-OF_6 and SYTO 61 dye for PPy-H_4 and PPy-Br_4) in red channel.

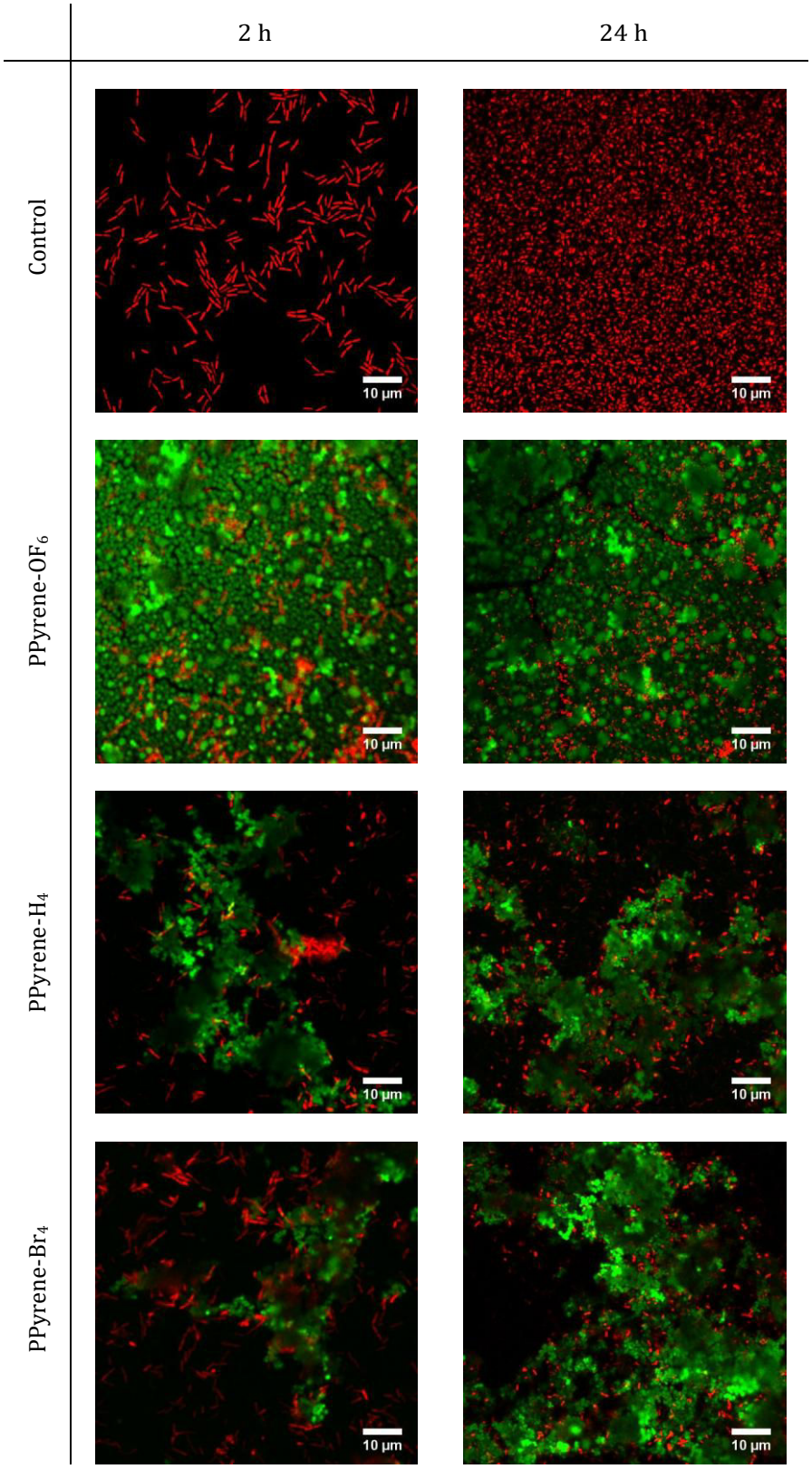

Figure 3.21. Fluorescence imaging of the surfaces after 2 h and 24 h incubation of *P. aeruginosa*. The surrounding medium is an aqueous saline (150 mM) solution. Images taken at zoom 3. Polymer marked in green channel and bacteria (FM®5-95 dye for PPy-OF_6 and SYTO 61 dye for PPy-H_4 and PPy-Br_4) in red channel.

3.6 COPOLYMERS Py-nF_6 *vs* Py-COOH: pH-sensitivity

Following new developments in the wettability of solids, smart surfaces with reversible and switchable wetting properties have attracted recent interest from the scientific community.[39–42] To develop such materials, it is necessary to introduce a material sensitive to the desired stimulus such as light irradiation, thermal/solvent/chemical treatments, electrical fields, counterion exchange, and so on. Indeed, various materials can be used to induce switchable wettability.

Surfaces which are pH-sensitive has been calling attention nowadays due their extend application and easier methods to fabricate.[43] Hiruta and co-workers reported the development of a fluorescent polymer with pH/temperature-responsivity synthesized by reversible addition-fragmentation chain transfer polymerization.[44] They showed results with potential to be applied for the selective imaging of acidic tumor microenvironments for early tumor detection and for tumor-selective intracellular drug delivery systems. In addition, a pH-responsive oil wettability surface was shown by Cheng and co-workers.[45] They reported a copper foil surface which shows superoleophilicity in acidic water and superoleophobicity in basic water which can be achieved thought alteration of pH.

Here we report a way to fabricate electrodeposited copolymers of pyrene with superhydrophobic properties which are able to switch their wettability as a function of the pH by a simple treatment in a basic and acid solution. In this work, copolymers were developed by eletropolymerization using fluorinated pyrenes (Py-OF_6 and Py-NF_6) to reach the superhydrophobicity and Py-COOH as the pH-responsive moiety to switch the water wettability (**Scheme 3.6**). Different proportions of Py-*n*F_6 and Py-COOH were used. Pyrenes bearing ester and amide functions were used to study the influence of the linker in the pH-sensitivity and wettability. Firstly, it will be presented the surface characterization of the copolymers by surface morphology and wettability. Then, the basic and acid treatment will be described followed by the results obtained.

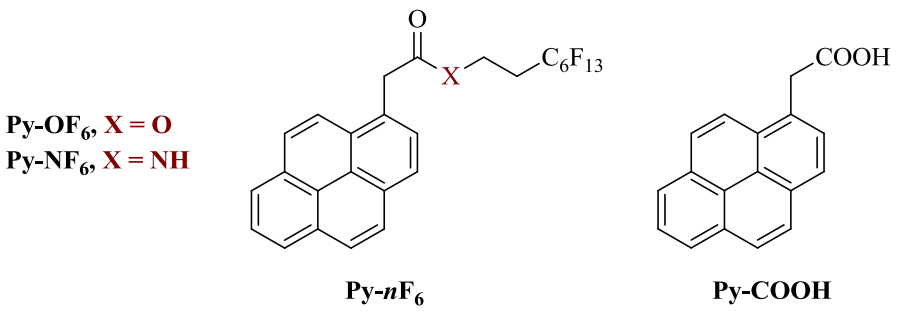

Scheme 3.6. Monomers used for the electro-copolymerization.

3.6.1. Characterization of Surface Morphology and Wettability

The polymeric films are formed by cyclic voltammetry after the 3 deposition scans from a potential -0.7 V to the E^w *vs* SCE at a scan rate of 20 mV s^{-1}. ***Table A2.7*** shows the E^{ox} and E^w for all the copolymers and homopolymers. A solution of 0.1 M of Bu_4NClO_4 in anhydrous acetonitrile was used with 0.01 M in total of Py-*n*F_6 and Py-COOH in molar percentage (mol%). The polymerization was performed in gold-coated plates.

The surface morphology was investigated as function of mol% of each monomer. **Figure 3.22** displays the SEM images for the polymers containing different proportions between Py-OF_6/Py-COOH (left) and Py-NF_6/Py-COOH (right). The homopolymer Py-OF_6 was composed by spherical particles in a micrometer size (diameter ∅ ≈ 2.0 µm) and contains also some rigid and porous nanoroughness on their surfaces as showed previously. The spherical structures are very agglomerate and a rough layer of polymer covered the entire surface. Similarly, the homopolymer Py-COOH also formed spherical particles. However, the particles are smaller compared to the Py-OF_6 (diameter ∅ ≈ 0.7 µm) and are covered by some nanofolds. The influence on the surface morphology as a function of the ratio between Py-OF_6 and Py-COOH monomers during the polymerization was evaluated. As a general trend, reduced number of structures and less agglomerate particles was observed with higher percentage of Py-COOH. The copolymer obtained using a mol% 75% of Py-OF_6 is very similar to the perfluorinated homopolymer presenting some cracks and porous nanostructures on the particles surfaces. However, for a mol% 25-50% of Py-OF_6, the particles covering are more similar to the homopolymer Py-COOH, presenting some nanofolds.

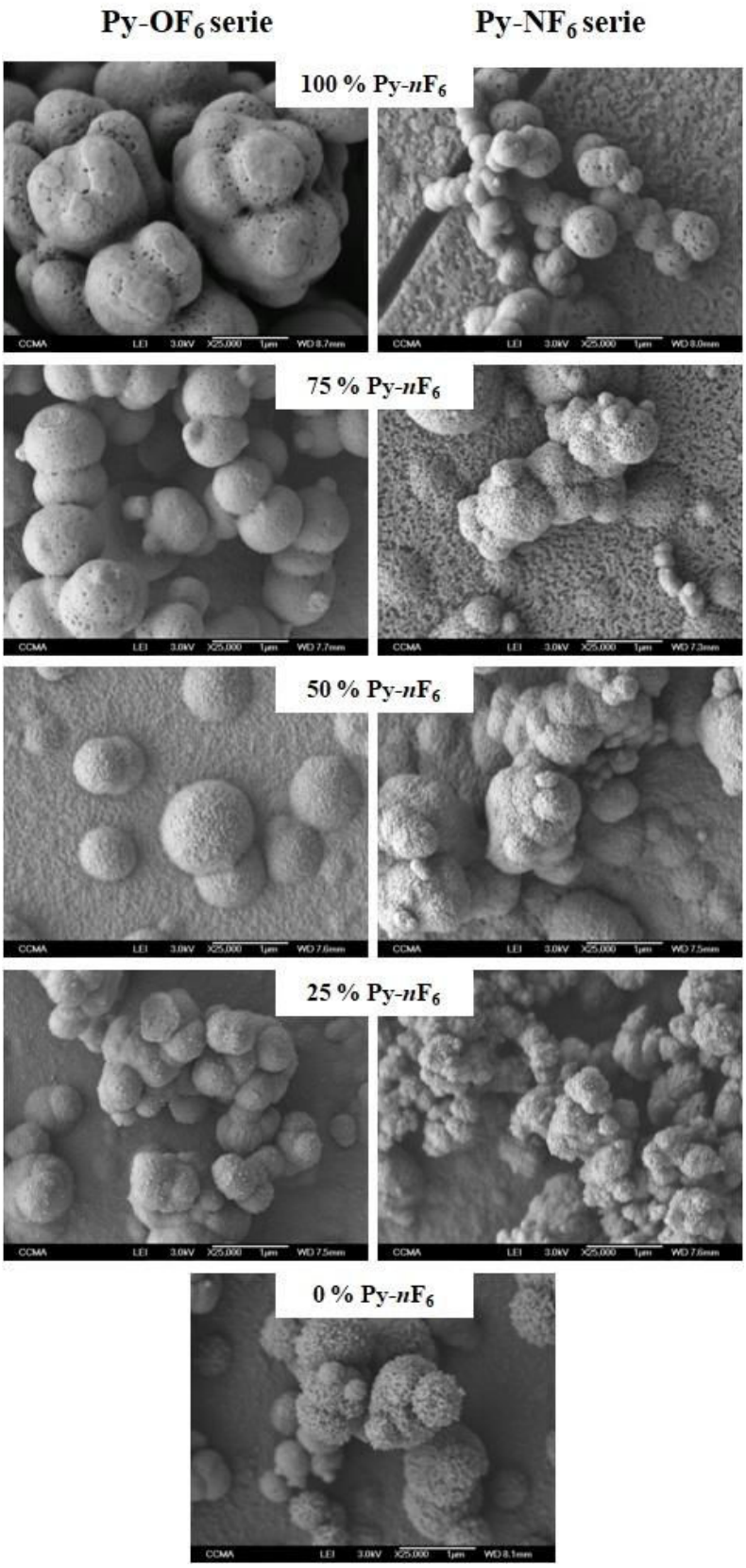

Figure 3.22. SEM images of the copolymers as function of mol% of Py-nF_6 *vs* Py-COOH. Polymerization at 0.1 M Bu_4NClO_4/acetonitrile solution after 3 deposition scans.

For the copolymers using Py-NF_6 *vs* Py-COOH, a similar behavior was observed. Spherical particles covered with porous nanostructures could be seen for the homopolymer Py-NF_6 surfaces. The copolymer with 75% of Py-NF_6 was more similar to the homopolymer Py-NF_6, while the 25% of Py-NF_6 was more similar to the homopolymer Py-COOH. The copolymer with 50% of Py-NF_6 presents an intermediate morphology between both homopolymers used: microstructures very well defined like as Py-NF_6 and the covering more similar to Py-COOH. These changes on the morphologies can be explained by the solubility of the different monomers and polymers formed. Increasing the amount of Py-COOH on the polymerization also increases the solubility of the copolymer formed in acetonitrile which is a very polar solvent.[46] Therefore, when the ratio in mol% of Py-COOH increases in both series (Py-OF_6 or Py-NF_6), the resulting copolymer will present a surface less structured than the previous one. Also, the structures formed by Py-OF_6 and Py-NF_6 presented the same shape, but with different sizes, which can be also due to the oligomers solubility. For the homopolymer Py-OF_6, the spherical particles presented higher diameter (∅ ≈ 2.0 µm), compared to its analogue Py-NF_6 (∅ ≈ 0.8 µm) as a result of the monomers and oligomers solubility solubility.

Curiously, the roughness of the two families of copolymers surfaces is more similar than the homopolymers as presented in **Figure 3.23**. The copolymers with a mol% between 25-75% of Py-OF_6 presented a Ra ≈ 230 nm. For the series with Py-NF_6, the surfaces obtained from 25-50% of Py-NF_6 showed a Ra ≈ 300 nm, while increasing the amount of Py-NF_6 to 75% reduces the roughness. By contrast, the homopolymers presented a different roughness. The fluorinated homopolymer for the Py-OF_6 series presented the highest roughness, as already indicated by the SEM images, with a Ra = 580 nm while its analogue Py-NF_6 seems to be around 5 times less rough (Ra = 114 nm). The homopolymer Py-COOH showed the lower roughness for all the surfaces presented in this work, with Ra = 94 nm.

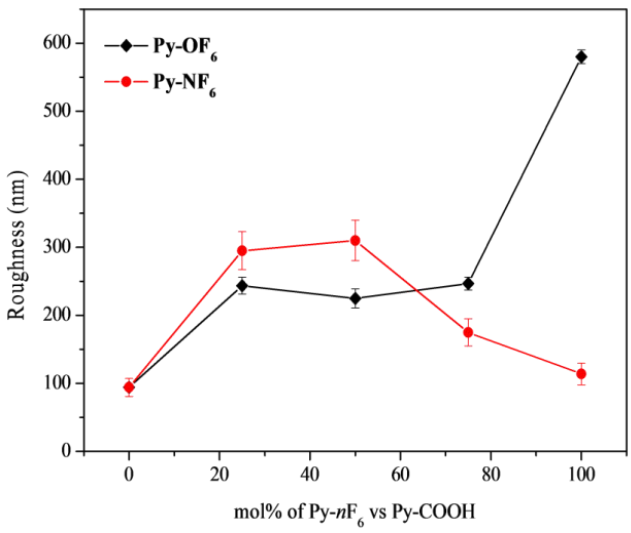

Figure 3.23. Roughness data for the copolymers as function of mol% of Py-nF$_6$ *vs* Py-COOH. Polymerization at 0.1 M Bu_4NClO_4/acetonitrile solution after 3 deposition scans.

The apparent contact angle as function of the probe liquid (water, diiodomethane and hexadecane) and the mol% of both copolymers are given in **Figure 3.24** and the dynamic contact angles in **Table 3.13**. Superhydrophobic surfaces with low H and low α were obtained for a mol% between 25-100% of Py-OF$_6$ while for the amide series only for surfaces containing mol% 25-50% of Py-NF$_6$. Surprisingly, the highest θ_w for the amide series were not obtained with the fluorinated homopolymer, but with the introduction of mol% of 50-75% of Py-COOH. This behavior has already been reported in the literature and it may be due to the differences imposed by morphology.[47] The homopolymer Py-COOH is slightly hydrophilic with a θ_w = 85.3º. In addition, high oleophobic properties were obtained with diiodomethane for the fluorinated homopolymers and for both series of copolymers (θ_w ~ 100 - 130º). Indeed, both fluorinated homopolymers are in the limit of oleophobicity using hexadecane as a probe liquid (θ_{hexa} ~ 90º) while the copolymers showed higher wettability increasing with the mol% of Py-COOH.

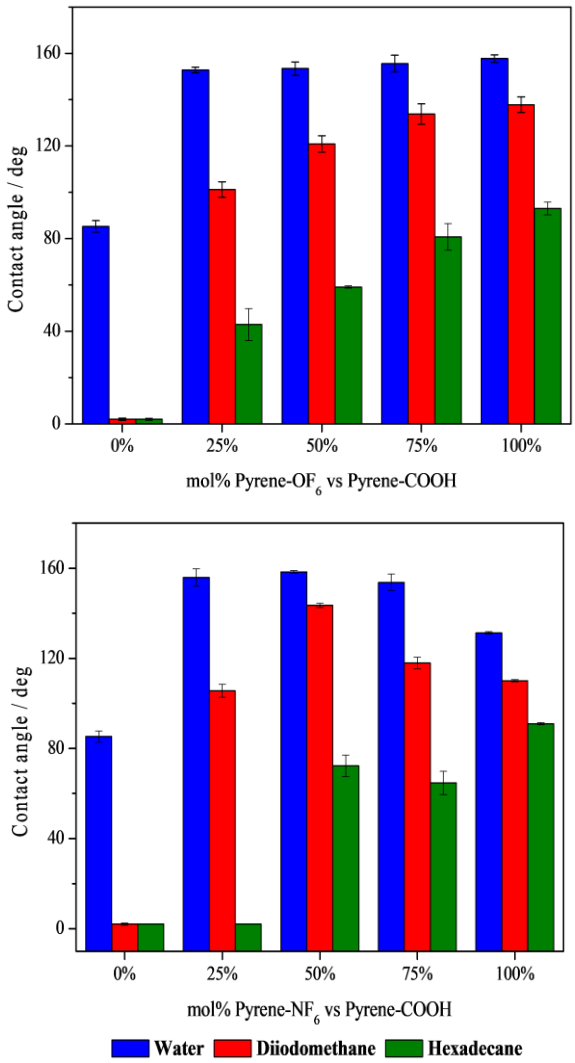

Figure 3.24. Static contact angle of the copolymers as function of mol% of Py-nF$_6$ *vs* Py-COOH. Polymerization at 0.1 M Bu_4NClO_4/acetonitrile solution after 3 deposition scans.

Table 3.13. Dynamic contact angle (hysteresis H and sliding angle α) of the copolymers as function of mol% of Py-nF$_6$ *vs* Py-COOH. Polymerization at 0.1 M Bu_4NClO_4/acetonitrile solution after 3 deposition scans.

% in Py-nF$_6$ *vs* Py-COOH	**Py-OF$_6$**		**Py-NF$_6$**	
	H [deg]	**α [deg]**	**H [deg]**	**α [deg]**
0	> 90º			
25	5.7	5.5	8.3	10.2
50	4.0	3.4	3.4	3.9
75	5.4	4.7	> 90º	
100	1.1	1.1	> 90º	

Tables 3.14 and **Table 3.15** show the θ^Y for all the probe liquids used and their respective surface tension. Both series of copolymers and the homopolymers Py-COOH and Py-NF_6 are intrinsically hydrophilic while the homopolymer Py-OF_6 is intrinsically hydrophobic. The presence of dual-scale structures allows trapping a high amount of air between the surface and the probe liquids which can explain the superhydrophobicity by Cassie-Baxter equation. However, for mol% of 75-100% of Py-NF_6, a composite interface between Wenzel and Cassie-Baxter is observed showing a parahydrophobic behavior.[48] **Figure 3.25** shows the improvement in the hydrophobic behavior of the copolymers from θ^Y_w to θ_w in around 60-80º. The homopolymer Py-COOH, even presenting a structured surface, the θ_w does not change significantly from the inherent θ^Y.

With the increasing in the concentration of Py-COOH, a slight increase in the surface tension was observed for the copolymers. However, a drastic increase in the surface tension of the homopolymer Py-COOH was showed due to its higher polarity when compared with the fluorinated homopolymers. Fluorocompounds are known to be low surface energy materials and for these reasons they are extensively used to obtain super-repellent surfaces due their good wetting properties (normally very high θ).

Table 3.14. Apparent contact angles and roughness data for analogous smooth polymers for mol% of Py-OF_6 *vs* Py-COOH. Polymerization at 0.1 M Bu_4NClO_4/acetonitrile solution after 3 deposition scans.

% mol Py-OF_6	Ra [nm]	θ_w [deg]	θ_{diiodo} [deg]	θ_{hexa} [deg]	γ_{SV} [mN m^{-1}]	γ^D_{SV} [mN m^{-1}]	γ^P_{SV} [mN m^{-1}]
0	10.1	65.6	24.1	0	70.1	36.4	33.7
25	9.2	81.4	45.2	0	74.2	32.1	42.1
50	8.7	81.3	55.7	13.3	34.4	28.9	5.5
75	8.3	87.2	51.6	15.6	33.0	29.9	3.1
100	9.1	90.2	43.6	15.8	33.9	32.0	1.9

Table 3.15. Apparent contact angles and roughness data for analogous smooth polymers for mol% of Py-NF_6 *vs* Py-COOH. Polymerization at 0.1 M Bu_4NClO_4/acetonitrile solution after 3 deposition scans.

% mol Py-NF_6	Ra [nm]	θ_w [deg]	θ_{diiodo} [deg]	θ_{hexa} [deg]	γ_{SV} [mN m^{-1}]	γ^D_{SV} [mN m^{-1}]	γ^P_{SV} [mN m^{-1}]
0	10.1	65.6	24.1	0	70.1	36.4	33.7
25	6.9	72.1	32.9	0	42.7	34.9	7.8
50	6.7	71.5	42.1	0	41.6	32.8	8.8
75	6.9	79.7	55.9	10.1	35.2	29.0	6.2
100	7.3	82.5	46.9	11.0	35.8	31.4	4.4

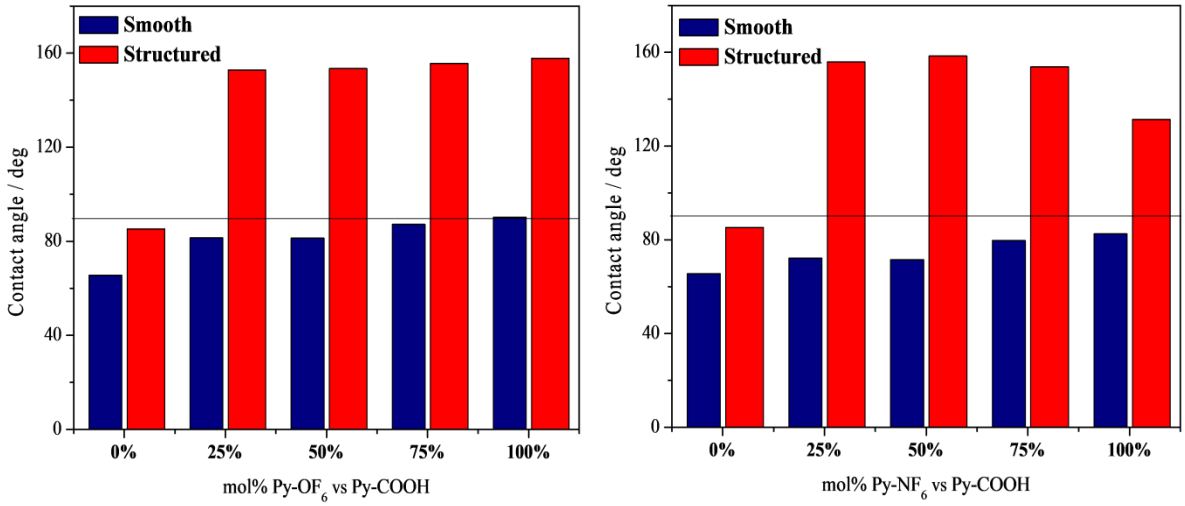

Figure 3.25. Comparison between the apparent contact angles of water for smooth and structured (3 deposition scans) surfaces for the mol% of copolymers of Py-nF$_6$ *vs* Py-COOH. Polymerization at 0.1 M Bu_4NClO_4/acetonitrile. Solid line: 90º.

3.6.2. Surface characterization after pH treatment

To study the effect of pH, the conducting copolymers were firstly submitted to a treatment in aqueous solutions of NaOH (0.01 and 0.1 M) during different times (1, 3 and 5 h). Indeed, a solution of 0.5 M of NaOH was also used in a first test, but an extensive damage on the structures was observed. For this first evaluation, surfaces containing a mol% 75% of Py-OF$_6$ were prepared using 3 deposition scans. Here, we study the treatment in basic media to transform the carboxylic acid groups into the more polar carboxylate anions in order to obtain more hydrophilic θ_w. **Figure 3.26** shows no significant results for θ_w for the solution 0.01 M NaOH even after 5 h of treatment. However, using the more concentrated 0.1 M solution resulted in a switch from θ_w = 152º to θ_w = 75º after 3 h of NaOH treatment. All the times used with this concentration presented switchability, but 3 h showed more homogeneous results compared to 1 h of treatment and not so long time as 5 h. For these reasons, 0.1 M and 3 h were chosen as the optimal NaOH concentration and treatment time, respectively, to continue the study.

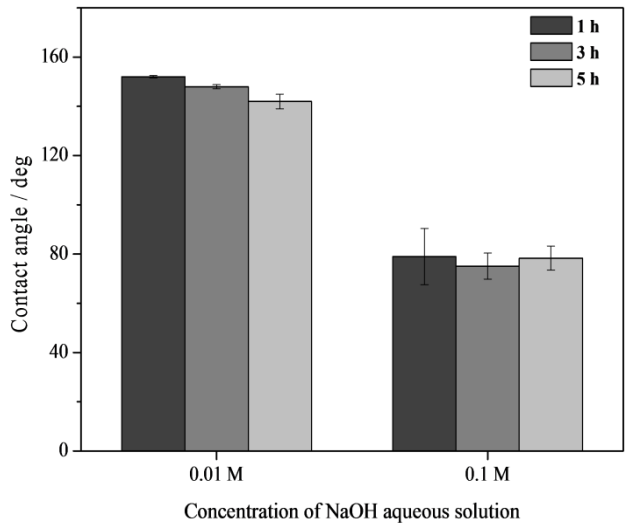

Figure 3.26. Static contact angle of copolymer mol% of 75% of Py-OF_6 *vs* Py-COOH for a treatment in solution 0.01 and 0.1 M NaOH during different times. Polymerization at 0.1 M Bu_4NClO_4/acetonitrile solution after 3 deposition scans.

Then, all the copolymers of mol% of Py-nF_6 *vs* Py-COOH were prepared after 3 depositions scans for the determination of the pH-switchable wettability. They were dipped in 0.1 M NaOH solution during 3 h, washed in acetonitrile and dried for 24 h before the characterization. These results are shown in **Figure 3.27**. The basic treatment induced a high decrease in θ_w for the homopolymer Py-COOH and for a mol% of Py-nF_6 between 25-50%. In contrast, a slighter decrease in the θ_w was also observed for both copolymers with a mol% 75% of Py-nF_6 turning the superhydrophobic surfaces to a hydrophilic (θ_w = 75º) and slightly hydrophobic (θ_w = 91º) for the ester and amide pyrenes, respectively. Clearly, the observed decrease on θ_w for the copolymers depends on the ratio between the hydrophobic component (Py-nF_6) and the sensitive group. As the incorporation of Py-COOH increased, the pH sensibility became higher. Besides, almost no changes could be seen after the basic treatment for the homopolymer Py-OF_6 while a decrease in θ_w of 18º ± 14º was observed for the homopolymer Py-NF_6. The θ_w loss can be explained by the difference of hydrophobic properties between the two materials. The superhydrophobic properties with ultra-low adhesion of homopolymer Py-OF_6 create a high amount of air inside the surface roughness which highly reduces the contact between the surface and NaOH aqueous solution. The homopolymer Py-OF_6 hence shows a high resistance to basic solution even if ester bonds are present.

Then, in order to recover the high hydrophobicity or even the superhydrophobicity on these surfaces, an acid treatment was performed by the immersion of the surfaces in 0.1 M H_2SO_4

aqueous solution during 3 h. After, the surfaces were also washed in acetonitrile and dried over 24 h before the characterization. θ_w for the homopolymer Py-COOH decreases of about 13º compared to the θ_w after the electrodeposition in opposition to the fluorinated homopolymers which recover their previous wettability (before any treatment). All the copolymers reached highly hydrophobic properties after the acid treatment which confirms the sensitivity of the copolymers to acidic and basic solutions.

Nevertheless, the Py-OF_6 copolymers presented a significant θ_w loss compared to Py-NF_6 copolymers after the basic and acid treatment, as presented in **Figure 3.27**. This time, this is due to a difference in pH-sensitivity between the two linkers. The ester functional group from Py-OF_6 is less stable and can be more easily hydrolyzed when the surface enters in contact with highly basic-acid solution and it might undergo the saponification of the ester groups during the basic treatment. The ester hydrolysis reduces the ratio between Py-OF_6 and Py-COOH, which drops the ability to recover the previous wettability. The homopolymer Py-OF_6 seems to be completely stable to the pH variation since no changes in the wettability was observed. However, the copolymers suffered with hydrolysis due to the easily contact of their hydrophilic interface post basic treatment with the aqueous media. In the opposition, the amide functional group from Py-NF_6 is more stable and less reactive to the basic-acid post-treatment than the ester group, being more resistant to the hydrolysis reaction. As a consequence, the copolymers and even the fluorinated homopolymer Py-NF_6 recover in a higher extension their hydrophobicity compared to the Py-OF_6 series.

The switchable process can be better illustrated in **Figure 3.28**. The water droplets on the surfaces of mol% of 50% of Py-NF_6 show that hydrophilic behavior was achieved after basic treatment and the high hydrophobicity could be recovered with the acid treatment. The reversible process could be repeated several times as shown in **Figure 3.29**. Both series exhibited similar behavior after 3 treatment cycles. It is clear that the copolymer with mol% 75% of Py-nF_6 is more robust and resistant to the basic-acid treatment than the copolymer with mol% 50% of Py-nF_6. The higher solubility of Py-COOH plays an important factor here dissolving the film and damaging the structures which, in consequence, decrease the θ_w for these surfaces. In opposition, for mol% 75% of Py-nF_6, the copolymer surfaces maintained the high hydrophobic behavior even after 3 cycles of treatment. The surfaces for both series with high θ_w are presented in the parahydrophobic state after the first cycle keeping the sticky behavior with the lost of the superhydrophobicity. Here, it indicates that the trapped air presented between the microstructures is not so important and the surfaces are now in the

composite state (Wenzel-Cassie-Baxter). Indeed, in the end of the third cycle, the surfaces presented few cracks on their structures which explain the decrease in the θ_w.

In resume, it is possible to reach superhydrophobic properties with switchable wettability to hydrophilic using a mol% 25 - 75% of Py-nF$_6$ *vs* Py-COOH by a basic and acid treatment. These results showed that the copolymer of pyrene may be good candidates to a potential application as bacterial anti-adhesive and adhesive surfaces since superhydrophobic properties are desired for repel bacteria and hydrophilic properties to attract them. Indeed, other potential applications are as non-biofouling material, membranes and sensors, for example.[43]

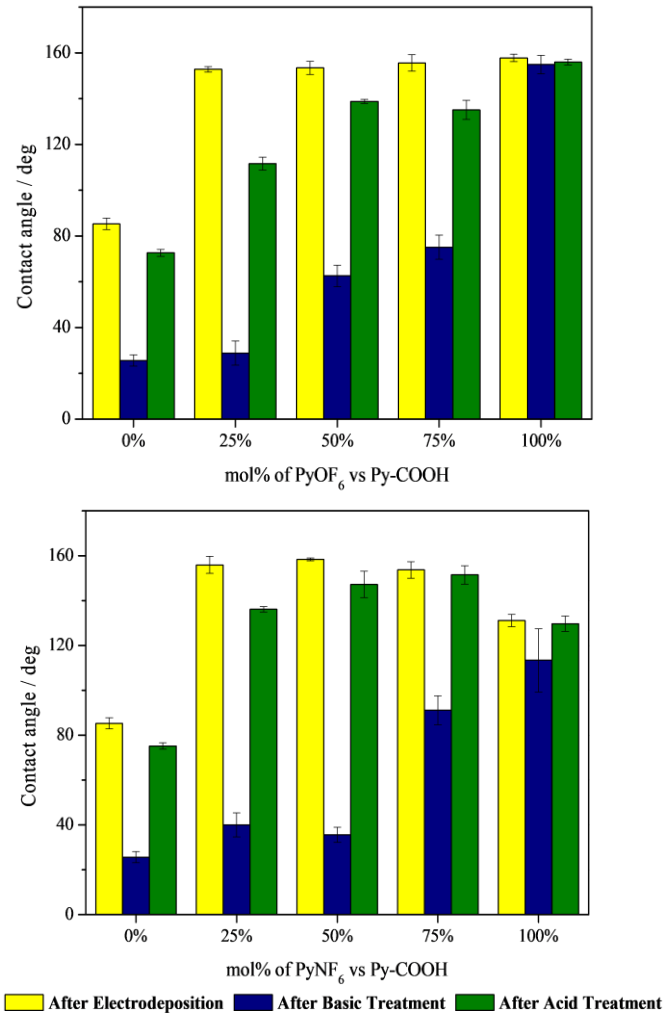

Figure 3.27. Static contact angle of the copolymers as function of mol% of Py-nF$_6$ *vs* Py-COOH after electrodeposition, NaOH and H_2SO_4 treatment. Polymerization at 0.1 M Bu_4NClO_4/acetonitrile solution after 3 deposition scans. Basic and acid treatment at 0.1 M aqueous solution and during 3 h of immersion.

Figure 3.28. Water droplet pictures after electrodeposition, basic treatment and acid treatment, respectively, on copolymer of mol% 50% of Py-NF_6 *vs* Py-COOH. Polymerization at 0.1 M Bu_4NClO_4/acetonitrile solution after 3 deposition scans. Basic and acid treatment at 0.1 M aqueous solution and during 3 h of immersion.

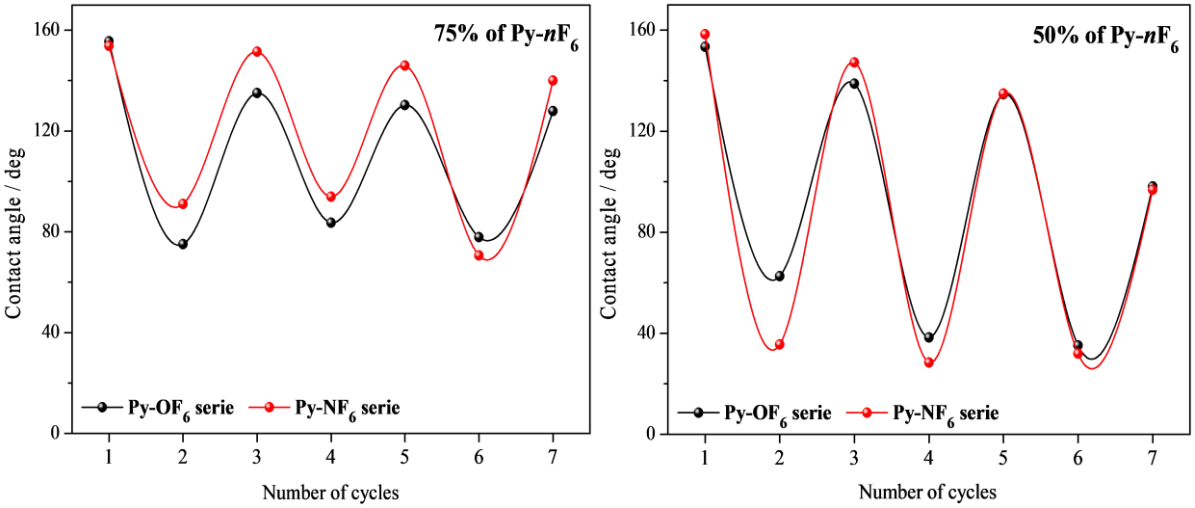

Figure 3.29. Reversible switching of the θ_w for the copolymer surfaces after 3 cycles of basic-acid treatment. Polymerization at 0.1 M Bu_4NClO_4/acetonitrile solution after 3 deposition scans. Basic and acid treatment at 0.1 M aqueous solution and during 3 h of imm

3.7 COPOLYMERS Py-OF_6 *vs* Py-Adam: water adhesion control

The control of both surface hydrophobicity and water adhesion is extremely important for various potential applications in water transport/harvesting and oil/water separation membranes, for example.[1] The most used method to evaluate the water adhesion in surface science is by the determination of the dynamic contact angle, such the hysteresis H, α, θ_{adv} and θ_{rec}, for example. The H, as already mentioned, is the difference of the θ_{adv} and θ_{rec} for a contact line moving in an opposite direction at the same velocity. Many are the methods used

to measure the water adhesion of non-sticky surfaces, such as tilted plate method, captive balance method, Wilhelmy method, etc.[49] However, there are few methods which are possible to measure the water adhesion of sticky surfaces. For example, works reported in the literature by Jiang and Law showed the development of a technique to measure the water adhesion using a microelectronic balance, which consists in measuring the adhesive forces when a drop of water touches a surface.[50,51]

In this work, all the measures of the H and α were done by the tilted drop method which is a very simple method requiring only a camera. Even though it is the most used method, there are some concerns about it. Krasovitski and Marmur showed a limitation on the hysteresis measure by only analyzing the shape of a droplet for an inclined substrate.[52] They reported that the droplet may begin to move while the advancing or receding angles are not reached. Indeed, they will not be necessarily equivalent to θ_{max} and θ_{min} for the droplet, respectively. Similar results were presented by Pierce and co-workers.[53] They showed that the shape and the placement of the droplet can have a significant influence in the wetting properties as well as the θ_{max} and θ_{min} when the surface is tilted.

With this aim, here we propose a novel experimental technique in order to determine the adhesion of a water droplet placed on a substrate of various water adhesions (from sticky to non-sticky). The novel test implemented consists in the ejection of water droplets placed on the substrates using a catapult system. For this study, two pyrene derivatives were selected: one with a perfluorohexyl chain (PPy-OF_6) to reach low water adhesion and one containing an adamantyl substituent (PPy-Adam) to reach high water adhesion (**Scheme 3.7**). We report the influence of percentage of each monomer on the surface morphology, hydrophobicity and water adhesion of the resulting copolymers. The detailed procedure for the ejection test is described in ***Annex A3.4***. This work was done in collaboration with the Prof. Franck Celestini and Dr. Christophe Raufaste from the Institut de Physique de Nice, in Université Côte d'Azur, in Nice, France.

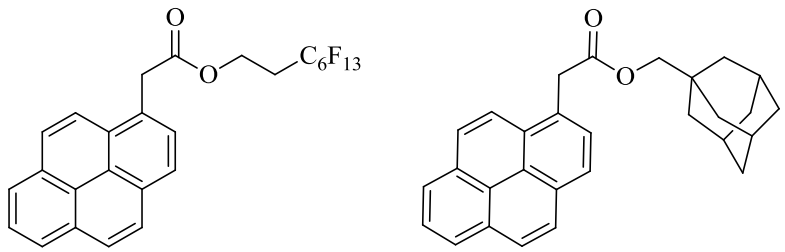

Py-OF$_6$ **Py-Adam**

Scheme 3.7. Monomers used for the electro-copolymerization of water adhesion control copolymers.

3.7.1. Characterization of Surface Morphology and Wettability

The electropolymerization of the copolymer surfaces was performed by cyclic voltammetry using an anhydrous acetonitrile solution with 0.1 M of Bu_4NClO_4 containing 0.01 M of pyrene monomer (Py-OF$_6$ + Py-Adam) in mol% in different proportions of each monomer. The copolymers were electrodeposited in ITO plates from -0.7 V until the E^w (1.56 – 1.59 V) at a scan rate of 20 mV s^{-1}. The E^{ox} obtained for each copolymer was between 1.60 – 1.66 V. ***Table A2.8*** shows the E^{ox} and E^w for all the copolymers and homopolymers. Two deposition scans were chosen because that leads to the highest hydrophobic properties with the homopolymer PPy-OF$_6$ using ITO plates.

The SEM images of the copolymers are given in **Figure 3.30** and the surface morphology was investigated as function of the mol% of each monomer. The morphology of the copolymers is relatively similar and composed of large microspheres similar as for the gold-coated plates. The homopolymer PPy-OF$_6$ was composed by spherical particles in a micrometer size (∅ ≈ 1.5 µm) which contain some nanoroughness on their surfaces. Similarly, the homopolymer PPy-Adam also formed spherical particles with raspberry shape and a mean diameter ∅ ≈ 1.0 µm. Here, the size of the spheres did not show a significant change, but their form changed from round spheres to raspberry-like shape from PPy-OF$_6$ to PPy-Adam, respectively. **Figure 3.31** shows the approximate SEM images for closer inspection. Contrary to other monomers where it was shown that the composition can highly change the surface morphology and the particles size due to difference in polymer solubility,[54–56] here the substituent effect is less important. Indeed, the polymerization degree (PD) data already suggested a similarity in the polymerization behavior for Py-OF$_6$ (PD = 1.34) and Py-Adam (PD = 1.41). This is may be caused by the solubility and the steric hindrance, since both monomers are voluminous. For

the copolymers, the shape of the particles turns more similar to raspberry-like structures as the mol% of Py-Adam increase. In addition, smaller particles can be also seen on the surface of the copolymers varying their size from ∅ ≈ 0.3 - 1.0 µm.

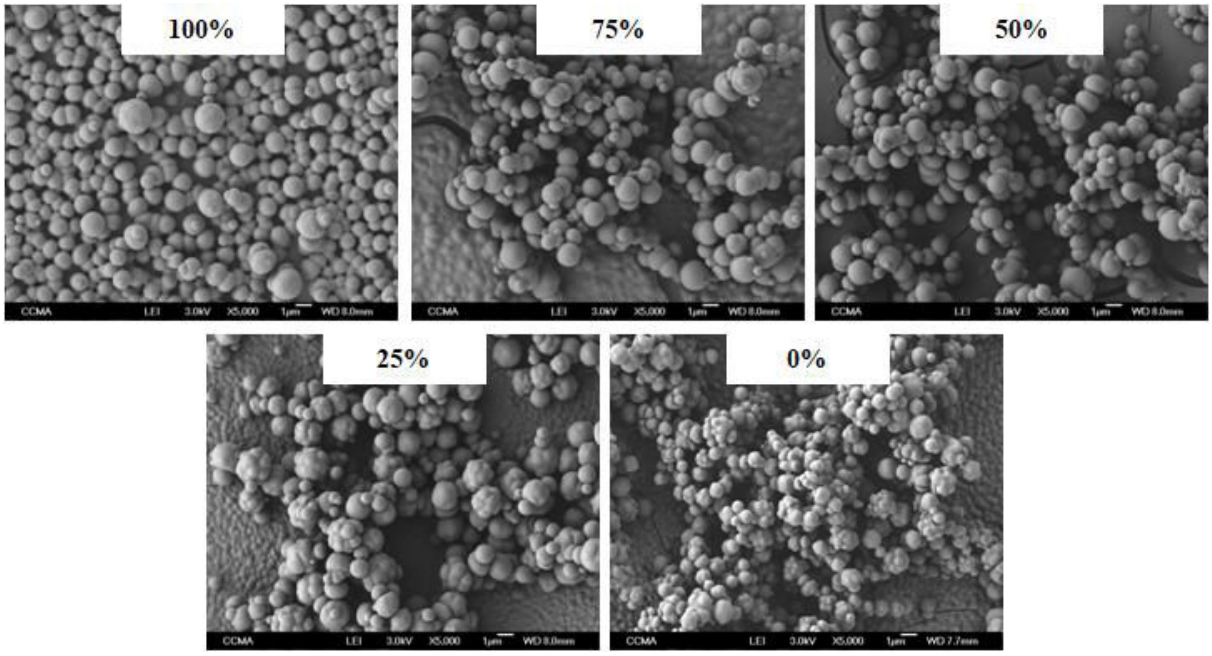

Figure 3.30. SEM images of the copolymers as function of mol% of Py-OF_6 *vs* Py-Adam. Polymerization at solution 0.1 M Bu_4NClO_4/acetonitrile. Number of scans: 2. Deposition in ITO plates.

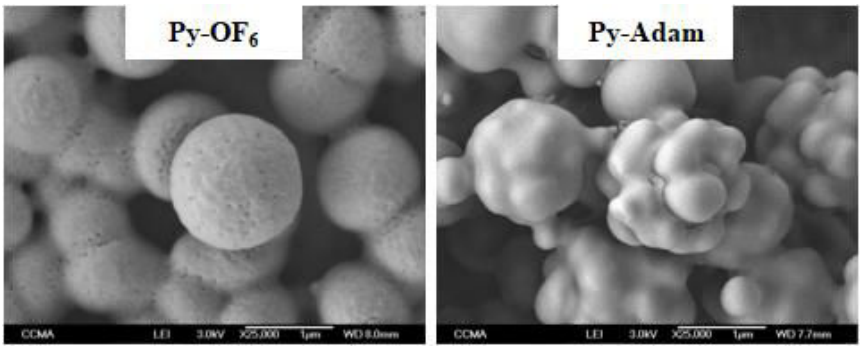

Figure 3.31. SEM images of the homopolymers Py-OF_6 and Py-Adam. Polymerization at solution 0.1 M Bu_4NClO_4/acetonitrile. Number of scans: 2. Deposition in ITO plates.

Although the particles shape change with the mol% of each homopolymer, the roughness does not change significantly for the copolymers (Ra ≈ 0.6 µm). Regarding the homopolymers, they both present also a similar roughness (Ra ≈ 1.2 µm) due to the presence of bigger particles in the surface, which can explain the differences observed when comparing the roughness of the homopolymers and copolymers.

Interestingly, even if the roughness of the homopolymers is similar, their wetting properties are different. **Figure 3.32** gathers the contact angles for different probe liquids. The homopolymer PPy-OF_6 is superhydrophobic with θ_w = 156º and ultra-low H and α as already showed before. A water droplet placed on this substrate can be moved very easily due to almost no adhesion between the substrate and the droplet. By contrast, the homopolymer PPy-Adam is parahydrophobic with θ_w = 105º and extremely high adhesion. A water droplet placed on this substrate does not move even if the substrate is tilted to 90º. **Figure 3.33** shows the moment when both surfaces are tilted to measure their dynamic properties. For the copolymers, θ_w increases from 105° to 115° and 140º with the introduction of mol% 25% - 50% of Py-OF_6, respectively, but the substrates remained completely sticky. Then, when mol% of Py-OF_6 increases to 75%, θ_w increases yielding a superhydrophobic state (θ_w = 155º) with very low water adhesion (H = 6º and α = 5º). Here the results are better distributed in the wetting range of both homopolymers due to their similar behavior in the electropolymerization confirmed by the polymerization degree data, differing from the wettability results observed for the copolymer series for Py-nF$_6$ *vs* Py-COOH where the solubility of Py-COOH is higher than the perfluorinated pyrenes. As expected, the higher oleophobic properties were found for the homopolymer PPy-OF_6 (θ_{diiodo} = 138º and θ_{hexa} = 108º). All the copolymers and the homopolymer PPy-Adam are oleophilic for both liquids.

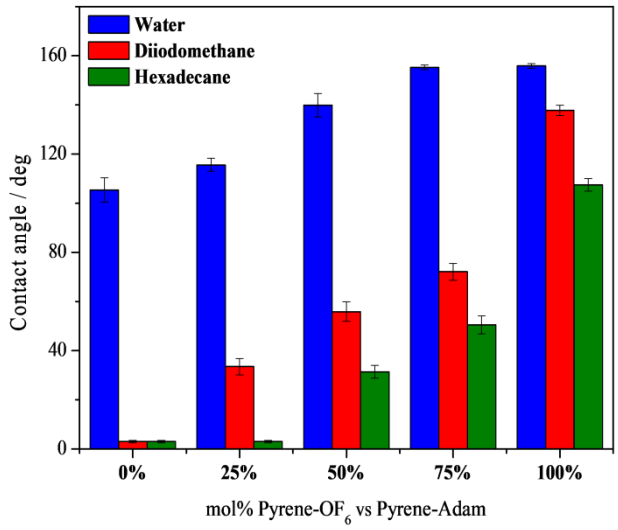

Figure 3.32. Static contact angle of the copolymers as function of mol% of Py-OF_6 *vs* Py-Adam. Polymerization at solution 0.1 M Bu_4NClO_4/acetonitrile. Number of scans: 2. Deposition in ITO plates.

PPy-OF_6	PPy-Adam
	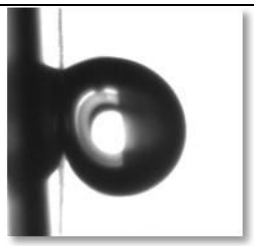
H = 1.3º ; α = 2.0º	α = 90º

Figure 3.33. Dynamic contact angle of the homopolymers PPy-OF_6 and PPy-Adam. Polymerization at solution 0.1 M Bu_4NClO_4/acetonitrile. Number of scans: 2. Deposition in ITO plates.

Regarding the smooth surfaces and the surface energy of the analogous copolymers, **Table 3.16** shows that only PPy-OF_6 is intrinsically hydrophobic while the other copolymers and the homopolymer Py-Adam are intrinsically hydrophilic. As usual for polypyrene surfaces, using Cassie-Baxter model, it is possible to explain these results due to the presence of air between the substrate and the water droplet. As mentioned before, the presence of trapped air is important for superhydrophobic surfaces and less important for parahydrophobic surfaces due to the presence of an intermediate state.[12] The greatest increase in θ_w from the inherent θ^Y is for the copolymer mol% 75% of Py-OF_6 with a wetting gain of 74º, but all the polymers and copolymers showed an improvement in the wettability (range from around 32 – 66º) (**Figure 3.34**).

Hence, because the surface morphology of all the copolymers is quite similar, we expected that the water adhesion increases as the mol% of Py-Adam increases as the polymer surface energy also increases. However, until the tilted angle reached, it is not possible to determine the difference in the water adhesion for surfaces with %mol of Py-Adam > 50% because the water droplet stuck. At this point, it is extremely important to develop a novel technique in order to discriminate the water adhesion of these sticky substrates.

Table 3. 16. Apparent contact angles and roughness data for analogous smooth polymers for mol% of Py-OF_6 *vs* Py-Adam. Polymerization at solution 0.1 M Bu_4NClO_4/acetonitrile. Number of scans: 2. Deposition in ITO plates.

% mol Py-OF_6	Ra [nm]	θ_w [deg]	θ_{diiodo} [deg]	θ_{hexa} [deg]	γ_{SV} [mN m^{-1}]	γ^D_{SV} [mN m^{-1}]	γ^P_{SV} [mN m^{-1}]
0	8.5	73.0	33.9	0	42.2	34.7	7.5
25	8.0	75.1	34.1	0	41.2	34.6	6.6
50	7.4	80.2	33.5	0	39.2	34.8	4.4
75	8.9	81.4	36.5	0	38.3	34.1	4.2
100	9.1	90.2	43.6	15.8	33.9	32.0	1.9

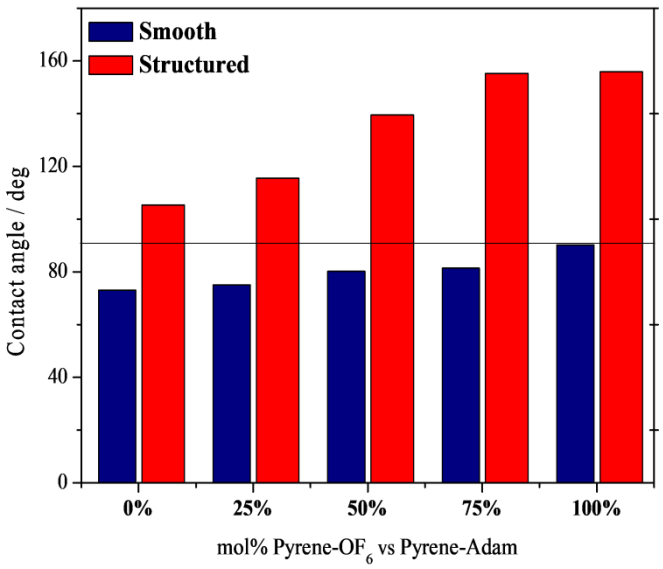

Figure 3.34. Comparison between the apparent contact angles of water for smooth and structured (2 deposition scans) surfaces for the %mol of copolymers Py-OF_6 *vs* Py-Adam. Polymerization at 0.1 M Bu_4NClO_4/acetonitrile. Solid line: 90º.

3.7.2. Water adhesion by ejection tests

In order to better evaluate the water adhesion of the surfaces described in the previous section and compare with the dynamic contact angle data, a novel technique was implemented. In this technique, a water droplet placed on a substrate is ejected using a catapult-like apparatus as illustrate in **Figure 3.35**. The catapult is initially loaded and maintained at rest position with an electro-magnet. A water droplet is placed on the substrate and then the electro-magnet is switched-on. The substrate is submitted to a sudden and large acceleration and, as a consequence, the water droplet is ejected from the substrate with a velocity dependent of the

amplitude of the initial substrate position and the surface adhesive behavior. An ultra-fast camera at the frequency of 4000 images per second was used to register the droplet trajectory. Different experiments were performed for initial deflections allowing us to vary the experimental parameters. Here, we will evaluate the capacity of the water droplet to leave each surface in the load amplitude A (position) by regarding their velocity of the plate/substrate, V_p, and velocity of the water droplet, V_g, both in the ejection time, t_e. The images taken will provide the information about the water droplet trajectory with the droplet shape and its possible fragmentation after ejection. The water adhesion is direct related to the droplet fragmentation: as faster (this is, for lower V_p) as the droplet fragment, more adhesive the surface is.

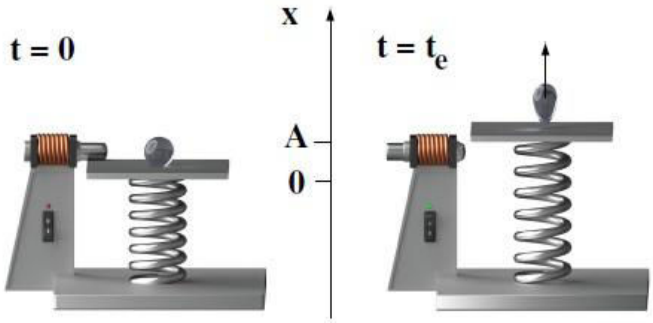

Figure 3.35. Schematic representation of the catapult-like apparatus. The first image displays the experimental setup loaded and maintained with an electro-magnet in the rest position. In the second image, the plate is suddenly accelerated and the droplet is ejected with a V_g at the take-off time (t_e).

To provide the results for this study, copolymers of mol% 50 - 100% of Py-OF_6 *vs* Py-Adam were used due to their water adhesion behavior. Surfaces with mol% 75 - 100% of Py-OF_6 provide superhydrophobic behavior with low water adhesion. In addition, to better evaluate the ejection test and find an approach to measure the water adhesion of sticky surfaces, the copolymer with mol% 50% of Py-OF_6 was also studied because it presents high water adhesion as measured by the tilted drop method.

Snapshots of the water droplets ejection are showed in **Figure 3.36** for a given V_p. The images were taken at a same range of amplitude ($A \approx 0.30$ cm) for all the surfaces before the water droplets fragmentation for the first surface (mol% 50% Py-OF_6). Each copolymer is represented by 4 images with the main steps of the water droplet ejection: first at rest position on the copolymer/homopolymer substrate, second during the initial acceleration of the plate,

third at the take-off time (ejection) and finally fourth during its flight. The size of the water droplet is taken into account and is kept constant for all the analysis (∅ ≈ 1.3 mm).

Here, the trajectory of the water droplet is quite similar for all the surfaces analyzed. Upon a closer inspection in the third and fourth images, there appears a slight difference in the shape of the water droplet after ejection from the surface. The droplet ejected from the homopolymer surface returns for its own droplet shape slightly faster than for the copolymer with mol% 75% of Py-OF_6 which in turn returns faster than for the copolymer with mol% 50% of Py-OF_6. This is not surprising because the V_g is related with the surface adhesion; this is, with the facility which the water droplet leaves the surface. Indeed, it is already noticed by dynamic contact angles measures that the water adhesion increases with the mol% of Py-Adam. For surfaces with mol% 50% of Py-OF_6, when $V_p > 0.68$ m/s, a multiple fragmentation of the water droplet happens as showed in **Figure 3.37**. It is clearly seen that in the ejection time, a droplet wire rest adhered on the surface when the "round" droplet is leaving, indicating a very adhesive behavior. In the sequence, this water wire fragmented in two parts: a very small water droplet that remains adhered on the surface while the water wire flies. In the last images, a multiple fragmentation of the water wire is observed during the flight.

100% Py-OF_6	75% Py-OF_6	50% Py-OF_6
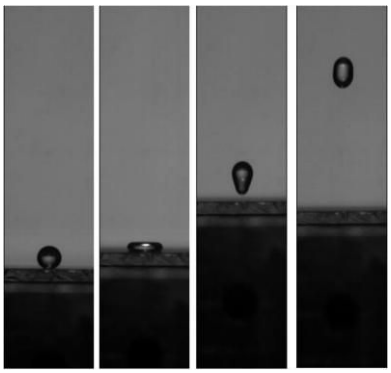	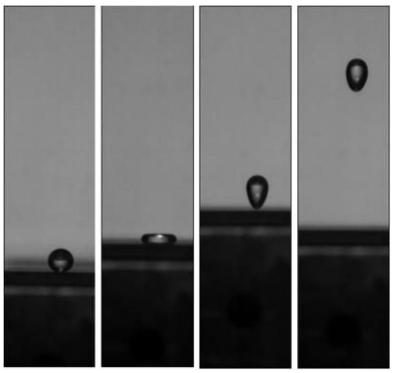	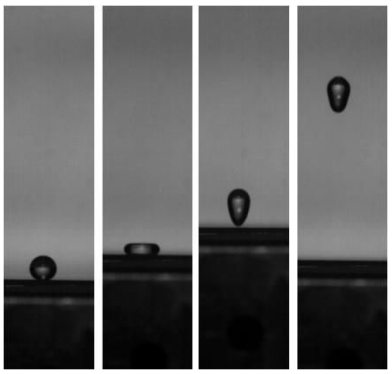
$V_p = 0.72$ m/s	$V_p = 0.72$ m/s	$V_p = 0.68$ m/s

Figure 3.36. Image sequences of the water droplet ejection at A ≈ 0.30 cm standing on the substrates for a given concentration of the homopolymer/copolymer in mol% of Py-OF_6 *vs* Py-Adam. Polymerization at 0.1 M solution Bu_4NClO_4/acetonitrile in ITO plates. Number of scans: 2.

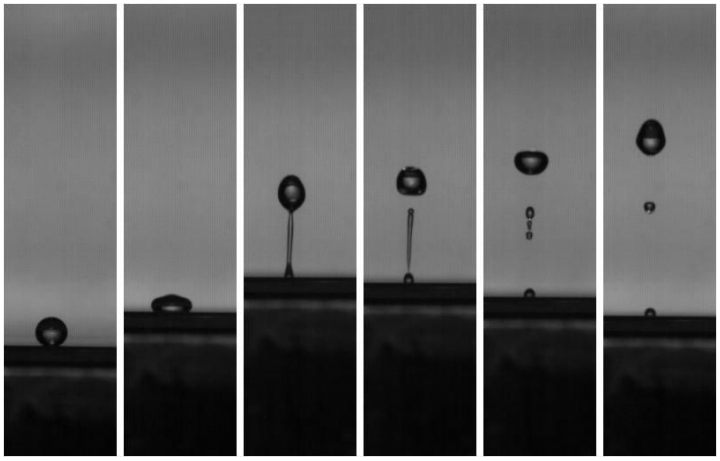

Figure 3.37. Image sequences of the water droplet ejection standing on the copolymer mol% 50% of Py-OF_6 *vs* Py-Adam substrate for a V_p > 0.68 m/s. Polymerization at 0.1 M solution Bu_4NClO_4/acetonitrile in ITO plates. Number of scans: 2.

Up to now, qualitatively the results are in agreement with the dynamic contact angles (*H* and α) presented before for the copolymer surfaces reinforcing our technique. In order to quantify these ejections, **Figure 3.38** reports the ratio of the V_g and V_p, also called as coefficient of restitution (*CR*), as a function of V_p. This was possible only for V_p where the fragmentation of the water droplet was not multiple. All the surfaces presented similar restitution, but a slightly lower *CR* is observed for mol% 50% of Py-OF_6 than for the non-sticky surfaces. The bars show the range of V_p over which the ejection of the water droplet is possible without fragmentation. The water droplets ejection occurs more easily for the fluorinated homopolymer surface (*A* = 0.02 cm, V_p = 0.06 m/s) than for mol% 75% of Py-OF_6 (*A* = 0.04 cm, V_p = 0.10 m/s), even with a lower *CR*. For the copolymer with mol% 50% of Py-OF_6, higher load amplitude (*A* = 0.10 cm, V_p = 0.25 m/s) is required to generate the necessary V_p for the water droplet ejects from the surface. **Table 3.17** showed that for the surfaces with mol% 75 - 100% of Py-OF_6, the ejection is possible for V_p > 0.72 m/s and no fragmentation was observed for both surfaces until the maximum loaded *A* achieved by the catapult apparatus for each experiment. However, for mol% 50% of Py-OF_6 the water droplet showed a multiple fragmentation for V_p > 0.68 m/s as already showed in **Figure 3.37**.

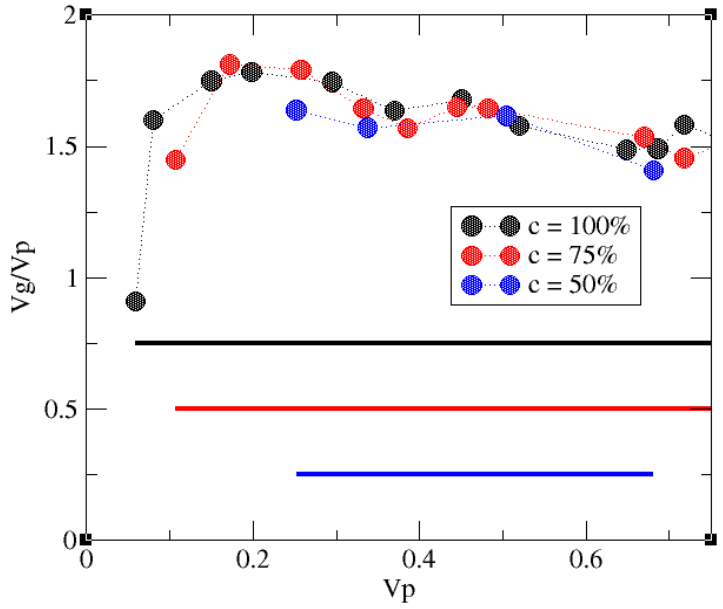

Figure 3.38. Coefficient of restitution (CR = V_g/V_p) as function of V_p for the surfaces containing a mol% 50-100% of Py-OF_6 *vs* Py-Adam. The bars represented the range of V_p studied with no fragmentation of the droplets. Polymerization at 0.1 M solution Bu_4NClO_4/acetonitrile in ITO plates. Number of scans: 2.

Table 3.17. Water adhesion data for the surfaces studied by dynamic contact angle and by the ejection tests. V_p is related with the maximum loaded *A* achieved until the water droplet fragmentation (NF = no fragmentation, F = fragmentation). Polymerization at 0.1 M solution Bu_4NClO_4/acetonitrile in ITO plates. Number of scans: 2.

Surfaces in mol% of Py-OF_6 *vs* Py-Adam	θ_w [deg]	*H* [deg]	α [deg]	*A* [cm]	$V_p$max [m/s]	Water droplet Fragmentation
50%	140.0	Sticky (> 90º)		0.28	0.68	F
75%	155.3	5.9	5.1	0.36	0.79	NF
100%	155.9	1.3	2.0	0.39	0.85	NF

To our knowledge, up to now there are no studies in the literature reporting the water droplets fragmentation and their ejecting parameters to evaluate the water adhesion attesting the innovation and authenticity of our work. These results corroborate with the results obtained by the dynamic contact angles. However, accordingly to the dynamic contact angles, the surfaces with mol% of 75 - 100% of Py-OF_6 provide a superhydrophobic and non-sticky behavior while for mol% 50% of Py-OF_6 a parahydrophobic with sticky behavior. However, with this new method we could show that is possible to measure the water adhesion for a sticky surface which was not possible by contact angle hysteresis. Then, copolymer of mol%

50% of Py-OF_6 is capable to eject water droplets in a given range of V_p with no droplet fragmentation indicating the possibility of this surface to repel water in a certain condition. At this way, for a given impulse, the surfaces with mol% of 50 - 100% of Py-OF_6 are capable to eject the water droplet from the surface using a catapult apparatus independently of their dynamic contact angles. This is a first tentative attempt to combine the water adhesion results obtained by contact angle hysteresis and ejection tests and opens new doors to explore this domain.

3.8 GENERAL DISCUSSION

In conclusion of this chapter, surfaces with various wetting properties were elaborated by electrochemical polymerization of pyrene monomers differing by their substituent size, hydrophobicity and rigidity. Generally, the electropolymerization of pyrene monomers induces a deposition of spherical particles of different sizes. For surfaces using the fluoroalkyl chains, the heteroatoms that connects the fluorinated chain with the pyrene unit does greatly impact in the wetting behavior. Superhydrophobic and highly oleophobic properties were obtained using fluoroalkyl chains for surfaces bearing ester, carbamate, thiol and thiocarbamate linkers due to the combination of the use of low surface energy compounds and the presence of nanostructured microparticles. However, the surfaces composed by polymers bearing amide and urea linker present high θ_w, but also high H and α showing a parahydrophobic behavior.

Highly hydrophobic properties were obtained for non-fluorinated polymers except for the glycol-substituent which shows θ_w = 62º after 3 deposition scans. Since the glycol is a hydrophilic polymer and its surface is less structured, this result is not surprising. For linear and branched alkyl chains as well as for the adamantyl- and phenyl-substituent, the polymers are extremely rough which explains the high θ_w obtained. Indeed, the fluorescent properties of all polypyrenes were studied showing a potential application to be used as sensors and optics with fluorescence in the green region.

Taking into account the versatility of pyrene moiety to form non-wetting surfaces with a wide range of roughness and different morphologies, we have shown that these materials have an appropriate design and wettability to:

- present a great stability concerning about the electrodeposition parameters, showing surfaces with similar wettability and morphologies when the electrodeposition method, electrolyte and/or solvent were changed;
- reduce the bacterial adhesion in 30-70% for non-fluorinated polypyrenes and 60-90% for the fluorinated polypyrene using *S. aureus* and *P. aeruginosa* as bacterial strains;
- be highly efficient against the biofilm formation by reducing in 90-99% the bacteria %cover using *S. aureus* and *P. aeruginosa* as bacterial strains;
- be used as a switchable superhydrophobic-hydrophilic pH-sensitive surface by the electro-copolymerization of pyrene monomers with fluorinated chains and acid groups;
- show different water adhesion by the use of copolymers with superhydrophobic and parahydrophobic properties by contact angle of hysteresis and by ejection tests;
- implement a new method using a catapult apparatus to eject water droplets from the surfaces to better study the water adhesion of sticky surfaces;

This work used an innovative strategy and completely original molecules to show a combination of superhydrophobicity with fluorescence properties on polypyrenes films generating surfaces with many potential applications.

REFERENCES OF CHAPTER 3

(1) Darmanin, T.; Guittard, F. Wettability of Conducting Polymers: From Superhydrophilicity to Superoleophobicity. *Prog. Polym. Sci.* **2014**, *39* (4), 656–682.

(2) Xu, L.; Tong, F.; Lu, X.; Lu, K.; Lu, Q. Multifunctional Polypyrene/Silica Hybrid Coatings with Stable Excimer Fluorescence and Robust Superhydrophobicity Derived from Electrodeposited Polypyrene Films. *J. Mater. Chem. C* **2015**, *3*, 2086–2092.

(3) Wolfs, M.; Darmanin, T.; Guittard, F. Effect of Hydrocarbon Chain Branching in the Elaboration of Superhydrophobic Materials by Electrodeposition of Conducting Polymers. *Surf. Coatings Technol.* **2014**, *259*, 594–598.

(4) Darmanin, T.; Mortier, C.; Eastoe, J.; Sagisaka, M.; Guittard, F. Sticky Superhydrophobic Hard Nanofibers from Soft Matter. *RSC Adv.* **2014**, *4*, 35708–35716.

(5) Mortier, C.; Darmanin, T.; Guittard, F. 3,4-Dialkoxypyrrole for the Formation of Bioinspired Rose Petal-like Substrates with High Water Adhesion. *Langmuir* **2016**, *32* (47), 12476–12487.

(6) Chen, Y.; Bai, H.; Chen, Q.; Li, C.; Shi, G. A Water-Soluble Cationic Oligopyrene Derivative: Spectroscopic Studies and Sensing Applications. *Sens. Actuators, B.* **2009**, *138*, 563–571.

(7) Piçarra, S.; Gomes, P. T.; Martinho, J. M. G. Fluorescence Study of the Coil-Globule Transition of a Poly(ε-Caprolactone) Chain Labeled with Pyrenes at Both Ends. *Macromolecules* **2000**, *33* (10), 3947–3950.

(8) Costa, T.; Seixas De Melo, J.; Burrows, H. D. Fluorescence Behavior of a Pyrene-End-Capped Poly(Ethylene Oxide) in Organic Solvents and in Dioxane-Water Mixtures. *J. Phys. Chem. B* **2009**, *113* (3), 618–626.

(9) Chen, S.; Duhamel, J.; Winnik, M. A. Probing End-to-End Cyclization beyond Willemski and Fixman. *J. Phys. Chem. B* **2011**, *115* (13), 3289–3302.

(10) Wenzel, R. N. Resistance of Solid Surfaces To Wetting By Water. *Ind. Eng. Chem.* **1936**, *28* (8), 988–994.

(11) Cassie, A. B. D.; Baxter, S. Wettability of Porous Surfaces. *Trans. Faraday Soc.* **1944**, *40* (5), 546–551.

(12) Marmur, A. Hydro- Hygro- Oleo- Omni-Phobic? Terminology of Wettability Classification. *Soft Matter* **2012**, *8*, 6867–6870.

(13) El-Maiss, J.; Darmanin, T.; Guittard, F. Controlling Electrodeposited Conducting Polymer Nanostructures with the Number and the Length of Fluorinated Chains for Adjusting Superhydrophobic Properties and Adhesion. *RSC Adv.* **2015**, *5* (47), 37196–37205.

(14) Darmanin, T.; Guittard, F. Enhancement of the Superoleophobic Properties of Fluorinated PEDOP Using Polar Glycol Spacers. *J. Phys. Chem. C* **2014**, *118*, 26912–26920.

(15) Honda, K.; Morita, M.; Otsuka, H.; Takahara, A. Molecular Aggregation Structure and Surface Properties of Poly(fluoroalkyl Acrylate) Thin Films. *Macromolecules* **2005**, *38* (13), 5699–5705.

(16) Honda, K.; Morita, M.; Sakata, O.; Sasaki, S.; Takahara, A. Effect of Surface Molecular Aggregation State and Surface Molecular Motion on Wetting Behavior of Water on Poly(fluoroalkyl Methacrylate) Thin Films. *Macromolecules* **2010**, *43* (1), 454–460.

(17) Sarkar, A.; Kietzig, A. Design of a Robust Superhydrophobic Surface: Thermodynamic and Kinetic Analysis. *Soft Matter* **2015**, *11* (10), 1998–2007.

(18) Szczepanski, C. R.; Darmanin, T.; Guittard, F. Using Poly(3,4-Ethylenedioxythiophene)

Containing a Carbamate Linker as a Platform to Develop Electrodeposited Surfaces with Tunable Wettability and Adhesion. *RSC Adv.* **2015**, *5* (109), 89407–89414.

(19) Cha, T.; Yi, J. W.; Moon, M.; Lee, K.; Kim, H. Nanoscale Patterning of Microtextured Surfaces to Control Superhydrophobic Robustness. *Langmuir* **2010**, *26* (11), 8319–8326.

(20) Verho, T.; Korhonen, J.; Sainiemi, L.; Jokinen, V.; Bower, C.; Franze, K.; Franssila, S.; Andrew, P.; Ikkala, O.; Ras, R. Reversible Switching between Superhydrophobic States on a Hierarchically Structured Surface. *Proc. Natl. Acad. Sci.* **2012**, *109* (26), 10210–10213.

(21) Morris, J. V; Mahaney, M. A.; Huberr, J. R. Fluorescence Quantum Yield Determinations. 9,10-Diphenylanthracene as a Reference Standard in Different Solvents. *J. Phys. Chem.* **1976**, *80* (9), 969–974.

(22) Niko, Y.; Kawauchi, S.; Otsu, S.; Tokumaru, K.; Konishi, G. Fluorescence Enhancement of Pyrene Chromophores Induced by Alkyl Groups through σ−π Conjugation: Systematic Synthesis of Primary, Secondary, and Tertiary Alkylated Pyrenes at the 1, 3, 6, and 8 Positions and Their Photophysical Properties. *J. Org. Chem.* **2013**, *78* (7), 3196–3207.

(23) Birks, J. B.; Christophorou, L. G. Excimer Fluorescence Spectra of Pyrene Derivatives. *Spectrochim. Acta* **1963**, *19* (2), 401–410.

(24) Ou, J.; Wang, Z.; Wang, F.; Xue, M.; Li, W.; Amirfazli, A. Washable and Antibacterial Superhydrophbic Fabric. *Appl. Surf. Sci.* **2016**, *364*, 81–85.

(25) Hasan, J.; Crawford, R. J.; Ivanova, E. P. Antibacterial Surfaces: The Quest for a New Generation of Biomaterials. *Trends Biotechnol.* **2013**, *31* (5), 295–304.

(26) Dou, X.; Zhang, D.; Feng, C.; Jiang, L. Bioinspired Hierarchical Surface Structures with Tunable Wettability for Regulating Bacteria Adhesion. *ACS Nano* **2015**, *9* (11), 10664–10672.

(27) Hoo, S.; Rungraeng, N.; Song, W.; Jun, S. Superhydrophobic and Superhydrophilic Nanocomposite Coatings for Preventing Escherichia Coli K-12 Adhesion on Food Contact Surface. *J. Food Eng.* **2014**, *131*, 135–141.

(28) Bruzaud, J.; Tarrade, J.; Celia, E.; Darmanin, T.; Taf, E.; Givenchy, D.; Guittard, F.; Herry, J.; Guilbaud, M.; Bellon-fontaine, M. The Design of Superhydrophobic Stainless Steel Surfaces by Controlling Nanostructures: A Key Parameter to Reduce the Implantation of Pathogenic Bacteria. *Mater. Sci. Eng. C* **2017**, *73*, 40–47.

(29) Organization, W. H. Global priority list of antibiotic-resistant bacteria to guide research, discovery, and development of new antibiotics.

(30) Sun, F.; Qu, F.; Ling, Y.; Mao, P.; Xia, P.; Chen, H.; Zhou, D. Biofilm-Associated Infections: Antibiotic Resistance and Novel Therapeutic Strategies. *Future Microbiol.* **2013**, *8* (7), 877–886.

(31) Valle, J.; Burgui, S.; Langheinrich, D.; Gil, C.; Solano, C.; Toledo-arana, A.; Helbig, R. Evaluation of Surface Microtopography Engineered by Direct Laser Interference for Bacterial Anti-Biofouling. *Macromoleuclar Biosci.* **2015**, *15* (8), 1060–1069.

(32) Díaz, C.; Schilardi, P. L.; Salvarezza, R. C.; Lorenzo de Mele, M. F. Nano/Microscale Order Affects the Early Stages of Biofilm Formation on Metal Surfaces. *Langmuir* **2007**, *23* (22), 11206–11210.

(33) Perera-Costa, D.; Bruque, J. M. Studying the Influence of Surface Topography on Bacterial Adhesion Using Spatially Organized Microtopographic Surface Patterns. *Langmuir* **2014**, *30* (16), 4633–4641.

(34) Liu, L.; Ercan, B.; Sun, L.; Ziemer, K. S.; Webster, T. J. Understanding the Role of Polymer Surface Nanoscale Topography on Inhibiting Bacteria Adhesion and Growth. *ACS Biomater. Sci. Eng.* **2016**, *2* (1), 122–130.

(35) Ivanova, E. P.; Hasan, J.; Webb, H. K.; Truong, V. K.; Watson, G. S.; Watson, J. A.; Baulin, V.

A.; Pogodin, S.; Wang, J. Y.; Tobin, M. J.; Löbbe, C.; Crawford, R. J. Natural Bactericidal Surfaces: Mechanical Rupture of Pseudomonas Aeruginosa Cells by Cicada Wings. *Small* **2012**, *8* (16), 2489–2494.

(36) Kelleher, S. M.; Habimana, O.; Lawler, J.; Reilly, B. O.; Daniels, S.; Casey, E.; Cowley, A. Cicada Wing Surface Topography: An Investigation into the Bactericidal Properties of Nanostructural Features. *ACS Appl. Mater. Interfaces* **2016**, *8* (24), 14966–14974.

(37) Lin, C.; Tang, P.; Zhang, W.; Wang, Y.; Zhang, B.; Wang, H.; Zhang, L. Effect of Superhydrophobic Surface of Titanium on Staphylococcus Aureus Adhesion. *J. Nanomater.* **2011**, *2011* (2), 1–8.

(38) Privett, B. J.; Youn, J.; Hong, S. A.; Lee, J.; Han, J.; Shin, J. H.; Schoenfisch, M. H. Antibacterial Fluorinated Silica Colloid Superhydrophobic Surfaces. *Langmuir* **2011**, *27* (15), 9597–9601.

(39) Chang, B.; Zhang, B.; Sun, T. Smart Polymers with Special Wettability. *Small* **2017**, *13*, 1–16.

(40) Meng, H.; Mohamadian, H.; Stubblefield, M.; Ozaydin-ince, G.; Coclite, A. M.; Gleason, K. K.; Hu, J.; Meng, H.; Li, G.; Ibekwe, S. I. A Review of Stimuli-Responsive Polymers for Smart Textile Applications. *Smart Mater. Struct.* **2012**, *21*, 53001.

(41) Hunter, A. C.; Moghimi, S. M.; Hunter, A. C. Polymer Chemistry Smart Polymers in Drug Delivery : A Biological Perspective. *Polym. Chem.* **2017**, *8*, 41–51.

(42) Roth, P. J.; Lowe, A. B.; Roth, P. J.; Lowe, A. B. Polymer Chemistry Stimulus-Responsive Polymers. *Polym. Chem.* **2017**, *8*, 10–11.

(43) Kocak, G.; Tuncer, C.; Bütün, V. pH-Responsive Polymers. *Polym. Chem.* **2017**, *8*, 144–176.

(44) Hiruta, Y.; Funatsu, T.; Matsuura, M.; Wang, J.; Ayano, E.; Kanazawa, H. pH/Temperature-Responsive Fluorescence Polymer Probe with pH-Controlled Cellular Uptake. *Sens. Actuators B.* **2015**, *207*, 724–731.

(45) Cheng, Z.; Lai, H.; Du, Y.; Fu, K.; Hou, R.; Li, C.; Zhang, N.; Sun, K. pH-Induced Reversible Wetting Transition between the Underwater Superoleophilicity and Superoleophobicity. *ACS Appl. Mater. Interfaces* **2014**, *6* (1), 636–641.

(46) Poverenov, E.; Li, M.; Bitler, A.; Bendikov, M. Major Effect of Electropolymerization Solvent on Morphology and Electrochromic Properties of PEDOT Films. *Chem. Mater.* **2010**, *22* (13), 4019–4025.

(47) Taleb, S.; Darmanin, T.; Guittard, F. Elaboration of Voltage and Ion Exchange Stimuli-Responsive Conducting Polymers with Selective Switchable Liquid-Repellency. *ACS Appl. Mater. Interfaces* **2014**, *6* (10), 7953–7960.

(48) Marmur, A. From Hygrophilic to Superhygrophobic: Theoretical Conditions for Making High-Contact-Angle Surfaces from Low-Contact-Angle Materials. *Langmuir* **2008**, *24* (14), 7573–7579.

(49) Eral, H. B.; Mannetje, D. J. C. M.; Oh, J. M. Contact Angle Hysteresis: A Review of Fundamentals and Applications. *Colloid Polym. Sci.* **2013**, *291* (2), 247–260.

(50) Cheng, Z.; Gao, J.; Jiang, L. Tip Geometry Controls Adhesive States of Superhydrophobic Surfaces. *Langmuir* **2010**, *26* (11), 8233–8238.

(51) Law, K.-Y. Definitions for Hydrophilicity, Hydrophobicity, and Superhydrophobicity: Getting the Basics Right. *J. Phys. Chem. Lett.* **2014**, *5*, 686–688.

(52) Krasovitski, B.; Marmur, A. Drops Down the Hill: Theoretical Study of Limiting Contact Angles and the Hysteresis Range on a Tilted Plate. *Langmuir* **2005**, *21* (9), 3881–3885.

(53) Pierce, E.; Carmona, F. J.; Amirfazli, A. Understanding of Sliding and Contact Angle Results in Tilted Plate Experiments. *Colloids Surf.A* **2008**, *323* (1–3), 73–82.

(54) Taleb, S.; Darmanin, T.; Guittard, F. Superhydrophobic Conducting Polymers with Switchable

Water and Oil Repellency by Voltage and Ion Exchange. *RSC Adv.* **2014**, *4* (10), 3550–3555.

(55) Taleb, S.; Darmanin, T.; Guittard, F. Superoleophobic/Superhydrophobic PEDOP Conducting Copolymers with Dual-Responsivity by Voltage and Ion Exchange. *Mater. Today Commun.* **2016**, *6*, 1–8.

(56) Darmanin, T.; Guittard, F. pH- and Voltage-Switchable Superhydrophobic Surfaces by Electro-Copolymerization of EDOT Derivatives Containing Carboxylic Acids and Long Alkyl Chains. *ChemPhysChem* **2013**, *14* (11), 2529–2533.

Conclusions

The elaboration of micro and nanostructured surfaces with tunable wettability is an emerging field of investigation and the use of electropolymerization as a fabrication method has been widely considered to prepare these kinds of surfaces. The global aim of this work was to study the surface wettability and morphology of electrodeposited pyrene and thienothiophene films and their properties.

The first polymerizable core analyzed, **thienothiophene** formed a range of nanostructures depending on the electrochemical parameters employed, typically resulting in parahydrophobic behavior. It was observed that the structure formed is highly dependent on the monomer core used to polymerize. However, by playing with other parameters, we could observe that for:

- ✓ Monomer and substituent: they are the main factors influencing the formation of specific nanostructures. Nanotubes, nanosheets, nanospheres and nanofibers are just some of the structures formed when the polymerizable core was changed. With the introduction of hydrocarbon substituents, the surface morphology was also deeply affected. More structured surfaces were formed by using aromatic and branched alkyl chains as substituents;
- ✓ Method: for nanotube structures, for example, it was shown that their formation is due to the stabilization by the polymer of O_2 and/or H_2 gas bubbles produced *in-situ* during electropolymerization process from trace water. The amount of the gas released during the process will influence the size and the amount of the tubes formed on the surface, and this is directly related to the electrochemical method chosen. For constant potential and galvanostatic deposition, only trace water can explain the formation of O_2 bubbles at high potential. For cyclic voltammetry and pulse deposition, trace water contributes to the formation of these features, but the formation of H_2 bubbles at low potential also favors the formation of nanotubular structures.
- ✓ Electrolyte: the shape and the type of the nanostructures changed with the supporting electrolyte due to differences in the solubility, nucleophilicity and conductivity of each salt used.

The formation of nanotubes without any template or use of surfactant must be highlighted. This work presented a one-step templateless method to produce this very interesting structure which could be tailored by the parameters of the electropolymerization to achieve the desired wetting properties. Nanotubes with open/closed tops, large/small porosity, sparse/agglomerated structures were formed as showed in **Figure 1C**.

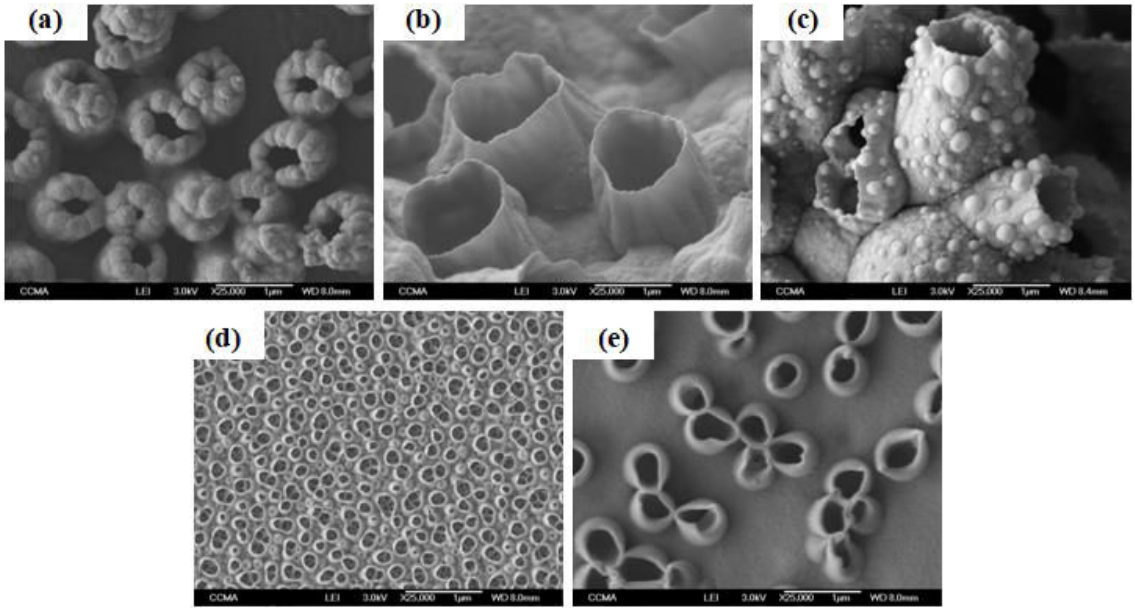

Figure 1C. SEM images of electropolymerization of: thieno[3,2-*b*]thiophene in Bu_4NClO_4/dichloromethane by cyclic voltammetry at (a) 3 scans, (b) 5 scans; thieno[3,2-*b*]thiophene in Bu_4NClO_4/dichloromethane + 0.5% of water by (c) cyclic voltammetry at 3 scans and (d) by constant potential at 12.5 mC cm^{-2}; (e) PTh-Na in Bu_4NClO_4/dichloromethane by cyclic voltammetry at 3 scans.

In this work, we also showed the versatility of the thienothiophenes monomers to create different structures on surfaces (spheres, tubes, hollow structures, fibers, tree-like structures, etc) with a wide range of wettability and surface roughness. This result is extremely important for the control of water adhesion by electropolymerization for various potential applications including water transportation and harvesting, oil/water separation membranes, energy systems and biosensing.

As for the study with **pyrenes**, we first observed a significant change in surface morphology when a substituent was grafted onto the monomer. The addition of side chains made the morphology vary from flower-like microstructures to sphere-like structures. The nature of the substituent induces the formation of microspheres in different shapes, as shown in **Figure 2C**.

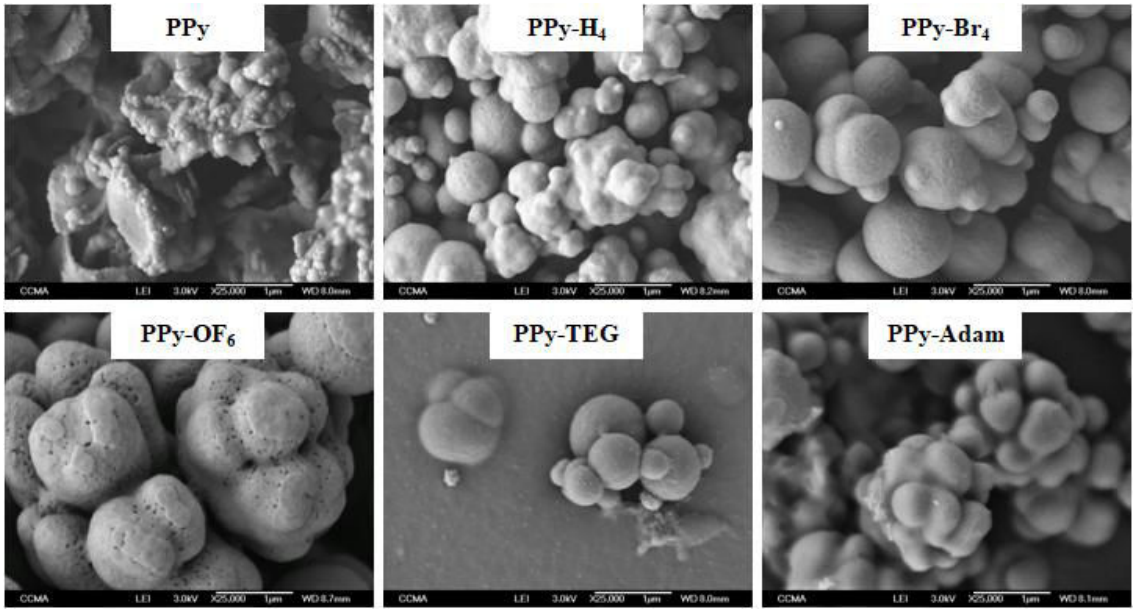

Figure 2C. SEM images of various polypyrene surfaces electrodeposited by cyclic voltammetry at 3 deposition scans in 0.1 M solution of Bu_4NClO_4/acetonitrile.

The morphology and the chemical composition of the substituent directly affected the wettability of the surfaces:

- ✓ PPy-TEG: the least hydrophobic surfaces was formed using triethylene glycol as a side chain due to the use of less hydrophobic substituent combined with smoother surface;
- ✓ PPy-Ph/PPy-H_n/PPy-Br_n: the alkyl and aryl hydrocarbon chains lead to hydrophobic surfaces with high water adhesion due to the presence of microspherical particles on their surfaces;
- ✓ PPy-Adam: presenting the most unique shape of particle for the pyrene series, the cyclic group generates raspberry-shaped microparticles and a parahydrophobicity;
- ✓ PPy-OF_n: use of low surface energy compounds combined with the formation of microparticles with nanoroughness on their surfaces yield superhydrophobic surfaces with a very low water adhesion (low H and α). In general, for the perfluorinated surfaces, very high contact angles were achieved independently of the connector and linker. Superhydrophobic and highly oleophobic properties were obtained using ester, thioester, carbamate and thiocarbamate linkers while parahydrophobic and oleophobic properties were observed with the amide and urea linkers. These differences are due to varying the intramolecular interactions between the molecules during electropolymerization.

The pyrene molecules proved to be very versatile for the electropolymerization process, generating surfaces with a wide range of morphologies and wettabilities. The superhydrophobicity of the fluorinated pyrenes opens new doors for many applications in the materials science field. Combining the superhydrophobic behavior of the fluorinated pyrene with the pH-responsivity of the Py-COOH, a copolymeric surface sensitive to a basic and acidic treatment in soft conditions (0.1 M aqueous NaOH solution, 0.1 M aqueous H_2SO_4 solution, room temperature) was prepared. The surface wettability could be reversibly switched from superhydrophobic to hydrophilic depending on the pH of the environment. Such materials are excellent candidates for separation membranes or bacterial anti-adhesive/adhesive surfaces. Fluorinated pyrenes were also used to prepare copolymers with Py-Adam in order to better quantify the water adhesion of sticky and non-sticky surfaces. The Py-OF_6 was used to attain superhydrophobicity with low water adhesion, while the Py-Adam afforded high water adhesion. We were able to implement a new methodology where we could measure the water adhesion of not only non-sticky surfaces, but also from sticky ones, which usually is not possible when employing the tilted-drop method. However, using a simple ejection test by a catapult system we were able to obtain the water adhesion results for parahydrophobic surfaces. As expected, as the mol% of Py-Adam increased, the surface became more adhesive.

The polypyrene films also have shown a potential application to serve as coatings with reduced bacterial adhesion and to prevent biofilm formation. Studying fluorinated and non-fluorinated surfaces, we have shown that is not totally necessary to use superhydrophobic surfaces to get anti-bacterial properties, but instead these properties rely on a combination between the wettability and the topography of the film. A reduction of 30-70% in the bacterial adhesion for non-fluorinated polypyrenes and 60-90% for fluorinated polypyrene was obtained *for S. aureus* and *P. aeruginosa* strains. After a long exposure to bacterial strains, polypyrene surfaces demonstrated a high efficiency against biofilm formation and reduced by 90-99% the bacteria coverage. These results demonstrate the capability of these surfaces to be used as coatings to prevent bacterial-interactions. Lastly, all the pyrene surfaces, independently of the grafted substituent, presented fluorescence emission in the green region, thus increasing the range of applications of these films.

*****

This study shows that pyrene and thienothiophene monomers can be used as polymerizable cores to create very interesting and relevant surfaces by electropolymerization processes. This method has been widely used by our research group to create original surfaces with different morphologies, adding value to their properties and high propensity for industrial applications in coatings and surface science.

*****

This work leads to six publications in peer-reviewed journals, seven presentations as part of international conferences and a best poster award. These works are listed below.

Bibliographic Production:

- **Chagas, G. R.**; Kiryanenko, D.; Godeau, G.; Guittard, F.; Darmanin, T. pH-driven wetting switchability of electrodeposited superhydrophobic copolymers of pyrene bearing acid functions and fluorinated chains. *ChemPhysChem* 10.1002/cphc.201700846. **2017**.
- Raufaste, C.; **Chagas, G. R.**; Darmanin, T.; Claudet, C.; Guittard, F.; Celestini, F. Superpropulsion of droplets and soft elastic solids. *Physical Review Letters*. **2017**, 119, 108001.
- **Chagas, G. R.**; Darmanin, T.; Godeau, G.; Amigoni, S.; Guittard, F. Superhydrophobic Properties of Electrodeposited Fluorinated Polypyrenes. *Journal of Fluorine Chemistry*. **2017**, 193, 73–81.
- **Chagas, G. R.**; Darmanin, T.; Guittard, F. A One-Step and Templateless Electropolymerization Process using Thienothiophene Derivatives to Develop Arrays of Nanotubes and Tree-Like Structures with High Water Adhesion. *ACS Applied Materials & Interfaces*. **2016**, 8, 22732–22743.
- **Chagas, G. R.**; Xie, X.; Darmanin, T.; Steenkeste, K.; Gaucher, A.; Prim, D.; Méallet-Renault, R.; Godeau, G.; Amigoni, S.; Guittard, F. Electrodeposition of polypyrenes with tunable hydrophobicity, water adhesion and fluorescence properties. *The Journal of Physical Chemistry C*. **2016**, 120, 7077–7087.
- **Chagas, G. R.**; Darmanin, T., Guittard, F. Nanostructured superhydrophobic films by electrodeposition of fluorinated polyindoles. *Beilstein Journal of Nanotechnology*. **2015**, 6, 2078-2087.

Incoming Publications:

- **Chagas, G. R.**; Akbari, R.; Godeau, G.; Mohammadizadeh, M.; Guittard, F.; Darmanin, T. Electrodeposited poly(thieno[3,2-*b*]thiophene) films for the templateless formation of nanotubes or nanocapsules by galvanostatic and square pulse deposition, *ChemPlusChem.* **2017** (Accepted in October).
- Akbari, R.; **Chagas, G. R.**; Godeau, G.; Mohammadizadeh, M.; Guittard, F.; Darmanin, T. Intrinsically water-repellent copper oxide surfaces; an electro-crystallization approach. *Applied Surface Science*. **2017** (Submitted in October).

Contributed Presentation & Abstracts in Conferences:

- **Chagas, G. R.**; Moran, G.; Darmanin, T.; Xie, X.; Gaucher, A.; Prim, D.; Godeau, G.; Amigoni, S.; Méallet-Renault, R.; Guittard, F. Eletrodeposited polypyrenes films: wettability, fluorescence, pH-responsivity and anti-bacterial properties. *European Polymer Federation Congress*, July/2017, Lyon, France (Oral presentation)
- **Chagas, G. R.**; Xie, X.; Darmanin, T.; Steenkeste, K.; Gaucher, A.; Prim, D.; Méallet-Renault, R.; Godeau, G.; Amigoni, S.; Guittard, F. Electrodeposition of polypyrenes with tunable hydrophobicity, water adhesion and fluorescent properties. *1st International Conference on Optics and Photonics and Materials.* October/2016, Nice, France. (Poster presentation)
- **Chagas, G. R.**; Darmanin, T.; Guittard, F. Hydrophobicity and water adhesion from nanotubes to nanospheres of structured polymeric surfaces. *3rd International Conference on Bioinspired and Biobased Chemistry and Materials*. October/2016, Nice, France. (Oral presentation)
- **Chagas, G. R.**; Darmanin, T.; Guittard, F. Nanostructured polymeric surfaces: Hydrophobicity and water adhesion from nanotubes to nanospheres. *4èmes Journées Méditerranéennes des Jeunes chercheurs*. October/2016, Nice, France. (Oral presentation)
- **Chagas, G. R.**; Xie, X.; Darmanin, T.; Steenkeste, K.; Gaucher, A.; Prim, D.; Méallet-Renault, R.; Godeau, G.; Amigoni, S.; Guittard, F. Controlling surface wettability and fluorescence properties of conducting polypyrenes containing different chains. *6th EuCheMS Chemistry Congress*, September/ 2016, Seville, Spain. (Oral presentation)
- **Chagas, G. R.**; Darmanin, T.; Guittard, F. Nanostructured polymeric surfaces: Hydrophobicity and water adhesion from nanotubes to nanospheres. *8ème Journées*

Scientifiques du C'Nano, May/2016, Île de Porquerolles, France. (Poster presentation and *Best Poster Award*)

- **Chagas, G. R.**; Darmanin, T.; Guittard, F. Superhydrophobic conducting polymer films by electrodeposition of fluorinated polyindoles. *14ème journées du Groupe Français des Polymères – Section Mèditerranée*, October/2015, Nice, France. (Oral presentation)

Highlights:

- Publication "Superpropulsion of droplets and soft elastic solids" in the Physical Review Letters was highlighted by the following sites:
    - Science & Vie: https://www.science-et-vie.com/article/les-gouttes-peuvent-faire-de-la-superpropulsion-9548
    - Physics: https://physics.aps.org/articles/v10/97
    - Physics World: http://physicsworld.com/cws/article/news/2017/sep/13/shape-shifting-soft-projectiles-travel-faster
    - Resonance Science Foundation: https://resonance.is/water-droplets-superpropulsion/
    - Journal Physical Review Letters: https://journals.aps.org/prl/issues/119/10

- Best poster award in the "Poster Section" of 8ème Journées Scientifiques du C'Nano, in Île de Porquerolles, France, with the work "Nanostructured polymeric surfaces: Hydrophobicity and water adhesion from nanotubes to nanospheres". May/2016.

Outlooks

This work contributed to the elaboration of new monomers and polymeric surfaces fabricated by one-step electropolymerization method. Many of the electrochemical parameters were tested and the results were presented previously.

Concerning the research on the electrochemical parameters, the method, solvent and electrolyte could be optimized for the thienothiophene substituted with a naphthyl group, which provided a very interesting morphology with nanotubular structures. Currently, electrochemical polymerization requires the use of organic solvents to prepare those conducting polymers. However, these solvents have been found toxic and hazardous for the environment. One alternative could be developed an electrochemical polymerization with an emulsion solution in order to reduce the toxicity and make an eco-friendly process.

Looking forward to the potential applications, it would be interesting testing the parahydrophobicity of the polythienothiophene surfaces to serve as coating for water harvesting applications. The water adhesion properties of these films were evaluated only by sessile-drop and tilted-drop method to measure the static and the dynamic contact angle, respectively, and they showed high water adhesion. A simple apparatus to collect water and evaluate this amount in humid conditions could give valuable insight to the technological part of this work.

Taking into account the superhydrophobicity of the polypyrenes, there are many possible potential applications. The importance and need to produce anti-icing surfaces for many types of materials is already well known. Here, the superhydrophobicity, fluorescence and anti-bacterial properties of the fluorinated and non-fluorinated polypyrenes could be combined with icephobic properties and, with this, increase their range of application. For this measure, it will be necessary to use a closed system with a high speed camera to analyze the delay time (time necessary to freeze a drop) and the durability of the surfaces through icing/deicing cycles. Then, it will be possible to understand the necessary conditions to achieve icephobicity with the pyrene films as well as to obtain surfaces with different behaviors that can effectively retard and/or prevent the ice formation.

ANNEX A1 – MONOMER SYNTHESIS

A1 1. SYNTHESIS OF THIENOTHIOPHENE MONOMERS

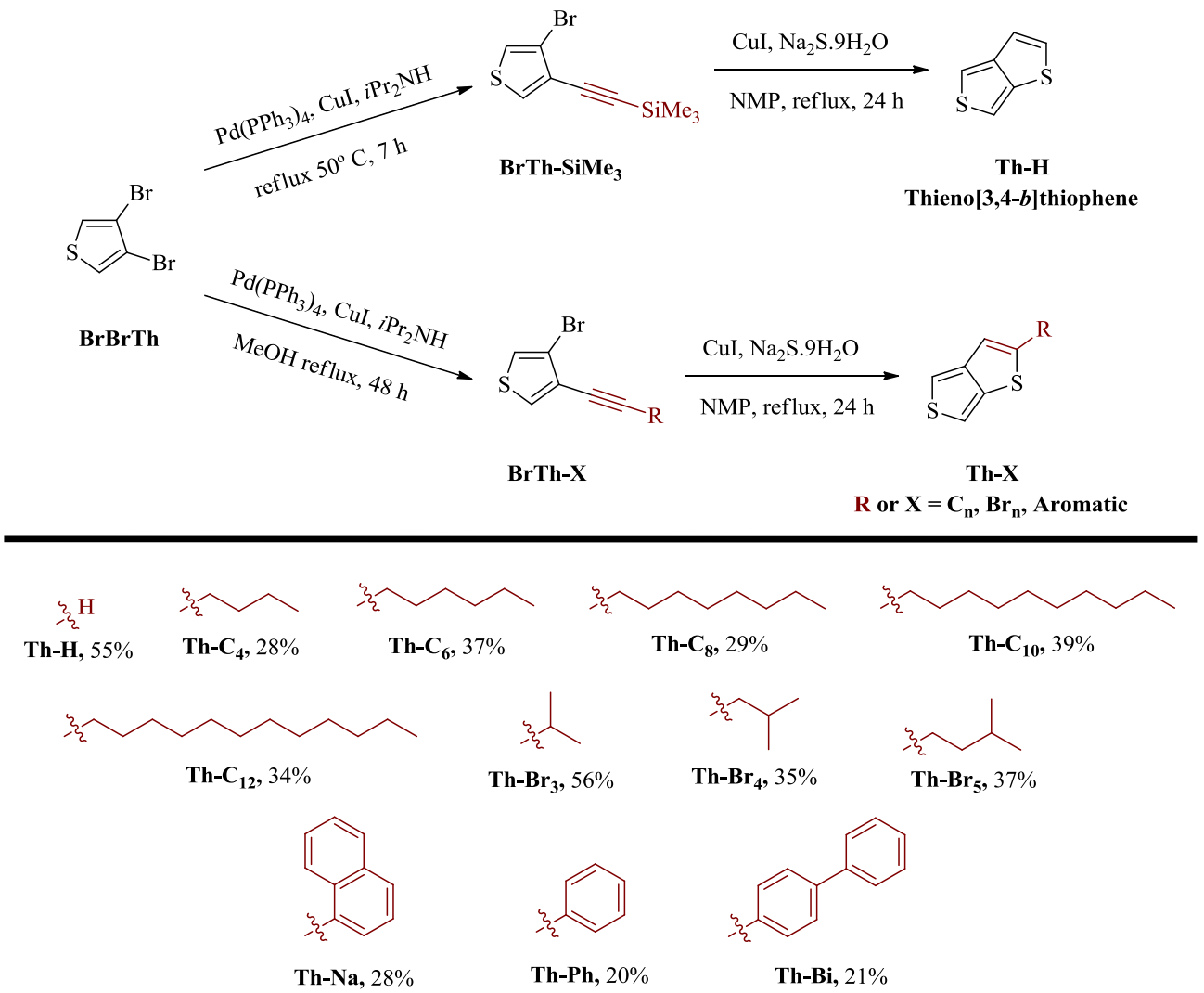

Scheme A1.1. Synthetic route to the thieno[3,4-*b*]thiophene derivatives synthesized in this study.

- **Procedure for BrTh-H**

1.03 mmol of dichlorobis (triphenylphosphine)palladium (II) ($Pd(PPh_3)_2Cl_2$) and 1.03 mmol of CuI were suspended in 20 mL of diisopropylamine. After N_2 purging for 10 min, 20.7 mmol of 3,4-dibromothiophene and 20.7 mmol of trimethylsilylacetylene were added into the flask in sequence with N_2 purging. The solution was heated at 50 ºC and let stirring for 7 h. The reaction was then allowed to cool until room temperature and the solvent was evaporated.

Then, 100 mL of dichloromethane was added and the product was extracted twice with 50 mL of water and 50 mL of $NaHCO_3$ aqueous solution, dried over Na_2SO_4 and filtered. The solvent was removed under reduced pressure and the product was purified by column chromatography using silica gel and petroleum ether. Methodology adapted from Patra et al [1]. **Scheme A1.1** showed the synthetic route.

BrTh-H: ((4-bromothiophen-3-yl)ethynyl)trimethylsilane

Yield 49%; Yellow liquid; δ_H(200 MHz, $CDCl_3$): 7.47 (d, *J* = 3.4 Hz, 1H), 7.22 (d, *J* = 3.4 Hz, 1H), 0.26 (s, 9H); δ_C(100 MHz, $CDCl_3$): 129.78, 124.77, 122.94, 114.00, 98.00, 97.88, 0.02.

- **Procedure for BrTh-C_n/BrTh-Br_n/BrTh-Aromatic**

To 40 mL of anhydrous methanol were added 1.03 mmol of dichlorobis (triphenylphosphine)palladium (II) ($Pd(PPh_3)_2Cl_2$) and 1.03 mmol of CuI. After N_2 purging for 10 min, 20.7 mmol of 3,4-dibromothiophene, 20.7 mmol of the correspondent alkyne and 20 mL of diisopropylamine were added into the flask in sequence with N_2 purging. The solution was heated at 85 ºC and let stirring for 48 h. The reaction was then allowed to cool until room temperature and the solvent was evaporated. Then, 100 mL of dichloromethane was added and the product was extracted twice with 50 mL of water and 50 mL of $NaHCO_3$ aqueous solution, dried over Na_2SO_4 and filtered. The solvent was removed under reduced pressure and the product was purified by column chromatography using silica gel and petroleum ether. Methodology adapted from Bae et al [2]. **Scheme A1.1** showed the synthetic route.

BrTh-C_4: 3-bromo-4-(hex-1-yn-1-yl)thiophene

Yield 39%; Yellow liquid; δ_H(200 MHz, $CDCl_3$): 7.34 (d, *J* = 3.4 Hz, 1H), 7.21 (d, *J* = 3.4 Hz, 1H), 2.44 (t, *J* = 6.8 Hz, 2H), 1.65 – 1.45 (m, 4H), 0.95 (t, *J* = 7.1 Hz, 3H); δ_C(100 MHz, $CDCl_3$): 127.88, 125.38, 122.68, 114.02, 93.74, 74.14, 30.81, 22.09, 19.27, 13.76.

BrTh-C_6: 3-bromo-4-(oct-1-yn-1-yl)thiophene

Yield 41%; Yellow liquid; δ_H(200 MHz, $CDCl_3$): 7.34 (d, *J* = 3.4 Hz, 1H), 7.21 (d, *J* = 3.4 Hz, 1H), 2.43 (t, *J* = 6.8 Hz, 2H), 1.66 – 1.47 (m, 4H), 1.35 – 1.28 (m, 4H), 0.90 (t, *J* = 6.6

Hz, 3H); δ_C(100 MHz, $CDCl_3$): 127.88, 125.37, 122.68, 114.02, 93.81, 74.09, 31.50, 28.71, 28.67, 22.72, 19.58, 14.22.

BrTh-C_8: 3-bromo-4-(dec-1-yn-1-yl)thiophene

Yield 36%; Yellow liquid; δ_H(200 MHz, $CDCl_3$): 7.34 (d, *J* = 3.3 Hz, 1H), 7.21 (d, *J* = 3.4 Hz, 1H), 2.43 (t, *J* = 7.0 Hz, 2H), 1.65 – 1.58 (m, 2H), 1.51 – 1.44 (m, 2H), 1.31 – 1.29 (m, 8H), 0.88 (t, *J* = 6.6 Hz, 3H); δ_C(100 MHz, $CDCl_3$): 127.87, 125.38, 122.68, 114.03, 93.82, 74.09, 32.00, 29.36, 29.25, 29.00, 28.74, 22.82, 19.58, 14.26.

BrTh-C_{10}: 3-bromo-4-(dodec-1-yn-1-yl)thiophene

Yield 47%; Yellow liquid; δ_H(200 MHz, $CDCl_3$): 7.34 (d, *J* = 3.4 Hz, 1H), 7.21 (d, *J* = 3.4 Hz, 1H), 2.43 (t, *J* = 6.8 Hz, 2H), 1.62 – 1.47 (m, 4H), 1.34 – 1.19 (m, 12H), 0.88 (t, *J* = 6.4 Hz, 3H); δ_C(100 MHz, $CDCl_3$): 127.87, 125.38, 122.68, 114.03, 93.82, 74.09, 32.06, 29.74, 29.70, 29.48, 29.29, 28.99, 28.74, 22.84, 19.58, 14.27.

BrTh-C_{12}: 3-bromo-4-(tetradec-1-yn-1-yl)thiophene

Yield 47%; Yellow liquid; δ_H(200 MHz, $CDCl_3$): 7.34 (d, *J* = 3.4 Hz, 1H), 7.21 (d, *J* = 3.4 Hz, 1H), 2.43 (t, *J* = 6.8 Hz, 2H), 1.66 – 1.57 (m, 3H), 1.50 – 1.44 (m, 2H), 1.34 – 1.19 (m, 16H), 0.88 (t, *J* = 6.4 Hz, 3H); δ_C(400 MHz, $CDCl_3$): 127.87, 125.37, 122.67, 114.02, 93.81, 74.09, 32.07, 29.82, 29.80, 29.78, 29.70, 29.51, 29.29, 28.99, 28.74, 22.84, 19.58, 14.27.

BrTh-Br_3: 3-bromo-4-(3-methylbut-1-yn-1-yl)thiophene

Yield 46%; Yellow liquid; δ_H(200 MHz, $CDCl_3$): 7.34 (d, *J* = 3.4 Hz, 1H), 7.21 (d, *J* = 3.4 Hz, 1H), 2.90 – 2.70 (m, 1H), 1.28 (d, *J* = 6.9 Hz, 6H); δ_C(100 MHz, $CDCl_3$): 127.74, 125.24, 122.67, 114.08, 99.09, 73.31, 23.04, 21.36.

BrTh-Br_4: 3-bromo-4-(4-methylpent-1-yn-1-yl)thiophene

Yield 49%; Yellow liquid; δ_H(200 MHz, $CDCl_3$): 7.34 (d, *J* = 3.4 Hz, 1H), 7.21 (d, *J* = 3.4 Hz, 1H), 2.33 (d, *J* = 6.4 Hz, 2H), 2.03 – 1.83 (m, 1H), 1.06 (d, *J* = 6.6 Hz, 6H); δ_C(100 MHz, $CDCl_3$): 127.87, 125.41, 122.68, 114.09, 92.66, 74.95, 28.73, 28.27, 22.17.

BrTh-Br$_5$: 3-bromo-4-(5-methylhex-1-yn-1-yl)thiophene

Yield 38%; Yellow liquid; δ_H(200 MHz, $CDCl_3$): 7.33 (d, *J* = 3.4 Hz, 1H), 7.21 (d, *J* = 3.4 Hz, 1H), 2.44 (t, *J* = 7.4 Hz, 2H), 1.86 – 1.76 (m, *J* = 13.4, 6.7 Hz, 1H), 1.52 (q, *J* = 7.3 Hz, 3H), 0.94 (d, *J* = 6.6 Hz, 6H); δ_C(100 MHz, $CDCl_3$): 127.87, 125.36, 122.68, 114.00, 93.80, 73.98, 37.62, 27.35, 22.33, 17.61.

BrTh-Na: 3-bromo-4-(naphthalen-1-ylethynyl)thiophene

Yield 16%; Light yellow solid; m.p. 89.0 °C; δ_H(200 MHz, $CDCl_3$): 8.57 (d, *J* = 8.3 Hz, 1H), 7.89 – 7.86 (m, 2H), 7.80 (dd, *J* = 7.1, 0.8, 1H), 7.64 – 7.60 (m, 2H), 7.57 – 7.53 (m, 1H), 7.47 (t, *J* = 8.1, 1H), 7.33 (d, *J* = 3.4 Hz, 1H); δ_C(100 MHz, $CDCl_3$): 133.35, 133.33, 130.78, 129.22, 129.02, 128.42, 127.07, 126.65, 126.54, 125.38, 124.95, 123.22, 120.59, 114.02, 90.54, 87.63.

BrTh-Ph: 3-bromo-4-(phenylethynyl)thiophene

Yield 42%; White solid; m.p. 201.8 °C; δ_H(200 MHz, $CDCl_3$): 7.59 – 7.55 (m, 2H), 7.52 (d, *J* = 3.4 Hz, 1H), 7.39 – 7.34 (m, 3H), 7.28 (d, *J* = 3.4 Hz, 1H); δ_C(100 MHz, $CDCl_3$): 132.64, 131.83, 128.87, 128.71, 128.51, 123.10, 122.91, 113.97, 92.32, 82.87.

BrTh-Bi: 3-([1,1'-biphenyl]-4-ylethynyl)-4-bromothiophene

Yield 32%; Light yellow solid; m.p. 86.6 °C; δ_H(200 MHz, $CDCl_3$): 7.67 – 7.57 (m, 6H), 7.54 (d, *J* = 3.4 Hz, 1H), 7.51 – 7.37 (m, 3H), 7.30 (d, *J* = 3.4 Hz, 1H); δ_C(100 MHz, $CDCl_3$): 141.29, 140.29, 132.11, 128.87, 128.72, 127.69, 127.03, 124.61, 122.97, 121.64, 113.84, 92.11, 83.40.

- **Procedure for Th-X**

Into a flask with a condenser, 1 eq. of BrTh-X, 1 eq. of copper oxide nanoparticles (CuO) and 2 eq. of sodium sulfide nonahydrate ($Na_2S.9H_2O$) were dissolved in *N*-methylpyrrolidinone (NMP) (0.05 M). The mixture was heated to 190 ºC for 24 h and then cooled to room temperature. The reaction mixture was poured into water and extracted with ethyl acetate, washed with brine, dried over Na_2SO_4 and filtered. The solvent was removed under reduced pressure and the product was purified by column chromatography using silica gel and petroleum ether. Methodology adapted from Homyak et al [3]. **Scheme A1.1** showed the synthetic route.

Th-H: thieno[3,4-*b*]thiophene

Yield 55%; Colourless incolor; δ_H(200 MHz, $CDCl_3$): 7.35 (d, *J* = 3.0 Hz, 1H), 7.33 (s, 1H), 7.25 (dd, *J* = 2.7, 0.8 Hz, 1H), 6.93 (dd, *J* = 5.6, 0.7 Hz, 1H); δ_C(100 MHz, $CDCl_3$): 147.59, 139.32, 132.39, 116.76, 111.60, 110.57.

Th-C_4: 2-butylthieno[3,4-*b*]thiophene

Yield 28%; Yellow liquid; δ_H(200 MHz, $CDCl_3$): 7.14 (s, 2H), 6.62 (t, *J* = 1.0 Hz, 1H), 2.77 (td, *J* = 7.5, 1.0 Hz, 2H), 1.76 – 1.61 (m, 2H), 1.51 – 1.33 (m, 2H), 0.95 (t, *J* = 7.2 Hz, 3H); δ_C(100 MHz, $CDCl_3$): 153.08, 147.71, 138.88, 113.33, 110.34, 110.14, 32.54, 31.73, 22.33, 13.95.

Th-C_6: 2-hexylthieno[3,4-*b*]thiophene

Yield 37%; Yellow liquid; δ_H(200 MHz, $CDCl_3$): 7.14 (s, 2H), 6.61 (t, *J* = 1.1 Hz, 1H), 2.76 (td, *J* = 7.6, 0.9 Hz, 2H), 1.77 – 1.62 (m, 2H), 1.43 – 1.27 (m, 6H), 0.90 (t, *J* = 6.5 Hz, 3H) ; δ_C(100 MHz, $CDCl_3$): 153.15, 147.72, 138.89, 113.32, 110.34, 110.14, 32.05, 31.72, 30.43, 28.92, 22.71, 14.22.

Th-C_8: 2-octylthieno[3,4-*b*]thiophene

Yield 29%; Yellow liquid; δ_H(200 MHz, $CDCl_3$): 7.13 (s, 2H), 6.61 (t, *J* = 1.0 Hz, 1H), 2.75 (td, *J* = 7.6, 1.0 Hz, 2H), 1.76 – 1.61 (m, 2H), 1.41 – 1.23 (m, 10H), 0.88 (t, *J* = 6.4 Hz, 3H); δ_C(100 MHz, $CDCl_3$): 153.15, 147.72, 138.89, 113.32, 110.34, 110.13, 32.05, 32.00, 30.47, 29.48, 29.35, 29.26, 22.80, 14.25.

Th-C_{10}: 2-decylthieno[3,4-*b*]thiophene

Yield 39%; Yellow liquid; δ_H(200 MHz, $CDCl_3$): 7.13 (s, 2H), 6.61 (t, *J* = 1.0 Hz, 1H), 2.76 (td, *J* = 7.7, 1.0 Hz, 2H), 1.77 – 1.62 (m, 2H), 1.41 – 1.21 (m, 14H), 0.89 (t, *J* = 6.4 Hz, 3H) ; δ_C(100 MHz, $CDCl_3$): 153.15, 147.72, 138.89, 113.32, 110.34, 110.13, 32.05, 30.47, 29.74, 29.69, 29.51, 29.47, 29.25, 22.83, 14.27.

Th-C_{12}: 2-dodecylthieno[3,4-*b*]thiophene

Yield 34%; Yellow solid; m.p. 42.4 °C; δ_H(200 MHz, $CDCl_3$): 7.13 (s, 2H), 6.61 (s, 1H), 2.75 (td, *J* = 7.7, 0.7 Hz, 2H), 1.73 – 1.66 (m, 2H), 1.41 – 1.27 (m, 18H), 0.89 (t, *J* = 6.8 Hz, 3H);

δ_C(100 MHz, $CDCl_3$): 153.16, 147.72, 138.90, 113.32, 110.34, 110.13, 32.07, 32.05, 30.47, 29.81, 29.78, 29.69, 29.51, 29.50, 29.25, 22.84, 14.27.

Th-Br$_3$: 2-isopropylthieno[3,4-*b*]thiophene

Yield 56%; Yellow liquid; δ_H(200 MHz, $CDCl_3$): 7.15 (s, 2H), 6.64 (d, *J* = 0.9 Hz, 1H), 3.13 – 3.03 (m, 1H), 1.35 (d, *J* = 6.9 Hz, 6H); δ_C(100 MHz, $CDCl_3$): 160.29, 147.59, 138.43, 111.15, 110.41, 110.41, 31.65, 23.83.

Th-Br$_4$: 2-isobutylthieno[3,4-*b*]thiophene

Yield 35%; Yellow liquid; δ_H(200 MHz, $CDCl_3$): 7.14 (s, 2H), 6.61 (s, 1H), 2.63 (dd, *J* = 7.2, 0.8 Hz, 2H), 2.01 – 1.91 (m, 1H), 0.99 (d, *J* = 6.6 Hz, 6H); δ_C(100 MHz, $CDCl_3$): 151.90, 147.69, 139.10, 114.28, 110.29, 110.16, 41.38, 29.72, 22.48.

Th-Br$_5$: 2-isopentylthieno[3,4-*b*]thiophene

Yield 37%; Yellow liquid; δ_H(200 MHz, $CDCl_3$): 7.13 (s, 2H), 6.62 (s, 1H), 2.77 (td, *J* = 7.9, 0.8 Hz, 2H), 1.70 – 1.56 (m, 3H), 0.95 (d, *J* = 6.4 Hz, 6H); δ_C(100 MHz, $CDCl_3$): 153.28, 147.70, 138.84, 113.22, 110.35, 110.14, 39.50, 29.96, 27.64, 22.53.

Th-Na: 2-(naphthalen-1-yl)thieno[3,4-*b*]thiophene

Yield 28%; Light yellow solid; m.p. 77.3 °C; δ_H(200 MHz, MeOD): 8.53 (dd, *J* = 7.8, 1.2 Hz, 1H), 7.93 – 7.89 (m, 2H), 7.83 (d, *J* = 3.4 Hz, 1H), 7.76 (dd, *J* = 7.1, 1.1 Hz, 1H), 7.62 – 7.45 (m, 5H); δ_C(100 MHz, MeOD): 134.74, 134.37, 131.53, 130.84, 130.19, 129.45, 128.00, 127.65, 127.17, 126.38, 125.66, 124.96, 121.60, 114.27, 90.95, 88.60.

Th-Ph: 2-phenylthieno[3,4-*b*]thiophene

Yield 20%; White solid; m.p. 196.3 °C; δ_H(200 MHz, $CDCl_3$): 7.67 – 7.60 (m, 2H), 7.47 – 7.30 (m, 4H), 7.24 – 7.20 (m, 2H); δ_C(100 MHz, $CDCl_3$): 150.06, 148.04, 138.44, 134.94, 129.02, 128.63, 126.32, 112.54, 112.20, 110.84.

Th-Bi: 2-([1,1'-biphenyl]-4-yl)thieno[3,4-*b*]thiophene

Yield 21%; White solid; m.p. 75.4 °C; (400 MHz, $CDCl_3$) δ 8.25 (s, 1H), 7.92 – 7.83 (m, 4H), 7.80 (d, J = 7.5 Hz, 2H), 7.62 (dd, J = 7.4, 1.4 Hz, 2H), 7.43 (t, J = 7.4 Hz, 2H), 7.37 – 7.32

(m, 1H); δ_C(100 MHz, $CDCl_3$): 140.84, 140.33, 140.29, 136.59, 128.95, 128.32, 127.49, 127.45, 127.05, 126.85, 126.38, 125.07, 123.09, 122.57.

A1.2 SYNTHESIS OF PYRENE MONOMERS

A1.2.1. Procedure for the non-fluorinated pyrenes

The monomers were synthesized by esterification between 1-pyreneacetic acid and the corresponding alcohol (**Scheme A1.2**). For these reactions, 0.5 g of 1-pyreneacetic acid (1.92 mmol), 3.84 mmol of EDC, 1.92 mmol of DMAP were added to 20 mL of anhydrous dichloromethane. After stirring for 30 min, 3.84 mmol of the corresponding alcohol were added and let stirring for 24 h at room temperature. The solvent was removed under reduced pressure and the product was purified by column chromatography using silica gel (eluent: dichloromethane:cyclohexane 1:1). The monomers characterization is reported in the following.

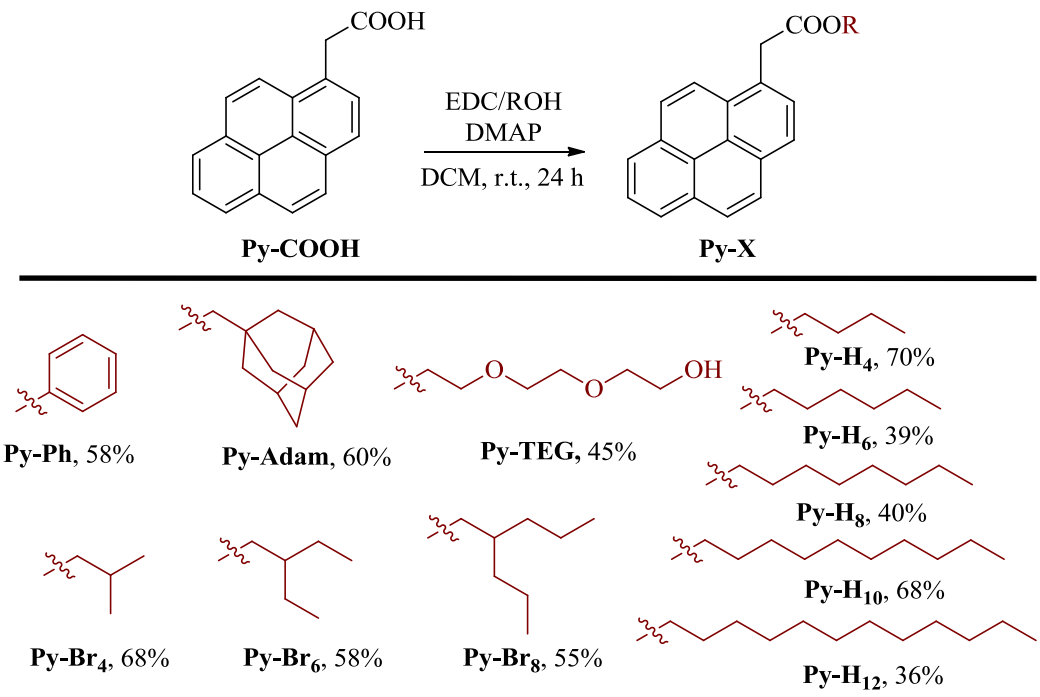

Scheme A1.2. Synthetic route to the non-fluorinated pyrenes synthesized in this study.

Pyrene-H_{12}: dodecyl 2-(pyren-1-yl)acetate

Yield 36%; Yellow crystalline solid; m.p. 56.1°C; δ_H(200 MHz, $CDCl_3$): 8.06 (9 H, m), 4.35 (2 H, s), 4.09 (2 H, t, *J* 6.6), 1.55 (2 H, m), 1.18 (18 H, m), 0.89 (3 H, t, *J* 6.4); δ_C(200 MHz, $CDCl_3$): 171.67, 131.29, 130.78, 130.75, 129.41, 128.35, 127.83, 127.38, 127.22, 125.93, 125.21, 125.06, 125.00, 124.82, 124.72, 123.32, 65.17, 39.69, 31.90, 29.58, 29.46, 29.42, 29.34, 29.10, 28.51, 25.76, 22.69, 14.13.

Pyrene-H_{10}: Decyl 2-(pyren-1-yl)acetate

Yield 68%; Yellow crystalline solid; m.p. 48.7 °C; δ_H(200 MHz, $CDCl_3$): 8.06 (m, 9H), 4.35 (s, 2H), 4.09 (t, *J* =6.6 Hz, 2H), 1.55 (m, 2H), 1.13 (m, 14H), 0.88 (t, *J* = 6.6 Hz, 3H); δ_C(50 MHz, $CDCl_3$): 171.67, 131.29, 130.78, 130.75, 129.41, 128.35, 127.83, 127.39, 127.22, 125.93, 125.21, 125.06, 125.00, 124.82, 124.73, 123.32, 65.18, 39.69, 31.84, 29.41, 29.24, 29.10, 28.51, 25.76, 22.66, 14.11.

Pyrene-H_8: octyl 2-(pyren-1-yl)acetate

Yield 40%; Yellow crystalline solid; m.p. 37.2°C; δ_H(200 MHz, $CDCl_3$): 8.06 (9 H, m), 4.35 (2 H, s), 4.10 (2 H, t, *J* 6.6), 1.55 (2 H, m), 1.14 (10 H, m), 0.84 (3 H, t, *J* 6.6); δ_C(200 MHz, $CDCl_3$): 171.66, 131.28, 130.77, 130.75, 129.41, 128.33, 127.82, 127.37, 127.21, 125.92, 125.20, 125.05, 125.00, 124.82, 124.72, 123.31, 65.17, 39.68, 31.64, 29.06, 28.51, 25.76, 22.56, 14.03.

Pyrene-H_6: hexyl 2-(pyren-1-yl)acetate

Yield 39%; Yellow crystalline solid; m.p. 29.7°C; δ_H(200 MHz, $CDCl_3$): 8.06 (9 H, m), 4.35 (2 H, s), 4.09 (2 H, t, *J* 6.6), 1.55 (2 H, m), 1.16 (6 H, m), 0.77 (3 H, t, *J* 6.5); δ_C(200 MHz, $CDCl_3$): 171.66, 131.29, 130.78, 130.75, 129.42, 128.35, 127.83, 127.39, 127.22, 125.93, 125.21, 125.06, 125.01, 124.83, 124.74, 123.32, 65.18, 39.68, 31.26, 28.47, 25.42, 22.41, 13.85.

Pyrene-H_4: butyl 2-(pyren-1-yl)acetate

Yield 70%; Yellow liquid; δ_H(200 MHz, $CDCl_3$): 8.06 (9 H, m), 4.35 (2 H, s), 4.11 (2 H, t, *J* 6.6), 1.60 (2 H, m), 1.27 (2 H, m), 0.85 (3 H, t, *J* 7.2); δ_C(200 MHz, $CDCl_3$): 171.67, 131.28, 130.78, 130.75, 129.41, 128.33, 127.81, 127.38, 127.21, 125.93, 125.20, 125.06, 125.00, 124.82, 124.72, 123.30, 64.91, 39.60, 30.54, 19.00, 13.59.

Pyrene-Br$_8$: 2-propylpentyl 2-(pyren-1-yl)acetate

Yield 55%; Yellow liquid; δ_H(200 MHz, $CDCl_3$): 8.28 (1 H, d, *J* = 9.3 Hz), 8.21 – 8.11 (4H, m), 8.06 – 7.93 (4H, m), 4.35 (2H, s), 3.99 (2 H, d, *J* = 5.7 Hz), 1.61– 1.49 (1H, m), 1.21 – 1.02 (8H, m), 0.70 (6 H, t, *J* = 6.6 Hz). δ_C(200 MHz, $CDCl_3$): 171.89, 131.45, 130.95, 130.90, 129.56, 128.52, 127.98, 127.54, 127.36, 126.08, 125.35, 125.21, 124.96, 124.89, 123.49, 67.91, 39.92, 36.92, 33.60, 19.85, 14.32.

Pyrene-Br$_6$: 2-ethylbutyl 2-(pyren-1-yl)acetate

Yield 58%; Yellow liquid; δ_H(200 MHz, $CDCl_3$): 8.29 (1 H, d, *J* = 9.3 Hz), 8.21 – 8.11 (4H, m), 8.06 – 7.93 (4H, m), 4.35 (2H, s), 4.03 (2 H, d, *J* = 5.7 Hz), 1.54 – 1.36 (1H, m), 1.30 – 1.16 (4H, m), 0.77 (6 H, t, *J* = 7.4 Hz). δ_C(200 MHz, $CDCl_3$): 171.91, 131.45, 130.94, 130.89, 129.56, 128.50, 127.96, 127.56, 127.36, 126.08, 125.35, 125.22, 125.15, 124.97, 124.88, 123.48, 67.19, 40.35, 39.83, 23.35, 11.04.

Pyrene-Br$_4$: isobutyl 2-(pyren-1-yl)acetate

Yield 68%; Yellow crystalline solid; m.p. 45.4 °C; δ_H(200 MHz, $CDCl_3$): 8.30 (1 H, d, *J* = 9.3 Hz), 8.21 – 8.12 (4 H, m), 8.06 – 7.94 (4 H, m), 4.36 (2 H, s), 3.90 (2 H, d, *J* = 6.6 Hz), 1.97 – 1.77 (1H, m), 0.82 (6 H, d, *J* = 6.7 Hz). δ_C(200 MHz, $CDCl_3$): 171.78, 131.45, 130.94, 130.90, 129.56, 128.51, 128.46, 127.98, 127.56, 127.38, 126.09, 125.36, 125.23, 125.16, 124.98, 124.89, 123.50, 71.24, 39.77, 27.81, 19.11.

Pyrene-Ph: Phenyl 2-(pyren-1-yl)acetate

Yield 58%; Yellow crystalline solid; m.p. 116.4 °C; δ_H(200 MHz, $CDCl_3$): 8.20 (m, 9H), 7.21 (m, 5H), 4.58 (s, 2H); δ_C(50 MHz, $CDCl_3$): 170.05, 150.74, 131.29, 130.98, 130.76, 129.32, 128.43, 128.13, 127.48, 127.38, 126.03, 125.82, 125.37, 125.22, 125.08, 124.94, 124.71, 123.08, 121.39, 39.70.

Pyrene-TEG: 2-(2-(2-Hydroxyethoxy)ethoxy)ethyl 2-(pyren-1-yl)acetate

Yield 45%; Slightly yellow liquid; δ_H(200 MHz, $CDCl_3$): 8.11 (m, 9H), 4.39 (s, 2H), 4.26 (m, 2H), 3.64 (m, 4H), 3.40 (m, 6H), 2.16 (s, 1H); δ_C(50 MHz, $CDCl_3$): 171.51, 131.24, 130.77, 130.73, 129.43, 128.40, 128.00, 127.88, 127.35, 127.26, 125.97, 125.24, 125.08, 124.96, 124.81, 124.67, 123.27, 72.26, 70.39, 70.10, 68.96, 64.13, 61.64, 39.37.

Pyrene-Adam: (3r,5r,7r)-Adamantan-1-ylmethyl 2-(pyren-1-yl)acetate

Yield 60%; Slightly yellow liquid; δ_H(200 MHz, $CDCl_3$): 8.11 (m, 9H), 4.37 (s, 2H), 3.69 (s, 2H), 1.49 (m, 15H); δ_C(50 MHz, $CDCl_3$): 171.67, 131.29, 130.79, 130.73, 129.42, 128.46, 128.41, 127.80, 127.39, 127.20, 125.92, 125.18, 125.04, 124.81, 124.72, 123.50, 74.45, 39.66, 39.00, 36.78, 33.22, 27.87.

A1.2.2. Procedure for the fluorinated pyrenes

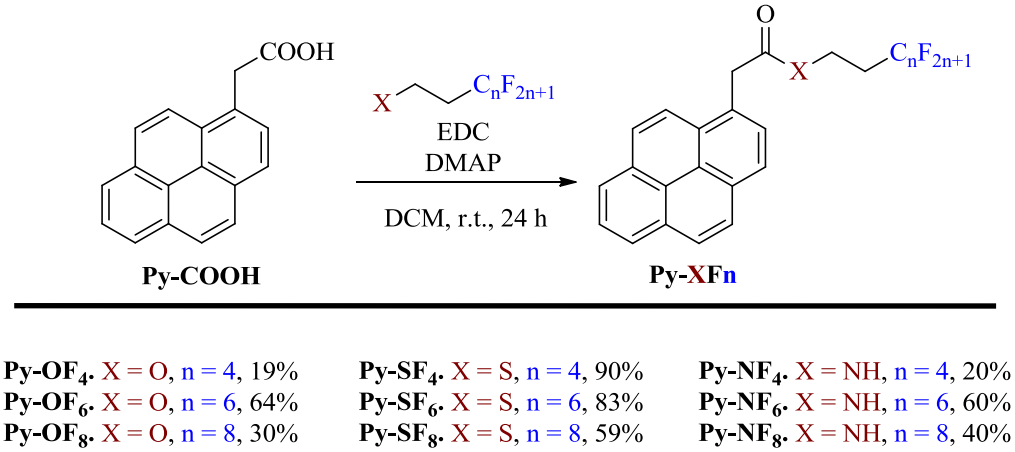

Py-OF$_4$. X = O, n = 4, 19% **Py-SF$_4$.** X = S, n = 4, 90% **Py-NF$_4$.** X = NH, n = 4, 20%
Py-OF$_6$. X = O, n = 6, 64% **Py-SF$_6$.** X = S, n = 6, 83% **Py-NF$_6$.** X = NH, n = 6, 60%
Py-OF$_8$. X = O, n = 8, 30% **Py-SF$_8$.** X = S, n = 8, 59% **Py-NF$_8$.** X = NH, n = 8, 40%

Scheme A1.3. Synthetic route to synthesize the fluorinated pyrenes bearing ester, thioester and amide linkers.

- **Procedure for Synthesis of pyrenes bearing ester linkers**

In an ice bath, 1.92 mmol of pyrene acetic acid (0.5 g), 3.84 mmol of EDC, 1.92 mmol of DMAP and 3.84 mmol of the corresponding alcohol were mixed to 20 mL of anhydrous dichloromethane. The mixture was stirred at room temperature for 24 h. After the solvent was removed under reduced pressure and the crude products were purified by column chromatography on silica gel (eluent: dichloromethane:cyclohexane, 1:1). **Scheme A1.3** showed the synthetic route.

Pyrene-OF$_8$: 3,3,4,4,5,5,6,6,7,7,8,8,9,9,10,10,10-Heptadecafluorodecyl 2-(pyren-1-yl)acetate.

Yield 30%; Yellow crystalline solid; m.p. 112.4 °C; δ_H(200 MHz, $CDCl_3$): 8.06 (m, 9H), 4.41 (t, J = 6.5 Hz, 2H), 4.37 (s, 2H), 2.43 (tt, J = 18.3 Hz, J = 6.5 Hz, 2H); δ_F(188 MHz, $CDCl_3$): -

80.74 (m, 3H), -113.56 (m, 2H), -121.91 (m, 6H), -122.73 (m, 2H), -123.51 (m, 2H), -126.12 (m, 2H); δ_C(50 MHz, $CDCl_3$): 171.17, 131.28, 130.95, 130.74, 129.41, 128.35, 128.04, 127.40, 126.02, 125.35, 125.19, 125.03, 124.86, 124.69, 123.00, 56.88 (t, *J* = 3.0 Hz), 39.21, 30.47 (t, *J* = 21.9 Hz).

Pyrene-OF_6: 3,3,4,4,5,5,6,6,7,7,8,8,8-Tridecafluorooctyl 2-(pyren-1-yl)acetate.
Yield 64%; Yellow crystalline solid; m.p. 82.0 °C; δ_H(200 MHz, $CDCl_3$): 8.06 (m, 9H), 4.41 (t, *J* = 6.6 Hz, 2H), 4.37 (s, 2H), 2.47 (tt, *J* = 18.3 Hz, *J* = 6.6 Hz, 2H); δ_F(188 MHz, $CDCl_3$): -80.77 (m, 3H), -113.60 (m, 2H), -121.95 (m, 2H), -122.94 (m, 2H), -123.62 (m, 2H), -126.18 (m, 2H); δ_C(50 MHz, $CDCl_3$): 171.18, 131.28, 130.95, 130.75, 129.41, 128.35, 128.05, 127.40, 126.03, 125.36, 125.19, 125.03, 124.86, 124.70, 123.00, 56.88 (t, *J* = 5.0 Hz), 39.22, 30.46 (t, *J* = 22.2 Hz).

Pyrene-OF_4: 3,3,4,4,5,5,6,6,6-Nonafluorohexyl 2-(pyren-1-yl)acetate.
Yield 19%; Yellow crystalline solid; m.p. 39.0 °C; δ_H(200 MHz, $CDCl_3$): 8.06 (m, 9H), 4.41 (t, *J* = 6.5 Hz, 2H), 4.37 (s, 2H), 2.45 (tt, *J* = 18.3 Hz, *J* = 6.5 Hz, 2H); δ_F(188 MHz, $CDCl_3$): -81.047 (m, 3H), -113.78 (m, 2H), -124.52 (m, 2H), -126.06 (m, 2H); δ_C(200 MHz, $CDCl_3$): 171.16, 131.26, 130.93, 130.73, 129.39, 128.33, 128.02, 127.38, 126.01, 125.34, 125.18, 125.00, 124.84, 124.67, 122.99, 56.83 (t, *J* = 4.8 Hz), 39.18, 30.35 (t, *J* = 22.7 Hz).

- **Procedure for Synthesis of pyrenes bearing thiol linkers**

To 20 mL of dichloromethane anhydrous, it was mixed 1.92 mmol of 1-pyreneacetic acid (0.5 g), 3.84 mmol of EDC, 1.92 mmol of DMAP, 1.92 mmol of triethylamine and 3.84 mmol of the corresponding thiol. The mixture was stirred at room temperature for 24 h. Then, the solvent was removed under reduced pressure and the product was purified by column chromatography using silicagel (eluent: dichloromethane:cyclohexane, 1:1). **Scheme A1.3** showed the synthetic route.

Pyrene-SF_8: S-(3,3,4,4,5,5,6,6,7,7,8,8,9,9,10,10,10-heptadecafluorodecyl) 2-(pyren-1-yl)ethanethioate
Yield 59%; Yellow crystalline solid; m.p. 157.4°C; δ_H(200 MHz, $CDCl_3$): 8.20 (m, 5H), 8.03 (m, 3H), 7.95 (d, *J* = 7.8 Hz, 1H), 4.58 (m, 2H), 3.04 (m, 2H), 2.31 (m, 2H). δ_F(188 MHz,

$CDCl_3$): -80.76 (t, *J* = 9.9 Hz, 3F), -114.63 (m, 2F), -121.88 (m, 6F), -122.78 (m, 2F), -123.42 (m, 2F), -126.16 (m, 2F). δ_C(101 MHz, $CDCl_3$): 197.20, 131.48, 131.46, 130.90, 129.94, 129.09, 128.51, 127.84, 127.53, 126.81, 126.32, 125.71, 125.54, 125.24, 125.05, 124.83, 123.11, 48.66, 31.61 (t), 20.54.

Pyrene-SF_6: S-(3,3,4,4,5,5,6,6,7,7,8,8,8-tridecafluorooctyl) 2-(pyren-1-yl)ethanethioate
Yield 83%; Yellow crystalline solid; m.p. 134.2°C; δ_H(200 MHz, $CDCl_3$): δ 8.19 (m, 5H), 8.04 (m, 3H), 7.95 (d, *J* = 7.8 Hz, 1H), 4.57 (s, 2H), 3.04 (m, 2H), 2.31 (m, 2H). δ_F(188 MHz, $CDCl_3$): -80.79 (tt, *J* = 9.7, 2.4 Hz, 3F), -114.65 (m, 2F), -121.97 (m, 2F), -122.94 (m, 2F), -123.45 (m, 2F), -126.20 (m, 2F). δ_C(101 MHz, $CDCl_3$): 197.20, 131.47, 131.45, 130.90, 129.93, 129.09, 128.51, 127.84, 127.52, 126.81, 126.32, 125.71, 125.54, 125.24, 125.04, 124.83, 123.11, 77.48, 77.16, 76.84, 48.65, 31.59 (t, *J* = 22.2 Hz), 20.53.

Pyrene-SF_4: S-(3,3,4,4,5,5,6,6,6-nonafluorohexyl) 2-(pyren-1-yl)ethanethioate
Yield 90%; Yellow solid; m.p. 114.7°C; δ_H(200 MHz, $CDCl_3$): 8.20 (m, 5H), 8.00 (m, 4H), 4.57 (s, 2H), 3.04 (t, *J* = 7.3 Hz, 2H), 2.31 (m, 2H). δ_F(188 MHz, $CDCl_3$): -81.05 (m, 3F), -114.89 (m, 2F), -124.42 (m, 2F), -126.12 (m, 2F). δ_C(50 MHz, $CDCl_3$): 197.23, 131.45, 131.43, 130.87, 129.90, 129.08, 128.50, 127.83, 127.51, 126.78, 126.31, 125.70, 125.53, 125.21, 125.03, 124.79, 123.09, 48.64, 31.47 (t, *J* = 21.7 Hz).

- **Procedure for Synthesis of pyrenes bearing amide linkers**

To 15 mL of anhydrous acetonitrile, it was mixed 1.92 mmol of 1-pyreneacetic acid (0.5 g), 3.84 mmol of EDC and 1.92 mmol of DMAP. The mixture was stirred for 30 min at room temperature and after 3.84 mmol of the corresponding amine was added with 10 mL of anhydrous acetonitrile. The mixture was let stirring for 24 h at room temperature. Then, the solvent was removed under reduced pressure and the product was purified by column chromatography using silicagel (eluent: dichloromethane:acetonitrile, 9:1). **Scheme A1.3** showed the synthetic route.

Pyrene-NF_8: N-(3,3,4,4,5,5,6,6,7,7,8,8,9,9,10,10,10-heptadecafluorodecyl)-2-(pyren-1-yl)acetamide

Yield 40%; Dark yellow solid; m.p. 158.7 °C; δ_H(200 MHz, $CDCl_3$): 8.28 (m, 5H), 8.05 (m, 3H), 7.87 (d, *J* = 8.3 Hz, 1H), 5.50 (t, J = 6.5 Hz, 1H), 4.27 (s, 2H), 3.40 (q, *J* = 6.3 Hz, 2H), 2.21 (m, 2H). δ_F(188 MHz, $CDCl_3$): -80.76 (t, *J* = 9.8 Hz, 3F), -114.30 (m, 2F), -121.98 (m, 6F), -122.83 (m, 2F), -123.75 (m, 2F), -126.21 (m, 2F). δ_C(101 MHz, $CDCl_3$): 171.43, 131.40, 131.38, 130.93, 129.68, 128.75, 128.60, 127.93, 127.89, 127.47, 126.44, 125.83, 125.62, 125.38, 125.32, 124.70, 122.77, 42.06, 32.31 (t, *J* = 4.6 Hz), 30.58 (t, *J* = 21.4 Hz).

Pyrene-NF_6: N-(3,3,4,4,5,5,6,6,7,7,8,8,8-tridecafluorooctyl)- 2-(pyren-1-yl)-acetamide

Yield 60%; Dark yellow solid; m.p. 148.3 °C; δ_H(200 MHz, $CDCl_3$): 8.29 (m, 5H), 8.04 (m, 3H), 7.87 (d, *J* = 8.3 Hz, 1H), 5.51 (t, J = 6.5 Hz, 1H), 4.29 (s, 2H), 3.42 (q, *J* = 6.3 Hz, 2H), 2.22 (m, 2H). δ_F(188 MHz, $CDCl_3$): -80.77 (m, 3F), -114.27 (m, 2F), -122.10 (m, 2F), -123.04 (m, 2F), -123.68 – (m, 2F), -126.26 (m, 2F). δ_C(50 MHz, $CDCl_3$): 171.44, 131.39, 131.36, 130.89, 129.67, 128.73, 128.62, 127.90, 127.84, 127.39, 126.46, 125.79, 125.65, 125.32, 125.27, 122.77, 42.01, 32.24 (t, *J* = 4.4 Hz), 30.66.

Pyrene-NF_4: N-(3,3,4,4,5,5,6,6,6-nonafluorohexyl)-2-(pyren-1-yl)acetamide

Yield 20%; Yellow crystalline solid; m.p. 160.4°C; δ_H(200 MHz, $CDCl_3$): 8.20 (m, 5H), 8.05 (m, 3H), 7.89 (d, *J* = 7.8 Hz, 1H), 5.49 (t, *J* = 5.2 Hz, 1H), 4.31 (s, 2H), 3.43 (q, *J* = 6.6 Hz, 2H), 2.21 (tt, *J* = 18.9, 6.7 Hz, 2H). δ_F(188 MHz, $CDCl_3$): -81.12 (tt, *J* = 9.7, 3.1 Hz, 3F), -114.50 – (m, 2F), -124.69 – (m, 2F), -126.19 (m, 2F). δ_C(101 MHz, $CDCl_3$): 171.41, 131.42, 131.39, 130.92, 129.69, 128.75, 128.63, 127.91, 127.88, 127.41, 126.48, 125.80, 125.67, 125.35, 125.29, 124.74, 122.79, 42.05, 32.26 (t, *J* = 4.6 Hz), 30.62 (t, *J* = 21.4 Hz).

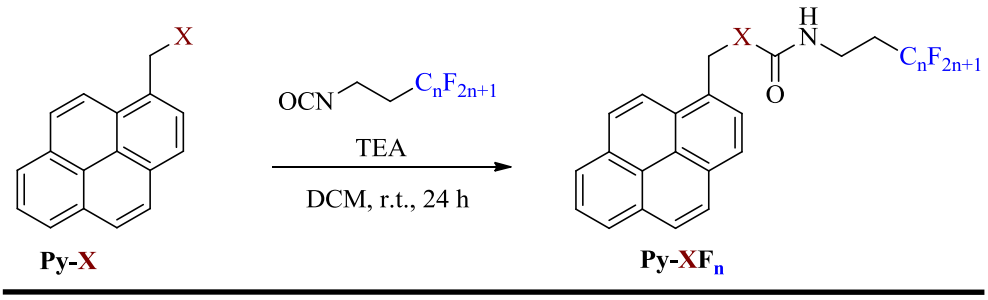

Py-NOF$_4$. X = O, n = 4, 13% **Py-NSF$_4$**. X = S, n = 4, 74% **Py-NNF$_4$**. X = NH, n = 4, 28%
Py-NOF$_6$. X = O, n = 6, 19% **Py-NSF$_6$**. X = S, n = 6, 66% **Py-NNF$_6$**. X = NH, n = 6, 27%
Py-NOF$_8$. X = O, n = 8, 13% **Py-NSF$_8$**. X = S, n = 8, 59% **Py-NNF$_8$**. X = NH, n = 8, 18%

Scheme A1.4. Synthetic route to synthesize the fluorinated pyrenes bearing carbamate, thiocarbamate and urea linkers.

- **Procedure for Synthesis of pyrenes bearing carbamate linkers**

To 20 mL of anhydrous diethyl ether, it was mixed 2.15 mmol of 1-pyrenemethanol (0.5 g), 2.15 mmol of the corresponding isocyanate and 1.2 mL of triethylamine. The mixture was stirred at room temperature for 24 h. Then, the solvent was removed under reduced pressure and the product was purified by column chromatography using silicagel (eluent: diethyl ether:cyclohexane, 1:1). **Scheme A1.4** showed the synthetic route.

Pyrene-NOF$_8$: pyren-1-ylmethyl (3,3,4,4,5,5,6,6,7,7,8,8,9,9,10,10,10-heptadecafluorodecyl)carbamate

Yield 13%; White solid; m.p. 168.8 °C; δ_H(200 MHz, $CDCl_3$): 8.16 (m, 9H), 5.84 (s, 2H), 5.02 (t, *J* = 6.0 Hz, 1H), 3.57 (q, *J* = 6.6 Hz, 2H), 2.39 (m, 2H). δ_F(188 MHz, $CDCl_3$): -80.74 (t, *J* = 9.9 Hz, 3F), -114.03 (m, 2F), -121.94 (m, 6F), -122.75 (m, 2F), -123.59 (m, 2F), -126.12 (m, 2F). δ_C(101 MHz, $CDCl_3$): 156.42, 131.95, 131.35, 130.84, 129.71, 129.16, 128.37, 128.01, 127.91, 127.50, 126.24, 125.69, 125.60, 125.04, 124.78, 123.05, 65.65, 33.65, 31.50.

Pyrene-NOF$_6$: pyren-1-ylmethyl (3,3,4,4,5,5,6,6,7,7,8,8,8-tridecafluorooctyl)carbamate

Yield 19%; White solid; m.p. 156.0°C; δ_H(200 MHz, $CDCl_3$): 8.15 (m, 9H), 5.83 (s, 2H), 5.04 (t, *J* = 5.5 Hz, 1H), 3.56 (q, *J* = 6.6 Hz, 2H), 2.38 (m, 2H). δ_F(188 MHz, $CDCl_3$): -80.78 (tt, *J* = 9.7, 2.3 Hz, 3F), -114.05 (m, 2F), -121.94 (m, 2F), -122.93 (m, 2F), -123.67 (m, 2F), -

126.17 (m, 2F).δ_C(50 MHz, $CDCl_3$): 156.42, 131.92, 131.31, 130.80, 129.67, 129.10, 128.35, 127.98, 127.90, 127.47, 126.22, 125.67, 125.59, 125.00, 124.76, 123.01, 65.65, 33.70, 31.59 (t, *J* = 19.4 Hz).

Pyrene-NOF$_4$: pyren-1-ylmethyl (3,3,4,4,5,5,6,6,6-nonafluorohexyl)carbamate

Yield 13%; White solid; m.p. 152.6°C; δ_H(200 MHz, $CDCl_3$): 8.14 (m, 9H), 5.82 (s, 2H), 5.05 (t, *J* = 5.9 Hz, 2H), 3.56 (m, 2H), 2.37 (m, 2H). δ_F(377 MHz, $CDCl_3$): -81.01 (t, *J* = 9.5 Hz, 2F), -114.18 (m, 2F), -124.54 (m, 2F), -126.00 (m, 2F). δ_C(101 MHz, $CDCl_3$): 156.42, 131.93, 131.33, 130.82, 129.68, 129.12, 128.35, 127.98, 127.88, 127.48, 126.22, 125.67, 125.59, 125.00, 124.76, 123.02, 65.64, 33.67 (t, *J* = 4.4 Hz), 31.34 (t, *J* = 20.9 Hz).

- **Procedure for Synthesis of pyrenes bearing thiocarbamate linkers**

Firstly, we reported the synthesis of the starting product pyren-1-ylmethanethiol (Py-SH) and in the following the fluorinated thiocarbamate pyrenes.

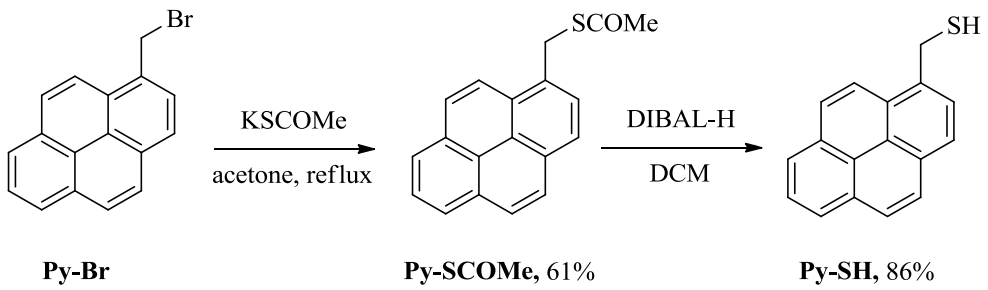

Scheme A1.5. Synthetic route to synthesize the starting product pyren-1-ylmethanethiol (Py-SH).

- **Procedure for Synthesis of Pyrene-SCOMe**

In a round bottomed flask, 1.0 g of 1-(bromomethyl)pyrene (3.39 mmol, 1 eq.) was dissolved in 50 mL of acetone. Then, a large excess of potassium thioacetate (33.9 mmol, 10 eq.) was added and the mixture was refluxed at 60 ºC for 48 h. After, the mixture was then cooled to room temperature and the solvent was removed under reduced pressure. The residue was dissolved in 200 mL of dichloromethane, extracted with water and the organic phase was dried over Na_2SO_4 and filtered. The solvent was removed under reduced pressure and the product was purified by column chromatography using silicagel (eluent:

dichloromethane:cyclohexane, 1:2). Methodology adapted from Balog et al [4]. **Scheme A1.5** showed the synthetic route.

Pyrene-SCOMe: S-(pyren-1-ylmethyl) ethanethioate

Yield 61%; Brown solid; m.p. 94.2 °C; δ_H(200 MHz, $CDCl_3$): 8.10 (m, 9H), 4.87 (s, 2H), 2.38 (s, 3H). δ_C(50 MHz, $CDCl_3$): 195.39, 131.40, 131.17, 130.90, 130.62, 129.01, 128.18, 128.08, 127.57, 127.52, 126.20, 125.52, 125.44, 125.19, 124.98, 124.87, 122.98, 31.82, 30.51.

- **Procedure for Synthesis of Pyrene-SH**

The thioester Py-SCOMe (0.53 g, 1.83 mmol, 1 eq.) was dissolved in 180 mL of anhydrous dichloromethane and the solution was cooled at -75 ºC using acetone/dry ice bath. Then, 5 eq. (9.15 mmol) of a solution of diisobutylaluminium hydrade (1.0 M in toluene) was added dropwise and the solution was stirred for 2 h. The reaction was quenched with 14 mL of aqueous solution of 3 M HCl followed by addition of 20 mL of water. The solution was let cooling to the room temperature and the organic phase was then extracted with water, dried over Na_2SO_4 and filtered. The solvent was removed under reduced pressure and the product was purified by column chromatography using silicagel (eluent: dichloromethane:cyclohexane, 1:2). Methodology adapted from Balog et al [4]. **Scheme A1.5** showed the synthetic route.

Pyrene-SH: pyren-1-ylmethanethiol

Yield 86%; Purple solid; m.p. 123.1 °C; δ_H(400 MHz, $CDCl_3$): 8.31 (d, J = 9.2 Hz, 1H), 8.18 (m, 3H), 8.12 (d, J = 7.8 Hz, 1H), 8.04 (m, 3H), 7.96 (d, J = 7.8 Hz, 1H), 4.47 (d, J = 7.1 Hz, 2H), 1.99 (t, J = 7.1 Hz, 1H). δ_C(101 MHz, $CDCl_3$): 134.76, 131.45, 130.95, 128.16, 128.08, 127.53, 127.44, 126.89, 126.20, 125.46, 125.37, 125.16, 125.02, 122.97, 27.10.

- **Procedure for Synthesis of thiocarbamate pyrenes**

To 10 mL of anhydrous dichloromethane, it was mixed 0.41 mmol of Py-SH (0.10 g, 1 eq.), 0.90 mmol of the corresponding isocyanate (1.8 eq.) and 1.5 mL of triethylamine. The mixture was stirred at room temperature for 24 h. Then, the solvent was removed under

reduced pressure and the product was purified by column chromatography using silicagel (eluent: dichloromethane:cyclohexane, 2:1). **Scheme A1.4** showed the synthetic route.

Pyrene-NSF$_8$: S-(pyren-1-ylmethyl) (3,3,4,4,5,5,6,6,7,7,8,8,9,9,10,10,10-heptadecafluorodecyl)carbamothioate

Yield 59%; Light yellow solid; m.p. 191.8 °C; δ_H(200 MHz, $CDCl_3$): 8.27 (d, *J* = 9.2 Hz, 1H), 8.21 – 8.18 (m, 2H), 8.16 (d, *J* = 9.3 Hz, 1H), 8.12 (d, *J* = 7.8 Hz, 1H), 8.07 – 7.99 (m, 4H), 5.53 (t, *J* = 5.3 Hz, 1H), 4.94 (s, 2H), 3.68 (q, *J* = 6.1 Hz, 1H), 2.42 (tt, *J* = 18.2, 6.3 Hz, 2H); δ_F(188 MHz, $CDCl_3$): -80.74 (t, *J* = 9.8 Hz, 3F), -114.61(m, 2F), -121.90– (m, 6F), -122.79 (m, 2F), -123.43 (m, 2F), -126.24 (m, 2F); δ_C(101 MHz, $CDCl_3$): 167.95, 131.42, 131.27, 130.93, 129.06, 128.17, 128.13, 127.62, 127.55, 126.22, 125.55, 125.47, 125.24, 125.00, 124.91, 123.09, 32.45.

Pyrene-NSF$_6$: S-(pyren-1-ylmethyl) (3,3,4,4,5,5,6,6,7,7,8,8,8-tridecafluorooctyl)carbamothioate

Yield 66%; White solid; m.p. 184.5 °C; δ_H(200 MHz, $CDCl_3$): 8.27 (d, *J*= 9.3 Hz, 1H), 8.25 – 8.10(m, 4H), 8.06 – 7.97 (m, 4H), 5.53 (t, *J* = 6.5 Hz, 1H), 4.93 (s, 2H), 3.68 (q, *J* = 6.4 Hz, 2H), 2.54 – 2.28 (m, 2H).; δ_F(188 MHz, $CDCl_3$): -80.76 (tt, *J* = 9.7, 2.5 Hz, 3F), -114.04 (m, 2F), -121.85 (m, 2F), -122.87 (m, 2F), -123.60 (m, 2F), -126.14 (m, 2F); δ_C(101 MHz, $CDCl_3$): 167.70, 131.41, 131.26, 130.91, 130.83, 129.05, 128.16, 128.12, 127.61, 127.53, 126.21, 125.54, 125.46, 125.23, 124.99, 124.89, 123.08, 33.92, 32.70,31.25 (t, *J* = 22.1 Hz).

Pyrene-NSF$_4$: S-(pyren-1-ylmethyl) (3,3,4,4,5,5,6,6,6-nonafluorohexyl)carbamothioate

Yield 74%; White solid; m.p. 180.1 °C; δ_H(200 MHz, $CDCl_3$): 8.13 (m, 9H), 5.55 (t, *J* = 6.0 Hz, 1H), 4.93 (s, 2H), 3.67 (q, *J* = 6.6 Hz, 2H), 2.41 (tt, *J* = 18.9, 6.6 Hz, 2H). δ_F(188 MHz, $CDCl_3$): -81.01 (tt, *J* = 9.7, 3.1 Hz, 2F), -114.27 (m, 2F), -124.51 (m, 2F), -126.01 (m, 2F). δ_C(101 MHz, $CDCl_3$): 167.73, 131.40, 131.25, 130.90, 129.04, 128.15, 128.11, 127.60, 127.53, 126.20, 125.53, 125.46, 125.21, 124.98, 124.88, 123.07, 33.87, 32.69, 31.15 (t, *J* = 21.7 Hz).

- **Procedure for Synthesis of pyrenes bearing urea linkers**

To 20 mL of anhydrous diethyl ether, it was mixed 1.87 mmol of 1-pyrenemethylamine (0.5 g), 1.87 mmol of the corresponding isocyanate and 1.5 mL of triethylamine. The mixture was

stirred at room temperature for 1 h. Then, the solvent was removed under reduced pressure and the product was purified by column chromatography using silicagel (eluent: diethyl ether). **Scheme A1.4** showed the synthetic route.

Pyrene-NNF$_8$: 1-(3,3,4,4,5,5,6,6,7,7,8,8,9,9,10,10,10-heptadecafluorodecyl)-3-(pyren-1-ylmethyl)urea

Yield 18%; White solid; m.p. 180.2°C; δ_H(200 MHz, Acetone-d$_6$): 8.45 (d, *J* = 9.5 Hz, 1H), 8.24 (m, 4H), 8.06 (m, 4H), 6.27 (t, *J* = 5.1 Hz, 1H), 5.89 (s, 1H), 5.10 (d, *J* = 5.6 Hz, 2H), 3.55 (m, 2H), 2.49 (m, 2H).; δ_F(377 MHz, Acetone-d$_6$): -81.64 (m, 3F), -114.51 (m, 2F), -122.43 (m, 6F), -123.25 (m, 2F), -124.15 (m, 2F), -126.72 (m, 2F). δ_C(101 MHz, Acetone-d$_6$): 158.64, 134.98, 132.28, 131.81, 131.60, 129.55, 128.42, 128.34, 127.93, 127.51, 126.99, 126.05, 125.98, 125.65, 125.52, 124.24, 42.58, 33.05, 32.08.

Pyrene-NNF$_6$: 1-(pyren-1-ylmethyl)-3-(3,3,4,4,5,5,6,6,7,7,8,8,8-tridecafluorooctyl)urea

Yield 27%; White solid; m.p. 187.9 °C; δ_H(200 MHz, Acetone-d$_6$): 8.42 (d, *J* = 9.3 Hz, 1H), 8.22 (m, 4H), 8.05 (m, 4H), 6.28 (t, *J* = 5.2 Hz, 1H), 5.91 (t, *J* = 5.3 Hz, 1H), 5.07 (d, *J* = 5.7 Hz, 2H), 3.57 (q, *J* = 6.6 Hz, 2H), 2.51 (tt, *J* = 20.4, 7.5 Hz, 2H). δ_F(377, Acetone-d$_6$): 81.68 (tt, *J* = 10.2, 2.5 Hz, 3F), -114.48 – (m, 2F), -122.44 – (m, 2F), -123.43 – (m, 2F), -124.21 – (m, 2F), -126.75 – (m, 2F). δ_C(101 MHz, Acetone-d$_6$): 158.64, 134.98, 132.28, 131.80, 131.59, 129.55, 128.41, 128.34, 127.93, 127.51, 126.99, 126.05, 125.98, 125.65, 125.52, 124.24, 42.58, 33.31, 32.27.

Pyrene-NNF$_4$: 1-(3,3,4,4,5,5,6,6,6-nonafluorohexyl)-3-(pyren-1-ylmethyl)urea

Yield 28 %; White solid; m.p. 185.1 °C; δ_H(200 MHz, Acetone-d$_6$): 8.42 (d, *J* = 9.3 Hz, 1H), 8.21 (m, 4H), 8.05 (m, 4H), 6.28 (t, *J* = 5.3 Hz, 1H), 5.90 (t, *J* = 6.1 Hz, 1H), 5.07 (d, *J* = 5.6 Hz, 2H), 3.55 (q, *J* = 6.5 Hz, 2H), 2.49 (tt, *J* = 19.5, 6.6 Hz, 1H). δ_F(188 MHz, Acetone-d$_6$): -81.95 (tt, *J* = 9.5, 3.3 Hz, 3F), -114.74 (m, 2F), -125.17 (m, 2F), -126.66 – (m, 2F).; δ_C(101 MHz, Acetone-d$_6$): 158.68, 134.91, 132.26, 131.78, 131.58, 129.52, 128.40, 128.32, 127.92, 127.46, 126.97, 126.04, 125.97, 125.64, 125.49, 124.19, 42.57, 33.27 (t, *J* = 5.2 Hz), 32.16 (t, *J* = 20.7 Hz).

REFERENCES FOR ANNEX A1

(1) Patra, A.; Wijsboom, Y. H.; Leitus, G.; Bendikov, M. Tuning the Band Gap of Low-Band-Gap Polyselenophenes and Polythiophenes: The Effect of the Heteroatom. *Chem. Mater.* **2011**, *23* (12), 896–906.

(2) Bae, W. J.; Scilla, C.; Duzhko, V. V.; Ho Jo, W.; Coughlin, E. B. Synthesis and Photophysical Properties of Soluble Low-Bandgap Thienothiophene Polymers with Various Alkyl Side-Chain Lengths. *J. Polym. Sci. Part A Polym. Chem.* **2011**, *49* (15), 3260–3271.

(3) Homyak, P. D.; Tinkham, J.; Lahti, P. M.; Coughlin, E. B. Thieno [3,4-*b*] Thiophene Acceptors with Alkyl, Aryl, Perfluoroalkyl, and Perfluorophenyl Pendants for Donor − Acceptor Low Bandgap Polymers. *Macromolecules* **2013**, *46*, 8873–8881.

(4) Balog, M.; Rayah, H.; Derf, F. Le; Salle, M. A Versatile Building Block for EDOT or PEDOT Functionalization W. *New J. Chem.* **2008**, *32*, 1183–1188.

ANNEX A2 – ELECTROPOLYMERIZATION PROCESS

A2.1 ELECTROPOLYMERIZATION OF CONDUCTING POLYMERS

The electropolymerization was carried by an Autolab potentiostat (Metrohm). A three-system electrode was used with the working electrode, a carbon-rod as the counter electrode and a SCE as a reference. Gold-coated silicon wafers of 2 cm^2 was used as a working electrode for all the experiments with thienothiophenes (*Chapter 2*) and usually used for the experiments with the pyrenes (*Chapter 3*). However, ITO plates (8 cm^2) substrates were also used for some experiments with the pyrenes (this is informed in the beginning of each experiment). A 0.1 M solution of the electrolyte in anhydrous solvent and 0.01 M of each monomer was added inside a glass cell under argon. The E^{ox} was first determined by cyclic voltammetry for all the experiments. The deposition was performed by different deposition methods:

- Cyclic Voltammetry: this method allows to obtain films highly homogeneous. The polymer films were obtained using a scan rate of 20 mV/s and the scans were done between -1.0 V (for thienothiophenes) and -0.7 V (for pyrenes) to E^w, of each monomer *vs* SCE. Surfaces were prepared after deposition of 1, 3 and 5 deposition scans to study the polymer growth.
- Constant Potential: also called as imposed potential. The E^{ox} was first determined by cyclic voltammetry. The polymer films were obtained applying different charges (Qs = 12.5, 25, 50, 100, 200 and 400 mC cm^{-2}) at an imposed E^w for each monomer *vs* SCE.
- Galvanostatic Deposition: the deposition was performed by an imposed current density during a fix time. Five currents (0.1, 0.5, 1, 5 and 10 mA) and five deposition times (10 20, 40, 80 and 160 s) were used in order to perform the polymerization.
- Square Pulse Deposition: for the thienothiophene monomers, the deposition occurs using 5 and 10 s as a polymerization time (t_p) at a potential 2.46 V (E^w used for Thienothiophene-2) and 2 s as a relaxing time (t_r) at a potential -1 V. For the first

experiment, repetition cycles of 4x and 16x were used for t_p = 5 s and 2x and 8x for t_p = 10 s. Posteriorly, the effect of more repetition cycles were studied (from 1 to 32 times). A schematic representation of the deposition by square pulse method is shown in ***Figure A2.1***.

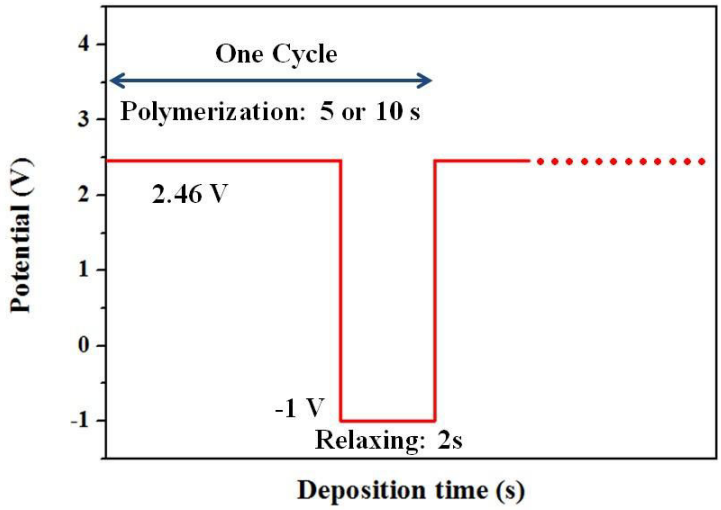

Figure A2.1. Schematic curve for square pulse deposition method.

After the electrodeposition, the surfaces were washed in the solvent used to remove the remaining electrolyte and the surfaces were let slowly drying. The characterization was done at least 24 h after the electropolymerization.

A2.2 ELECTROPOLYMERIZATION OF ANALOGOUS SMOOTH POLYMERS

Smooth surfaces of each monomer were also prepared by a two-step electrodeposition method to obtain the Young's contact angle (θ^Y). First, a thin layer of film was deposited with an imposed potential method and a low charge (1 mC cm^{-2}) in a very low concentration of each monomer (± 2 mg) in a solution of 0.1 M electrolyte/anhydrous solvent. A reduction step was followed by cyclic voltammetry performed at 1 scan from 1.5 V to 0 V *vs* SCE at a scan rate of 20 mV/s just in the 0.1 M solution containing the electrolyte/anhydrous solvent, without addition of the monomer (free polymer solution). The same apparatus was used to prepare the smooth surfaces.

A2.3 OXIDATION POTENTIAL AND WORKING POTENTIAL

Here is presented all the E^{ox} and E^{w} for all the monomers used in this work. The data are presented for surfaces prepared in gold plate substrates and polymerized in 0.1 M solution of Bu_4NClO_4/anhydrous dichloromethane for the thienothiophenes (*Chapter 2*) and in 0.1 M solution of Bu_4NClO_4/anhydrous acetonitrile for the pyrenes (*Chapter 3*). Any change in these conditions will be informed.

A2.3.1 Oxidation Potential and Working Potential for the Thienothiophene Monomers presented in *Chapter 2*

Table A2.1. E^{ox} and E^{w} for each monomer presented in the *Section 2.1* by electrochemical process. Electropolymerization in 0.1 M of Dichloromethane/Bu_4NClO_4.

Monomers	E^{ox} (V)	E^{w} (V)
Thienothiophene-1	2.49	2.28
Thienothiophene-2	2.68	2.46
Thienothiophene-3	2.49	2.13
Thienothiophene-4	2.34	2.06
Thienothiophene-5	2.76	2.45

Table A2.2. E^{ox} and E^{w} for Thienothiophene-2 presented in the *Section 2.1* by electrochemical process using different conditions of polymerization.

Solution 0.1 M	E^{ox} (V)	E^{w} (V)
Bu_4NBF_4/dichloromethane	2.76	2.52
Bu_4NPF_6/dichloromethane	2.75	2.56
Bu_4NClO_4/dichloromethane + 0.5 % water	2.74	2.57
Bu_4NClO_4/dichloromethane + 1 % $HClO_4$	2.75	2.57

Table A2.3. E^{ox} and E^{w} for each monomer presented in the *Section 2.2* by electrochemical process. Electropolymerization in 0.1 M of Dichloromethane/Bu_4NClO_4.

Monomers	E^{ox} (V)	E^{w} (V)
Th-H	2.35	2.21
Th-C_4	1.57	1.50
Th-C_6	1.65	1.57
Th-C_8	1.65	1.59
Th-C_{10}	1.67	1.57
Th-C_{12}	1.62	1.53
Th-Br_3	1.70	1.60
Th-Br_4	1.73	1.61
Th-Br_5	1.71	1.63
Th-Na	2.11	2.01
Th-Ph	2.35	2.24
Th-Bi	2.22	2.11

A2.3.2 Oxidation Potential and Working Potential for the Pyrene Monomers presented in *Chapter 3*

Table A2.4. E^{ox} and E^{w} for each non-fluorinated pyrene monomer presented in the *Section 3.1* by electrochemical process. Electropolymerization in 0.1 M of Acetonitrile/Bu_4NClO_4.

Monomers	E^{ox} (V)	E^{w} (V)
Py	1.67	1.57
Py-H_{12}	1.60	1.52
Py-H_{10}	1.61	1.53
Py-H_8	1.61	1.54
Py-H_6	1.64	1.56
Py-H_4	1.65	1.56
Py-Br_8	1.60	1.53
Py-Br_6	1.61	1.54
Py-Br_4	1.62	1.55
Py-Ph	1.67	1.58
Py-TEG	1.58	1.50
Py-Adam	1.59	1.50

Table A2.5. E^{ox} and E^{w} for each fluorinated pyrene monomer presented in the *Section 3.2* by electrochemical process. Electropolymerization in 0.1 M of Acetonitrile/Bu_4NClO_4.

Monomers	E^{ox} (V)	E^{w} (V)
Py-OF_4	1.65	1.59
Py-OF_6	1.61	1.56
Py-OF_8	1.60	1.54
Py-SF_4	1.61	1.56
Py-SF_6	1.63	1.55
Py-SF_8	1.56	1.51
Py-NF_4	1.46	1.40
Py-NF_6	1.51	1.44
Py-NF_8	1.54	1.49
Py-NOF_4	1.47	1.44
Py-NOF_6	1.48	1.45
Py-NOF_8	1.47	1.43
Py-NSF_4	1.55	1.49
Py-NSF_6	1.53	1.47
Py-NSF_8	1.51	1.46
Py-NNF_4	1.55	1.51
Py-NNF_6	1.54	1.50
Py-NNF_8	1.54	1.49

Table A2.6. E^{ox} and E^{w} for polymerization of Py-OF_6 presented in the *Section 3.3* by electrochemical process using different conditions.

Solution 0.1 M	E^{ox} (V)	E^{w} (V)
Bu_4NClO_4/dichloromethane	2.07	1.90
Bu_4NClO_4/acetonitrile	1.62	1.55
Bu_4NBF_4/acetonitrile	1.70	1.63
Bu_4NPF_6/acetonitrile	1.59	1.56
Bu_4NTf_2N/acetonitrile	1.68	1.61
$Bu_4NCF_3SO_3$/acetonitrile	1.63	1.55
$Bu_4NC_4F_9SO_3$/acetonitrile	1.70	1.61
$LiClO_4$/acetonitrile	1.61	1.52
$LiTf_2N$/acetonitrile	1.49	1.45

Table A2.7. E^{ox} and E^{w} as function of mol% of Py-*n*F_6 *vs* Py-COOH presented in the *Section 3.6*. Electropolymerization at 0.1 M of Bu_4NClO_4/acetonitrile.

mol% of Py-*n*F_6 vs Py-COOH		E^{ox} (V)	E^{w} (V)
Py-OF_6	**0**	1.66	1.59
	25	1.65	1.58
	50	1.65	1.59
	75	1.64	1.58
	100	1.61	1.56
Py-NF_6	**25**	1.64	1.58
	50	1.60	1.54
	75	1.55	1.49
	100	1.51	1.47

Table A2.8. E^{ox} and E^{w} as function of mol% of Py-OF_6 *vs* Py-Adam presented in the *Section 3.7*. Electropolymerization at 0.1 M of Bu_4NClO_4/acetonitrile.

mol% of Py-OF_6 *vs* Py-Adam	E^{ox} (V)	E^{w} (V)
0	1.60	1.54
25	1.60	1.53
50	1.64	1.56
75	1.66	1.58
100	1.61	1.55

ANNEX A3 – METHODS

A3.1 MONOMER CHARACTERIZATION

A3.1.1 NMR (Nuclear Magnetic Ressonance)

NMR spectra were obtained with a W-200 MHz and W-400 MHz (Bruker). The monomers were characterized by proton, fluorine and carbon NMR. Acetone, chloroform and methanol were used as deuterated solvent for the analysis.

A3.1.2 DSC (Differential Scanning Calorimetry)

Melting points of each monomer were determined *via* DSC (Jade DSC-Perkin Elmer) using a thermal scan from 0 ºC to 250 ºC at a rate of 10 ºC min^{-1}.

A3.1.3 Photophysical characterization

UV-visible absorption spectra were measured with a Varian CARY 4000 double-beam spectrophotometer in quartz cells with path length 1 cm, by using slit widths of 2 nm and scan rate of 600 nm/min. Excitation and fluorescence spectra were measured on a Horiba Fluorolog-3 (in quartz cells with path length 1 cm for liquid solution in right angle configuration), by using slit widths of 1.5 nm and an integration time of 0.1 s. The solvents were of spectrometric grade (dichloromethane), optical density was adjusted below 0.1 to avoid reabsorption artifacts. This work was done in collaboration with the Prof. Rachel Méallet-Renault research group from the Université Paris-Saclay, in Orsay, France.

A3.2 SURFACE CHARACTERIZATION

A3.2.1 Surface Wettability

Contact angles measurements were determined by the sessile drop method using a DSA30 goniometer (Krüss). The static contact angles (θ) were measured using the sessile drop method where droplets of 2 µL were gently deposited on the surface at room temperature using a microsyringe. The images were captured using the software "Drop Shape Analysis System". Liquids of different surface tensions (γ_{LV}) were used to evaluate the wettability: deionized water (72.8 mN/m), diiodomethane (50.0 mN/m) and hexadecane (27.6 mN/m).

When the surfaces had high contact angles, the dynamic contact angles were analyzed usually using the tilted-drop method. In this method, droplets of 6 µL were deposited and the surface was inclined until the drops roll off until the maximum inclination of the surface, also called as sliding angle (α). The advanced (θ_{adv}) and receding (θ_{rec}) contact angles are taken just before the droplet moving giving the hysteresis $H = \theta_{adv} - \theta_{rec}$. If the droplet does not move after an inclination of 90 °, the substrate is called sticky.

Using the Owens–Wendt equation ($\gamma_{LV}(1+\cos\theta) = 2(\gamma^D_{LV}.\gamma^D_{SV})^{1/2} + 2(\gamma^P_{LV}.\gamma^P_{SV})^{1/2}$) is possible to determine the surface free energy (γ_{SV}) and its dispersive (γ^D_{SV}) and polar (γ^P_{SV}) parts of the smooth surfaces. Three different liquids (water, diiodomethane and hexadecane) can be used which γ_{LV}, γ^D_{LV} and γ^P_{LV} are known, γ^D_{SV} and γ^P_{SV} can be calculated by drawing the function y = ax + b where $y = \gamma_{LV}(1+\cos\theta)/2(\gamma^D_{LV})^{1/2}$ and $x = (\gamma^P_{LV})^{1/2}/(\gamma^D_{LV})^{1/2}$. Then, $\gamma^D_{SV} = b^2$ and $\gamma^P_{SV} = a^2$ are determined. In our case, γ^D_{SV} and γ^P_{SV} were directly obtained using the software "Drop Shape Analysis" of our goniometer.

A3.2.2 Surface Morphology

The scanning electron microscopy (SEM) images were given by a 6700F microscope (JEOL) and 3 kV electron acceleration.

A3.2.3 Surface Roughness

The mean arithmetic (Ra) and quadratic (Rq) roughness of the surfaces were determined by an optical profilometry (Wyko NT 1100 of Bruker). The measurements were done with the High Mag Phase Shift Interference (PSI), the 50× objective and the 0.5× field of view. The results were taken using the software "Vision".

A3.2.4 Infrared Spectroscopy (IR)

The IR spectra were obtained using a Spectrum Spotlight 300 FT-IR microscope (Perkin Elmer). The spectra were collected using the ATR mode and the in reflectance on gold plates with a spectral resolution of 4 cm^{-1} and 32 scans.

A3.2.5 Gel Permeation Chromatography (GPC)

The polymer chain lengths were determined by GPC. The polymers were dissolved in chloroform and after they were concentrated in tetrahydrofuran. The number-average molar mass (Mn) and weight-average molar mass (Mw) and as a consequence the polymerization degrees (PD) were determined by the society Specific Polymers with the method SP_RI_THF-PS (polystyrene calibration).

A3.2.6 Photophysical characterization

UV-visible absorption spectra of films on ITO surfaces were measured with a Varian CARY 4000 double-beam spectrophotometer, by using slit widths of 2 nm and scan rate of 600 nm/min. Excitation and fluorescence spectra were measured on a Horiba Fluorolog-3 in a front-face configuration, by using slit widths of 1.5 nm and an integration time of 0.1 s.
Fluorescence images were acquired using Leica TCS SP5-AOBS confocal laser scanning microscope. The surfaces were rinsed by distilled water and imaged using ×63-1.4 numerical aperture plan apochromat oil immersion objective. The size of the *xy* image was 512 × 512 pixels (image size 20 × 20 μm^2) recorded on 8 bits. UV laser (364 nm) was used as the excitation source regardless of the fluorescent probes. The corresponding fluorescence was

collected in the 380-750 nm spectral range. Each fluorescence intensity image corresponds to an average of 4 frames. This work was done in collaboration with the Prof. Rachel Méallet-Renault research group from the Université Paris-Saclay, in Orsay, France.

A3.3 BIOEXPERIMENTS

This work was done in collaboration with the Prof. Rachel Méallet-Renault research group from the Université Paris-Saclay, in Orsay, France.

A3.3.1 Bacterial Strains

Two collection strains, *Methicillin-susceptible Staphylococcus aureus* (SA) ATCC 27217 and *Pseudomonas aeruginosa* (PA) ATCC 15442 were kept at -80 °C in tryptic soy broth (TSB) (bioMérieux, France) containing 20% (vol/vol) glycerol as stock solutions. Before usage, cells were diluted 10 times and reinoculated in TSB twice (overnight culture, after 8 h culture). Bacterial growth and incubation were carried out at 37 °C.

A3.3.2 Confocal Laser Scanning Microscopy

Fluorescence images were acquired using a Leica TCS SP5-AOBS confocal laser scanning microscope. Polypyrene films and glass (as control) surfaces were incubated with the bacterial strain in static mode during 2 h for bacterial adhesion and 24 h for biofilm formation. Prior to observation of 2 h bacterial adhesion on polymeric films and glass control surfaces, the samples were washed 3 times with 150 mM NaCl sterile saline solution to eliminate non-adherent cells. For biofilm formation, culture medium was gently removed from all surfaces and replaced with saline solution (in two times, first one to gently eliminate floating cells).

Prior to each observation, bacteria were stained with 50 µg/mL of each dye: SYTO 61 (λ_{exc} = 633 nm) for PPy-H_4 and PPy-Br_4, and FM®5-95 (λ_{exc} = 633 nm) for PPy-OF_6. To analyze the toxicity of the polymer film for the ratio of dead/live cells, bacteria were also stained with 0.4 µM SYTOX® Red Dead Cell Stain (Life Technologies, France) (λ_{exc} = 488 nm), a nucleic acid stain that easily penetrates cells with compromised plasma membranes (dead cells) only.

Experiment was done in PPy-OF_6 surfaces. The polymer films were sequentially excited at 364 nm.

Fluorescence emissions were collected between 700 nm and 800 nm for FM®5-95, 650 nm and 700 nm for SYTOX® Red and SYTO 61 and between 450 nm and 550 nm for polypyrene films. Images were acquired using ×63 - 1.4 numerical aperture plan apochromat oil immersion objective. The size of the xy image was 512 × 512 pixels (image size as follows, zoom 1: 246.03 µm², zoom 3: 82.01 µm²) and the zooms were taken on triplicate. Each fluorescence intensity image corresponds to an average of 3 frames. Bacteria coverage area percentage was calculated and compared between the images corresponding to the same zoom for each sample using "Image J" software. The quantitative results presented in this section correspond to zoom 1 which represents a larger area of analysis leaving out the bias that could be introduced by selecting specific areas while the confocal images were presented for zoom 3.

A3.4 EJECTION TESTS

The catapult-like apparatus was built with a spring of variable stiffness. The catapult is initially loaded and maintained in the rest position with an electro-magnet. The initial distance between the plate and its equilibrium position can be varied and is typically of a few millimeters. Once the electro-magnet is switched-on, the plate is subject to a sudden and large acceleration, typically 10 times the gravity acceleration. Droplets are propelled with this device and the ejection dynamics is imaged by a high speed camera with frame rates ranging from 500 to 5000 fps. For each ejection, a space-time diagram is built along a vertical line passing through the center of the droplet and it displays both the plate and the droplet motion as functions of time. The amplitude A, the velocity of the plate or velocity of the substrate (V_p) and the velocity of ejection (V_g) are directly measured from the diagram.

Experiments were performed with a water droplet diameter ∅ ≈ 1.3 mm and catapult frequencies between 20 and 60 Hz. For a given water droplet size and a given catapult frequency, a linear regime is found and characterized by the ejection velocity or water droplet velocity (V_g), which means the velocity when the droplets left the surface, and by the velocity of the plate or velocity of the substrate (V_p). Both V_g and V_p are directly related to the load amplitude (A). At low A, the adhesion with the substrate cannot be neglected anymore and the

ejection is less efficient. At large A, the velocity is smaller than expected as well, which seems related to the non-linear response of the drop (large deformation and/or fragmentation) to strong solicitations.

Abstract

Controlling surface hydrophobicity and water adhesion is a fundamental tool for various applications. Electropolymerization is a very versatile method that can be used to control these parameters and for the production of tunable nanostructured materials. Here, we show that by differentiating the polymerizable core (thienothiophene or pyrene), varied surface morphologies and wettabilities are produced by a direct electropolymerization process. Nanotubes and tree-like structures are obtained starting from thienothiophene derivatives without using any template. Depending on the electrodeposition method and parameters, different kinds of nanotubes are obtained. The electrochemical method and the grafted substituent play an important role on the surface structuration. The surfaces display different contact angles, but always with high water adhesion. On the other hand, pyrenes with various substituents are employed to produce hydrophobic/ superhydrophobic and fluorescent surfaces and, for the first time, with anti-bioadhesion and anti-biofilm properties. Copolymers of pyrenes were electrodeposited to yield surfaces with pH-responsivity and controllable water adhesion. A new method using a catapult system was implemented to measure the adhesive behavior of sticky and non-sticky surfaces. Thus, it has been shown the important role of the monomer core on the final properties of the surfaces opening new doors to explore this domain in the surface science field and applications.

Résumé

Le contrôle de l'hydrophobie de surface et de l'adhésion à l'eau est un outil fondamental pour diverses applications. L'électropolymérisation est une méthode très polyvalente qui peut être utilisée pour contrôler ces paramètres et pour la production de matériaux nanostructurés à façon. Ici, nous montrons qu'en différentiant le noyau polymérisable (thienothiophène ou pyrène), des morphologies et des mouillabilités de surface variées sont produites par un procédé direct d'électropolymérisation. Des nanotubes et des structures en forme d'arbre sont obtenus en utilisant des dérivés de thienothiophène sans utiliser de membrane structurante. En fonction de la méthode d'électrodéposition et des paramètres, différents types de nanotubes sont obtenus. La méthode électrochimique et le substituant greffé jouent un rôle important dans la structuration de surface. Les surfaces affichent différents angles de contact, mais toujours une forte adhésion à l'eau. D'autre part, des pyrènes avec divers substituants sont utilisés pour conduire à des propriétés hydrophobes/superhydrophobes, fluorescentes et, pour la première fois, à des applications en anti-bioadhesion et anti-biofilm. Des copolymères de pyrène ont été électrodéposés pour donner des surfaces avec une sensibilité au pH et une adhérence contrôlable à l'eau. Une nouvelle méthode utilisant un système de catapult a été mise en œuvre pour mesurer le comportement adhésif de surfaces collantes et non collantes. Ainsi, il a été montré le rôle important du noyau de monomère sur les propriétés finales des surfaces ouvrant de nouvelles portes pour explorer ce domaine dans le domaine des sciences de surface et de leurs applications.